Fluidized Bed Ice Slurry Generator

for

Enhanced Secondary Cooling Systems

Proefschrift

ter verkrijging van de graad van doctor
aan de Technische Universiteit Delft,
op gezag van de Rector Magnificus prof.dr.ir.J.T.Fokkema,
voorzitter van het College voor Promoties,
in het openbaar te verdedigen op dinsdag 1 juni 2004 om 15.30 uur

door Jeroen Willem MEEWISSE

scheikundig ingenieur

geboren te Pijnacker

Dit proefschrift is goedgekeurd door de promotor:
Prof.ir. H. van der Ree

Toegevoegd promotor: Dr.ir. C.A. Infante Ferreira

Samenstelling promotiecommissie:

Rector Magnificus, voorzitter
Prof. ir. H. van der Ree, Technische Universiteit Delft, promotor
Dr.ir. C.A. Infante Ferreira, Technische Universiteit Delft, toegevoegd promotor
Prof. dr. G.J. Witkamp, Technische Universiteit Delft
Prof. dr. R.F. Mudde, Technische Universiteit Delft
Prof. dr. P.W. Egolf, University of Applied Sciences of Western Switzerland
Prof. dr. J. Paul, Technical University of Denmark
Dr. D.G. Klaren, Klaren BV

Dit onderzoek is gedeeltelijk gefinancierd door Novem in het kader van het BSE-NECST programma.

ISBN 90-9018122-9

Contents

Fluidized Bed Ice Slurry Generator for Enhanced Secondary Cooling Systems

Summary

Scope

The risks involved with ammonia or hydrocarbon cooling can be reduced by installing a secondary cooling cycle. In such a system cold is generated in a primary cooling cycle and then transferred to a non-toxic, non-flammable secondary cooling fluid. The system components that contain primary refrigerant, can be located in a controlled machine room, while the cooling capacity is distributed to consumer areas with the safe secondary fluids.

Ice slurries are efficient secondary cooling fluids because they utilize the latent heat effect involved with the ice/water phase change. A high heat capacity is available at relatively constant temperatures, while ice slurries are also pumpable. Furthermore, ice slurries can be stored in tanks for later use, which allows for benefits of peak load reduction and also allows for shifting of the cooling load to the nighttime, when electricity tariffs are low and the primary cycle efficiency is high. Ice slurries can therefore result in a significant reduction of the energy consumption, both compared with direct cooling systems and compared with secondary cooling systems based on non-phase change cooling fluids.

The objective of the research described in this thesis is to enhance secondary cooling system performance by using a fluidized bed ice slurry generator. The research was initiated because ice slurries, though efficient cold carriers, are not applied widely in secondary cooling systems yet. The main obstacle is the ice slurry generator. The fluidized bed ice slurry generator may be an attractive alternative because it potentially has a high heat transfer performance, steady operation and low maintenance costs. In this new type of ice slurry generator the impacts of solid inert particles of a fluidized bed are used to keep heat exchanger walls free of ice and to also increase heat transfer coefficients.

In this research the heat and mass transfer processes in the fluidized bed ice slurry generator are studied in detail. Also the properties of the ice slurries and their behavior in secondary cooling cycles are evaluated. This with the final aim to determine in which applications the novel ice slurry systems will be practicable.

Method

In order to evaluate the applicability of fluidized bed ice slurry generators, the heat transfer performance, the mechanism of ice formation and the type of ice crystals formed are determined. Also the range of steady operating conditions is evaluated, where attention is focused on freeze-up conditions of the fluidized bed because of ice adhesion. An improved understanding of these processes may also be applicable in other fields where fluidization, crystallization or (ice) scaling play a role. For these purposes an experimental set-up of a fluidized bed ice slurry generator is developed.

The influence of various ice slurry parameters and fluidization conditions on the ice slurry generation is determined in the set-up, which can be operated in stationary or circulating mode. Furthermore, a first experimental evaluation of a rotary device is done in the set-up. A theoretical discussion of parallel fluidization of multiple beds is also included.

The fluidized bed ice slurry generator is then optimized as part of a secondary cooling system. The optimization includes the possible energetic and economic benefits involved with ice slurries. The properties of the ice slurries themselves are required for this optimization, as well as the ice slurry behavior in other components of the secondary cooling system, which include transport, storage and utilization of the ice slurries.

Finally a dynamic simulation model is developed, in which the energy consumption of ice slurry systems for a given cooling load profile and circumstantial parameters can be determined. With the dynamic model case studies are done in air-conditioning, supermarket cooling and food cooling and freezing, in order to determine in which applications the novel ice slurry systems may result in a reduction of the energy consumption and total costs.

Results

The ice slurry crystals produced in the experimental set-up of the fluidized bed ice slurry generator are similar to those generated with other methods already applied in ice slurry cooling systems. This is confirmed with NaCl, ethylene glycol and dextrose as freezing point depressants and therefore performance of the fluidized bed ice slurry generator in this respect is sufficient.

The formation of ice crystals does not have a large effect on heat transfer coefficients in the fluidized bed ice slurry generator. If at a given set of operating conditions stable ice slurry production is possible, heat transfer coefficients are similar to those in the fluidized beds before start of ice crystal formation.

The ice fraction is the most relevant parameter that determines the thermophysical properties of ice slurries. Property models predicting freezing point, density, thermal conductivity, enthalpy and heat capacity of ice slurries reported in literature can be applied in models to predict wall-to-bed heat transfer coefficients. An empirical model using hydraulic Nusselt and Reynolds numbers is proposed that predicts heat transfer coefficients in the fluidized bed ice slurry generator accurately:

$$Nu_h = 0.0612 \cdot Re_h^{0.724} Pr^{0.625}$$

Exponents of this model are similar to those of generalized models for liquid/solid fluidized beds found in literature. Significant differences are only found in the proportional factor. Relatively low temperature levels during ice slurry production are the most likely cause for the differences, because no clear influence of the ice crystals is observed.

The maximum wall-to-bed temperature difference allowable during ice slurry generation before freeze-up of the fluidized bed is observed to depend linearly on the concentration of freezing point depressant in the range of conditions investigated. This is caused by a remarkably constant ice crystal growth velocity at the walls, which is primarily determined by the solute mass transfer. At increasing freezing point depressant concentration a larger temperature difference can be applied, while the ice crystal growth velocity at the wall remains constant. Additional heat transferred above the crystal growth velocity at the wall, but under the maximum wall-to-bed temperature difference allowable, results in ice crystal formation in the bulk of the fluidized bed.

Fluidization conditions must be such that the constant ice crystal growth velocity at the walls can be removed, in order to prevent freeze-up. The varying maximum temperature difference allowable between freezing point depressants is determined by the ice removal capacity. This ice removal capacity depends on the number of effective particle-wall impacts. Whether a particle impact is effective, depends on the adhesive strength of the ice to the wall and on the kinetic energies of the solid particles at the wall of the fluidized bed.

An approach is introduced in which the work of adhesion of ice to the walls and an exponential distribution of the kinetic energies of the solid particles are used to determine the number of effective particle impacts. The results correspond qualitatively well with the trends observed of the maximum temperature differences allowable. The approach is expected to be applicable for quantitative prediction of freeze-up conditions during ice crystal formation.

The stationary fluidization process of the experimental set-up has been quantified in detail. The general theory on liquid/solid fluidization of Richardson and Zaki has been validated for use in the fluidized bed ice slurry generator. An evaluation of the number of effective particle-wall impacts has been used to optimize the stationary fluidized bed ice slurry generator, by determining the optimal bed voidage, particle size and particle/bed diameter ratio.

Preliminary experiments with circulation of the fluidized bed particles have not led to an improvement of the fluidized bed systems, due to limitations of the experimental set-up. The installation of a rotor system also has not shown improvement of the fluidized bed performance, mainly because of the hindrance effects of the rotor on the fluidization. From the theoretical evaluations it follows that from circulation more benefits are to be expected, while it is considered unlikely that a rotor system will lead to further improvements.

A theoretical study of parallel fluidization of multiple beds has shown that there are methods feasible for use with ice slurries, although some parallel fluidization systems are excluded.

Because the ice fraction is such a relevant parameter, the use of ice concentrators or separation methods in between stages of a secondary cooling cycle, is likely to improve system performance. The freezing point depressant used is of influence mainly at lower temperature applications, where the viscosity and the apparent heat capacity may vary widely. Significant differences at higher temperatures are obtained only if additives increase the maximum allowable temperature difference in the ice slurry generator.

The dynamic simulations and the case studies showed that the size of the cooling load, the cooling load profile, the temperature requirements and the electricity tariffs are decisive factors for the feasibility of ice slurries in cooling applications. For a cooling load profile in which there are only small load shifting options, the relative advantage of ice slurries is small. Ice slurries can only be applied at temperatures below 0 ^{o}C and have a disadvantage compared to non-phase changing systems in applications where cooling at temperatures above 0 ^{o}C is required. The benefits obtained with load shifting can however be large enough to compensate for this disadvantage.

The fluidized bed ice slurry generator is expected to perform well in relatively large applications. The limited temperature difference allowable in the fluidized bed ice slurry generator does not prevent its application at relatively high temperature applications.

Conclusion

The fluidized bed ice slurry generator can enhance secondary cooling systems by reducing both investment costs and energy consumption. The investment costs required for the ice slurry generator are lower than for other ice slurry generators because of high heat transfer coefficients. For larger applications the investment costs are relatively even lower because the fluidized bed ice slurry generator can be scaled up more efficiently than for example scraped surface systems.

A maximum temperature difference between wall and fluidized bed is observed in the experiments, above which a permanent ice layer forms on the heat exchanger walls and freeze-up of the fluidized bed occurs. Because of the high heat transfer coefficients however, only a small temperature difference is required. It is shown with the dynamic model that the fluidized bed ice slurry generator may be a competitive option even in air-conditioning applications. The load shift and peak leveling benefits make up for the relatively low temperatures of ice slurries compared with non-phase change secondary cooling systems in air-conditioning.

Wervelbed IJs Slurry Generator voor Verbeterde Secundaire Koelsystemen

Samenvatting

Doelstelling
De risico's van koelen met ammoniak of koolwaterstoffen kunnen gereduceerd worden door gebruik te maken van een secundair koelsysteem. In een dergelijk systeem wordt de koude opgewekt in een primair koudecircuit en vervolgens overgezet op een niet giftige, onschadelijke, secundaire koudedrager. De systeemonderdelen die het primaire koudemiddel bevatten, kunnen opgesteld worden in een gecontroleerde machinekamer, terwijl de koude gedistribueerd wordt naar consumentenruimtes met de veilige secundaire koudemiddelen.
IJs slurries zijn efficiënte secundaire koudemiddelen omdat deze gebruik maken van het latente warmte effect van de ijs/water faseovergang. Een hoge warmtecapaciteit is daardoor beschikbaar bij relatief constante temperaturen, terwijl de ijs slurries goed verpompbaar zijn. Bovendien kunnen ijs slurries opgeslagen worden in vaten voor later gebruik, wat voordelig kan zijn vanwege het reduceren van piekbelasting en vanwege de mogelijkheid de koelbelasting naar de nacht te verschuiven, waar elektriciteitstarieven lager zijn en het rendement van het primaire koudecircuit hoger. IJs slurries kunnen daarom resulteren in een significante reductie van het energieverbruik in diverse koel applicaties, zowel vergeleken met directe koelsystemen als vergeleken met secundaire koelsystemen waarin koudedragers zonder fase overgang gebruikt worden.

Het doel van het onderzoek beschreven in dit proefschrift is de prestaties van secundaire koelsystemen te verbeteren door een wervelbed ijs slurry generator toe te passen. Het onderzoek werd geïnitieerd omdat ijs slurries, hoewel het efficiënte koudedragers zijn, nog niet breed toegepast worden in secundaire koelsystemen. Een belangrijk obstakel is de ijs slurry generator. De wervelbed ijs slurry generator kan een aantrekkelijk alternatief vormen vanwege een potentieel hoge warmteoverdracht, een stabiel bedrijf en lage onderhoudskosten. In dit nieuwe type ijs slurry generator worden de impacts van vaste, inerte deeltjes van een wervelbed gebruikt om warmtewisselende wanden ijsvrij te houden en bovendien warmteoverdrachtscoëfficiënten te verhogen.
In dit onderzoek worden warmte- en stofoverdrachtsprocessen in de wervelbed ijs slurry generator in detail bestudeerd. Ook worden de eigenschappen van de ijs slurries zelf en hun prestaties in de secundaire koelsystemen geëvalueerd. Dit met het uiteindelijke doel te bepalen voor welke toepassingen de nieuwe ijs slurry systemen bruikbaar zullen zijn.

Methode
Om de toepasbaarheid van de wervelbed ijs slurry generator te evalueren, worden de warmteoverdracht, het ijsvormingsmechanisme en de aard van de gevormde ijskristallen bepaald. Ook wordt het bereik van stabiele werkcondities geëvalueerd, waarbij de aandacht vooral gericht is op de omstandigheden waarbij het wervelbed dichtvriest door aanhechten van ijs. Een verbeterd inzicht in deze processen kan ook toepasbaar zijn in andere gebieden waar wervelbedden, kristallisatie of vaste stof afzetting een rol spelen. Voor deze doelen is een experimentele opstelling van een wervelbed ijs slurry generator ontwikkeld.
De invloed van verschillende ijs slurry parameters en de wervelbed condities op de vorming van ijs slurry is bepaald in de opstelling, die bedreven kan worden als een stationair en als een circulerend wervelbed. Ook is een eerste experimentele evaluatie van een rotor in het wervelbed uitgevoerd. Tenslotte is een theoretische discussie over parallelle fluïdisatie van meerdere wervelbedden gevoerd.

De wervelbed ijs slurry generator is dan geoptimaliseerd als een deel van een secundair koelsysteem. Deze optimalisatie bevat de mogelijke energetische en economische voordelen die voort komen uit het gebruik van ijs slurries. Zowel de thermofysische eigenschappen van de ijs slurries zijn benodigd voor de optimalisatie, als ook het gedrag van de ijs slurries in de overige componenten van het secundaire koelsysteem, welke transport, opslag en toepassing van de ijs slurries bevatten.
Tenslotte is een dynamisch simulatie model ontwikkeld, waarmee het energieverbruik van de ijs slurry systemen voor een gegeven koelbelasting en omgevingsomstandigheden bepaald kan worden. Met het dynamische model zijn case studies uitgevoerd voor airconditioning, supermarkt koeling en koelen en vriezen in de voedingsindustrie, om te bepalen voor welke applicaties de nieuwe ijs slurry systemen kunnen resulteren in een reductie van het energieverbruik en de totale kosten.

Resultaten
De ijskristallen geproduceerd in de experimentele opstelling van de wervelbed ijs slurry generator zijn vergelijkbaar met die geproduceerd met andere methodes die reeds toegepast worden in ijs slurry koelsystemen. Dit is bevestigd met NaCl, ethyleenglycol en dextrose als vriespuntdalend additief. De wervelbed ijs slurry generator voldoet op dit gebied.
De vorming van ijskristallen heeft geen groot effect op de warmteoverdrachtscoëfficiënten in de wervelbed ijs slurry generator. Als stabiele ijs kristallisatie mogelijk is onder bepaalde condities, dan is de warmteoverdracht vergelijkbaar met die in het wervelbed vlak voor de start van de ijskristallisatie.
De ijsfractie is de meest relevante parameter die de thermofysische eigenschappen van de ijs slurries bepaald. Modellen uit de literatuur voor de eigenschappen vriespunt, dichtheid, warmtegeleiding, enthalpie en warmtecapaciteit, kunnen worden toegepast in modellen om warmteoverdrachtscoëfficiënten van wand naar bed te voorspellen. Het volgende empirische model, gebaseerd op hydraulische Nusselt en Reynolds getallen, is bepaald om de warmteoverdrachtscoëfficiënten in de wervelbed ijs slurry generator nauwkeurig te voorspellen:

$$Nu_h = 0.0612 \cdot Re_h^{0.724} Pr^{0.625}$$

De exponenten van dit model zijn vergelijkbaar met die van gegeneraliseerde modellen voor vloeistof/vast wervelbedden uit de literatuur. Significante verschillen zijn alleen gevonden in de proportionele factor. De relatief lage temperaturen tijdens de ijs slurry productie zijn hiervoor de meest waarschijnlijke oorzaak, omdat geen duidelijke invloed van de ijskristallen gevonden is.

Het maximale temperatuurverschil tussen wand en wervelbed dat toelaatbaar is tijdens de ijs slurry productie voordat het wervelbed dichtvriest, hangt lineair af van de concentratie vriespuntdalend additief voor de onderzochte condities. Dit wordt veroorzaakt door een opvallend constante ijskristal groeisnelheid aan de wanden, wat vooral bepaald wordt door de massaoverdracht van de opgeloste stof. Bij een verhoogde concentratie vriespuntdalend additief kan een groter temperatuurverschil aangelegd worden, terwijl de kristalgroeisnelheid aan de wand constant blijft. Warmte overgedragen boven deze kristalgroeisnelheid, maar onder het maximaal toelaatbare temperatuurverschil, resulteert in kristalvorming in de bulk van het wervelbed.

Wervelbed condities moeten zodanig zijn dat de constante ijskristalgroeisnelheid aan de wanden verwijderd kan worden om dichtvriezen te voorkomen. De verschillen in het maximaal toelaatbare temperatuurverschil tussen de vriespuntdalende additieven, worden bepaald door de capaciteit tot ijsverwijdering van de wand. Deze capaciteit wordt weer bepaald door het aantal effectieve botsingen van wervelbed deeltjes met de wand. Of een botsing effectief is, hangt af van de adhesiekracht van het ijs aan de wand en de kinetische energie van de vaste deeltjes die op de wand botsen.

Een aanpak is geïntroduceerd waarin de arbeid van de adhesie van ijs aan de wanden en een exponentiele verdeling van de kinetische energieën van de vaste deeltjes gebruikt worden om het aantal effectieve botsingen te bepalen. De resultaten zijn kwalitatief in overeenstemming met de trends die gevonden werden voor de maximale toelaatbare temperatuurverschillen. De aanpak wordt verwacht ook toepasbaar te zijn voor kwantitatieve voorspellingen van de condities waaronder vastvriezen tijdens ijskristallisatie optreedt.

Het stationaire wervelbed in de experimentele opstelling is gekwantificeerd in detail. De algemene theorie voor vast/vloeistof fluïdisatie van Richardson en Zaki is gevalideerd voor het gebruik in de wervelbed ijs slurry generator. Een evaluatie van het aantal effectieve impacts van deeltjes op de wand is gebruikt om de stationaire wervelbed ijs slurry generator verder te optimaliseren, waarbij het optimale deeltjesgehalte van het bed, de deeltjesgrootte en de optimale deeltjes/bed diameter ratio bepaald zijn.

De eerste experimenten met circulatie van de wervelbed deeltjes hebben niet geleid tot een verbetering van het wervelbedsysteem, vanwege beperkingen van de experimentele opstelling. De installatie van een rotor heeft ook geen verbetering van de wervelbed prestaties laten zien, voornamelijk door het hinderende effect van de rotor op de fluïdisatie. Uit de theoretisch beschouwingen volgt dat van circulatie van de deeltjes nog verbeteringen te verwachten zijn, terwijl het onwaarschijnlijk geacht wordt dat het rotor systeem tot verbeteringen zal leiden. Een theoretische studie van parallel fluïdisatie van meerdere wervelbedden laat zien dat er methodes geschikt zijn voor ijs slurries, hoewel enkele parallelle wervelbed systemen uitgesloten zijn.

Omdat de ijsfractie een belangrijke parameter is, is het waarschijnlijk dat het gebruik van ijs concentrators of afscheiders tussen de verschillende delen van een secundair koelsysteem de prestaties verbetert. Het vriespuntdalend additief is vooral van invloed voor applicaties op lagere temperaturen, waar de viscositeit en de schijnbare warmtecapaciteit veel kunnen variëren. Significante verschillen bij hogere temperaturen worden alleen verkregen als de additieven het maximaal toelaatbare temperatuurverschil in de ijs slurry generator verhogen.

De dynamische simulaties en de case studies laten zien dat de koelbelasting, het profiel van de belasting, de temperatuureisen en de elektriciteitstarieven doorslaggevende factoren zijn voor de toepasbaarheid van ijs slurries in koel applicaties. Voor een koelbelastingsprofiel waarin slechts weinig mogelijkheden zijn voor het schuiven van de koellast, is het relatieve voordeel van ijs slurries klein. IJs slurries kunnen alleen toegepast worden op temperaturen onder 0 ^{o}C en hebben daarom een nadeel ten opzichte van systemen met koudedragers zonder faseovergang in toepassingen boven 0 ^{o}C. De voordelen die voortkomen uit het schuiven van de koellast kunnen echter groot genoeg zijn om dit nadeel te compenseren.

De wervelbed ijs slurry generator wordt verwacht goed te presteren in relatief grote applicaties. Het gelimiteerde maximale temperatuurverschil in de wervelbed ijs slurry generator verhindert de toepassing bij relatief hoge temperaturen niet.

Conclusie
De wervelbed ijs slurry generator kan secundaire koelsystemen verbeteren door zowel energie als investeringskosten te verminderen. De investeringskosten benodigd voor de wervelbed ijs slurry generator zijn vooral lager dan die van andere ijs slurry generatoren door de hoge warmteoverdrachtscoëfficiënten. Voor grotere toepassingen zijn de investeringskosten relatief nog lager, omdat de wervelbed ijs slurry generator efficiënter opgeschaald kan worden dan bijvoorbeeld geschraapte systemen.

Er is een maximaal temperatuurverschil vastgesteld tussen de wand en het wervelbed in de experimenten, waarboven een permanente ijslaag gevormd wordt op de warmtewisselende wanden en het wervelbed dichtvriest. Door de hoge warmteoverdrachtscoëfficiënten is echter slechts een laag temperatuurverschil vereist. Met behulp van het dynamische model is gedemonstreerd dat de wervelbed ijs slurry generator een aantrekkelijke optie kan zijn, zelfs voor airconditioning toepassingen. De voordelen van het verschuiven en verdelen van de koellast over de dag en nacht, compenseren voor de relatief lage temperaturen van de ijs slurries vergeleken met koudedragers zonder fase overgang in airconditioning.

1 Introduction

Secondary cooling cycles which have ice slurries as their working fluid, can provide an alternative to traditional cooling systems by reducing both energy consumption and investment levels. In this research ice slurry systems with a fluidized bed heat exchanger as the ice generator will be investigated and optimized. The novel ice slurry generation technique will be characterized for heat and mass transfer, knowledge of which will be applicable in other fields involving fluidization, crystallization and heat transfer. The ice slurry cycle itself will then be evaluated. An overview will be given of the range of applications for which the newly developed cooling systems may prove advantageous.

1.1 Primary and Secondary Refrigerants

The Montreal protocol of 1987 and its subsequent amendments, including those agreed upon in Vienna in 1995 and Montreal in 1997, prescribe the world-wide phase-out of refrigerants consisting of CFCs and HCFCs, because of their ozone depleting properties. An alternative to those widely used refrigerants is temporarily found in HFCs, but the disadvantage of those substances is their high global warming potential.

During the climate conference in Kyoto in 1997 the industrialized countries agreed to a protocol that will reduce emissions of global warming substances. For HFCs this protocol resulted in a goal to reduce emissions world-wide by an average of 5.2% over the period from 2008 to 2012, compared to the levels of the period from 1990 to 1995. The mean reduction for the European Union was set at an even higher level of 8%. Although the Kyoto protocol may not be ratified by many countries, reduction of global warming is still an important issue.

An overview of the measures affecting the cooling industry because of the phasing out or reduction of widely used refrigerants is given in Table 1.1.

Table 1.1: Regulations affecting chemical refrigerants (IIR, 2003)

	CFCs	*HCFCs*	*HFCs*
Ozone depleting potential	+	+	0
Global warming potential	+	+	+
Treaty of	Montreal (1987)	Montreal (1987)	Kyoto (1997)
World-wide Regulations			
Developed countries	banned 1.1.1996	banned 1.1.2030	
Developing countries	banned 1.1.2010	banned 1.1.2040	
Industrialized countries			mean emission reduction of 5.2% in 2008-2012 compared to 1990-1995 levels
European Regulations			
Production	banned 1.1.1996	banned 1.1.2026	
Sales	banned 1.1.2000	banned 1.1.2010	
Use in maintenance	banned 1.1.2001	banned 1.1.2010	
Use in new equipment		banned 1.1.2000 for equipment >150 kW	
			mean emission reduction of 8%

Because of legislation concerning the ozone layer and global warming problems, the refrigeration industry is again focusing on refrigerants that were used before the CFC-era and which were never abandoned in some application fields. Those alternative refrigerants are known as 'natural' refrigerants, because they are either part of the natural environment or because, in the long run, they do not harm the natural environment if they are emitted. These refrigerants include air, water, carbon dioxide, hydrocarbons and ammonia, and others that play a minor role. Of these refrigerants hydrocarbons, especially propane and butane, and ammonia have high energetic performance. Of these two, hydrocarbons are often applied in smaller scale installations, while ammonia is applied in larger systems.

Though environmentally sound, the alternative refrigerants have some disadvantages because of their immediate safety and health hazards. Propane for example, is very flammable and ammonia is slightly flammable and toxic. These properties of natural refrigerants can however be managed satisfactorily as is already known from other application fields where the same substances are used. Hydrocarbons, for example, are widely applied as automotive fuel. The risks involved in traveling with 50 liter of highly flammable hydrocarbons at a speed of 100 km/h are considered to be acceptable.

As for ammonia, its presence is detected long before concentrations reach toxic levels because of its smell. With correct procedures, small leaks are detected and repaired before severe health hazards occur. In some applications however even small leaks are unacceptable. The smell of ammonia around supermarket cooling and freezing displays will certainly decrease frozen food sales.

The risks attached to ammonia or propane cooling are manageable, but the safety measures required can be very costly. One way of reducing the safety hazards is by decreasing the total load of refrigerant by installing a secondary cooling cycle. In such a system cold is generated in the primary cooling cycle and then transferred to a secondary cooling cycle with a heat exchanger. In this secondary cooling cycle a non-toxic, non-flammable cold carrier is used to distribute the cooling capacity to the locations where it is required. The basic chart for a secondary cycle is given in Figure 1.1.

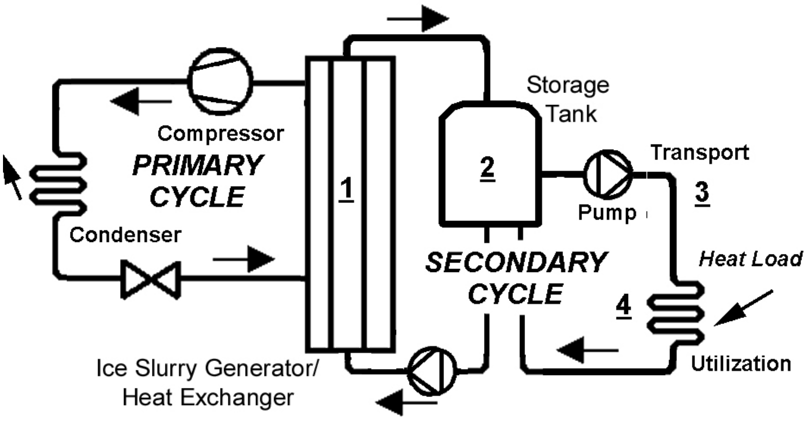

Figure 1.1: Primary and secondary cooling cycles

Safety is increased by installing a secondary cooling cycle. The primary cooling cycle containing the hazardous substances can then be installed in a machine room in which conditions are well controlled, and to which only trained, authorized personnel has access. Another advantage attached to installing a secondary cycle is that a smaller amount of primary refrigerant is required, which often implies that the entire cooling system can be placed in a different safety class. These safety classes are established according to the total amount of hazardous substance contained in an installation. If a chemical refrigerant, for example an HFC, is applied in a refrigeration system, the benefits of a secondary cooling cycle can also be substantial. Secondary cooling cycles are not limited to natural refrigerants.

A secondary cooling cycle also increases flexibility of a refrigeration system. If cold is stored in a tank in the cooling cycle, electrical loads can be shifted towards less expensive parts of the day. Even if there is no dual electricity tariff structure, still energetic benefits may be obtained, because the efficiency of the primary refrigeration cycle is higher during the nighttime, provided that a lower condensation temperature can be used. Also peak loads can be reduced by leveling them over a longer period of the day, so that the size of the primary refrigerant compressor can be smaller.

Secondary cooling fluids traditionally employed are often based on brines like calcium chloride or potassium formate, or are based on organic fluids like ethylene glycol. These fluids use the sensible heat capacity for cold storage, which can be sufficient for many applications, but which also has serious disadvantages. The most important are the large storage volumes required and the limited flexibility in cold storage applications.

Recently ice slurries have been introduced as secondary cooling fluids. The principal difference compared to traditional secondary fluids is the use of a phase change to store cold in the form of ice crystals, instead of using the sensible heat capacity. This can substantially increase the energetic and economic performance of secondary cooling systems.

Unfortunately the investment costs needed for the production apparatus of the ice slurries largely cancels out the energetic benefits of ice slurries so far. A promising alternative is to use a fluidized bed heat exchanger to produce ice slurries. Such a heat exchanger may lead to significantly reduced investment costs and make ice slurries feasible for a larger range of applications.

1.2 Applications of Secondary Cooling Cycles

Apart from reducing safety and health risks, there are other reasons for installation of a secondary cooling system. Both energetic and economic benefits can often be obtained because of the increased cold storage flexibility. Certain specific properties of secondary cooling fluids can also be very advantageous in some applications. Examples are systems in which direct contact cooling between the refrigerant and the product to be cooled is possible.

Because of the wide variety of reasons in favor of installing secondary cooling cycles, they can be found in numerous applications (Paul, 1996). They are used in supermarkets for the cooling and freezing in display cabinets and in storage rooms. Secondary cycles are applied in medium to large-sized buildings for air-conditioning purposes. They are also found in various other industrial applications, of which the food industry forms a great part. Large secondary cooling cycles are also used to provide cooling in mines and for district cooling. Examples of district cooling systems are large cold storage centers or systems in fruit or vegetable terminals in for example auctions or ports. Apart from these general categories there are also some specific considerably sized applications, like artificial ice skating rinks.

The total energy consumption of these applications is substantial. For example in the Netherlands there are ca. 4000 supermarkets using 5.4 PJ/year for cooling purposes, which equals 1.9% of the yearly electricity consumption of the Netherlands (CBS 1996;Unipede 1996). By carefully designing and optimizing the secondary cooling cycles a significant contribution can be made towards reducing overall energy consumption.

Size and safety considerations

In Figure 1.2 typical applications and cooling capacities are displayed.

The scale of a refrigeration system will have a major influence on the installation of a secondary system. The size of a system determines what safety measures have to be taken and this will depend on the amount of refrigerant a system is holding. In small systems a secondary cycle will not be required, because the amount of hazardous refrigerant is already small and the installation is already categorized in a less strict safety class.

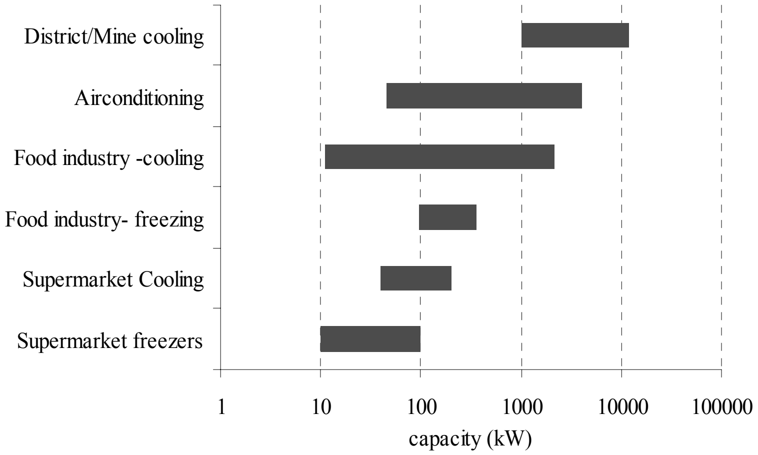

Figure 1.2: Typical cooling capacities of applications

The size of a system determines the investments possible with a reasonable payback time. In a cooling system with a capacities under 1 kW, for example a household refrigerator, the investment costs are relatively important compared to those of larger systems and extra investments required for a secondary cycle will be less likely.

Depending on the severity of the safety restrictions on the primary refrigerant, the option to invest in extra safety precautions in order to run the entire cooling system on ammonia or hydrocarbons might be more economical than investing in a secondary cycle. Much depends on local legislation, but other factors can also be of influence. To illustrate that there is no best option yet, an example is given of the beer brewing industry. Some breweries have always used ammonia in primary cycles for entire breweries (Bardov, 1988), while others have installed secondary cycles based on brines.

Temperature levels

Each of the application fields has its own specific requirements as far as temperature levels are concerned. Typical temperature ranges are shown in Figure 1.3. These temperature levels are important when it comes to deciding on the type of installation required. The higher the temperature required for the secondary fluid, the lower the energy consumption for the primary cooling cycle will be. The temperature difference between the secondary fluid and the primary refrigerant also needs to be as low as possible to obtain low energy consumption. In general, the temperature difference to obtain a cost efficient process will be around 5 to 10 K.

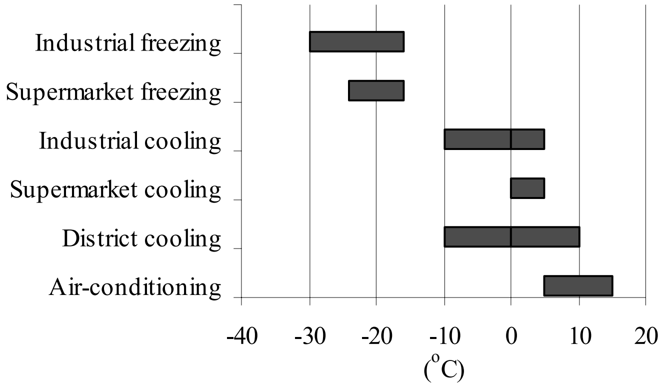

Figure 1.3: Typical temperature levels required in applications

1.3 Ice Slurries in Secondary Cooling Systems

Ice slurries consist of a water solution of a freezing point depressing substance, e.g. ethanol or sodium chloride, in which small (0.01 mm-0.5 mm diameter) ice crystals are present. Depending on the amount and type of freezing point depressing additive used, ice slurries are available in the range from just below 0 ^{o}C to –30 ^{o}C or even lower. To reach lower temperatures more of the freezing point depressing substance is necessary. Some additional additives can be used in ice slurries, for example those that improve flow properties and corrosion inhibitors.

Ice slurries remain pumpable at higher ice concentrations. The viscosity of ice slurries with up to 20% vol. ice concentration has the same order of magnitude as water. At the expense of more pumping power higher ice concentrations are also possible. In storage vessels, up to 40% vol. ice concentration has been reported to be manageable (Kauffeld et al., 1999).

Heat transferred to an ice slurry will melt a small amount of ice, which is energetically more efficient than when the heat transferred is used for fluid temperature increase without phase change. The latent heat of fusion of water is 333.5 kJ/kg (at 0 ^{o}C), so in a 10% wt. ice slurry 33.4 kJ per kg of slurry is stored. The sensible heat capacity of a $CaCl_2$-brine is 3.6 kJ/kgK, which implies a temperature change of approximately 9 K is necessary to store an equal amount of heat per kg $CaCl_2$-brine. Due to the higher heat capacity of the ice slurries, smaller pipe diameters will be sufficient and cold can be stored at high density and at relatively constant temperature.

The heat transfer coefficients for ice slurry flows reported are promising compared to those of traditional secondary coolants based on brines (Bellas et al. 2002). This is partially because of the higher heat capacity, but it may also be partially caused by the presence of crystals in the ice slurry. Crystals may increase heat transfer by breaking up laminar boundary layers at heat exchanging walls.

For most freezing point depressants it can be accurately assumed that the ice formed consists of pure H_2O. As a result of this, the freezing point depressant concentration in the remaining solution will increase when ice is formed. The freezing point of the remaining solution will drop and a freezing range occurs. A higher concentration of freezing point depressant is required to reach lower ice slurry operating temperatures and the distinct freezing point will become an increasingly large freezing range at lower temperatures.

Because of the increasing freezing range at low temperature applications, the advantage that ice slurries have over traditional secondary fluids decreases. This is because of the smaller amount of latent heat involved at lower temperatures. The freezing range gets larger and a larger part of the cold removed is used for lowering the temperature of the fluid rather than for the formation of ice.

Typical design temperature for water based air-conditioning systems are 12 to 6 ^{o}C. The optimal temperature difference between a cooling fluid and a product is 5 to 10 K in order to obtain a cost efficient process, so that a typical evaporation temperature of around 2 ^{o}C is used in practice for water based systems. Since ice slurries are not available above 0 ^{o}C, ice slurries have the disadvantage of low temperature levels when used in air-conditioning systems, but this may be compensated by the benefits of efficient cold storage properties.

In what temperature ranges ice slurries will be feasible and how these ranges can be extended will be investigated in this thesis. Apart from the effects already mentioned, there may also be specific requirements related to applications that make ice slurries especially favorable or unfavorable. For example when freezing freshly caught fish, a fluid is needed to cool the fish rapidly, but the fish also needs to be stored on ice until it can be brought to land.

1.4 Ice Slurry Generation: Fluidized Bed Heat Exchanger

A number of methods are currently known for ice slurry generation. Commercially available are scraped surface evaporators and vacuum freezing systems (Zakeri, 1997). These two methods are however only applied in a limited number of applications. The scraped surface method is suitable for cooling capacities of 1 kW to 500 kW, the vacuum method for cooling capacities of 150 kW to 2000 kW (Paul,1997). Other ice slurry generation methods are based on supercooling of a fluid, after which in a separate vessel the ice is formed, or are based on direct contact evaporation without heat exchanging walls (Fukusako et al., 1999). Ice slurries may also be prepared by crushing plate or flake ice, however with limited efficiency.

Most methods have one or more major drawbacks that limit wide application. Scraped surface evaporators require high investment levels and have high maintenance costs. Vacuum systems are generally only feasible in large scale applications. Supercooling systems can be unstable in operation and direct contact systems can only be used with a few primary refrigerants and then also have leakage problems.

The fluidized bed heat exchanger is expected to reduce investment costs considerably while increasing the heat transfer performance. Also stable operation over longer periods is expected, as well as benefits from large scale operations.

In the early nineties, Klaren and Van der Meer (1991) proposed using fluidized bed heat exchangers for the production of ice slurries. Up until then the fluidized bed heat exchanger as a refrigeration technique had only been used in desalination applications. The fluidized bed heat exchanger itself has already been presented more than twenty-five years ago (Klaren, 1975). In most cases this type of heat exchanger was installed to solve severe fouling problems in a wide range of applications.

A schematic layout of a possible fluidized bed evaporator is shown in Figure 1.4. It consists of a number of vertical tubes arranged in a shell-and-tube configuration. A primary refrigerant evaporates outside the vertical tubes. The fluidized bed is located inside the tubes and consists of solid particles that are fluidized by the upward flowing ice slurry feed flow. The solid particles remove the ice crystals formed from the inner tube surface and transport them to the main flow. The solid particles are separated at the heat exchanger outlet and recycled to the inlet through a downcomer tube. The heat exchanger displayed in Figure 1.4 has an internal downcomer. Alternatively an external downcomer can be employed. This can be advantageous when it is more difficult to separate the particles from the main flow. A separator such as a cyclone can then be used.

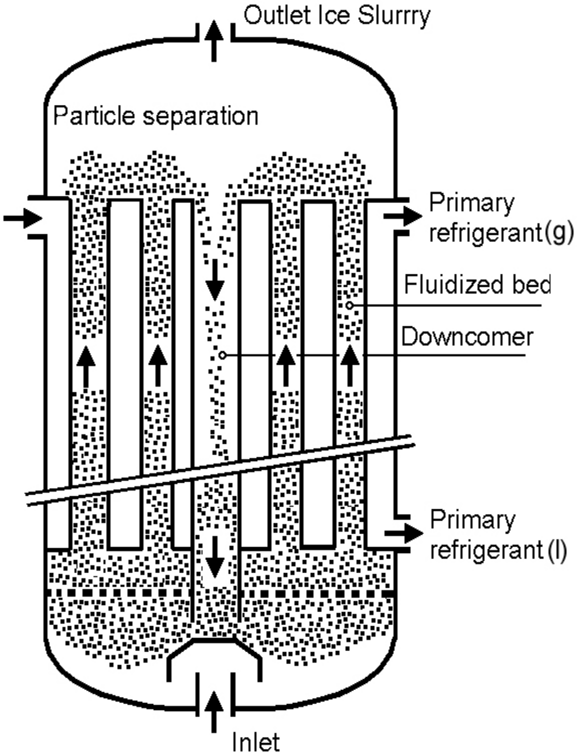

Figure 1.4: Fluidized bed heat exchanger

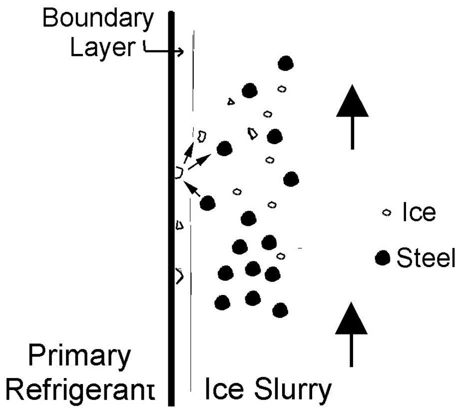

Figure 1.5: Working principle

The basic working principle of the fluidized bed system is displayed in Figure 1.5. The ice slurry feed stream fluidizes the steel particles, that remove the ice that is formed on the heat exchanging walls to the main ice slurry flow. In doing so, the steel particles also increase heat transfer, by breaking up the laminar boundary layer, which has large heat transfer resistance.

The principle of the fluidized bed heat exchanger is similar to the working principle of the scraped surface evaporator. The particles, for example glass beads or cut iron wire, can be seen as large quantities of small local scrapers. The heat exchanger is driven by a relatively simple pump. It is not necessary to install a precisely smooth heat exchanging surface, which results in relatively low investment costs.

If the installation is scaled up, more tubes must be installed, but these can still be driven by a single pump. Only the devices needed for an even fluidization of the multiple tubes will increase the investment costs.

Advantageous of the fluidized bed is that there are no heat exchanging area limitations. Relatively large velocities can be obtained in the tubes without mechanical problems. With larger velocities the particles are expected to impact harder on the walls and break up the thermal boundary layer more efficiently than would be possible with a large rotating scraper.

1.5 Objective

The objective of this research is to enhance ice slurry secondary cooling cycle performance by means of a fluidized bed ice slurry generator. It is expected that the fluidized bed heat exchanger applied to produce ice slurries will greatly increase the energetic and economic performance of the secondary cooling cycles. This novel technique therefore forms the central part of this research.

An experimental set-up of a fluidized bed ice slurry generator is used to improve understanding of the ice formation and ice removal mechanisms. Initially the heat transfer in the fluidized bed heat exchanger will be quantified, to identify its energetic performance. The ice crystallization mechanism, freeze-up conditions and ice adhesion effects will then be studied. An increased understanding of these mechanisms is expected to be relevant also for other crystallization and heat transfer processes. In this research it will be used to optimize the fluidization conditions and thus further improve the ice slurry generator performance.

The heat exchanger between the primary and secondary cycles is an important part of the cooling system, but it cannot be seen apart from the rest of the cooling system. The ice slurry system as a whole will therefore also be considered. Both on small scale, with focus on the properties of the ice slurries, as on large scale, in a simulation of the entire cooling system. Possible benefits of ice slurries during storage and distribution of cold in various cooling applications will be evaluated, with the final aim to quantify the performance of the entire cooling system and to find the applications where the novel ice slurry systems will be practicable.

1.6 Thesis Outline

In Chapter 2 the ice slurries themselves are evaluated. Main questions are: What are the ideal properties of ice slurries and what substances can be used to obtain ice slurries with those properties? Crystallization is introduced, together with microscopic pictures of typical ice crystals of the slurries of this research. Effects of freezing point depressants and other additives are also discussed.

Chapter 3 focuses on the heat transfer performance of the fluidized bed heat exchanger. The effects of the particles of the fluidized bed on heat transfer are studied and compared with fluidized bed systems in other, mainly heating, applications. Possible effects of the ice slurries are examined and a quantitative model is developed.

In Chapter 4 the mass transfer processes in the fluidized bed ice slurry generator are evaluated. A linear trend is observed between the concentration of freezing point depressant and the maximum wall-to-bed temperature difference, above which freeze-up of the fluidized bed occurs. Wall effects such as crystallization, ice adhesion and particle impacts are considered, to explain differences between various freezing point depressants.

The fluidization technique and the various operating modes are evaluated in Chapter 5. Stationary fluidization is evaluated for particle and bed diameters, as well as the type of ice slurries applied. A preliminary experimental evaluation of circulating fluidized beds and a novel technique using a rotor device are discussed. A theoretical discussion of the likely effects of using multiple beds fluidized in parallel, required for scale-up, is also included.

In Chapter 6 the four distinct stages of a secondary cooling system are discussed and optimized. Ice slurry generation, storage, transport and utilization stages are evaluated separately and their relative influence on the secondary cooling cycle. For each of the stages the performance of the ice slurries is quantified.

The separate stages are integrated into one secondary cooling cycle in Chapter 7. Interactions between secondary and primary cooling cycles are studied in several case studies. A static and a dynamic model are developed to simulate the secondary cooling cycle. With this model the economic and energetic performance can be quantified accurately for comparison with other systems. The reduction of energy consumption that may or may not be obtained with ice slurry systems as well as the economic benefits are thus estimated. In this way an overview can be given of likely applications and corresponding temperature and capacity ranges for which ice slurry systems based on fluidized bed technology can be successfully applied.

References

Bardov, R., 1988, *Ammonia Refrigeration in large scale brewing technology*, Proc. IIAR 10th annual meeting Savannah Georgia, p99

Bellas, J., Chaer I., and Tassou, S.A., 2002, *Heat transfer and pressure drop of ice slurries in plate heat exchangers*, Applied Thermal Engineering 22 (7), p721-732

CBS *Jaarboek statistiek*, 1999, CBS, Den Haag.

Fukusako, S., Kozawa, Y., Yamada, M., Tanino, M., 1999, *Research and Development Activities on Ice Slurries in Japan.* Proceedings of the 1st Workshop on Ice Slurries by the IIR, Yverdon-les Bains, May 1999. Eds. Egolf, P.W., Sari, O., IIF/IIR, p83-105

IIR, 2003, *IIR-Summary on the Montreal Protocol; IIR-Summary on the Kyoto Protocol,* Website of the International Institute of Refrigeration (IIR), www.iifiir.org

Kauffeld, M., Christensen, K.G., Lund, S., Hansen, T.M., 1999, *Experience with Ice Slurry*, Proc. of the 1st workshop on Ice Slurries, Yverdon-les-Bains, Switzerland, IIR. p42-73

Klaren, D.G., 1975, *Development of a vertical flash evaporator*, Ph.D. Thesis, Delft University of Technology, Delft, the Netherlands

Klaren, D.G., van der Meer, J.S., 1991, *A fluidized bed chiller: A new approach in making slush-ice,* Industrial Energy Technology Conference Houston Proceedings

Paul, J., 1996, *Compressors for refrigeration plants and ice makers with 'water as refrigerant'*, Proceedings of the Aarhus Conference of the IIF/IIR, p.577-584

Paul, J.,1997, *Binäreis-Anwendungserfahrungen in der Supermarktkälte,* Ki Luft-und Kältetechnik, vol.5, p209-213

Unipede, 1996, *Electricity tariff structure in the EU member states*, Eurelectric/Unipede

Zakeri, G. R., 1997, *Vacuum freeze refrigerated circuit, a new system design for energy effective heat pumping applications*, Proc. Linz (Austria) Conf, IIF/IIR, comm. E1,E2,B2: p182-190

2 Ice Slurry Fundamentals

2.1 Physical Properties

Physical properties of ice slurries are for a great part determined by the amount of freezing point depressant required to produce ice at the temperature level of an application. Detailed knowledge of the freezing point depressing effect is therefore essential. Heat and mass transfer processes of ice slurries in secondary cooling systems are described by the following ice slurry dependant properties: Thermal conductivity, density, dynamic viscosity and enthalpy. The heat capacity is obtained from the enthalpy. These properties depend on the ice fraction of the ice slurry, on the type of freezing point depressant and on other additives used in the ice slurry. For low concentrations of freezing point depressant, far from the eutectic point, it is assumed that the ice formed in a slurry consists of pure water. Ice slurry properties are then estimated by combining properties of the liquid solution and those of pure ice.

2.1.1 Freezing Point Depression

In order to make ice slurries available at temperatures in the range from 0 °C down to below –30 °C, a soluble freezing point depressing substance is added to water. A thermodynamic evaluation of freezing point depression assuming an ideal solution yields predictions of the freezing point of a solution (Ben Lakhdar, 1998; Bevan Ott and Rex Goates, 1992).

If a solution is in equilibrium at its freezing temperature, the chemical potential of water, μ_w, is equal to the chemical potential of ice μ_i:

$$\mu_i^* = \mu_w^* \tag{2.1}$$

the chemical potential of water is expressed with the water activity:

$$\mu_i^* = \mu_w^0 + RT_f \ln a_w \tag{2.2}$$

The activity of water in a solution, a_w, depends on the concentration of freezing point depressant and is given by:

$$a_w = \frac{1}{1 + \dfrac{w_{fpd} \cdot M_w}{(1 - w_{fpd}) \cdot M_{fpd}}} \tag{2.3}$$

For salts that are dissociated in solution, the molecular weights and concentrations of the ions in solution need to be used in Equation 2.3.

From Equation 2.1 follows that the Gibbs energy change for the phase change is 0, so that:

$$\Delta G_f = \Delta H_f - T_f \Delta S_f = 0 \tag{2.4}$$

with:

$$\left(\frac{\partial \mu}{\partial T}\right)_p = -S \tag{2.5}$$

a correlation for the equilibrium freezing temperature is obtained:

$$T_f = \frac{1}{\dfrac{1}{T_0} - \dfrac{R \cdot \ln(a_w)}{\Delta \bar{H}_f \cdot M_w}} \tag{2.6}$$

in which T_0 is the reference temperature, the freezing point of water at 273.15 K. ΔH_f is also a weak function of temperature and therefore the mean heat effect of the phase change between the freezing temperature and the reference temperature is used in Equation 2.6, $\Delta \bar{H}_f$.

The prediction of the freezing point assuming ideal solutions is only valid for dilute solutions. It ignores interactions between solute molecules and specific interactions caused by various molecular properties as polarity, ion charge and other properties. The prediction of the freezing temperature of a solution is however fairly accurate for many freezing point depressants. For NaCl solutions for example the freezing point depression is predicted with an absolute error within 0.25 K down to a freezing temperature of –9 °C. In Figure 2.1 the freezing points of some freezing point depressants are given versus the mole fraction. At lower temperatures non-idealities become more significant, so that at lower temperatures the freezing point depression can not be estimated accurately assuming ideal solutions.

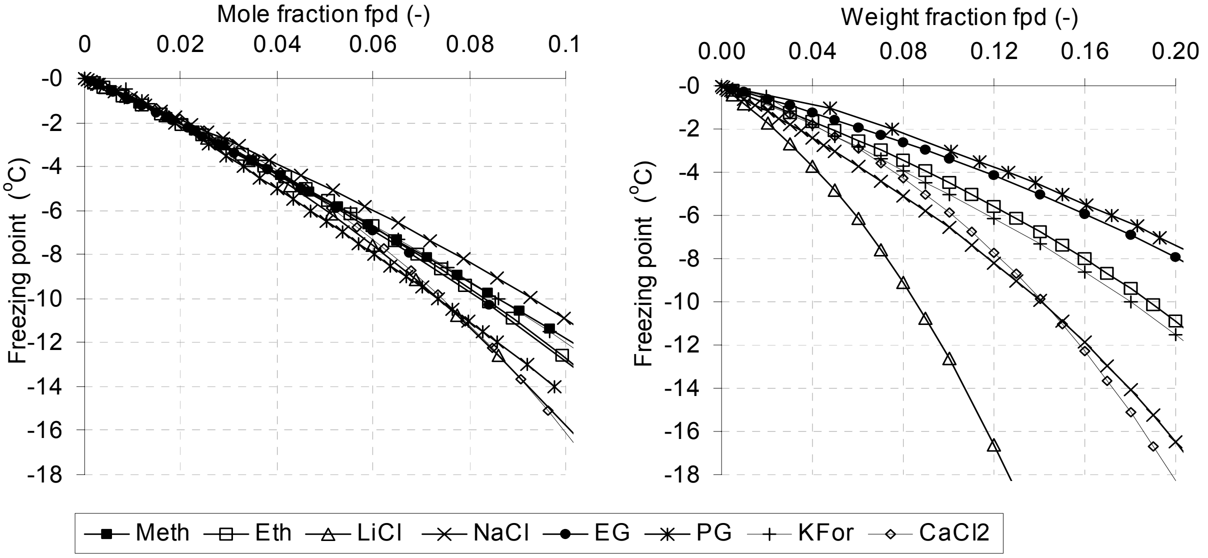

Figures 2.1 and 2.2: Freezing point depression of some additives vs. mole fraction and weight fraction (Model data; the markers do not represent experimental results)

In Figure 2.2 the freezing curves of a few freezing point depressants are displayed versus the weight fraction of freezing point depressant. Two effects can be distinguished that determine the efficiency of the freezing point depression with regard to the weight fraction. The first concerns the absolute amount of freezing point depressant added, the second the slope of the freezing curves.

Ice formed in a slurry is assumed to consist of pure water. This assumption is valid for dilute solutions, for low to moderate ice formation rates and also the eutectic point of the solution should be at relatively high concentration and low temperature. Because of this assumption, solutions have a freezing range rather than a freezing point: If ice is formed, water is removed from the solution and the concentration of freezing point depressant in the remaining solution increases. The freezing point of the remaining solution will drop. The temperature needs to be lowered further before more ice can be formed. This lowering is determined by the sensible heat capacity of the ice slurry and not by the latent heat effect of the phase change. Cold storage using sensible heat capacity is less efficient than cold storage using latent heat, therefore the occurrence of a freezing range decreases the efficiency of the ice slurry.

This is illustrated in Figure 2.3, where a freezing curve is displayed. It is observed that substances with a relatively flat slope of the freezing curve, are relatively more efficient than substances with steep freezing curves, because the share of the latent heat in the heat capacity is larger. Most freezing point depressants have a decreasing slope at increasing concentration, similar to Figure 2.3.

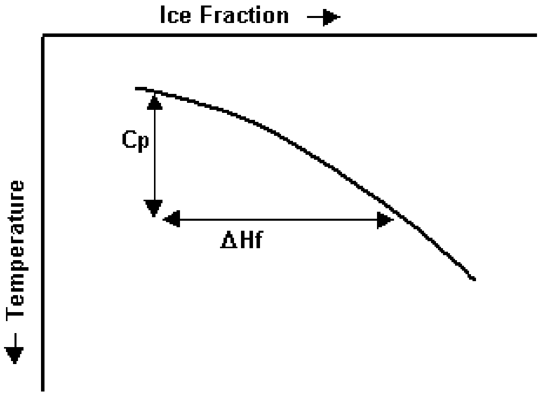

Figure 2.3: Ice slurry heat capacity consists of both sensible and latent heat effects

If two freezing curves with equal slopes at a certain freezing point are compared, the freezing point depressant at the lowest concentration is the most efficient. If for example 20% ice is formed in an initial 5% solution, the concentration in the remaining solution will increase to 6.25%, an increase of 1.25%. This results in additional depressing of the freezing point that is half as much as the additional depression if 20% ice is formed from an initial 10% solution. The concentration of the remaining solution increases to 12.5%, an increase of 2.5%.

In Table 2.1 the freezing point depression is given required to obtain a 20 wt% ice slurry at –5 ^{o}C for various freezing point depressants. The freezing temperatures of the substances are relatively close to each other. Calculations are therefore very sensitive to small errors in the determination of the freezing temperature. The additional freezing point depression of the substances is the lowest for sodium chloride and the highest for calcium chloride. The heat capacity of an ice slurry is an *apparent* heat capacity, because apart from the sensible heat effects it also contains a part describing the heat effect of the phase change. The estimated average apparent heat capacity is also given in Table 2.1 over the range of ice fractions from 0-0.20. These are determined using a constant heat effect for the phase change $\Delta\overline{H}_f$ of 333.5 kJ/kg and a constant sensible heat capacity for all ice slurries of 3.8 kJ/kgK. This property also depends on the freezing point depressants used, but is of relatively minor influence on the apparent heat capacity.

Table 2.1: Freezing point depression for 20% ice formation at -5^oC

Freezing point depressant	*Initial conc.*	*Tfreeze initial*	*Conc. increase*	*Additional freezing point depression*	*Est. avg. apparent heat capacity over 0-0.20 ice*
	wt%	^oC	wt%	K	kJ/kgK
$CaCl_2$	7.27	-3.68	1.82	1.32	54.2
LiCl	4.09	-3.81	1.02	1.19	59.8
NaCl	6.31	-3.91	1.58	1.09	65.0
Dextrose	24.74	-3.63	6.18	1.37	52.4
Ethanol	8.94	-3.87	2.23	1.13	62.9
Ethylene glycol	11.19	-3.84	2.80	1.17	61.0

Sodium chloride has the highest apparent heat capacity, approximately 24% higher than dextrose. Ice slurries based on sodium chloride are expected to be the most efficient cold carriers of the freezing point depressants of Table 2.1.

2.1.2 Ice Fraction

The ice weight fraction (w_i) determines for the largest part the amount of cold stored in an ice slurry. It is also important for the other heat and mass transfer properties of the ice slurry. The ice weight fraction is calculated from the freezing temperature of the solution, which is a function of the solute concentration.

$$T = T_f\left(w_{fpd}\right) \tag{2.7}$$

Once the initial concentration ($w_{fpd,0}$) and temperature are known, the equilibrium ice weight fraction is calculated with:

$$w_i = 1 - \frac{w_{fpd,0}}{w_{fpd}(T)} \tag{2.8}$$

in which $w_{fpd}(T)$ is found from the freezing curve, the inverse of Equation 2.7. Various references include data for freezing curves (Melinder, 1997; Lide, 1998). For low concentrations an estimation can be made with Equation 2.6, discussed in Section 2.1.1.

2.1.3 Density

Density of ice slurries is obtained by weighted addition of the density of pure ice and the density of the liquid solution.

$$\rho_{is} = \frac{1}{w_i/\rho_i + (1-w_i)/\rho_l} \tag{2.9}$$

The density of pure ice is estimated with the following correlation:

$$\rho_i = \rho_0 + c \cdot T \tag{2.10}$$

with T in ^{o}C, ρ_0 =917 and the coefficient c=1.73.10^{-4} (Ben Lakhdar, 1998). Reference works that include data for liquid mixtures are Melinder (1997); Soehnel (1985) and Lide (1998).

2.1.4 Enthalpy and Heat Capacity

Heat capacity is obtained by differentiation of the enthalpy with respect to temperature:

$$c_{p\_app} = \left(\frac{\partial h_{is}}{\partial T} \right) \tag{2.11}$$

The enthalpy of ice slurries is given by:

$$h_{is}(T) = w_i(T) \cdot \left(h_i(T) - \Delta H_f \right) + \left(1 - w_i(T) \right) \cdot h_l(T) \tag{2.12}$$

The heat capacity of an ice slurry is then:

$$c_{p\_app} = \left(\frac{\partial w_i}{\partial T} \right) \cdot \left(h_i - \Delta H_f - h_l \right) + w_i \cdot \left(\frac{\partial h_i}{\partial T} \right) + \left(1 - w_i \right) \cdot \left(\frac{\partial h_l}{\partial T} \right) \tag{2.13}$$

Heat capacities of pure ice and of the liquid solution can be substituted in Equation 2.13 to obtain:

$$c_{p\_app} = \left(\frac{\partial w_i}{\partial T} \right) \cdot \left(h_i - \Delta H_f - h_l \right) + w_i \cdot c_{p\_i} + \left(1 - w_i \right) \cdot c_{p\_l} \tag{2.14}$$

The heat capacity of an ice slurry is an *apparent* heat capacity (c_{p_app}), because apart from the sensible heat effects it also contains a part describing the heat effect of the phase change, the first term of Equation 2.14. This term contains the change in ice weight fraction with temperature. At sufficiently small temperature intervals this change can be estimated with:

$$\left(\frac{\partial w_i}{\partial T} \right) \approx \left(\frac{\Delta w_i}{\Delta T} \right) \tag{2.15}$$

Equation 2.15 is directly related to the freezing curve of a substance through equations 2.7 and 2.8. The apparent heat capacity is directly determined by the slope of the freezing curve. A steep freezing curve results in a low apparent heat capacity, because the effect of the phase transition is relatively less important, as is illustrated in Figure 2.3. The apparent heat capacity should be used in ice slurry calculations only if ice formation is relevant for the process considered.

In Figure 2.4 an enthalpy diagram of an ice slurry with NaCl as freezing point depressant is given. In the ice slurry part of the diagram, where the two phases are solid ice and a liquid NaCl-solution, lines of equal ice fraction are sketched as well as isotherms. Point *E* is the eutectic point. The phase diagram is adapted from Melinder (2001).

The enthalpy change for ice formation (ΔH_f) at 0 °C is 333.5 kJ/kg (point *G* in Figure 2.4). ΔH_f is a function of temperature. The enthalpy of ice at lower temperatures is lower, which is also displayed in Figure 2.4. ΔH_f is also a function of the concentration of freezing point depressant. If ice is formed, the concentration of freezing point depressant in the solution increases. A mixing heat effect must therefore also be taken into account. This heat of mixing can be observed in Figure 2.4, where the enthalpy isotherms of the solutions without ice are not equally spaced at increasing NaCl fraction.

Enthalpies and heat capacities of the liquid solutions can be obtained from: Melinder (1997), Lide (1998). Data for pure ice are obtained form Hyland and Wexler (1983).

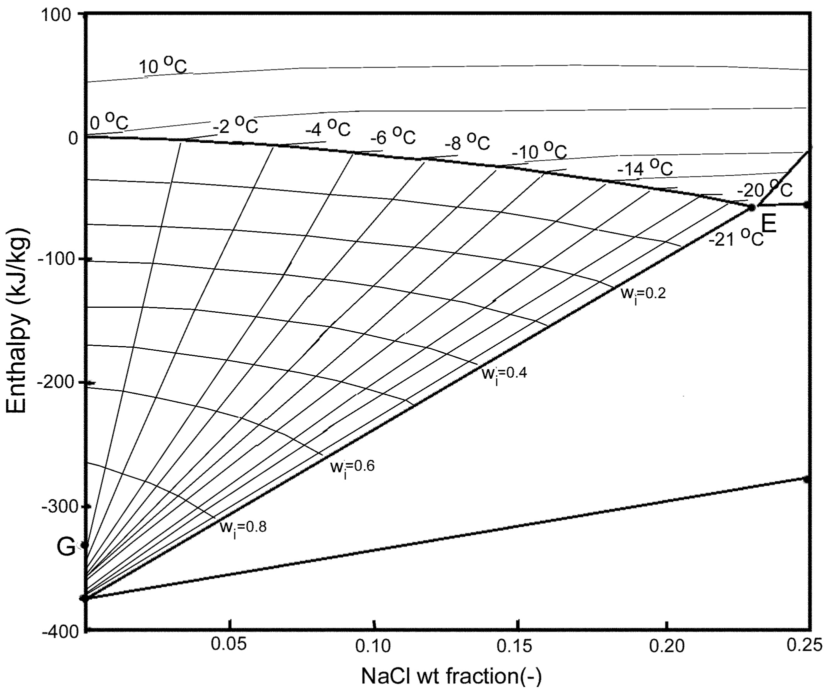

Figure 2.4: Enthalpy diagram of ice slurry based on NaCl

2.1.5 Thermal Conductivity

Several researchers have investigated the thermal conductivity of solid/liquid mixtures. Most models incorporate the conductivity of the liquid solution, the conductivity of the solid and some interaction effect. The model generally used for ice slurries is based on the theory of Maxwell, who derived a model assuming a solid phase consisting of spherical particles (Levy, 1981).

Ben Lakhdar (1998) has shown that the model proposed by Tareef (1940) yields satisfactory results for ethanol ice slurries up to an ice volume fraction of 0.4:

$$\lambda_{is} = \lambda_l \cdot \left(\frac{2\cdot\lambda_l + \lambda_i - 2\cdot\phi_i\cdot(\lambda_l - \lambda_i)}{2\cdot\lambda_l + \lambda_i + \phi_i\cdot(\lambda_l - \lambda_i)} \right) \tag{2.16}$$

At increasing ice fraction, the thermal conductivity of the ice slurry increases according to Equation 2.16. Models have not been experimentally validated directly due to the absence of a reliable method to measure thermal conductivity for ice slurries.

An alternative model was proposed by Kauffeld, who used a variation of the model developed by Eucken (Levy, 1981). This model yields values very similar to those of the Tareef model. The

model by Tareef is used here because it is claimed to be valid over a larger range of ice fractions than the other models.
Thermal conductivity of solutions are obtained from Melinder (1997), data for pure ice from Dorsey (1940).

2.1.6 Rheology and Viscosity

The dynamic viscosity μ of ice slurries is estimated from the viscosity of the liquid solution and the ice volume fraction. Homogeneous Newtonian flow behavior is assumed that complies with Equation 2.17, which relates yield stress (τ) with shear rate (γ):

$$\tau = \mu \cdot \frac{dv_z}{dr} = \mu \cdot \gamma \tag{2.18}$$

For calculations of the dynamic viscosity of ice slurries a number of theoretical models have been proposed, most of which are based on the model of Einstein (Thomas, 1965):

$$\mu_{is} = \mu_l \cdot (1 + 2.5 \cdot \phi_i) \tag{2.18}$$

One of the most accurate models similar to the model of Einstein is the model of Thomas (1965), which is used for viscosity estimations by various researchers (Bel and Lallemand, 1999; Kauffeld et al., 1999).

$$\mu_{is} = \mu_l \cdot \left(1 + 2.5 \cdot \phi_i + 10.05 \cdot \phi_i^{\,2} + 0.00273 \cdot \mathrm{e}^{\left(16.6 \cdot \phi_i\right)} \right) \tag{2.19}$$

This model is an empirical model correlated from ten different researches. Experimental validation by Kauffeld et al. (1999) for the case of ice slurries with ethanol as freezing point depressant showed that this model induces considerable errors at ice fractions above 0.20. It was assumed that at higher ice fractions ice slurries no longer have Newtonian flow behavior. The boundary of the transition into non-Newtonian behavior is however not sharp. In the transition area around 0.20 ice slurries may still be considered as Newtonian fluids if a small inaccuracy is allowed in calculations.
An incongruity of Equation 2.19 is that it does not yield the exact liquid viscosity if the ice fraction becomes zero. A modification of the following form corrects this:

$$\mu_{is} = \mu_l \cdot \left(1 + 2.5 \cdot \phi_i + 10.05 \cdot \phi_i^{\,2} + 0.00273 \cdot \left(\mathrm{e}^{\left(16.6 \cdot \phi_i\right)} - 1 \right) \right) \tag{2.20}$$

The modification introduces a relative difference of 0.273% between Equations 2.19 and 2.20 at an ice volume fraction of zero. At increasing ice fractions the relative difference decreases down to 0.14% at an ice volume fraction of 0.20.

For ice fractions above 0.20 two types of rheology have been proposed, pseudo-plastic (Guilpart et al., 1999; Ben Lakhdar, 1998) and Bingham type of flow behavior (Egolf et al., 1999; Frei and Egolf, 2000).
Pseudo-plastic rheology is described by a power law correlation:

$$\tau = K \cdot \gamma^{n} \tag{2.21}$$

in which n is the power law index and K the consistency. For a Newtonian fluid n=1, $K=\mu$ and Equation 2.21 reduces to the Newtonian case, Equation 2.17. If n is smaller than 1, the flow behavior is pseudo-plastic. Relations for K and n depending on the ice fraction were determined by Guilpart et al. (1999). The index n found by these authors was consistently smaller than 1 for ice fractions up to 0.28.
The viscosity of power law fluids depends on the shear rate and is therefore an apparent viscosity. It is determined with:

$$\mu_{app} = \frac{\tau}{\gamma} = K \cdot \gamma^{(n-1)} \tag{2.22}$$

For the case of a Bingham type of flow behavior, the Newton equation 2.17 is extended with a critical shear stress (τ_0):

$$\tau = \mu \cdot \gamma + \tau_0 \tag{2.23}$$

If the shear stress is lower than the critical value ($\tau<\tau_0$) the shear rate is zero ($\gamma=0$). For the Bingham model the viscosity also depends on the shear rate:

$$\mu_{app} = \frac{\tau}{\gamma} = \mu + \frac{\tau_0}{\gamma} \tag{2.24}$$

Experimental results of various researches differ widely, therefore a conclusion about the type of rheology that is valid for ice slurries above 20% vol. cannot be drawn. According to Frei and Egolf (2000) the differences are caused by dynamic properties of ice slurries. Under influence of shear, for example in storage tanks, shape and size of ice particles may alter and therefore also the rheological behavior of the ice slurries, this while density and heat capacity remain the same. Size and type of equipment, e.g. pumps, and residence times in storage tanks and pipes are also of considerable importance to ice slurry properties. In each research these parameters are different, so rheograms detected also differ. Frei and Egolf suggested a variation of the Bingham model which includes these effects in a parameter, s, describing the alteration of ice slurry properties over time (Frei and Egolf, 2000).

$$\tau = \mu \cdot \gamma + \left(1 - e^{-s \cdot \gamma}\right) \cdot \tau_0 \tag{2.25}$$

Instead of using an empirical parameter, it would be more accurate to determine the actual influence of ice crystal size and shape on the rheological behavior. Viscosity experiments for ice slurries with a known ice crystal size distribution are required to determine the rheological behavior.

Researchers have used various methods to measure viscosity of ice slurries. During the measurements the properties of the ice slurry need to remain constant. The ice particles should not melt or alter otherwise, which is hard to achieve in mechanical viscometers, as for example the rotary viscometer. One of the more reliable methods is to obtain viscosity data from pressure drop measurements at various throughputs of ice slurry flows in a cylindrical tube. This method was used in the researches of Frei and Egolf (2000) and of Kauffeld et al. (1999).

2.1.7 Overview

In Figure 2.5 relative trends of the properties heat conductivity, density, apparent viscosity and apparent heat capacity are given versus the ice fraction. Figure 2.5 is determined for an ice slurry with an initial fraction of 0.05 of sodium chloride as freezing point depressant. Reference values were set at 100% at a small ice fraction of 0.005. Density and heat capacity were calculated with Equations 2.9 and 2.14 respectively. The thermal conductivity was estimated with the model of Tareef, Equation 2.16. Viscosity was calculated with the modified method of Thomas (Equation 2.20).

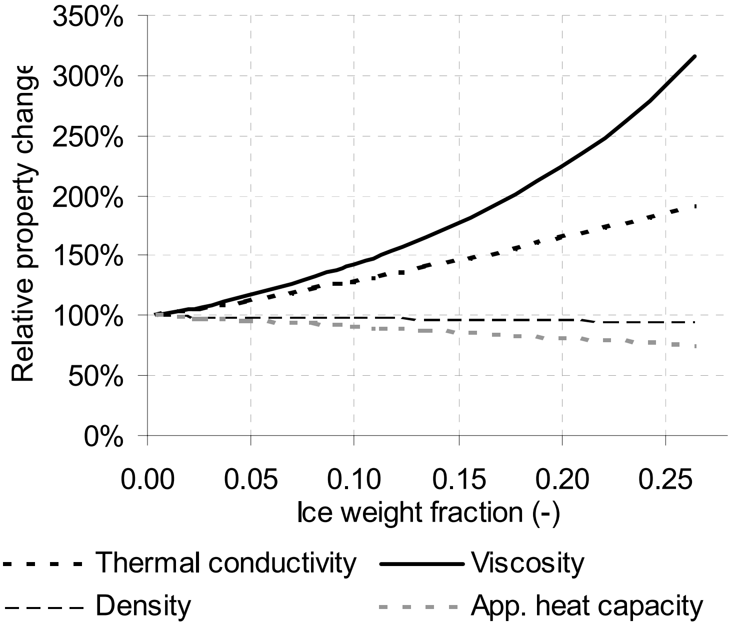

Figure 2.5: Relative trends of NaCl-ice slurry properties at –6 ^oC

At higher ice concentrations a Newtonian method is no longer valid and an apparent viscosity applies that depends on the shear rate. In Figure 2.6 the apparent viscosity is displayed for a few shear rates for ice slurries based on ethanol. Data determined by Ben Lakhdar (1998) are used that are fit with a pseudo-plastic rheogram. The shear stresses are relatively high compared to other researches, as pointed out by Frei and Egolf (2000). The increase in apparent viscosity will therefore probably be less than appears from Figure 2.6.

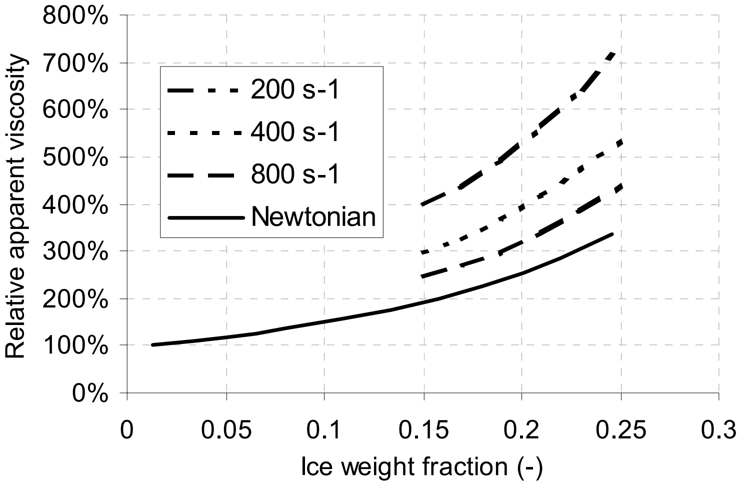

Figure 2.6: Relative trends in apparent viscosity of ethanol ice slurry at various shear rates (Ben Lakhdar, 1998)

In Figure 2.5 the viscosity is subject to the largest relative change going from low to high ice fractions. Especially in the non-Newtonian region viscosities can rise considerably, about three times as high at 0.25 ice fraction than for the solution without ice. Thermal conductivity also increases considerably at higher ice fraction slurries (Twice as high at 0.25 ice fraction than for no ice present). Density of an ice slurry remains relatively constant with varying ice fraction, while the apparent heat capacity decreases at increasing ice fraction, about 30% lower at 0.25 ice fraction than with no ice present.

Most of the experimental data available for ice slurry properties have been determined for ice slurries with sodium chloride or with ethanol as the freezing point depressant. To predict properties of ice slurries with other freezing point depressants, the same models as discussed in this section may be used, because most properties are based on the properties of the liquid solution, which are well known for most freezing point depressants. Only at high ice fractions deviations may occur for other freezing point depressants, mainly in viscosity predictions.

All ice slurry properties discussed in this section are estimated based on the properties of the liquid solutions. Differences in performance of freezing point depressants that have similar freezing curves are caused by the properties of the liquid solution. Solutions that are efficient secondary cooling fluids without phase change are expected to also be efficient as ice slurries. The most important property determining performance however is the freezing curve of a freezing point depressant.

Some freezing point depressant may freeze partially into the ice, so that the ice is not as pure and freezing points are not depressed as much as theoretically possible. Ice properties may be different in such cases.

2.2 Requirements of Ice Slurry Properties in Secondary Cooling Systems

Typical heat and mass transfer processes occurring in secondary cooling cycles are evaluated to determine what properties are required of ice slurries. Some models are reported specifically for ice slurries, others are more generally valid. In this section Newtonian rheology is assumed.

2.2.1 Processes in Secondary Cooling Systems

Important processes required in a secondary cooling system are heat transfer, transport and mixing. In this paragraph these are discussed in general terms.

Heat Transfer; Laminar Flow Conditions
For the case of an isothermal tube wall, theoretical correlations have been derived for heat transfer in circular tubes under laminar flow conditions. The average Nusselt number is given by (Chhabra and Richardson, 1999):

$$Nu = \frac{\alpha \cdot D}{\lambda} = 1.75 \cdot Gz^{1/3} \tag{2.26}$$

valid for Gz>100, with *Gz* the Graetz number, for circular tubes:

$$Gz = Re \cdot Pr \cdot \frac{\pi D}{4L} \tag{2.27}$$

Some heat transfer correlations have been determined specifically for ice slurries. An empirical model for the internal heat transfer coefficient under laminar flow conditions in circular tubes is presented by Guilpart *et* al (1999):

$$Nu = 38.3 \cdot Gz^{0.15} \cdot w_i^{0.52} \tag{2.28}$$

Equation 2.28 was developed for $3<Re<2000$ and $0.04<w_i<0.35$.

Heat Transfer; Turbulent Flow Conditions
For turbulent flow conditions and Newtonian flow behavior, several empirical relations are known, most of which are similar to Equation 2.29 of Dittus and Boelter, expanded with the correction factor for the viscosity near the wall (Holman, 1997):

$$Nu = c_1 \cdot Re^{c_2} \cdot Pr^{c_3} \cdot \left(\frac{\mu}{\mu_{wall}} \right)^{0.14} \tag{2.29}$$

where the constants differ depending on conditions. Typical values are: c_1=0.027, c_2=0.8 and c_3=0.33.

Some correlations have been reported for fluids of relatively high viscosity. For example Equation 2.30, based on the Stanton number which is reported to be valid for turbulent flow conditions of non-Newtonian fluids (Chhabra and Richardson, 1999):

$$St = \frac{\alpha}{\rho \cdot \mathrm{v} \cdot c_p} = 0.0152 \cdot Re^{-0.155} \cdot Pr^{-2/3} \tag{2.30}$$

Heat Transfer; Natural Convection

Heat losses in pipes and equipment where the ice slurry is in motion, either in turbulent or laminar flow, are calculated using the models above. These are significantly higher than if the ice slurry is standing still. A basic relation to predict natural convection is the Nusselt correlation (Green and Maloney, 2000):

$$Nu = c_1 \cdot \left(Gr \cdot Pr\right)^{c_2} \tag{2.31}$$

in which Gr is the Grashof number, given by:

$$Gr = \frac{D^3 \rho^2 g}{\mu^2} \bar{\gamma} \Delta T \tag{2.32}$$

where $\bar{\gamma}$ is the volumetric thermal expansion coefficient (K^{-1}).

The coefficients c_1 and c_2 of Equation 2.31 depend on the system geometry. For example for vertical plates, c_1=1.36 and c_2 =0.2, valid for $Gr \cdot Pr < 10^4$.

Ice Slurry Pumping

Power required for pumping ice slurries is determined by the pressure drop of ice slurries flowing in tubes (Sinnot, 1993; Janssen and Warmoeskerken, 1991):

$$\Delta p = 2f \cdot \rho \mathrm{v}^2 \cdot L / D \tag{2.33}$$

where f is the friction factor, for laminar flow conditions given by:

$$f = \frac{16}{Re} \tag{2.34}$$

Under turbulent flow conditions the friction factor of Equation 2.33 can be estimated with the Blasius equation:

$$f = \frac{c}{Re^{0.25}} \tag{2.35}$$

where c is an empirical constant of approximately 0.08. For the index to the Reynolds number also different values have been reported (e.g. 0.2). Knodel et al. (2000) reported that the turbulent

friction factor is somewhat reduced by the presence of ice crystals, depending on size and concentration of the ice crystals.
From the previous relations it is observed that the pressure drop for turbulent ice slurry flows depends on both density and rheology of ice slurries.

The following equation relates the pressure drop to the throughput for laminar flow in round tubes and is valid for all types of rheological behavior (Janssen and Warmoeskerken, 1991).

$$\varphi_v = -\frac{\pi r^3}{\tau_{wall}} \int_0^{\tau_{wall}} \tau^2 \dot{\gamma} d\tau \tag{2.36}$$

After substitution of the rheological model for Newtonian flow, Equation 2.17, into Equation 2.36 the following relation between pressure drop and throughput is obtained:

$$\varphi_v = -\frac{\pi r^4}{8\mu} \cdot \frac{\Delta p}{\Delta z} \tag{2.37}$$

Equation 2.37 is known as the Hagen-Poiseuille equation. It can be used to obtain rheological parameters and viscosity of ice slurries from pressure drop versus throughput measurements.
Pumping efficiency is also determined by the ice slurry properties. Rotary displacement pumps for example become more efficient for higher viscosity fluids, as leakage flow through seals reduces.

Stirring

Stirring of ice slurries will be necessary to get a homogeneous ice slurry, which may however not be required in all systems. Stirring of ice slurries is achieved by circulating pumps or by agitators or stirrers. Power input required for a stirrer (*P*) can be estimated with the Power number N_P (Sinnot, 1993):

$$N_P = \frac{P}{D_s^5 N^3 \rho} = c_1 \cdot Re^{c_2} Fr^{c_3} \tag{2.38}$$

where *Fr* is the Froude number ($D_s N^2/g$) and c_1 to c_3 are constants depending on vessel and stirrer geometry. *N* is the rotational speed of the stirrer, D_s the stirrer diameter. Under laminar flow conditions the index c_2 equals –1, which implies that stirring power in the laminar flow regime is proportional to the viscosity and does not depend on other ice slurry properties. Low viscosity ice slurries will have the lowest power consumption for stirring. In the turbulent flow regime both indexes c_2 and c_3 tend to zero. Stirring power input then depends on the density of the ice slurry (Nagata, 1975). Ice slurries with low density will have a low power consumption.

2.2.2 Overview of Optimal Ice Slurry Properties

An overview of the influence of thermophysical ice slurry properties on various processes is given in Table 2.2. For each property the exponent of Equation 2.39 is given that results after evaluation of the dimensionless groups:

$$Process = f\left(\rho^a {c_p}^b \lambda^c \mu^d\right) \tag{2.39}$$

It should be noted that the validity of many of the models for ice slurries still needs to be confirmed. The exact value of the exponents may therefore differ slightly for ice slurries, it is however not expected that different qualitative trends will be observed.

The ice fraction influences the other properties and thereby indirectly influences all processes, apart from a possible direct influence that it may have, as for example in Equation 2.28. In Table 2.2 only the qualitative influence of an increasing ice fraction is given. A '+' indicates that at higher ice fractions the value of the process increases, while '-' indicates a decreasing influence on he process. The trends are valid for the range of properties typical for ice slurries up to 0.25 ice fraction. Trends were verified numerically with NaCl and ethanol as freezing point depressants.

It should be noted that a negative influence of the ice fraction on a process, is not necessarily negative for process performance. A higher ice fraction for example reduces the ice slurry density, which reduces stirring power required under turbulent conditions.

Table 2.2: Influence of ice slurry properties on value of parameter 'Process'. Values of exponents of Equation 2.39 or qualitative trends '+' and '-'.

Process	*Equation*	*Ice Fraction (w_i)*	*Density (ρ)*	*Heat Capacity (C_p)*	*Thermal conduc-tivity (λ)*	*Viscosity (μ)*
	2.39		*a*	*b*	*c*	*d*
Laminar heat transfer	2.26	+	0.33	0.33	0.67	0
	2.28	+	0.15	0.15	0.85	0
Turbulent heat transfer	2.29	-	0.8	0.33	0.67	-0.47
	2.30	-	0.845	0.33	-0.67	-0.512
Heat losses (nat.convection)	2.31	+	0.4	0.2	0.8	-0.2
ΔP laminar flow	2.33	+	0	0	0	1
ΔP turbulent flow	2.33	+	0.75	0	0	0.25
Volumetric throughput (lam)	2.37	0	0	0	0	0
Volumetric throughput (turb)	2.37	-	0.75	0	0	-0.75
Pump efficiency (centrif.)	x	-	-	0	0	-
Pump eff. (displacement)	x	+	-	0	0	+
Tube diameter	2.14	-	-	-1	0	0
Laminar stirring power	2.38	+	0	0	0	1
Turbulent stirring power	2.38	-	1	0	0	0
Storage tank size	2.14	-	-	-1	0	0

The size of the storage tanks and the tube diameter required during ice slurry pumping are directly determined by the apparent heat capacity. In Table 2.2. therefore only the heat capacity, estimated with Equation 2.14, is included. Other properties, for example density, also have a mild influence, but small compared with the apparent heat capacity.

From Table 2.2 the importance of process conditions can be observed clearly: Under laminar flow conditions an increasing ice fraction results in higher heat transfer, while under turbulent flow conditions a higher ice fraction results in lower heat transfer. It depends on which sub-process of the secondary cooling system is under consideration which should be chosen. In heat exchangers high heat transfer performance is required, while during transport in tubes heat transfer rates need to be kept low in order to keep heat losses minimal.

Requirements of ice slurry properties may be contradictory between sub-processes. A high ice slurry density for example improves heat transfer, but it also increases the pressure drop of ice slurry flow. The relative importance of such contradicting ice slurry property requirements depends on the specific cooling application. Especially sizes of storage tanks and ice slurry tubing can vary greatly between applications. If the ice slurry generator can be installed very near the utilization heat exchangers, considerations of tube size and pressure drop will be unimportant compared with heat transfer performance.

Some sub-processes may be relatively unimportant because of system design or external factors. If for example a storage tank is insulated well, heat losses will be unimportant compared to stirring power input. Also if the ice slurry does not need to be stored homogeneously, a great reduction of stirring power consumption can be obtained.

A high ice fraction results in a low turbulent heat transfer coefficient, because high ice fractions have a high viscosity and a lower heat capacity. Goal of an ice slurry generator is however to increase the ice fraction, during which the heat transfer efficiency reduces, even if there is no build-up of solid ice on heat exchanger walls. For each generator an average ice fraction needs to be selected at which the heat transfer is still reasonable: Ice generators may operate with multiple passes through the heat exchanger. In the storage tank the ice fraction can be raised to the desired levels, while in the generator the ice fraction can be much lower, keeping heat transfer coefficients high. The ice slurry feed flow to the generator can be kept low in ice content by using an ice concentrator after the ice generator, or by using a storage tank that is not kept homogenous, so that a high ice content layer will form in the upper section of the storage tank.

If the ice fraction is high during pumping of the ice slurry, smaller tube diameters suffice. Pressure drops however increase because of an increased viscosity. Also possible transitions to non-Newtonian flow behavior may occur, increasing apparent viscosity and therefore pressure drop and energy consumption. For ice slurry pumping it may also be advantageous to apply a lower ice content than present in storage tanks, for example by not keeping the storage tanks fully homogeneous.

In utilization heat exchangers also various requirements of ice slurries may occur. Laminar or turbulent conditions have different effects on heat transfer. In closed systems and turbulent conditions, where the ice slurry flow needs to be recycled, it is probably most efficient to just melt all ice at the point where the ice slurry is returned to the storage tank. In open systems, for example in fishery, the ice fraction itself is more important than the heat transfer and therefore a system design should be made aiming for high ice fractions during utilization.

The effect of ice slurry properties on the likely performance of the secondary cooling system is evaluated qualitatively using Table 2.2. Generally, the viscosity of the ice slurries should be kept low and density, heat capacity and thermal conductivity high. Only if applications require long pumping distances or large turbulent storage tanks, densities of ice slurries should be kept low. It is concluded from Table 2.2 that variation of the ice fraction between the different stages of a secondary cooling system may yield considerable benefits, for example by using ice concentrators or ice separation methods.

2.3 Freezing Point Depressants

2.3.1 Ice Slurry Types

Various freezing point depressing substances have been investigated for use in ice slurries, some of which have already been applied in commercial cooling systems. These are sodium chloride (mainly seawater), ethanol and ethylene glycol, All three are relatively inexpensive and easy to use. Especially ethylene glycol is also widely used as secondary refrigerant without phase change. Many other additives have been proposed, calcium chloride ($CaCl_2$), propylene glycol, potassium acetate, magnesium chloride, ammonia and others.

Property requirements of ice slurries are very similar to the requirements of fluids in non-phase change systems. As ice slurry properties depend for a great part on the liquid phase properties, it is a logical step to first look into the substances that are applied successfully without phase change. For example calcium chloride, potassium formate and betaine may also prove efficient in ice slurries.

Some additional parameters need to be considered for ice slurries compared with non-phase change fluids. The freezing curve needs to be investigated as it determines the ratio between sensible and latent heat effect of the ice slurry and therefore the apparent heat capacity. The eutectic temperature may also limit the applicability of the ice slurry. For example sodium chloride, with eutectic temperature –20.7 ^{o}C, cannot be applied at freezing temperatures (utilization temperature of –18 ^{o}C). Size and shape of the ice crystals generated with a certain freezing point depressant also needs to be considered. Several effects may occur during the ice crystallization, for example an additive may actively interfere with the crystallization (for example antifreeze proteins) or an additive may be incorporated into the ice crystal structure, altering the properties of the ice crystals.

Alternatively, a freezing point depressant may be selected based on the specific ice slurry properties. For example freezing point depressants that have a high freezing point depressing effect at low concentrations (lithium chloride), or that have a relatively flat freezing curve so that an increase of the ice fraction leads to just a small decrease of temperature. In the current research dextrose was investigated as freezing point depressant experimentally, to determine if the diffusion coefficient of dextrose in water has an effect on the ice crystallization. For ice slurries in cooling applications dextrose is however not suitable as it has a too high eutectic point (-5 ^{o}C)

In some applications there is no choice or only limited choice in type and concentration of freezing point depressant. For example in fishery applications, sea water is required as feed of the ice slurry generators. Sea water can be evaluated accurately as a sodium chloride solution of 3 wt% and initial freezing point of –2 ^{o}C.

Freezing point depressing substances can be roughly divided into two categories: Brines of inorganic salts and mixtures of organic substances. These are evaluated in the next two sections. It is not necessary for all applications to use a freezing point depressant, therefore pure water is also evaluated as fluid from which ice slurries can be generated.

2.3.2 Organic Freezing Point Depressants

Potential organic freezing point depressants need to be fully soluble in water at a relatively low viscosity. Attention is therefore principally directed towards alcohols and poly-ols of relatively low molecular weight.

Ethanol is mostly suitable for closed systems, because of its volatility. In open systems ethanol evaporates from the ice slurry, thereby reducing the freezing point depression activity. The low boiling and flash points results in classification of ethanol as a safety hazard for flammability and explosion risk. These risks however occur at higher concentrations than typically applied in ice slurries. After leakages or other system faults high ethanol concentrations may occur. Ethanol is mildly toxic if swallowed. Ethanol solutions have a low density and a high apparent heat capacity. Ethanol solutions have a relatively high viscosity at lower temperatures.

Methanol solutions have a lower viscosity than ethanol and also a higher apparent heat capacity. The sensible heat capacity, thermal conductivity and density are similar. Disadvantageous is that it is much more toxic than ethanol, as well as more volatile and hazardous as a vapor. Both methanol and ethanol solutions may require addition of corrosion inhibitors, depending on the concentration.

Ethylene glycol solutions have good properties as secondary cooling fluid and are therefore widely applied in many commercial systems. They have a low viscosity compared with other solutions of organic substances. At temperatures below –10 ^{o}C however, the viscosity becomes high compared with most inorganic brines. For applications in ice slurries ethylene glycol also has a relatively low apparent heat capacity. Corrosion inhibitors are applied in most ethylene glycol systems. Ethylene glycol is toxic if swallowed and also irritating upon contact, but is not flammable.

Propylene glycol is less toxic and irritating than ethylene glycol. Disadvantageous is however the higher viscosity and the lower apparent heat capacity for ice slurry applications. It is applied in similar systems as ethylene glycol, where also corrosion inhibitors are required.

Betaine is a relatively novel cooling fluid for secondary cooling applications. It has only been investigated theoretically for ice slurry applications, because of the parallel that is often valid between ice slurry performance and non-phase change cooling fluid performance. Betaine has a relatively low viscosity compared with other organic substances, at low temperatures the viscosity however increases rapidly. Ice crystals produced with betaine must be analyzed, as the molecule may interfere with the crystallization. Betaine is more expensive than the other organic substances, but comparable to other inorganic cooling fluids, for example based on potassium formate. It is produced as a side product of beet sugar refining.

Anti-freeze proteins have been proposed as freezing point depressant in ice slurries by some authors, for example Grandum and Nakagomi (1997). Due to the thermal hysteresis effect however, this will not be a feasible option (see also section 2.4.4). Proteins may still be used to stabilize ice slurries by controlling the crystal size and shape, or to improve flow properties. The cost of antifreeze proteins is however relatively high for bulk applications.

Sugars as sucrose, fructose and dextrose (=*D*-glucose) have in common that the viscosity of the sugar solutions is very high. The relatively high molecular weights result in high weight fractions required for only a small freezing point depression. Also long term stability may be a problem, as low concentration solutions of sugars may form feed material for organic growth. In the present research dextrose is investigated as freezing point depressant to determine possible effects of a low diffusivity in water on ice crystallization.
Many other organic freezing point depressants can be used, provided that they have a good solubility in water in the temperature range considered. Also a relatively low molecular weight is advantageous for effective freezing point depression.

2.3.3 Inorganic Freezing point depressants

Inorganic freezing point depressants or salts used in ice slurries, are considered to be fully dissociated in solution. Densities of inorganic solutions are generally higher than densities of organic solutions. Inorganic additives are generally more corrosive then organic additives and there are more issues of material incompatibility.

Sodium chloride is widely applied in ice slurries, especially in fishery where sea water is an obvious ice slurry feed solution. The thermophysical properties of NaCl solutions are reasonable, as they have high density and high heat conductivity and relatively low viscosity. The main disadvantage of NaCl is the increased material costs it incorporates. It is highly corrosive, especially in open systems where oxygen from outside increases corrosivity. The NaCl solutions may cause pit-corrosion in stainless steel, so that special types of stainless steel are required.
The eutectic point of NaCl in water is around –21 ^{o}C, so that application at deep freezing temperatures is not possible.

Calcium chloride is also corrosive, especially under presence of oxygen. Corrosion inhibitors based on chromates make $CaCl_2$ solutions toxic as well as an environmental hazard. Thermophysical properties of $CaCl_2$ are efficient in non-phase changing secondary cooling applications. For ice slurries only preliminary experiments have been carried out.
Lithium chloride may be an alternative freezing point depressant, selected because of its low molecular weight. LiCl-solutions have a low viscosity and high density. The apparent heat capacity is relatively low, because of its steep freezing curve. Corrosion is also significant for LiCl, so that material costs are relatively high.

Potassium formate solutions have a low viscosity, also at low temperatures (below -20 ^{o}C) and high apparent heat capacity and density. Solutions have a relatively high pH and are incompatible with a number of materials, especially those containing zinc or aluminum. Long term corrosion effects are not established yet for all materials, but suitable inhibitors are available. Potassium formate is highly hygroscopic. It is irritating upon skin contact. Potassium acetate is similar to potassium formate, in some secondary cooling fluids also mixtures of the two are used. Potassium acetate has a higher viscosity, but there are less corrosion problems than for potassium formate. Potassium formate and potassium acetate are expensive compared to other salts.

Ammonia has also been suggested as freezing point depressant. Ammonia used as primary refrigerant however incorporates severe safety and environmental hazards, which is one of the main reasons to install a secondary system in the first place. Ammonia has a strong smell and is toxic. It has a low boiling point and a flammability risk. The freezing point depression capacity of ammonia is however large. Typical concentrations applied in household cleaning products are already suitable for ice slurry freezing point depression. A 3%wt. ammonia solution has an initial freezing point of –3.8 ^{o}C. A secondary system based on ammonia still requires many precautions to reduce the safety hazards.

Experiments with ice slurries based on magnesium chloride have also been reported (Kauffeld et al., 1999). Other salts suggested are potassium chloride, potassium carbonate and ammonium chloride.

2.3.4 Other Systems

For applications around 0 ^{o}C (some cooling applications, air-conditioning) it is not required to lower the freezing point of the ice slurry. In fact lowering of the freezing point in these applications even reduces efficiency, because of a lower evaporation temperature of the primary refrigerant. Clear water can be used as a feed for ice slurries at 0 ^{o}C. So far however ice slurry generators are not able to produce pumpable ice slurries from clear water. Large direct vacuum systems, in which water is used as the primary refrigerant, are able to produce ice slurries at –0.5 ^{o}C, with still a small amount of freezing point depressant in the mixture (Paul, 1996).
In some large mining applications, vacuum systems are used to produce ice slurry which is then concentrated (w_i>0.50). The ice is conveyed downwards into the mines more than it is pumped. A requirement in this particular application is that the ice contains no additives, so that it can be consumed by workers in the mines as refreshment (Sheer et al., 2003).

An alternative ice slurry system, proposed by Royon et al. (1999), uses water that is absorbed in small porous polymeric particles in a liquid phase of oil. Due to the immiscibility of water with oil, the water stays in the particles. The phase change to ice also occurs in the polymeric particles. The main advantage is that the ice will not adhere to heat exchanging surfaces, so that freeze-up can not occur. Disadvantageous is the increased complexity of the system. Heat transfer rates may be lower as heat must be transferred through the oil first. Also the ice formation and melting may be slow inside the particles.

Other phase change materials, for example based on paraffin, are under investigation by several researchers (Ure, 1999). Solutions based on water however have a high latent heat effect compared to the materials that have been proposed. Advantageous of the non-water phase change materials is the phase change temperature that can also be at temperatures above 0 ^{o}C.

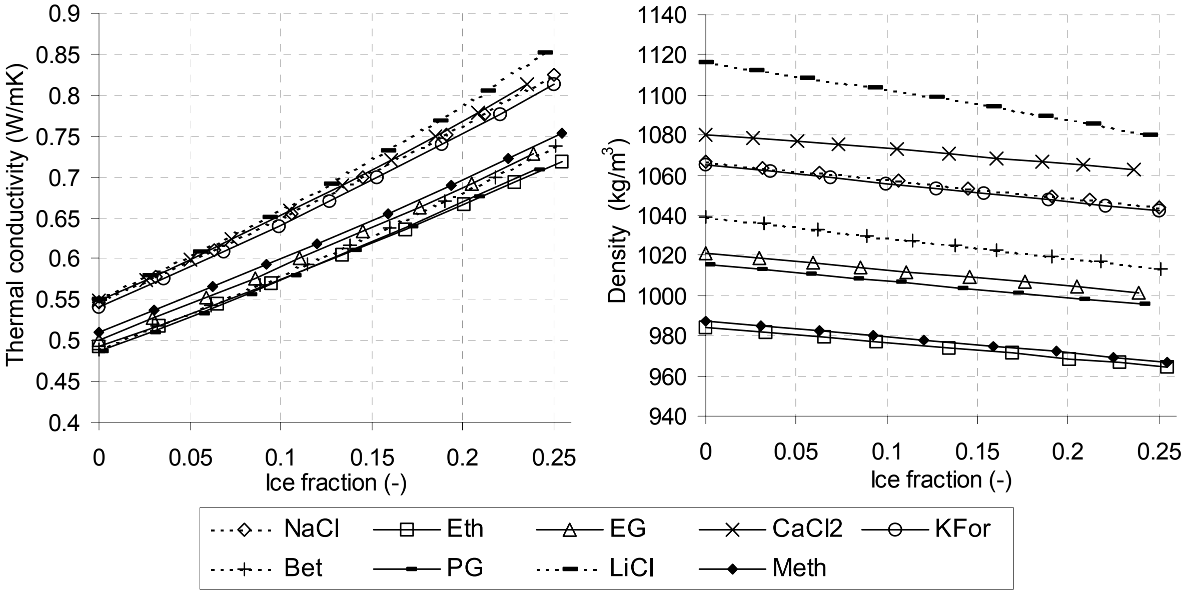

Figure 2.7: Thermal conductivity of ice slurries of various freezing point depressants, T_{f_init}= –5 °C, predicted with Equation 2.16

Figure 2.8: Density of ice slurries of various freezing point depressants, T_{f_init}= –5 °C, predicted with Equation 2.9

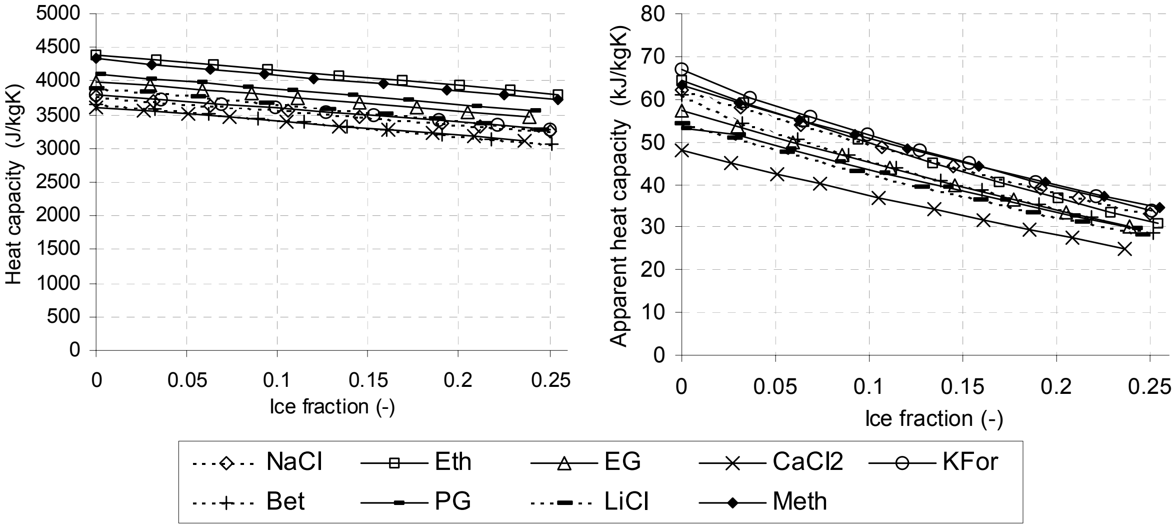

Figure 2.9: Sensible heat capacity of liquid phase of ice slurries of various freezing point depressants, T_{f_init}= –5 °C

Figure 2.10: Apparent heat capacity of ice slurries of various freezing point depressants, T_{f_init}= –5 °C, predicted with Equation 2.14

2.3.5 Overview of properties

In Figures 2.7-2.12 an overview of thermophysical properties of the ice slurries as predicted with the models discussed in section 2.1 is given for nine freezing point depressants. Ethanol, ethylene glycol and NaCl are included because these have already been applied in ice slurries. $CaCl_2$, Potassium formate (KFor) and betaine (Bet) are included because these are applied as secondary fluids without phase change. Other substances included are LiCl, methanol and propylene glycol. In the Figures the properties of solutions with initial freezing points of –5 ^oC are given, i.e. the overall concentrations of freezing point depressants is constant at increasing ice fraction.

The thermal conductivity predicted for ice slurries, displayed in Figure 2.7, can be divided into two groups: The ice slurries based on inorganic freezing point depressants (NaCl, LiCl, $CaCl_2$, KFor) have a thermal conductivity that is in the order of 10% lower than those based on organic additives (ethanol, methanol, EG, PG, Betaine).
Differences observed between freezing point depressants for the ice slurry density are also in the order of 10% maximum, see Figure 2.8. Ethanol and methanol have the lowest density, while LiCl and $CaCl_2$ have the highest. The organic additives generally have the lowest density.
The sensible heat capacity of the liquid phase of the ice slurry is given in Figure 2.9, the largest difference observed, between ethanol and $CaCl_2$ is around 24%. No trend is observed between inorganic and organic freezing point depressants for sensible heat capacity.
The apparent heat capacity, including both the latent heat effect of ice formation and sensible heat of ice and liquid phase is displayed in Figure 2.10. This property indicates the cold storage capacity of an ice slurry and a high value directly corresponds to small storage tanks and pipe diameters. Differences between freezing point depressants are considerable, from 40% at zero ice fraction to 47% at 0.25 ice fraction. The most efficient ice slurries are based on potassium formate, methanol, ethanol and sodium chloride, while $CaCl_2$ is the least efficient.

The dynamic viscosity of the ice slurries is displayed in Figure 2.11, assuming Newtonian flow behavior. The differences in viscosity observed between freezing point depressants is considerably larger than that of thermal conductivity and density. At zero ice fraction the dynamic viscosity of ethanol is 1.8 times the viscosity of potassium formate. At an ice fraction of 0.20, the viscosity of ethanol and propylene glycol ice slurries is approximately 2.3 times the viscosity of the NaCl ice slurry. Generally, the ice slurries with organic additives have a higher viscosity than the ice slurries with inorganic freezing point depressants. Methanol, betaine and ethylene glycol have a relatively low viscosity compared with propylene glycol and ethanol.
The differences predicted for the viscosity are larger than the differences of thermal conductivity and the liquid phase heat capacity, so that the Prandtl-numbers are higher for organic ice slurries than for inorganic ice slurries, as is displayed in Figure 2.12.

At lower temperatures, too high eutectic points make some freezing point depressants unsuitable. For others the viscosity becomes unacceptably high. In Figure 2.13, the viscosity is given for ice slurries at initial freezing points of –20 ^oC, a typical temperature for deep freezing applications. NaCl and LiCl could not be included because of too high eutectic temperatures.
Only ice slurries with viscosities below 100 mPa.s are given in Figure 2.14. Potassium formate, methanol and $CaCl_2$ retain acceptably low viscosities.

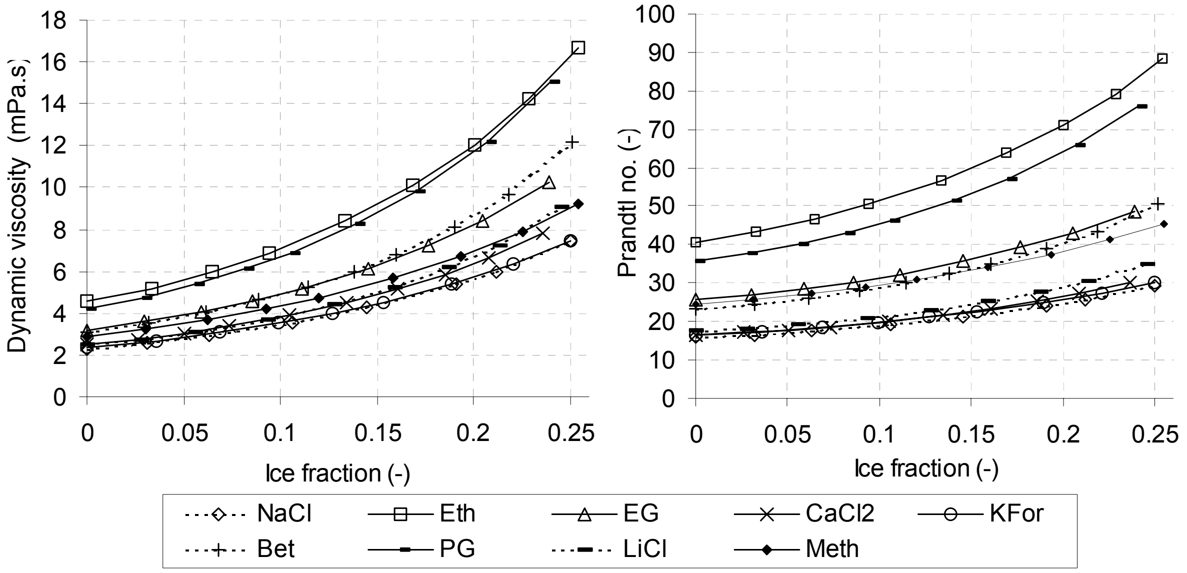

Figure 2.11: Dynamic viscosity of ice slurries of various freezing point depressants, T_{f_init}= –5 °C, predicted with Equation 2.20

Figure 2.12: Prandtl number of ice slurries of various freezing point depressants, T_{f_init}= –5 °C, $Pr=\mu C_p/\lambda$ calculated with data of Figures 2.7, 2.9 and 2.11

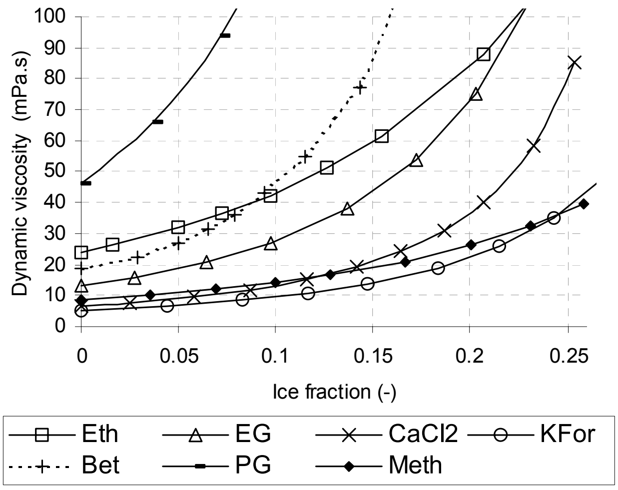

Figure 2.13: Dynamic viscosity of ice slurries of various freezing point depressants, T_{f_init}= –20°C, predicted with Equation 2.20

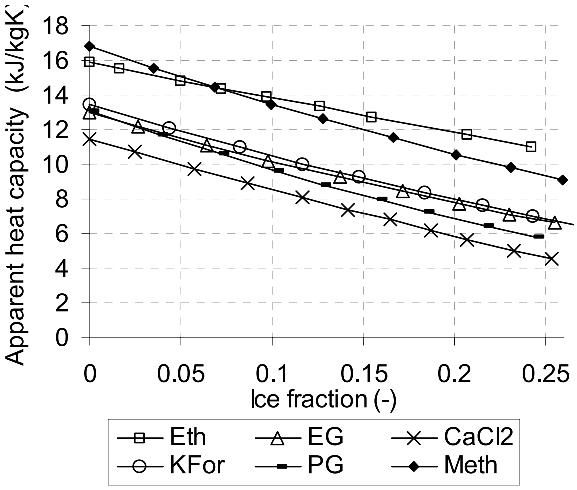

Figure 2.14: Apparent heat capacity of ice slurries of various freezing point depressants, T_{f_init}= –20 °C, predicted with Equation 2.14

The apparent heat capacity at temperatures below –20 °C is considerably lower than at –5 °C, as is displayed in Figure 2.14. Methanol and ethanol have the highest, while $CaCl_2$ the lowest. The apparent heat capacity for betaine could not be calculated at this temperature, because the freezing curve is not known accurately enough.
The diagrams of density, thermal conductivity and specific heat capacity of the liquid phase are similar to those at –5 °C and are therefore not given for –20 °C.
If the ice slurry properties are calculated at a constant temperature at increasing ice concentration instead of at a constant concentration of freezing point depressant, similar trends are found as given in figures 2.7-2.14.

It was discussed in the previous section that there is not one set of properties that is efficient for all applications. Selection of a freezing point depressant should be evaluated considering the specific application requirements. In the current evaluation however some freezing point depressants appear to be more efficient than others. These are potassium formate, methanol, LiCl and NaCl. Except for NaCl, the quality of the ice crystals needs to be confirmed for these freezing point depressants. For these freezing point depressants the corrosivity of the ice slurries may be a significant issue, while the high toxicity is an important disadvantage for methanol.

In the current evaluation only pure freezing point depressants were discussed. It is in many cases also possible to use a mixture. Mixtures of ethylene glycol and propylene glycol and mixtures of potassium formate and potassium acetate are known as non-phase changing cooling fluids. Thermophysical properties of such ice slurries are expected to be generally in between the properties of ice slurries using pure freezing point depressants.

2.3.6 Other Additives

A number of additives can be used in ice slurries to enhance performance in cooling systems. Additives have been reported for the following goals:

Corrosion inhibitors. Depending on the type of freezing point depressant used. For brines of sodium chloride and potassium formate and glycol solutions corrosion inhibitors are definitely required and choice of materials may still be limited. In closed systems it may be advisable to remove oxygen or de-air ice slurry solutions to reduce corrosion.

Anti-Recrystallization agents. During long term ice slurry storage (several hours), ice crystals may cluster or change in size through ripening. This can be prevented using stabilizing agents, for example anti-freeze proteins or other macromolecules. Some substances may also help to reduce the supercooling effect and start nucleation of ice crystals very near to the equilibrium freezing temperature.

Surfactants. Mainly used to enhance ice slurry flow properties, especially in high viscosity ice slurries (Suzuki et al., 2001). Surfactants may also interfere with the crystallization process in various ways. Surfactants may stabilize ice slurry crystals, so that size and shape remain similar during long term storage. Anti-foaming agents may be required in combination with surfactants.

Acidity. The pH of an ice slurry may be relevant for a number of processes, for example corrosion, ice crystallization and the biological stability of organic freezing point depressants. During ice formation concentrations of freezing point depressants change. Also the pH may change, especially if acidic or basic agents, for example potassium formate, potassium acetate, are used. A pH-buffer may then be added to prevent large fluctuations of the acidity.

Biological stability. Some ice slurries, especially with organic freezing point depressants at low concentrations, may be susceptible to biological infection with bacteria or growth of algae. In open systems this may cause problems. Light should be kept out or the ice slurry can be denatured in a number of ways, depending on which freezing point depressant is used.

Frost damage. If food products are frozen using ice slurries, damage to the products may occur in a number of ways. The shape of the crystals may be a factor, because needle shaped crystals may puncture cell tissue. The concentration of additives may also be of influence. Osmotic effects may cause damage to cells and alter liquid content and taste. Plants from arctic regions contain high glycol levels to prevent such effects. The liquid phase can be filtered of the ice, so that only the ice contacts the food.

2.4 Ice Crystals

2.4.1 Introduction

The main feature of ice slurries is the presence of small ice crystals. Many researchers have reported on typical crystal sizes and shapes. Almost all report crystals that are shaped like spheres or disks, with typical characteristic diameters in the order of 0.1 mm. Some researchers have observed smaller ice crystals, down to 10 μm, and also larger ice crystal sizes up to 3 mm were reported. Dendritic or needle shaped ice crystals were observed under some conditions, however not in commercially applied systems. Needle shaped ice crystals may damage organic tissue and must therefore be avoided in fishery and other food cooling and freezing applications.
Ice crystals are formed mainly in the ice slurry generator, but size and shape may also change in other parts of secondary cooling systems. Ice crystal dimensions may be important for the ice slurry properties. The ice crystal surface area is relevant, as it determines on what area ice crystals may grow or melt. It is therefore a measure of how fast latent heat can be released or stored. Also the rheology and viscosity may be affected, as was already seen in section 2.1.6, where the differences of ice slurries between researchers was summarized in a parameter s (Frei and Egolf, 2000). Also the thermal conductivity may be slightly affected by crystal shapes.

2.4.2 Crystallization

The formation mechanism of ice crystals is described, as well as other processes involved in crystallization that may affect ice slurries.

Supersaturation
Ice slurry generation involves crystallization of water from an aqueous solution of a freezing point depressing substance. It can only occur if there is a sufficient driving force that makes the

solution supersaturated with water. Supersaturation can for example be created by cooling the solution or by applying pressure under triple point conditions.

A solution that is supersaturated with water by means of cooling at constant pressure is said to be supercooled. In a supercooled solution, constantly clusters of water molecules are formed and broken again in a configuration as in ice. Upon increase of the supercooling the formation and growth of the clusters becomes more likely than the break-up of the clusters and nucleation starts.

Nucleation

In a supersaturated solution nuclei are formed if molecules form stable clusters, either homogeneously or heterogeneously. In homogeneous nucleation the new phase is formed in a clear liquid, which generally happens at low temperatures (e.g. below –40 ^{o}C). This type of nucleation is not common in applications, because tiny foreign objects are often present in solutions that assist the formation of initial nuclei, which is called primary heterogeneous nucleation. The surface of foreign materials helps orienting molecules and a crystal lattice is more easily formed. Heterogeneous nucleation starts at higher temperatures than homogeneous nucleation. The foreign particles (for example dirt or dust) can be so small that they may not be visible in the solution. Also equipment walls can induce heterogeneous primary nucleation.

Secondary nucleation occurs if new nuclei are formed from existing crystals of the material being crystallized. This can happen by a number of mechanisms, for example similar to the foreign surface effects or by attrition.

Growth

In crystal growth nuclei grow into crystals by addition of solute molecules from the supersaturated solution. Growth can generally be subdivided into three steps: Diffusion of molecules from the bulk of the solution through the boundary layer around the nucleus, incorporation into the crystal lattice and heat transfer of the latent heat effect.

Attrition

If a crystal is subjected to stress, part of the crystal may break off in a process called attrition. Stresses can occur because of fluid shear during mixing and pumping or because of collisions with other solids, such as other crystals, walls, mixing impellers, circulation pumps or other. The fragments of the crystals form secondary nuclei.

Attrition is influenced by several factors. Crystals with a rough surface will produce more fragments upon attrition than crystals with a smooth surface, especially under conditions with high liquid shear. Crystals with sharp edges are more susceptible to attrition than crystals with smooth edges. Finally, small crystals will show less attrition.

Agglomeration

Agglomeration is the process in which crystals collide and adhere and eventually form a stable crystal or agglomerate together. The degree of agglomeration decreases with increasing intensity of agitation. High degrees of supersaturation also increase agglomeration.

In ice slurries the individual crystals generally stick together due to surface tension effects. This clustering however is not considered agglomeration, as the different ice crystals still have separate crystal structures.

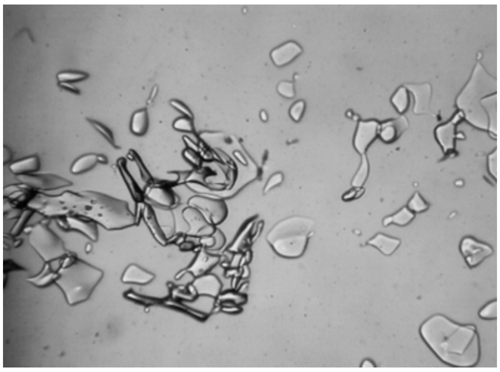

Figure 2.15: Microscopic picture of 4.9 wt% NaCl ice slurry, produced in fluidized bed ice slurry generator, just after nucleation. Width of picture = 2.6 mm

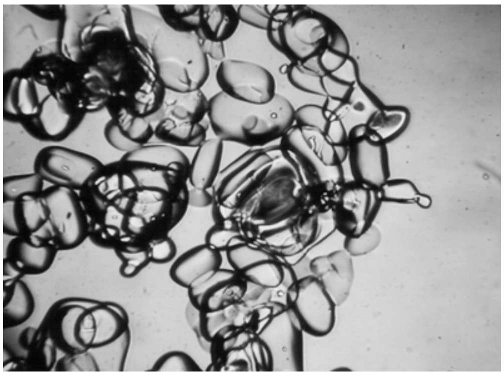

Figure 2.16: Microscopic picture of 4.9 wt% NaCl ice slurry, produced in fluidized bed ice slurry generator. Sample after 90 minutes of ice slurry generation. Width of picture = 2.6 mm

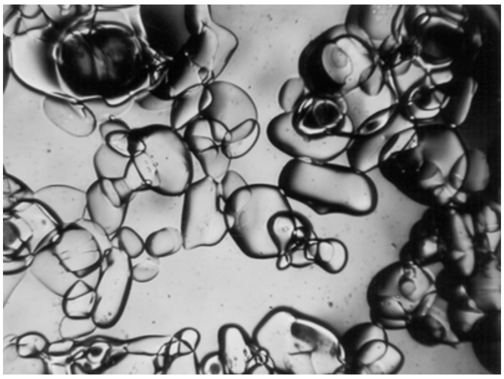

Figure 2.17: Microscopic picture of NaCl ice slurry, produced in fluidized bed ice slurry generator. Sample after 100 minutes of ice slurry storage without generation or melting. Width of picture = 2.6 mm

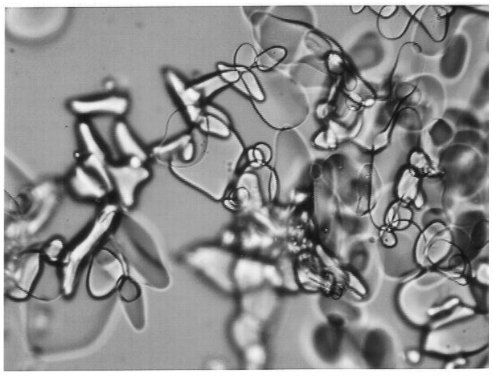

Figure 2.18: Microscopic picture of 5.6 wt% EG ice slurry, produced in fluidized bed ice slurry generator. Sample just after nucleation. Width of picture = 2.6 mm

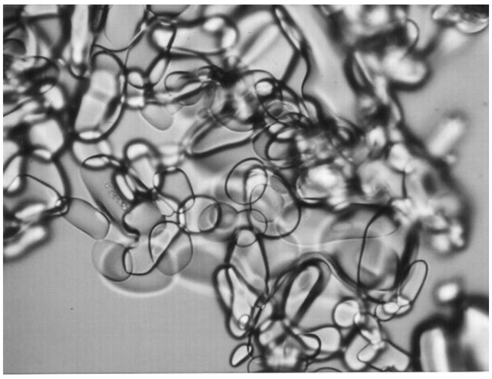

Figure 2.19: Microscopic picture of 5.6 wt% EG ice slurry, produced in fluidized bed ice slurry generator. Sample during ice slurry generation Width of picture = 2.6 mm

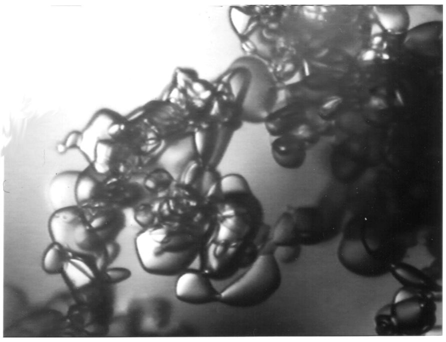

Figure 2.20: Microscopic picture of 19.8 wt% Dextrose ice slurry, produced in fluidized bed ice slurry generator. Sample during ice slurry generation. Width of picture = 1.5 mm

Ostwald ripening

The crystal size distribution of crystals dispersed in a saturated solution can change because of Ostwald ripening. The driving force for ripening is a difference in solubility between small and large crystals. Smaller crystals tend to dissolve, while the resulting solute is deposited on the larger crystals. The solid phase in a saturated solution strives towards a minimum total surface free energy. Ripening generally occurs at very low supersaturation. It also occurs in isothermal systems, changing the crystal size distribution of an ice slurry over time. Effects of Ostwald ripening need to be considered if applications require long storage times of the ice slurry.

2.4.3 Ice Crystals of the Present Research

During the fluidized bed heat exchanger experiments of the present research, a number of ice slurry samples were taken to verify the quality of the ice slurry produced. The samples were all taken from the ice slurry storage tank, at various times during test runs. The samples were analyzed using a microscope and digital video camera set-up, with which a series of pictures was taken of each sample. The microscope was equipped with a thermostatic cell, so that pictures could be taken at the actual ice slurry temperature without melting or growing of the ice crystals.
Samples were analyzed of ice slurries based on three different freezing point depressants: NaCl, ethylene glycol and dextrose.
For NaCl ice slurries, pictures were taken at three different moments, one just after initial nucleation, one after 90 minutes of regular ice slurry generation, and one after the ice slurry was kept in the storage tank without ice slurry generation for 100 minutes. In the storage tank a propeller was used to mildly stir the ice slurry. Example pictures of the three samples are given in Figure 2.15-2.17. Also for ethylene glycol ice slurry samples were taken just after nucleation and during ice slurry generation. In Figure 2.18 and 2.19 typical pictures of ethylene glycol ice slurry are given. In Figure 2.20 an example picture of an ice slurry based on dextrose is given. The pictures of the dextrose ice slurry were taken using different microscopic equipment than used for the other samples. Pictures taken with this other equipment were less sharp, and therefore the analysis of the pictures less accurate. The sample of the dextrose ice slurry was taken after several hours of steady state ice slurry generation, where a heater was used to melt ice in the storage tank, while also the fluidized bed ice slurry generator operated continuously.

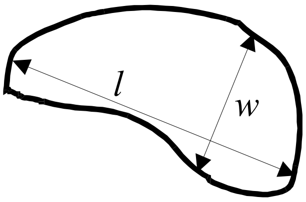

Figure 2.21: Length and width measurement of an ice crystal

The digital pictures were analyzed using the Image Processing toolbox of Matlab, to determine the typical dimensions of the ice crystals. The longest dimension of the crystal was taken as the length, *l,* and the largest width perpendicular to this length was taken as the width, *w.* See also Figure 2.21. For each sample at least 80 crystals were analyzed. The number of crystals present in a single picture does not indicate the ice concentration of the sample, because samples were not kept homogeneous during the microscopic analyses.
Results of the ice slurry samples are given in Table 2.3. The ice slurry crystals produced were shaped similar to disks or spheres. No sharp edges or needle type crystals were observed in any of the samples. Just after nucleation the crystals were relatively small and shaped slightly irregular. After several minutes of operation, crystals were more similar in shape to disks or spheres and were also larger. It is likely that the crystals were subjected to attrition and have also

grown, as the crystals have passed through the fluidized bed heat exchanger a number of times. After 100 minutes of storage of the NaCl ice slurry, the crystal shapes were very similar to those during ice slurry generation. The crystals were slightly larger, but the difference is small. In order to determine if a ripening effect occurs, more experiments are required, in which the ice crystals are also stored over longer periods, e.g. overnight.

The crystal dimensions of different freezing point depressants cannot be compared accurately, as the process conditions in the fluidized bed experimental set-up were not the same for the different additives. It is only concluded that for all three additives, the ice crystal size and shape comply with the requirements for ice slurry cooling systems, which have been discussed by for example Kauffeld et al., (1999) and Bel (1996).

For a more accurate evaluation of size and shape of ice crystals, other characteristic dimensions can be used. For example the Feret diameter, which is defined as the diameter of a circular shape with equal area as the ice crystal. This dimension allows for an evaluation based on a single characteristic, so that numerical predictions of crystal size distributions can be made.

Table 2.3: Average ice slurry crystal dimensions, generated with fluidized bed experimental set-up for three freezing point depressants (fpd)

Fpd	*wt%*	*Sample*	*Length (mm)*	*Width (mm)*	*Shape*	*Fig.*
NaCl	4.9	Just after nucleation	0.16	0.091	Irregular	2.15
		90 min. generation	0.29	0.19	Spherical/disks	2.16
		100 min. stirred storage	0.30	0.20	Spherical/disks	2.17
EG	5.6	Just after nucleation	0.26	0.14	Irregular	2.18
		20 min. generation	0.35	0.22	Spherical/disks	2.19
Dextrose*	19.8	225 min. generation	0.14	0.098	Spherical/disks	2.20

* *Pictures taken with other microscopic equipment than NaCl and EG pictures.*

2.4.4 Thermal Hysteresis vs. Freezing Point Depression

The freezing point depression as discussed so far is a colligative property. The freezing point depression depends on the number of solute molecules present and not on the nature of these molecules. There is however also a class of substances that depresses the freezing point actively by interfering with the ice crystallization process. Examples of these substances are antifreeze proteins, which is found in the blood of polar fish, that lower the freezing point with only very small concentrations, in the order of μg/l. Apart from anti-freeze proteins found in fish, insects and some plants, also some other macromolecules have been reported to actively depress freezing points (Grandum and Nakagomi, 1997).

A colligative freezing point depressant interferes with the ice formation passively, by occupying the water molecules or occasionally blocking the water molecules path to crystallization sites. For example an ion present in a solution is surrounded by water molecules, which are then hindered to form the molecular clusters that start a new ice crystal. Also, if an ion is at the surface of an ice crystal it must move out of the way before water can bind to the crystals and the solid phase can grow.

Anti-freeze proteins on the other hand actively bind to beginning ice clusters. In this process the further development of the beginning ice crystal is stopped. This binding and stopping is very effective in anti-freeze proteins, so that until several tens of degrees below zero ice formation can be blocked. If however ice formation has commenced, the anti-freeze proteins are no longer effective for the depression of the freezing point. The melting of ice will still occur at a temperature of around 0 ^{o}C. The difference between the freezing and melting of solutions with these molecules is called thermal hysteresis. In ice slurries applications this hysteresis effect causes an extra temperature difference between production and utilization. The ice slurries need to be generated at lower temperatures which is energetically less efficient, while they still melt at the higher temperature.

There are still reasons to use the thermal hysteresis substances in ice slurry applications. The anti-freeze proteins may be used as stabilizing agents, that prevent changes in ice crystal size during longer periods of storage. Also these class of substances may have effects on the shape of crystals of ice slurries, which might improve ice slurry flow properties (Suzuki et al., 2001).

2.5 Conclusions

The thermophysical property models required to describe the relevant heat and mass transfer processes occurring in a secondary cooling cycle have been discussed. Accurate models to predict freezing points, density, enthalpy and heat capacity of ice slurries are available and their specific use for ice slurries has been validated by various researchers. Also for the viscosity of ice slurries with relatively low ice fractions, up to 0.20, accurate models are available, provided that Newtonian rheology can be assumed. At higher ice fractions results of researches vary, which is likely caused by differences in the ice crystals produced between various researches. The thermal conductivity of ice slurries cannot be measured directly, but the various predictive models are generally accepted and do not yield different predictions.

The variation of the thermophysical properties with ice fraction is large. In the range of ice fractions from 0 to 0.25, the viscosity approximately triples and the thermal conductivity doubles. The apparent heat capacity and the density are relatively constant.

The relevant heat and mass transfer processes in secondary cooling systems have been introduced and evaluated for the specific thermophysical ice slurry properties. The optimal properties contradict each other on several points, so that an optimization is required depending on the application. Application of ice concentrators is expected to yield considerable benefits throughout the various stages of a secondary cooling cycle.

The ice fraction is the most relevant parameter that determines the properties of ice slurries. The choice of freezing point depressant can however also be of considerable influence. Especially for ice slurries applied at lower temperatures, the viscosity and the apparent heat capacity may vary widely depending on the freezing point depressant used. Some freezing point depressants appear to be more efficient in secondary cooling applications because of a relatively low viscosity and high apparent heat capacity. These are potassium formate, methanol, LiCl and NaCl.

The fundamental processes of ice crystallization have been introduced. Supersaturation, nucleation and crystal growth during the crystal formation. Also additional effects as agglomeration, attrition and Ostwald ripening are discussed. Microscopic pictures of the ice slurry crystals of the present research, i.e. ice crystals generated in the fluidized bed generator experimental set-up, have been analyzed. The ice crystals generated are similar to those generated with other methods already successfully applied in cooling systems. Influences of several factors, type of freezing point depressant, generator operating conditions and storage times is noted, however only a few pictures are evaluated, so that predictive modeling is not yet possible.

Nomenclature

a	activity
a,b,c,d	parameters
$c_{1..3}$	constants
c_p	heat capacity (J/kgK)
D	diameter (m)
f	friction factor (-)
G	Gibbs energy
g	gravitational acceleration (m/s^2)
h	enthalpy (J/kg)
ΔH_f	enthalpy of fusion (J/kg)
K	consistency (-)
l	characteristic length (m)
L	length (m)
M	mole weight (kg/mol)
N	revolutions (s^{-1})
n	coefficient (-)
P	Power (W)
p	pressure (Pa)
R	gas constant
r	radius (m)
S	entropy (J/kgK)
ΔS_f	entropy of fusion (J/kgK)
s	parameter of Equation 2.25
T	temperature (K or ^{o}C)
T_f	Freezing temperature (^{o}C)
v	velocity (m/s)
w	characteristic width (m)
$w_{substance}$	weight fraction of substance (-)
z	height (m)

Greek

α	heat transfer coefficient (W/m^2K)
γ	shear rate (s^{-1})
γ	thermal expansion coefficient (K^{-1})
λ	heat conductivity (W/mK)
μ	dynamic viscosity (Pa.s)
$\boldsymbol{\mu}$	chemical potential
ρ	density (kg/m^3)
τ	shear stress (Pa)
τ_0	yield stress (Pa)
ϕ	volume fraction (-)
φ_v	volumetric flow (m^3/h)

Dimensionless groups

Fr	Froude
Gr	Grashof
Gz	Graetz
Nu	Nusselt
N_P	Power
Pr	Prandtl
Re	Reynolds
St	Stanton

Substances

Bet	Betaine
EG	Ethylene glycol
Eth	Ethanol
KFor	Potassium formate
Meth	Methanol
PG	Propylene glycol

Subscript

0	reference condition
app	apparent
f	freezing
fpd	freezing point depressant
i	ice
init	initial
is	ice slurry
l	liquid phase (solution)
s	stirrer
w	water
wall	wall
z	z-direction

Superscript

*	equilibrium

References

Bel., O., 1996, *Contribution a l'étude du comportement thermo-hydraulique d'un melange diphasique dans une boucle frigorifique a stockage d'energie,* Thesis de l'INSA de Lyon, France

Bel, O., Lallemand, A., 1999, *Etude d'un fluide frigoporteur diphasique*. International Journal of Refrigeration vol 22: p.164-187

Ben Lakhdar, 1998, M.A. *Comportement thermo-hydraulique d'un fluide frigoporteur diphasique: Le coulis de glace*, Thesis de l'INSA de Lyon, France

Bevan Ott, J., Rex Goates, J., 1992, *Temperature measurement with application to phase equilibria studies,* In: Rossiter, B.W., Baetzold, R.C., Physical Methods of Chemistry vol VI: Determination of Thermodynamic Properties, John Wiley & Sons, ISBN 0-471-57087-7

Chhabra and Richardson, 1999, *Non-newtonian flow in the process industries*, B& H.

Dorsey, N.E., 1940, *Properties of ordinary water substance in all its phases: Vapor, water and all the ices*, NewYork, Reinhold Publishing Co.

Egolf, P.W., Sari, O., Meili F., Moser, P., Vuarnoz, D., 1999, *Heat transfer of ice slurries in pipes*. Proceedings of the 1st workshop on ice slurries of the IIR, Yverdon-les-Bains, Switzerland, IIR, p106

Frei, B., Egolf, P.W., 2000, *Viscometry applied to the Bingham substance ice slurry*, Proceedings of the 2nd workshop on Ice Slurries, IIR Paris, p 48-60

Grandum, S., Nakagomi, K., 1997, *Characteristics of Ice Slurry Containing Antifreeze Protein for Ice Storage Applications*, Journal of Thermophysics and Heat Transfer 11 (3), p461-466

Green, D.W., Maloney, J.O., 2000, *Perry's Chemical Engineering Handbook* 7thed, McGraw-Hill

Guilpart, J., Fournaison, L., Ben Lakhdar, M.A., Flick, D., Lallemand, A., 1999, *Experimental study and calculation method of transport characteristics of ice slurries*, Proceedings of the 1st workshop on ice slurries of the IIR, Yverdon-les-Bains, Switzerland, IIF/IIR p74-82

Holman, J.P., 1997, *Heat Transfer* 8th ed. , McGraw-Hill

Hyland, W. and Wexler, A., 1983, *Formulations for the thermodynamic properties of the saturated phases of H2O from 173.15 K to 473.15K.*, ASHRAE Transactions 89 (2A), p500-519

Janssen, L.P.B.M., Warmoeskerken, M.M.C.G., 1991, *Transport phenomena data companion*, 2e druk 1991, Delftse Uitgevers maatschappij (DUM)

Jeffrey, D.J., 1973, *Conduction through a random suspension of spheres*, Proc. R. Soc. London A. 335, p355-367

Kauffeld, M., Christensen, K.G., Lund, S., Hansen, T.M., 1999, *Experience with Ice Slurry*, Proceedings of the 1st workshop on Ice Slurries, Yverdon-les-Bains, Switzerland, IIR, p42-73

Knodel, B.D., France, D.M., Choi, U.S., Wambsganss, M.W., 2000, Heat transfer and pressure drop in ice-water slurries, Applied Thermal Engineering, vol. 20, p671-685

Levy, 1981, *A modified Maxwell-Eucken equation for calculating the thermal conductivity of two-component solutions*, International Journal of Refrigeration 4(4), p223

Lide et al., 1998, *CRC Handbook of Chemistry and Physics*, 78th edition, CRC Press Boca Raton

Melinder, A., 1997, *Thermophysical properties of liquid secondary refrigerants*, Handbook no. 12 of the Swedish Society of Refrigeration, Stockholm

Melinder A., 2001, *Enthalpy phase diagrams as an aid in estimating the performance of ice slurries*, Proceedings of the 4th workshop on Ice Slurries of the IIR, Osaka, Japan, IIR. p115-122

Nagata, S., 1975, *Mixing Principles and Applications,* Halstead Press, Wiley.

Paul, J., 1996, *Compressors for refrigeration plants and ice makers with 'water as refrigerant'*, Proc. Aarhus Conf., IIF/IIR: p577-584

Royon, L., Perrot, P., Colinart, P., Guiffant, G., 1999, *Transport of cold thermal energy with a new secondary biphasic refrigerant: the stabilized ice slurry*, Proc. Sydney Conf., IIR, paper 041

Sheer, T., McGarry, R., Chan, C., Butterworth, M., 2003, *The Transportation of Ice Through Pipelines Within Cooling Systems for Deep Mines,* Proceedings of the 21st International Congress of Refrigeration of the IIR, Washington DC, paper ICR0195

Sinnot, R.K., 1993, *Coulson & Richardson's Chemical Engineering vol. 6*, 2nd ed. 1993, Pergamon, Oxford.

Soehnel, O., 1985, *Densities of aqueous solutions of inorganic substances*, Physical Sciences Data 22, Elsevier

Suzuki, H., Modak, P.R., Usui, H., 2001, *Rheological Characteristics of ice/water slurry dispersed with surfactant additives*, Proceedings of the 4th workshop on Ice Slurries of the IIR, Osaka, Japan, IIR, p135

Tareef, B.M., 1940, *cited in:* Gambill, W.R., 1957, *Predict thermal conductivity-II,* Chemical Engineering, March 1957, p271-277

Thomas, D.G., 1965, *Transport characteristics of suspension: VIII. A note on the viscosity of Newtonian suspensions of uniform spherical particles*, Journal of Colloid Science 20, p267-277.

Ure, Z., 1999, *Positive temperature eutectic thermal energy storage sytems*, Proceedings of the 20th International Congress of Refrigeration of the IIR, Sydney, Australia, paper 004

3 Heat Transfer Models of Liquid/Solid Fluidized Beds for Ice Slurry Generation

3.1 Introduction

Ice slurries are advantageous because of the latent heat effect involved with ice formation. Major drawback of the ice slurry systems has been the high cost associated with the ice slurry generator. An alternative ice slurry generator that reduces initial investment cost and may improve heat transfer coefficients and lower maintenance cost is sought in a fluidized bed heat exchanger.

Fluidized bed heat exchangers are used to prevent fouling in various process applications (Klaren, 2000; Rautenbach and Katz, 1996). These heat exchangers consist of one or several parallel tubes with heated or cooled walls. In an ice slurry generator the walls are cooled by evaporation of a primary refrigerant such as an HFC, a hydrocarbon or ammonia. Inert solid particles are fluidized inside the tubes. The solid particles are fluidized by the ice slurry feed flow. After the feed flow is supercooled below its freezing point in the fluidized bed, initial nucleation takes place and ice crystal growth starts. Solid particles prevent build-up of a solid ice layer on the heat transfer surfaces and also enhance heat transfer coefficients (Haid et al., 1994). Maximum size of ice crystals produced is limited by the continuous interactions with solid particles of the fluidized bed (Klaren and van der Meer, 1991).

A section is installed on top of the fluidized bed heat exchanger to separate the solid particles from the ice slurry. The fluidized beds can either operate stationary or with recirculation of the solid particles through a downcomer pipe. A schematic lay-out of a fluidized bed system with an evaporating primary refrigerant is given in Figure 3.1.

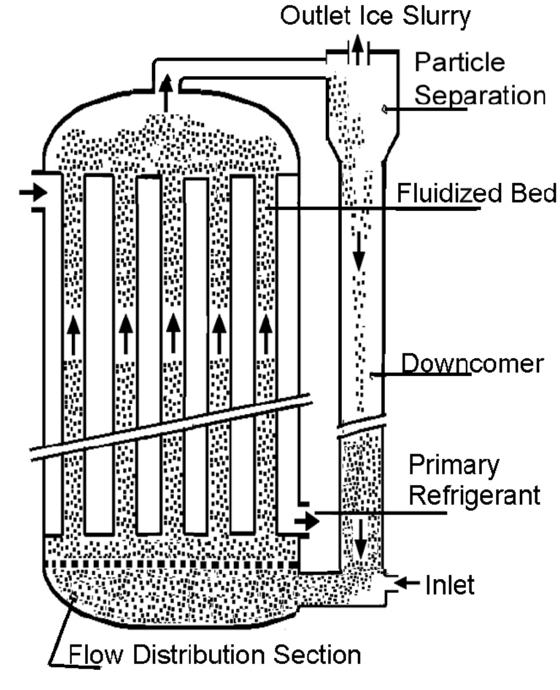

Figure 3.1: Schematic lay-out of a fluidized bed ice slurry generator

The research of this Chapter aims to determine heat transfer coefficients in stationary fluidized bed heat exchangers applied for ice slurry generation. The mechanism of ice slurry formation in the fluidized bed ice slurry generator may be clarified using the heat transfer coefficients.

Numerous correlations for wall to fluidized bed heat transfer have been reported by Haid et al., 1994; Haid, 1997; Jahmialahmadi et al., 1996 and others. These literature correlations will be examined experimentally for the specific case of ice slurry generation, after which a heat transfer model will be developed for ice slurry generation in fluidized beds.

3.2 Heat Transfer in Fluidized Bed Ice Slurry Generators

3.2.1 Heat Transfer Mechanisms

Wall-to-bed heat transfer coefficients in fluidized bed heat exchangers are higher compared to those in pipes without particles (Haid et al., 1994). This is caused by three enhancement mechanisms:

1. The solid particles break up the laminar boundary layer that has a large heat transfer resistance. This positive effect is expected to be dominant during ice crystallization.
2. The solid particles transfer heat by conduction during direct contact with the walls. This positive effect may be reduced by the presence of ice crystals, if the ice crystals prevent contact of particles with the walls. This effect is particularly important in gas/solid fluidized beds and in liquid/solid fluidized beds with dense and highly conductive solid particles such as copper particles (van Heerdan et al., 1953).
3. The heat exchanging walls are kept clear of fouling. This effect is the main reason to apply fluidized bed heat exchangers in various process applications with severely fouling process fluids (Klaren and van der Meer, 1991). The solid particle impacts prevent the build-up of a permanent ice layer at the heat exchanger walls.

The exact heat transfer mechanism is not known for wall-to-bed heat transfer in a fluidized bed ice slurry generator. The presence of ice crystals probably affects heat transfer. Several possibilities are distinguished:

1. There are no effects of the ice crystals. Heat transfer coefficients will be as in regular liquid/solid fluidized beds. Properties of the liquid phase of the ice slurry are required to predict heat transfer coefficients.
2. The ice crystals interfere with heat transfer coefficients, but do not stick to the heat transfer surfaces. The ice slurry can be regarded as a single fluid.
3. There is a semi-permanent layer of ice at the heat transfer surfaces. Ice crystals are removed continuously by the mechanical impact of solid particles of the fluidized bed.
4. A combination is also possible: Heat transfer coefficients may be affected by ice crystals, while there also is a semi-permanent ice layer stuck to walls.

Heat transfer coefficients may also be affected by varying local ice fractions. Ice crystals may be formed principally in the laminar boundary layer near walls. Slow mass transport of ice crystals to the bulk of the fluidized bed may then result in an uneven distribution of ice crystals.

By measuring wall to bed heat transfer coefficients, an attempt is made to determine the heat transfer mechanism. Heat transfer models for liquid/solid fluidized bed heat exchangers are used as starting point for this evaluation. Thermophysical properties of liquid phase and ice slurry as a whole are examined in the models, to determine which properties are significant and which heat transfer mechanism prevails.

Heat transfer measurements may result in a better understanding of the ice formation mechanism. If during ice formation there is a semi-permanent ice layer sticking to the walls, heat transfer coefficients are expected to be significantly lower compared to liquid/solid fluidized bed heat transfer under similar conditions where no ice crystals are formed. In experiments these conditions are obtained just before the start of ice crystallization, therefore a comparison of heat transfer coefficients with and without crystallization within a test run is possible.

3.2.2 Ice Slurry Properties

Various property models have been used in calculations of ice slurry systems, for example discussed by Bel and Lallemand (1999) and Christensen and Kauffeld (1997). Models used by different researchers yield a wide range of errors, which are often made because the ice slurry is seen as a single fluid and the influence of properties such as size and shape of individual ice crystals is disregarded. The following set of thermophysical property models, introduced in Chapter 2, is used in the heat transfer calculations of this chapter.

Density of ice slurries is calculated by weighted addition of the density of pure ice and the density of the solution.

$$\rho_{is} = \frac{1}{w_i / \rho_i + (1 - w_i) / \rho_l} \tag{3.1}$$

Ben Lakhdar (1998) has shown that the model proposed by Tareef (1940) to predict *thermal conductivity* of solid/liquid mixtures yields satisfactory results for ethanol ice slurries up to an ice volume fraction of 0.4:

$$\lambda_{is} = \lambda_l \cdot \left(\frac{2 \cdot \lambda_l + \lambda_i - 2 \cdot \phi_i \cdot (\lambda_l - \lambda_i)}{2 \cdot \lambda_l + \lambda_i + \phi_i \cdot (\lambda_l - \lambda_i)} \right) \tag{3.2}$$

Enthalpy of ice slurries is given by:

$$h_{is}(T) = w_i(T) \cdot [h_i(T) - \Delta H_f] + [1 - w_i(T)] \cdot h_l(T) \tag{3.3}$$

The *heat capacity* is found by differentiation of enthalpy with respect to temperature. For sufficiently small ΔT of the ice slurry the apparent heat capacity can be estimated with:

$$c_{p\_app} = \left(\frac{\Delta w_i}{\Delta T} \right) \cdot [h_i - \Delta H_f - h_l] + w_i \cdot c_{p\_i} + [1 - w_i] \cdot c_{p\_l} \tag{3.4}$$

This apparent heat capacity is only valid in situations where ice crystals actually grow or melt. Otherwise the heat capacity is determined using the sensible heat capacities of ice and liquid solution, disregarding the latent heat term of Equation 3.4. It is not known if the apparent heat capacity or the sensible heat capacity must be used for heat transfer calculations in the fluidized bed ice slurry generator.

An empirical model predicting ice slurry *dynamic viscosity* is based on the model of Thomas (1965), which was introduced in section 2.1.6.

$$\mu_{is} = \mu_l \cdot (1 + 2.5 \cdot \phi_i + 10.05 \cdot \phi_i^2 + 0.00273 \cdot \left(e^{16.6 \cdot \phi_i} - 1 \right)) \tag{3.5}$$

Equation 3.5 is valid for slurries with ice fractions up to 0.20 (Kauffeld et al., 1999).

3.2.3 Correlations for prediction of heat transfer in liquid/solid fluidized beds

Many researchers have reported empirical correlations to predict heat transfer in liquid/solid fluidized beds as given in Equation 3.6:

$$Nu_p = c_1 Re_p^{c_2} Pr^{c_3} (1-\varepsilon)^{c_4} \varepsilon^{c_5} \left(\frac{d_p}{D}\right)^{c_6} \left(\frac{\rho_s - \rho_l}{\rho_l}\right)^{c_7} \tag{3.6}$$

In which ε is the bed voidage, defined as the fraction of space not occupied by solid particles, where ice crystals are included in the fluid phase. A collection of 36 models and 2665 experimental data points was compiled by Jamialahmadi et al. (1996). Based on the same data collection a generalized model of the form of Equation 3.6 was developed by Haid et al. (1994). The following parameters predicted the experimental data of this database with 32.4% average error: c_1=0.1493, c_2=0.72, c_3=0.52, c_4=0.19, c_5=-1.41, c_6= 0.17, c_7=0.03.

The model of Equation 3.6 was simplified to a model with 3 constants by Haid (1997), with an increase of the relative error to 34.4%:

$$Nu_h = c_1 \cdot Re_h^{c_2} Pr^{c_3} \tag{3.7}$$

With parameters c_1=0.0734, c_2=0.75 and c_3=0.63. The simplified model includes hydraulic Nusselt and Reynolds numbers, which are calculated using Equations 3.8 and 3.9:

$$Nu_h = \frac{\alpha d_p}{\lambda} \frac{\varepsilon}{1-\varepsilon} \quad (3.8) \qquad Re_h = \frac{\rho u_s d_p}{\mu} \frac{1}{1-\varepsilon} \quad (3.9)$$

A large range of errors was found between different researches: The average error of the model predicting the experimental data was 34.4%, but errors of over a 100% higher than predicted were reported. Most models in the database of Jamialahmadi et al. (1996) were obtained using an electrical heating device to heat the fluidized bed, with the objective of heating the fluid. Coefficients for the case of cooling of a fluid can differ significantly, for example the exponent of the Prandtl number in the Dittus-Boelter model (Holman, 1997), which is 0.3 for heating and 0.4 for cooling applications in tubes.

Some data sets have been reported where the fluids were of relatively high viscosity, which is also the case for ice slurries. For example Kraft black liquor in the research of Bremford et al. (2000). In this paper considerable errors were found if experimental data were compared to the generalized models of Equation 3.6. Other models predicted the experimental data more accurately, for example the model of Kim et al. (1986). This model is of the form of Equation 3.6 but also includes the Archimedes number (Ar):

$$Nu_p = c_1 Re_p^{c_2} Pr^{c_3} Ar^{c_4} \left(\frac{1-\varepsilon}{\varepsilon}\right)^{c_5} \tag{3.10}$$

with c_1 = 0.0722, c_2= 0.25, c_3= 0.5, c_4= 0.25 and c_5=0.25.

Models that were fit to experimental data for heat transfer to black liquor gave different results at different black liquor solids concentrations. This indicates that the presence of solids influencing fluid viscosity has considerable impact on heat transfer coefficients.

3.3 Experimental Method

A single tube fluidized bed heat exchanger was used to determine heat transfer coefficients during ice crystallization. Cooling capacity was provided by a secondary fluid which was cooled in a water cooled commercial chiller. Solid particles were separated from the ice slurry on top of the fluidized bed. The ice slurry was collected in a stirred storage tank equipped with a heater to melt the ice. A schematic layout of the fluidized bed test set-up is given in Figure 3.2.

Fluidized beds of internal diameters of 43 mm and 55 mm were tested. The tubes were made of stainless steel type 316 with 2.8 mm wall thickness and a height of 4.55 m. Cylindrical stainless steel particles with equal height and diameter of 3 mm and 4 mm, were used. A rotary positive displacement pump was used to pump the slurry through the ice slurry generator and to fluidize the steel particles. All experiments were carried out with the fluidized bed in stationary operation without circulation of solid particles.

In the 43 mm bed a transparent section was installed halfway to observe the fluidization regime. On top of both fluidized beds transparent sections were used to control the height of the fluidized beds during stationary operation. By weighing of the solid particles present in the fluidized beds before or after experiments, the bed voidage could be accurately determined. A pressure difference transmitter with accuracy of ±1 mbar was installed to measure pressure difference between top and bottom of the fluidized bed. This indicated possible blockages by freezing. The pressure difference is also a measure of the bed voidage, however in the experiments weighing of the particles was used to determine bed voidage.

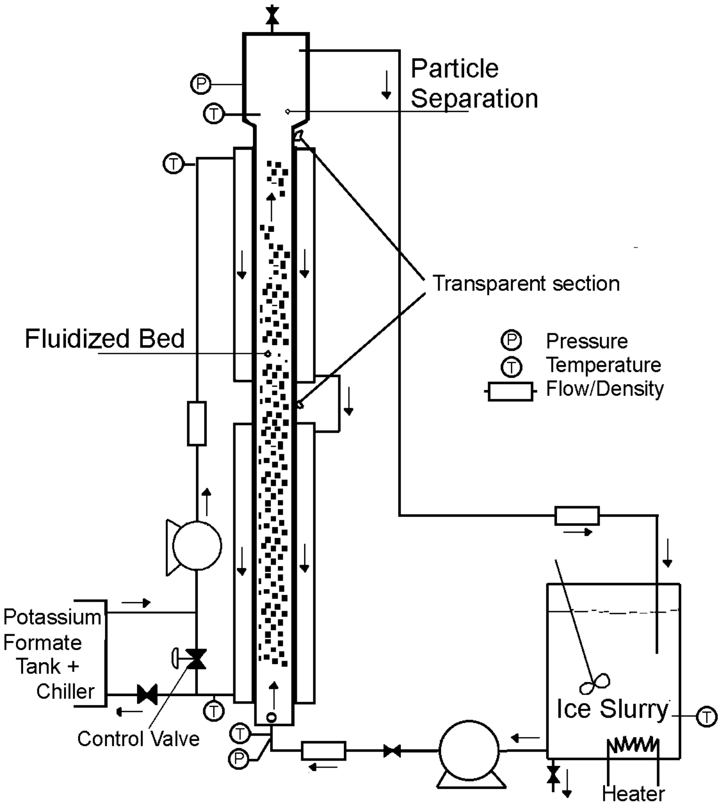

Figure 3.2: Experimental set-up for determination of heat transfer coefficients, single tube counter-current fluidized bed

In the ice slurry storage tank a propeller type stirrer was installed that could keep ice slurries homogeneous up to ice weight fractions of approximately 0.15. At the given chiller capacity, a maximum increase of the ice weight fraction of 0.04 could be obtained for one pass through the fluidized bed. As the ice slurry feed to the fluidized bed is taken from the bottom of the storage tank, the maximum ice weight fraction expected in the fluidized bed is around 0.19. Higher ice weight fractions can be formed in the ice slurry storage tank, where ice crystals then form a floating layer rich of ice. As in the fluidized bed ice slurry generator no ice weight fractions higher than 0.19 are expected, Equation 3.5 is considered suitable for viscosity calculations inside the fluidized bed systems.

In the annular space around the fluidized bed a secondary refrigerant without phase change was used. In- and outlet temperatures of this secondary refrigerant, a 34% potassium formate solution with initial freezing point -25 ^{o}C, were measured with PT-100 sensors. The sensors were calibrated with an accuracy of ±0.02 K. In and outlet temperatures of the fluidized bed were also measured using PT-100 sensors with ±0.02 K accuracy. Other temperatures were measured with thermocouples type T with accuracy of ±0.05 K. The annular tube was well insulated. Flow rates of ice slurry and secondary refrigerant were measured using Coriolis-type mass flow meters, with accuracy of ±0.1% of the measured value. Also the density of the ice slurry could be determined using the Coriolis-type flow meters, also with accuracy of ±0.1% of the measured value.
The enthalpy difference of the secondary refrigerant at the in- and outlet was calculated from the temperature data. Using Equation 3.11 the overall heat transfer coefficient, U, was determined.

$$Q = U \cdot A \cdot \Delta T_{\ln} \tag{3.11}$$

with A the outside surface area of the tube. The wall-to-bed heat transfer coefficient (α_{in}) was then determined with Equation 3.12:

$$\frac{1}{U} = \frac{1}{\alpha_{out}} + \frac{D_{out}}{2\lambda_w} \ln\left(\frac{D_{out}}{D_{in}}\right) + \frac{D_{out}}{D_{in}} \cdot \frac{1}{\alpha_{in}} \tag{3.12}$$

The overall heat transfer resistance ($1/U$) consists of three parts: The annular side heat transfer resistance, the heat transfer resistance of the stainless steel walls and the wall-to-bed heat transfer resistance on the fluidized bed side. The heat transfer coefficient on the annular side was estimated with the model of Gnielinski (VDI, 1994), valid for turbulent conditions (Re>2300):

$$Nu = \frac{\frac{\xi}{8}\left(Re - 1000\right)Pr}{1 + 12.7\sqrt{\frac{\xi}{8}}\left(Pr^{2/3} - 1\right)} \cdot \left(1 + \left(\frac{D}{z}\right)^{2/3}\right)\left(\frac{\mu}{\mu_{wall}}\right)^{0.14} \tag{3.13}$$

with: $\xi = \left(1.82 \cdot {}^{10}\log\left(Re\right) - 1.64\right)^{-2}$

For the 55 mm fluidized bed the annular heat transfer coefficient was approximately 2 kW/m^{2}K, for the 43 mm fluidized bed this was 4 kW/m^{2}K. A reference experiment with pure water and no fluidized bed present indicated that this model determined annular heat transfer coefficients with a maximum error of 12 % (6% average error). The temperature measurement error on the ice slurry side needs to be added to this error. The maximum measurement error was up to 20% at low temperature differences. Measurements became more accurate at higher temperature differences between primary cooling fluid and ice slurry.

The freezing point of a liquid solution is determined by the concentration of freezing point depressant. It is assumed that the ice formed consists of pure water. The ice fraction can thus be calculated from the initial freezing point depressant weight concentration and temperature measurements according to the method discussed in section 2.2.1:

$$w_i = 1 - \frac{w_{fpd,0}}{w_{fpd}(T_f)} \tag{3.14}$$

Freezing point data, $w_{fpd}(T_f)$, were obtained from Melinder (1997). Accuracy of this method was confirmed with the Coriolis mass flow and density meters.

In the experiments, two types of freezing point depressing additive were used: Sodium chloride and ethylene glycol. Microscopic pictures used to evaluate size and shape of ice crystals, indicated that ice crystals generated in the fluidized bed system were similar for both additives. The microscopic pictures are discussed in detail in section 2.4. Ice crystals were rounded, without sharp edges and shaped like disks or spheres. Diameters of ice crystals produced in the fluidized bed were in the range of 0.1 mm to 0.3 mm. Possible effects of different size or shape of ice crystals on heat transfer coefficients were assumed to be less relevant in these experiments.

The capacity of the chiller was approximately 5 kW at –10 °C. This limited the amount of heat that could be transferred, imposing a limit on the temperature difference that could be attained in the set-up. In the ice slurry storage tank a heater of 3.4 kW maximum capacity was installed to melt ice and maintain a constant ice fraction. Initial freezing points of solutions of both freezing point depressants were in the range of –1 °C to –7 °C.

An ice slurry production run was considered stable if a constant heat transfer coefficient was maintained up to an ice fraction in the tank of at least 0.19. Stable operation also required the fluidized bed to remain fluidized without being blocked by ice or showing an outflow of solid particles. Using the heater, steady state conditions were assumed after 20 minutes of ice slurry production without change in heat transfer coefficient or fluidization conditions.

Initial ice nucleation was started in experiments by seeding with small ice crystals after the liquid in the storage tank just became supercooled. In the experimental set-up initial nucleation could also occur without seeding at 0.5 to 1.5 K of supercooling. To prevent the sudden formation of large ice fractions which might cause instability, seeding was however used in most experiments. Approximately 100 ice slurry production tests were conducted at various operating conditions, 75 of these resulted in stable ice slurry production conditions, suitable for heat transfer calculations.

3.4 Results & Discussion

3.4.1 Operating Range of Fluidized Bed Ice Generator

Ice slurry generation in a fluidized bed heat exchanger can only be stable within a certain range of operating conditions. The solid particles need to impact on the heat exchanging surfaces frequent enough to keep them free of ice. Several factors may prevent this:

1. If the temperature driving force is too high, ice crystal growth will be too fast and a solid ice layer will build-up regardless of the impact of solid particles.
2. A too low liquid phase velocity, encountered at low bed voidage, will not give the solid particles enough momentum. The particles can then not impact hard enough on walls to keep ice from sticking to the walls. Ice will also stick to walls if particles are too light or too small.
3. An inhomogeneous fluidization regime or a too high bed voidage might cause parts of the heat exchanging walls to be without particle impacts for too long, allowing for build-up of an ice layer.

Heat transfer rates decrease if there is a solid (growing) layer of ice sticking to the heat exchanging surface. Also the fluidized bed will expand and flow out of the tube, because there is less volume available for the fluidized bed. The fluidized bed operation becomes unstable and it will eventually be completely blocked by ice.

The factors mentioned above are not independent: For each set of operating conditions there appears to be a maximum temperature difference above which ice will stick to walls.

A few parameters are essential to control the generation of ice slurry: The temperature driving force for crystallization, the bed voidage and superficial velocity. Also fluid properties, bed and particle dimensions impose limits on the operating range of the fluidized bed ice generator, as these determine the fluidization regime.

In the experiments no stable ice slurry generation was obtained at a bed voidage of 0.75 or lower. At a bed voidage of 0.88 ice slurry could only be produced at very low temperature differences. Higher bed voidages may be possible at small temperature differences but were not tested. Optimum heat transfer coefficients have been predicted around a bed voidage of 0.73 by Jamialahmadi et al. (1996). This optimum bed voidage is probably hard to obtain during ice slurry generation. The limits on the operating range complicate determination of an accurate heat transfer model, because parameters as the bed voidage can not be altered over a wide range.

The maximum allowable wall-to-bed temperature difference strongly depends on the weight concentration of freezing point depressant. At low freezing point depressant weight concentrations build-up of an ice layer at walls is more likely and the allowable temperature difference is low.

In Figure 3.3 wall-to-bed temperature differences are given versus the freezing point depressant concentration for all experiments with sodium chloride at 0.79 bed voidage. The line between stable and unstable ice slurry generation conditions gives the maximum allowable wall-to-bed temperature difference. The limit appears to depend linearly on the sodium chloride concentration. It was found that at a higher bed voidage the maximum allowable wall-to-bed temperature difference was smaller than in the experiments of Figure 3.3.

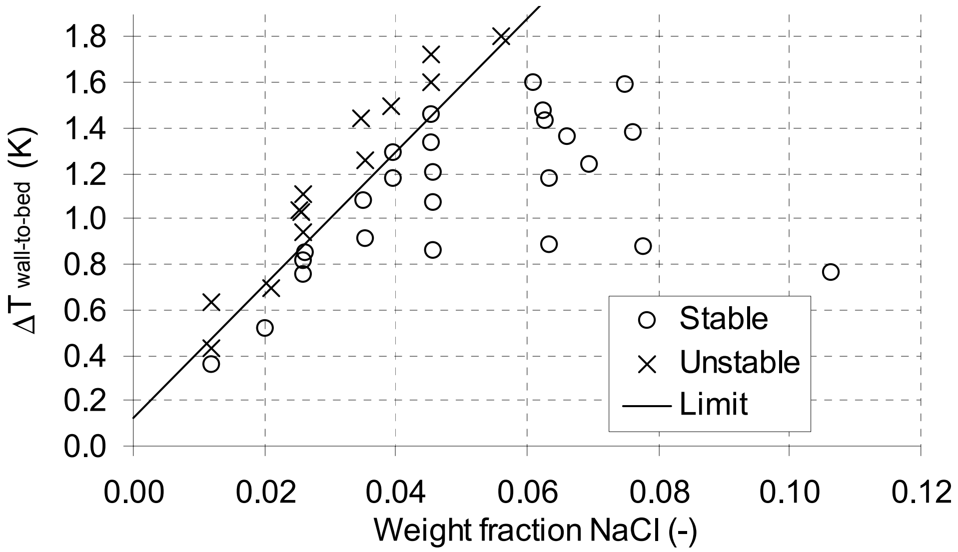

Figure 3.3: Maximum wall-to-bed temperature difference for NaCl based ice slurry. Bed voidage of 0.79, 4 mm cylindrical steel particles in 55 mm diameter fluidized bed set-up

In the experiments with ethylene glycol as freezing point depressant instead of sodium chloride, the stable operating range was larger. At equal freezing points, approximately 33% larger temperature differences could be applied with ethylene glycol. The limit again depended linearly on the concentration. A further discussion of the stable operating range is given in Chapter 4.

3.4.2 Thermophysical Properties

The thermophysical property models for ice slurries of Section 3.2.2 combine properties of liquid solution, ice, and their interactions. It is however not known if there are interaction effects during ice formation in the fluidized beds. If heat is transferred primarily from walls to the liquid phase of the slurry and ice crystallization occurs in the bulk of the fluidized bed, only properties of the liquid phase are required for heat transfer calculations. Otherwise, if the ice slurry behaves as a single fluid, property models of the ice slurry including the solid ice phase need to be used.

In Figure 3.4 heat transfer results of a typical production run are displayed for an ice slurry based on sodium chloride. Also the ice fraction at the outlet of the fluidized bed heat exchanger is displayed in Figure 3.4. In this experiment the inlet temperature of the secondary refrigerant was kept constant. At higher ice fractions the temperature of the ice slurry decreases as the freezing point is further depressed, therefore the overall temperature difference slightly decreases. In other experiments the primary cooling fluid temperature was adjusted to obtain a constant overall temperature difference. The experiment was stopped at an ice weight fraction of approximately 0.17. The heat transfer coefficient observed is practically constant. The average heat transfer coefficient can therefore be calculated for comparison with other experiments.

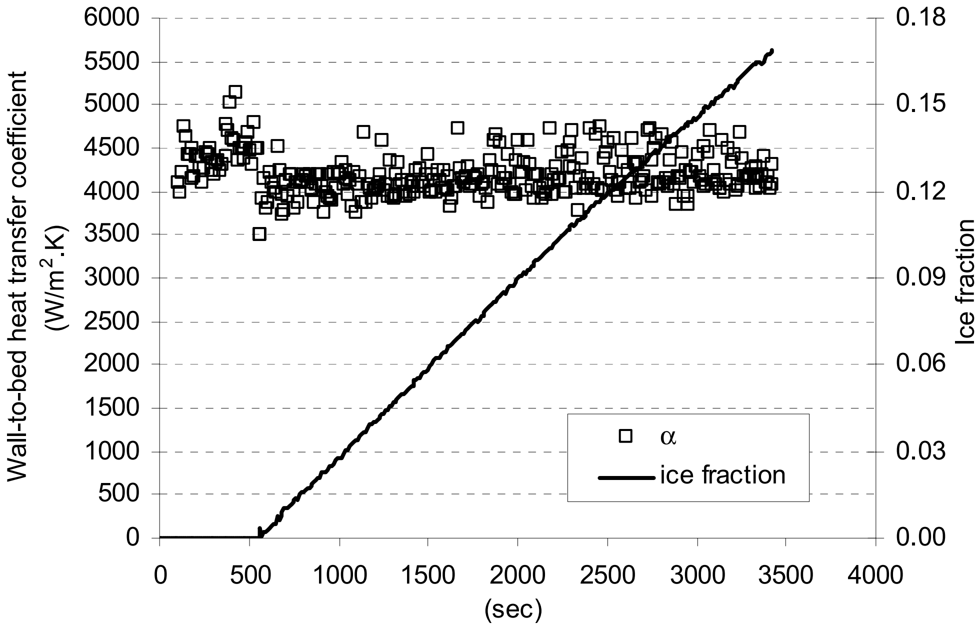

Figure 3.4: Wall to bed heat transfer and ice fraction for NaCl ice slurry production run in 55 mm diameter fluidized bed with 4 mm particles and 0.80 bed voidage. NaCl concentration: 6.6%wt, -4.1 ^{o}C initial freezing point. Ice crystallization starts at t=500 sec

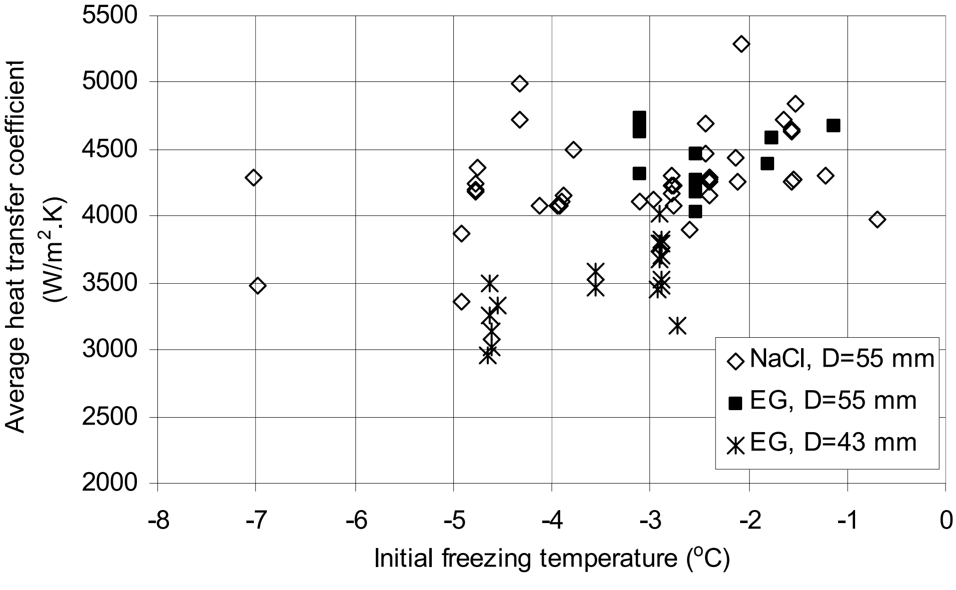

Figure 3.5: Overview of the average heat transfer coefficients vs. the initial ice slurry freezing temperature. Experiments with ice slurries based on NaCl and on ethylene glycol (EG) in the 55 mm diameter fluidized bed with 4 mm particles and with ice slurries based on ethylene glycol in the 43 mm diameter fluidized bed with 3 mm particles

In Figure 3.5 the range of the average heat transfer coefficient is given for the experiments with NaCl in the 55 mm diameter tube and for the experiments with ethylene glycol in both the 43 mm and the 55 mm tube. Heat transfer coefficients appear higher at higher freezing temperatures, but effects of other significant parameters, such as bed voidage and superficial velocity, are not shown in Figure 3.5. The heat transfer coefficients are plotted versus the superficial velocity in Figure 3.6 for the same experiments as in Figure 3.5. The heat transfer coefficients predicted with the Dittus-Boelter model (Holman, 1997) for fluids with similar thermophysical properties but in single phase flow without fluidized bed, are also shown in Figure 3.6. The heat transfer coefficients are significantly higher with the fluidized bed present, which is consistent with earlier work on fluidized bed heat transfer (Haid et al., 1994).

It should be noted that it was not possible to produce ice slurry in the experiments without the fluidized bed.

In the experiment of Figure 3.4 the heater in the ice storage tank was not used, so effects of an increasing ice fraction could be observed. The heat transfer coefficient remained at a practically constant level at increasing ice fraction. As temperature differences and ice fractions only change very gradually, the system was assumed near steady-state for heat transfer calculations. To obtain a true steady state however, the heater is required to melt the ice crystals produced. A number of experiments have been performed under constant ice fraction conditions.

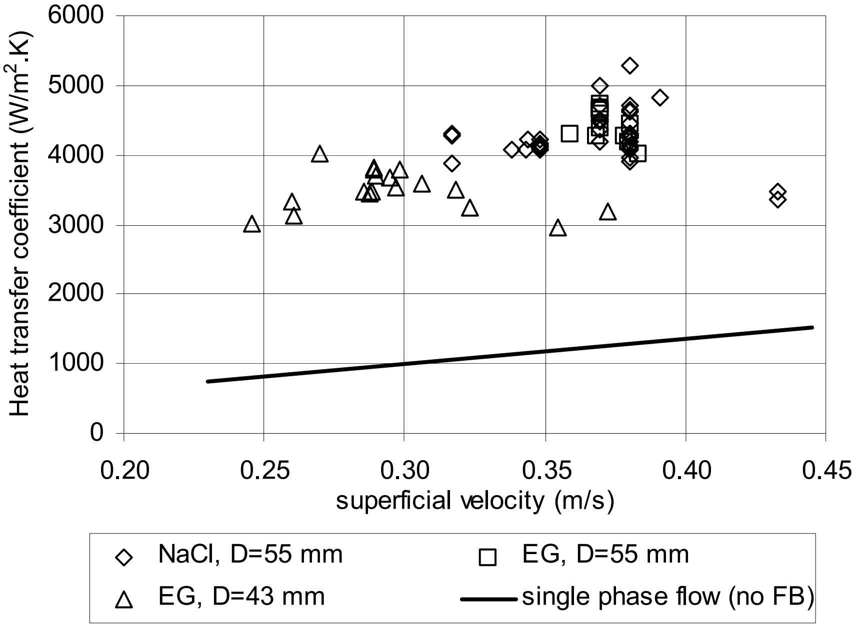

Figure 3.6: Overview of the average heat transfer coefficients vs. the superficial velocity in the fluidized bed. Results of the same experiments as displayed in Figure 3.5, with heat transfer coefficients under equal conditions without fluidized bed

The general model of Equation 3.7 was used to initially examine heat transfer trends at increasing ice fractions. This generalized model was considered suitable as an initial model to test effects of different thermophysical properties, as it was obtained from researches under a wide range of conditions. If the *apparent* heat capacity including the latent heat effect is used in this model to calculate the Prandtl number, a step change up to more than double the heat transfer coefficient would be seen after the start of ice formation. In the experimental data however no such step could be identified, as can be seen in Figure 3.4. Instead a small step down is observed. This step is caused partially by the different temperature of the ice slurry, as the supercooling decreases after the start of ice formation. It may also be partially caused by a small ice layer present at the wall.
The Prandtl number at the start of ice formation calculated with apparent heat capacity in this experiment is 309, which predicts a heat transfer coefficient of 4.3×10^4 W/m^{2}K, using Equation 3.7. Such a large heat transfer coefficient was not observed in the experiments. The Prandtl number calculated with the sensible heat capacity only is 14.5, which predicts a heat transfer coefficient of 6.50×10^3 W/m^{2}K, which is more consistent with the order of magnitude of the heat transfer coefficient measured of 4.17×10^3 W/m^{2}K. The latent heat effect of the phase change was therefore disregarded and only sensible heat of the liquid phase and the sensible heat of the ice are relevant for heat transfer calculations. Equation 3.7 then still overpredicts heat transfer coefficients during ice formation, but is within the error range of the models that were used to obtain the generalized equation, where the models of individual researches could differ up to 100% higher or lower (Haid et al., 1994).

Viscosity of ice slurries increases if ice fractions increase, according to Equation 3.5. If the model of Equation 3.7 is used, this would imply a decreasing heat transfer coefficient at higher ice fractions, as viscosity has a sum of exponents of –0.12. Thermal conductivity increases at higher ice fractions according to Equation 3.2, which would give higher heat transfer coefficients because of a total exponent of 0.37. These two effects cancel each other at low ice fractions. At higher ice fractions the viscosity effect is dominant and heat transfer coefficients are predicted to decrease. The density and the sensible heat capacity only slightly change at higher ice fractions and are less influential in heat transfer models, which was discussed in Section 2.1.7.

In Figure 3.7 heat transfer coefficients calculated with Equation 3.7 for the experimental conditions of Figure 3.4 are displayed. Also heat transfer coefficients calculated with thermophysical properties of only the liquid phase of the ice slurries are displayed, which would be valid if ice crystals would not affect heat transfer. Both curves are very similar; relative difference between the curves is smaller than 2%. The curves do not provide enough detail to be certain about the type of thermophysical property models that need to be used. At low ice fractions, the influence of ice crystals appears to be relatively unimportant for the heat transfer coefficients in the fluidized bed ice slurry generator. Thermophysical property models of the ice slurry as a single fluid, including the solid ice properties, are used in the next section to obtain an accurate heat transfer model. These predict a more constant heat transfer coefficient than if only the properties of the liquid phase were used. This is more consistent with the experimental results.

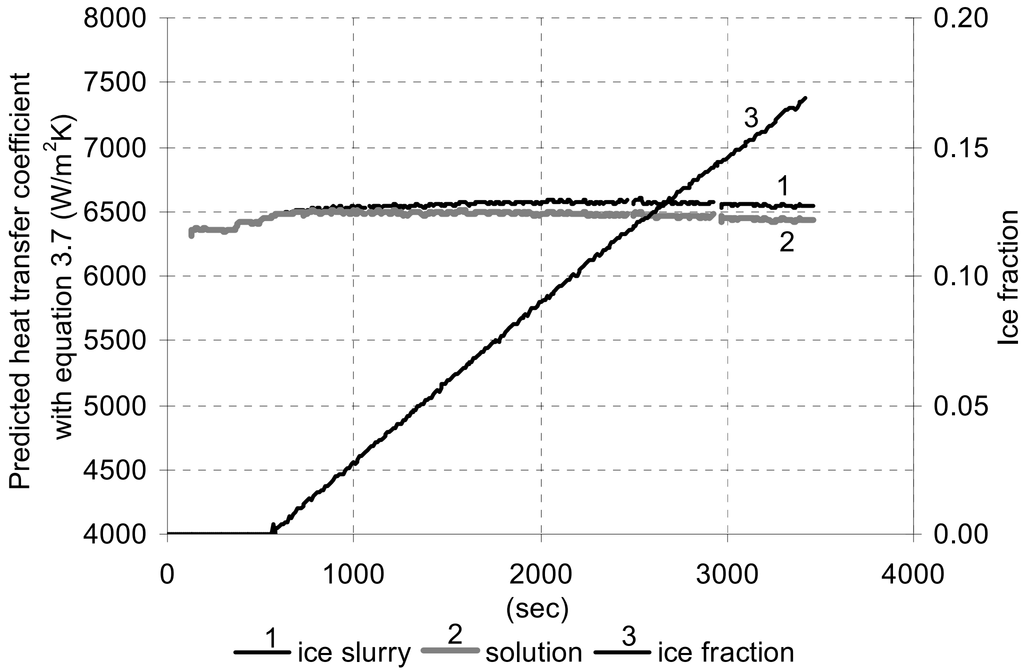

Figure 3.7: Estimated heat transfer coefficients with Equation 3.7 using thermophysical properties of ice slurry and of liquid solution at increasing ice fraction. Conditions as in Figure 3.4

At higher ice weight fractions both curves predict a slightly decreasing heat transfer coefficient. In the experiments however this was not observed. Instead, heat transfer coefficients increased slightly at higher ice fractions, as can be seen in Figure 3.4. The ice crystals themselves may have a positive effect on heat transfer, similar to those of the inert steel particles. The effect is small and could also be caused by the slightly different temperature levels at higher ice fractions. Furthermore, this slightly increasing trend was not obvious in all experiments.

3.4.3 Heat Transfer Model

Because of the practical limits of ice slurry generation in the fluidized beds, discussed in Section 3.4.1, the bed voidage and the ice slurry temperatures were altered over a relatively small range. Some parameters concerning system dimensions were not varied. If not enough experimental data were obtained to get a meaningful fit value for exponents of these parameters, literature values were used. For example the ratio between the particle diameter and the column diameter was hardly varied in experiments, as in the smaller diameter fluidized bed also smaller steel particles were used. In Table 3.1 an overview of the range of operating parameters is given.

Table 3.1: Range of operating parameters

Parameter		*Min*	*Max*
Re_p	-	207	1121
Pr	-	13	29
ε	-	0.77	0.88
d_p	m	0.003	0.004
D	m	0.043	0.055
u_s	m/s	0.25	0.46
T	K	266	272
w_{fpd}	-	0.012	0.132
w_i	-	0	0.19
μ_{is}	Pa.s	0.0017	0.0045
λ_{is}	W/mK	0.53	0.69
ρ_{is}	kg/m^3	995	1080
c_{p_is}	kJ/kg.K	3.63	4.16
Nu_p	-	18	39
α	W/m^{2}K	2960	5280

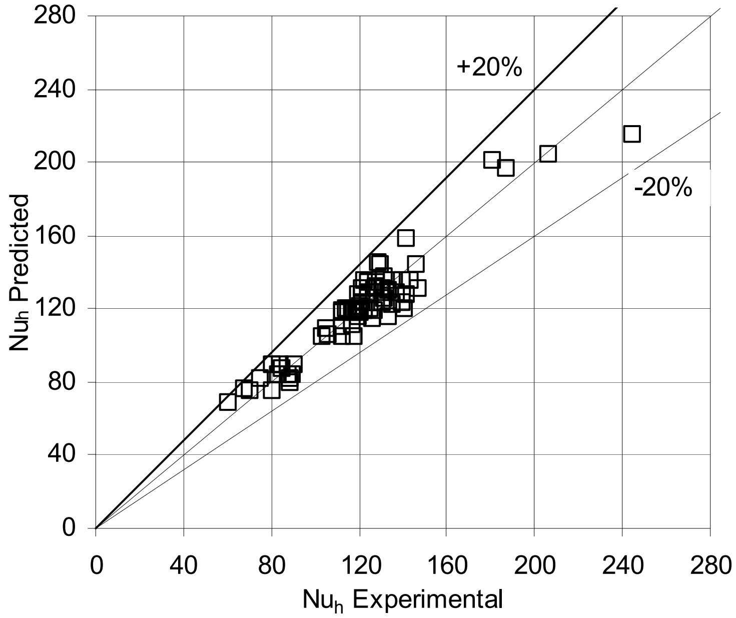

Figure 3.8: Comparison of experimental and predicted values of hydraulic Nusselt number with Equation 3.7 and lsq-fit model. +20% and –20% margins; $R^2=0.905$; avg. error=5.7%; max.error= 14.4%

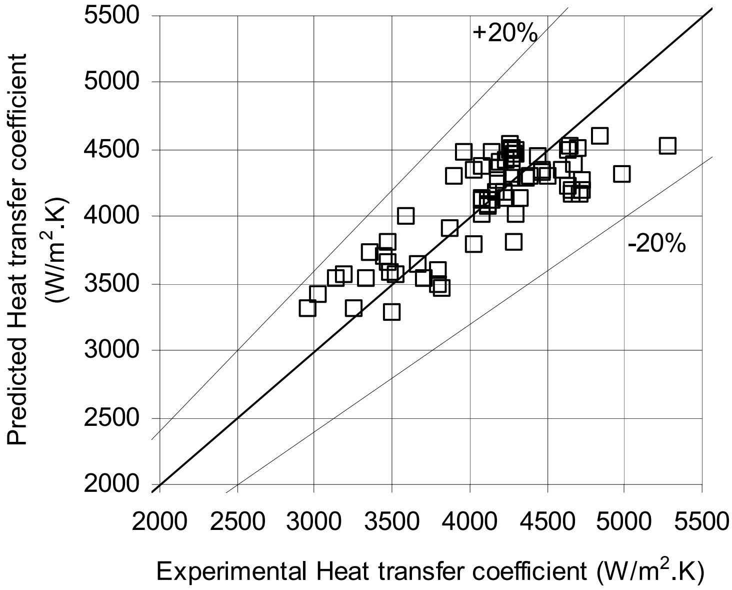

Figure 3.9: Comparison of experimental and predicted values of heat transfer coefficient with Equation 3.7 and +20% and –20% margins

The heat transfer data obtained were compared with predictions of literature models of Equations 3.6, 3.7 and 3.10 and with some literature models that were used to obtain the generalized correlations (Rückenstein et al., 1959; Kang et al.,1991; Muroyama et al., 1986; Kollbach, 1987). Results are given in Table 3.2. The literature models overpredict the experimental results with 7% to 50%. These differences are large, but are within the range of errors of the individual researches that were used to obtain the generalized models of Equations 3.6 and 3.7 (Haid et al., 1994).

If the proportional factor, c_1, in the models is adjusted, accuracy of models is improved and acceptable error levels are obtained. If all exponents of Equations 3.6 and 3.7 are used as parameters for fitting with a least sum of squares method, accuracy is further improved, as is displayed in Table 3.2. The resulting coefficients for the Reynolds and Prandtl numbers are close to those of the literature models. Trends in heat transfer during ice slurry production are therefore similar to heat transfer without ice, only the proportional coefficient is different.

The model similar to Equation 3.7, with fit parameters, c_1=0.0612, c_2=0.724 and c_3=0.625 gave the most accurate predictions. Nusselt numbers predicted for all the experiments with stable ice slurry production are displayed in Figure 3.8, corresponding heat transfer coefficients in Figure 3.9.

Table 3.2: Comparison of literature heat transfer models and least square fits of Equations 3.6, 3.7 and 3.10 applied to all experimental data for ice slurry generation

Model	*Parameters*							*Rel.avg error*	*R^2*
	c_1	*c_2*	*c_3*	*c_4*	*c_5*	*c_6*	*c_7*		
Haid et al., (1997), Eq.3.7	0.0734	0.75	0.63	-	-	-	-	50%	-
..adjusted c_1	0.0486	0.75	0.63	-	-	-	-	5.7%	0.902
..lsq fit c_1..c_3	0.0612	0.724	0.625	-	-	-	-	5.7%	0.905
Haid (1994), Equation 3.6	0.1493	0.72	0.52	0.19	-1.41	0.03	0.17	24%	-
..adjusted c_1	0.121	0.72	0.52	0.19	-1.41	0.03	0.17	7.5%	0.785
..lsq fit c_1..c_3	0.052	0.749	0.671	0.19	-1.41	0.03	0.17	5.6%	0.827
Kim et al., (1986) Eq.3.10	0.0722	0.25	0.5	0.25	0.25	-	-	7.7%	-
..adjusted c_1	0.0679	0.25	0.5	0.25	0.25	-	-	6.0%	0.780
..lsq fit c_1..c_4	0.0132	0.347	0.781	0.267	0.25	-	-	5.7%	0.869
Ruckenstein et al. (1959), Equation 3.10	0.067	-0.237	0.33	0.522	-	-	-	50%	-
..adjusted c_1	0.0436	-0.237	0.33	0.522	-	-	-	7.7%	0.718
..lsq fit c_1..c_4	0.0028	-0.130	0.853	0.565	-	-	-	6.6%	0.832
Kang et al. (1991) Eq. 3.6	0.191	0.69	0.33	0.31	-1	-	-	7.1%	-
..adjusted c_1	0.184	0.69	0.33	0.31	-1	-	-	6.5%	0.796
..lsq fit c_1..c_4	0.0401	0.772	0.713	0.363	-1	-	-	5.6%	0.876
Muroyama et al. (1986)* Eq. 3.6	0.137	0.729	0.33	0.271	-1	-	-	22%	-
..adjusted c_1	0.11	0.729	0.33	0.271	-1	-	-	7.4%	0.757
Kollbach (1987)* Eq. 3.6	0.118	0.7	0.5	0.2	-1	-	-	31%	-
..adjusted c_1	0.0893	0.7	0.5	0.2	-1	-	-	5.9%	0.847

* *Least squares fit parameters are the same as for the model of Kang et al. (1991)*

Typically the literature models overpredict heat transfer coefficients during ice generation with a proportional factor. A likely cause might be interference of ice crystals or interference of the ice crystallization process. However, heat transfer coefficients just before start of ice formation are similar or almost equal to heat transfer coefficients just after start of ice formation, which can be seen in Figure 3.4. Heat transfer coefficients appear slightly lower after start of ice crystallization at t=500 sec, but the difference is 10% at most. There could be a small ice layer at the walls that has a minor impact on heat transfer coefficients, but it is not likely that all ice is formed in a semi-permanent layer at the walls.

Another reason for the difference with the literature models might be the temperature levels close to the freezing point of the solutions. The viscosity of solutions is relatively high close to the freezing point and a high viscosity is a likely cause for modified behavior, as was reported by Bremford et al. (2000). Temperature levels of the various researches were typically above 300 K, 28 to 34 K higher than in the current research. An experiment measuring heat transfer coefficients at higher temperatures was conducted to compare heat transfer coefficients at conditions more similar to the various literature researches. The difference in the proportional factor was reduced considerably at higher temperatures, as can be seen in Table 3.3. In this table experimental heat transfer coefficients at temperatures between 0 ^{o}C and 22 ^{o}C are compared with the model of Haid of Equation 3.7. This generalized model already slightly overpredicted the experimental data discussed in Haid et al. (1997), which also explains the differences partially. In the current ice slurry experiments the generalized model of Equation 3.7 also predicted relatively high heat transfer coefficients compared to some other models (Kang et al., 1991; Muroyama et al., 1986; Kollbach, 1987). Another possible cause for differences is the heat transfer determination method. Most literature models use an electrical heater for heating of a fluidized bed to determine heat transfer coefficients, while in current experiments cooling with a fluid is used. In the models of Equations 3.6 and 3.7, both column diameter and particle diameter influence the heat transfer only indirectly, as these parameters codetermine superficial velocity and bed voidage. It is likely that parameters such as column diameter and particle diameter also have a significant impact and can also partially explain differences found in the proportional factor.

Table 3.3: Comparison of heat transfer coefficients at steady state with Haid model of Equation 3.7 in 2^{o}C to 22^{o}C temperature range

exp	*Average T slurry (no ice) ^{o}C*	*Experimental heat transfer W/m^{2}K*	*Predicted heat transfer W/m^{2}K*	*Relative difference*
1	22.2	6205	6733	9%
2	15.2	5516	6929	26%
3	12.5	5121	6118	19%
4	8.7	4820	6433	33%
5	7.5	3883	6006	55%
6	2.2	3474	5634	62%

3.5 Conclusion

The formation of ice crystals did not have a large effect on heat transfer coefficients in the fluidized bed ice slurry generator. If at a given set of operating conditions stable ice slurry production was possible, heat transfer coefficients were similar to those in fluidized beds before start of ice crystal formation. Heat transfer coefficients measured using the fluidized beds were significantly higher than those predicted for single phase flow.
A range of temperature differences was determined in which stable ice slurry generation was possible. The limit of this range depended linearly on the concentration of freezing point depressant.

Thermophysical property models reported for ice slurries in literature could be applied in models to predict wall-to-bed heat transfer coefficients. The heat capacity without the latent heat term should be used for this. An empirical model using hydraulic Nusselt and Reynolds numbers was proposed that predicted heat transfer coefficients in the fluidized bed ice slurry generator accurately:

$$Nu_h = 0.0612 \cdot Re_h^{0.724} Pr^{0.625} \tag{3.15}$$

Exponents of this model were similar to those of generalized models found in literature. Significant differences were only found in the proportional factor. Relatively low temperature levels during ice slurry production were the most likely cause for the differences, because no significant influence of ice crystals was observed.

Nomenclature

A	heat transfer surface area (m^2)
Ar	Archimedes number (-)
$c_{1....7}$	constant coefficients (-)
c_p	heat capacity (J/kg.K)
c_{p_app}	apparent heat capacity (J/kg.K)
d_p	equivalent particle diameter (m)
D	bed/tube diameter (m)
g	gravitational acceleration (m/s^2)
h	enthalpy (J/kg)
ΔH_f	enthalpy of fusion (J/kg)
Nu_p	Nusselt number ($=\alpha.d_p/\lambda$) (-)
Nu_h	hydraulic Nusselt number (-)
Pr	Prandtl number ($\mu.c_p/\lambda$) (-)
Q	Heat transfer rate (W)
Re_p	Reynolds number ($=\rho.u_s.d_p/\mu$) (-)
Re_h	hydraulic Reynolds number (-)
T	temperature (^oC)
T_f	freezing temperature (^oC)
ΔT	temperature difference (K)
ΔT_{ln}	logarithmic mean temperature difference (K)
U	overall heat transfer coeff($W/m^2.K$)
u_s	superficial velocity (m/s)
w	weight fraction of ice (-)
z	height (m)

Greek

α	wall-to-bed heat transfer coefficient ($W/m^2.K$)
ε	bed voidage (-)
λ	thermal conductivity (W/m.K)
μ	dynamic viscosity (Pa.s)
ρ	density (kg/m^3)
ϕ_i	volumetric ice fraction (m^3/m^3)

subscripts

0	initial concentration
i	ice
in	inside
is	ice slurry
fpd	freezing point depressant
l	liquid
out	outside
p	particle
s	solid
w	wall

References

Bel, O., Lallemand, A., 1999, *Study of a two phase secondary refrigerant: Intrinsic thermophysical properties of an ice slurry*, International Journal of Refrigeration 22 (3), p164-174

Ben Lakhdar, M.A., 1998, Comportement thermo-hydraulique d'un fluide frigoporteur diphasique: Le coulis de glace, PhD-thesis, INSA de Lyon, France.

Bremford, D.J., Müller-Steinhagen, H., Duffy, G.G., 2000, *Heat Transfer to Kraft Black Liquor in a Liquid-Solid Fluidized Bed*, Heat Transfer Engineering 21, 57-69

Christensen, K.G., Kauffeld, M., 1997, *Heat Transfer Measurements with Ice Slurry*, in: IIR commission B1 with E1 & E2 conference proceedings, College Park USA, p161-175

Haid, M., Martin, H., Müller-Steinhagen, H., 1994, *Heat transfer to liquid-solid fluidized beds*, Chemical Engineering and Processing 33, p211-225

Haid, M., 1997, *Correlations for the prediction of heat transfer to liquid-solid fluidized beds*, Chemical Engineering and Processing 36, p143-147

van Heerdan, C., Nobel, A.P.P., van Krevelen, D.W., 1953, Mechanism of Heat Transfer in Fluidized Beds, Industrial and Engineering Chemistry 45, 1237

Holman, J.P., 1997, *Heat Transfer*, 8th ed., McGraw-Hill

Jamialahmadi, M., Malayeri, M.R., Müller-Steinhagen, H., 1996, *A unified correlation for the prediction of heat transfer coefficients in liquid/solid fluidized bed systems*, Transactions of the ASME, Journal of Heat Transfer 118, 952-959

Kang, Y. Fan, L.T., Kim, S.D., 1991, Immersed heater to bed heat transfer in Liquid-solid fluidized beds, AIChE Journal 37 (7), p1101-1106

Kauffeld, M., Christensen, K.G., Lund, S., Hansen, T.M., 1999, Experience with Ice Slurry, in: Proceedings of the 1st workshop on Ice Slurries, Yverdon-les-Bains, Switzerland, IIR Paris, p42-73

Kim, S.D., Kang, Y., Kwon, H.K., 1986, *Heat Transfer Characteristics in two and three phase Slurry Fluidized Beds*, AIChE Journal 32, p1397-1400

Klaren, D.G., van der Meer, J.S, 1991, *A fluidized bed chiller: A new approach in making slush-ice*, Industrial Energy Technology Conference Houston Proceedings, Texas A and M University

Klaren, D.G., 2000, *Self cleaning heat exchangers*, In: Handbook heat exchanger fouling: Mitigation and cleaning technologies ed. by H. Müller-Steinhagen, Rugby Institution of Chemical Engineers, p186-199

Kollbach, J.S., 1987, *Entwicklung eines Verdampfungsverfahrens mit Wirbelschicht warme austauscher zum eindampfen krustenbildender Abwasser*, PhD Thesis, Universität Aachen.

Melinder, A., 1997, Thermophysical properties of liquid secondary refrigerants, Handbook no. 12 of the Swedish Society of Refrigeration, Stockholm

Muroyama, K., Fukuma, M., Yasumishi, A., 1986, Wall-to-bed- Heat transfer in Liquid-Solid and Gas-Liquid-Solid Fluidized Beds part 1,Canadian Journal of Chemical Engineering 64 (3), p399-418

Rautenbach, R., Katz, T., 1996, *Survey of long time behavior and costs of industrial fluidized bed heat exchangers*, Desalination 108, p335-344

Rückenstein, E., Shorr, V., Suciu, G., 1959, *Despre transferul de caldura dintre un strat fluidizat cu lichid si peretele vasului care-l contine*, Studii cercetari fizica, Akad.Rep. Populare Romine 10, p235

Tareef, B.M., 1940, *cited in:* Gambill, W.R., 1957, *Predict thermal conductivity-II,* Chemical Engineering, March 1957, p271-277

Thomas, D.G., 1965, *Transport Characteristics of Suspension: VIII*, Journal of Colloid Science 20, p267-277

VDI, 1994, *VDI Wärmeatlas: Berechnungsblatter für den Wärmeübergang*, 7^{e} Ed. VDI Düsseldorf

4 Ice Adhesion in a Fluidized Bed Ice Slurry Generator

4.1 Introduction

Fluidized bed heat exchangers have been applied for several years (Rautenbach and Katz, 1996; Meijer et al., 1986) to prevent scaling and fouling in various applications in process industry. Application of fluidized beds as ice slurry generator was first proposed by Klaren and van der Meer (1991). Wall-to bed heat transfer coefficients during ice slurry formation in fluidized beds are high, compared with other ice slurry generators, typically in the range of 3-5 kW/m^{2}K, see also Chapter 3. Temperature differences that can be applied are however limited, as was observed in section 3.4.1, because the fluidized bed may freeze up by ice adhering to heat exchanger walls.

If the build-up of ice at fluidized bed heat exchanger walls could be predicted accurately, the fluidized bed systems may also be applied successfully in other fields where formation of solids is sought, for example in crystallization, precipitation, purification and concentration processes and in eutectic freeze crystallization. Increased understanding of the phenomena that determine the build-up of solids at heat exchanger walls could also be applied in other equipment, for example in scraped surface heat exchangers.

In this Chapter the maximum driving force for crystallization above which the build-up of an ice layer starts is determined experimentally. The results are used to identify the ice formation mechanism and the relevant processes that determine ice adhesion to heat exchanger surfaces.

4.2 Fluidized Bed Ice Slurry Generator

4.2.1 Operating Principle and Heat Transfer

In a fluidized bed ice slurry generator a primary refrigerant is evaporated at one side of a heat exchanger wall, on the fluidized bed side ice is formed. The ice slurry feed flow is used to fluidize a bed of solid particles, made of for example stainless steel. The solid particles impact on the heat exchanger walls and thereby prevent build-up of deposits on the walls, either by removing the deposits from the walls or by preventing ice adhesion to the walls. Furthermore, the impacts break-up the laminar boundary layer which reduces heat transfer resistance. Heat transfer coefficients in fluidized bed heat exchangers are typically a number of times higher than for single phase heat transfer (Jahmialahmadi et al. 1996). This is also the case during ice slurry production where heat transfer coefficients were a factor of 4 times higher than for heat transfer without fluidized beds (Meewisse and Infante Ferreira, 2003).

A suitable model to determine wall-to-bed heat transfer coefficients during ice slurry production is determined in Chapter 3. The model is based on empirical correlations of Haid et al.(1994):

$$Nu_h = c_1 \cdot Re_h^{c_2} Pr^{c_3} \tag{4.1}$$

with the coefficients c_1=0.0612, c_2=0.724 and c_3=0.625 for ice slurry generation. The model includes hydraulic Nusselt and Reynolds numbers, defined in Equations 4.2 and 4.3:

$$Nu_h = \frac{\alpha d_p}{\lambda} \frac{\varepsilon}{1-\varepsilon} \qquad (4.2) \qquad Re_h = \frac{\rho u_s d_p}{\mu} \frac{1}{1-\varepsilon} \qquad (4.3)$$

Heat transfer coefficients determined with Equation 4.1 apply at the temperatures of ice formation, from –1 to –7 °C. Typical heat transfer coefficients are lower than for heating applications in the temperature range of 20-100°C, for which Haid et al. (1994) determined c_1=0.0734, c_2=0.75 and c_3=0.63.

4.2.2 Scaling

Ice has a tendency to adhere to solid walls of heat exchangers: The higher the temperature difference between ice and wall, the stronger the adhesion force (Petrenko and Whitworth, 1999). There is a maximum temperature difference that can be applied above which the fluidized bed will freeze up because of ice adhesion to the walls.

For calculation of the ice layer build-up at heat exchanger walls, two processes are distinguished: A deposition and a removal process. These processes are not independent, both are determined by ice crystallization, ice adhesion and fluidization conditions. If the deposition rate per unit area, $\dot{m}_d$, becomes larger than the removal rate per unit area, $\dot{m}_r$, an ice layer with thickness δ builds up and heat transfer coefficients decrease (Förster et al., 1999).

$$\frac{d\delta}{dt} = \frac{1}{\rho_i}(\dot{m}_d - \dot{m}_r) \qquad (4.4)$$

The fluidized bed heat exchanger will eventually malfunction because the ice layer narrows the fluidized bed and eventually blocks it. If however during the build-up of an ice layer the removal rate becomes equal to or larger than the deposition rate, there is no further ice layer build-up or it may even be reduced. The presence of an ice layer at the walls does not exclude steady ice crystal production.

4.2.3 Ice Crystallization

Ice deposition at the walls is determined by ice nucleation, ice crystal growth and transport of ice crystals from the bulk to the walls. For nucleation and subsequent crystal growth a driving force is required. The aqueous solution must be supersaturated with water, which is obtained by supercooling of the solution below the initial freezing point in a fluidized bed ice slurry generator.

Primary nucleation is likely to occur heterogeneously in fluidized beds, as the walls and solid particles provide a large foreign surface area. In many of the experiments however, it was required to seed ice crystals to start ice formation through secondary nucleation, see also section 3.3. Without seeding the fluidized bed could freeze up soon after initial nucleation. Once nucleation is started initially, fresh nuclei are formed mainly by secondary nucleation because of crystal-crystal, crystal-particle and crystal-wall contacts.

Once formed, ice crystals undergo a growth phase consisting of three steps: Transport of molecules from the bulk of the solution to the boundary layer around the nucleus, incorporation of the molecules at the crystal surface and heat transfer of the released latent heat. In case of ice crystallization from a solution, transport of water molecules towards the ice crystal can also be considered as transport of solute away from the crystal.

The crystal growth velocity for mass transfer as the limiting step is given by de Goede and Rosmalen (1990):

$$G_d = \frac{k_d}{w_{int}} \cdot \left(w_{int} - w_b \right) \cdot \frac{\rho_l}{\rho_i} \tag{4.5}$$

in which the driving force is the difference between the ice crystal interface concentration (w_{int}) and the bulk concentration (w_b) of freezing point depressant. The rate constant for mass transfer (k_d) is reduced at increasing freezing point depressant concentration at the interface.

The rate of the surface integration is estimated using the temperature difference between the interface (T_{int}) and the crystal in equilibrium(T_{int}^*):

$$G_{surf} = k_{surf} \cdot \left(T_{int}^* - T_{int} \right)^n \tag{4.6}$$

In this study data for ice surface integration kinetics determined by Huige and Thijssen (1972) are used in Equation 4.6: k_{surf}=2.7·10^{-3} m/s and n=1.55.

The latent heat released because of crystallization at the walls (ΔH_f) is removed to the heat exchanger wall by conduction through the ice crystal, assuming that the heat transfer resistance to the wall is much lower than the heat transfer resistance to the bulk of the fluidized bed.

$$G_{heat} = \frac{\lambda_i \left(T_{int} - T_w \right)}{\delta \rho_i \Delta H_f} \tag{4.7}$$

The total linear crystal growth rate at the wall is obtained by combination of Equations 4.5, 4.6 and 4.7 into:

$$G_{tot} = k_{surf} \left(T_b^* - T_b - G_{tot} \cdot \left(\frac{w_b}{k_d} \cdot \frac{\rho_i}{\rho_l} \cdot \frac{dT_b^*}{dw_b} + \frac{\delta \rho_i \Delta H_f}{\lambda_i} \right) \right)^n \tag{4.8}$$

in which dT_b^*/dw_b is the derivative of the equilibrium freezing temperature with respect to the concentration of freezing point depressant. The detailed derivation of Equation 4.8 is given in de Goede and van Rosmalen (1990).

4.2.4 Ice Adhesion

For the removal of ice crystals from a surface, work is required larger than the work of adhesion of the crystals. The work of adhesion is determined from the interfacial energies, γ_{ij}, of the three phases involved.

In Figure 4.1 an ice crystal is displayed that is adhered to a solid wall. The work of adhesion for this crystal per unit area compared with the same crystal in solution is given by Equation 4.9 (Förster et al., 1999):

$$W_A = \gamma_{13} + \gamma_{23} - \gamma_{12} \tag{4.9}$$

in which subscript 1 denotes the ice crystal, 2 the solid surface and 3 the solution. The interfacial tensions are related by the contact angle (θ) of the crystal attached to the solid surface.

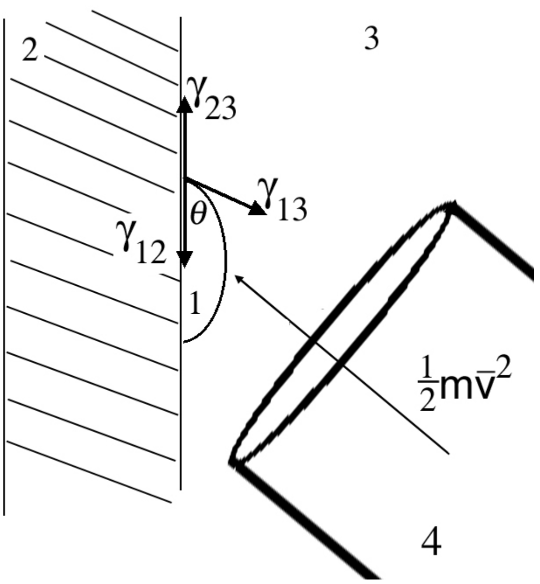

Figure 4.1: Ice crystal adhered to the wall and approaching fluidized bed particle. 1: Ice crystal, 2: Stainless steel heat exchanger wall, 3: Ice slurry solution, 4: Stainless steel particle (not to scale with ice crystal)

The interfacial energy between two materials can be determined from their surface tensions. The surface tension is the lumped sum of various molecular interaction forces that are assumed to be independent material properties. Fowkes (1963) introduced an approach in which the surface tension is divided into a dispersive (γ^d), and a non-dispersive component (γ^{nd}). An alternative method was proposed by van Oss (1993), in which the surface tension is divided into a-polar Lifshitz-vanderWaals interactions (γ^{LW}) and polar acid/base interactions (γ^{AB}). The γ^{LW} component consists of the dispersive molecular interactions γ^d and additionally includes dipole-dipole interactions and dipole-induced dipole interactions (Freitas and Sharma, 2001). If these interactions do not occur γ^d equals γ^{LW} as is the case for a-polar substances. For many other substances these interactions are relatively small compared with the dispersive forces (Schneider et al., 1997) therefore data of γ^{LW} can often be used to estimate γ^d.

Yamada et al., (2002) investigated the work of adhesion of ice to copper in ethylene glycol solutions using the method of Fowkes and the assumption that the interfacial tension is dominated by the dispersive components of the surface tension:

$$\gamma_{ij} = \gamma_i + \gamma_j - 2\sqrt{\gamma_i^{\,d}\gamma_j^{\,d}} \tag{4.10}$$

in which the subscripts *i* and *j* denote the substances of Equation 4.9.

For interactions of ice with ethylene glycol solutions it is probably not acceptable to disregard the polar component of the interfacial tension. Data for the polar components of the surface energies are however not available in literature for all substances of the current study, Equation 4.10 is therefore still used to estimate the work of adhesion.

Table 4.1: Surface tension and dispersive component data used to estimate the work of adhesion of ice to stainless steel in various solutions

	Conc. (wt%)	*T (^oC)*	*γ (mJ/m^2)*	*γ^d (mJ/m^2)*	*Sources*
Ice	-	0	62.4	29.6	van Oss (1993)
Water	-	0	75.8	22.8	van Oss (1993)
	-	20	72.8	21.8	
Stainless steel	-	20	53.0	41.9	Jullien et al. (2002)
EG solution	6.3	-2.0	73.7	23.5	Yamada et al. (2002)
	11.8	-4.1	72.0	24.1	
NaCl solution	saturated	20	73.5	33.8	Veeramasuneni et al. (1997)
	3.4	-2.0	77.1	24.0	Matubayashi et al. (1999)
	6.6	-4.1	78.3	25.2	
Dextrose solution	17.1	20	74.2	22.0	Docoslis et al. (2000)
	15.9	-2.0	77.2	25.0	
	27.1	-4.1	78.6	26.8	

In Table 4.1 the data of surface tensions and dispersive components used in the calculations of the work of adhesion are given. If γ^d values are not available, data of γ^{LW} are used. The dispersive components of the solutions are estimated from those of the pure substances with Equation 4.11. With this equation also the temperature dependence of the dispersive components is estimated, assuming that it is similar to the variation of the solution surface tension with temperature.

$$\gamma_{sol}{}^{d} = \left(\gamma_{wat}^{d}\left(1-w_{fpd}\right)+\gamma_{fpd}^{d}w_{fpd}\right)\frac{\gamma_{sol\_20^o}}{\gamma_{sol\_Tf}} \qquad (4.11)$$

Additional interfacial effects not included in Equation 4.10 may be electrostatic forces and Brownian motion (van Oss, 1993; Freitas and Sharma, 2001). Furthermore stainless steel roughness, surface geometries, impurities and defects in the ice crystal structure may be of influence. The work of adhesion calculated with Equation 4.9 is therefore an indicator for the adhesive strength, but not the only factor involved (Sonwalkar et al., 1993). Also the cohesive strength of the ice crystals should be considered. During ice removal in practice, forces may be exerted on the ice that are high enough to also cause cohesive breaks in the ice crystals.

4.2.5 Particle Impacts

Ice adhered to heat exchanger walls will be removed if the sum of forces exerted on the ice is larger than the adhesion strength or larger than the cohesive strength of the ice for a sufficient period of time. Forces that can remove ice crystals from walls are exerted mainly by the impacts of the solid particles of the fluidized bed, other forces of minor importance are caused by fluid shear and buoyancy of ice crystals.

The particle impact frequency and the force exerted by the particle impacts on the walls or on ice crystals adhered to the walls, determine the removal rate of ice crystals from the fluidized bed walls. The following correlations were developed by Ottjes (1981) for perpendicular impacts of spherical particles on solid walls. Accuracy in fluidized beds was confirmed experimentally by Meijer et al. (1986). The maximum impact force depends on the particle velocity in the perpendicular direction u_x, by:

$$F_{max} = 0.76 \cdot \left(\frac{\mathrm{E}}{1-\nu^2} \right)^{0.4} \cdot d_p^{\ 2} \cdot \rho_p^{\ 0.6} \cdot u_x^{\ 1.2} \tag{4.12}$$

In which ν is the Poisson ratio and E is the combined elasticity modulus defined as:

$$\mathrm{E} = \frac{\mathrm{E}_1 \cdot \mathrm{E}_2}{\left(\mathrm{E}_1 + \mathrm{E}_2\right)} \tag{4.13}$$

The subscripts 1 and 2 denote the materials involved in the impact, ice and stainless steel. The mean impact frequency of spherical particles on the wall of a tube is given by:

$$\bar{f} = \frac{6 \cdot \bar{u}_x \cdot (1-\varepsilon)}{4 \cdot \pi \cdot d_p^{\ 3}} \tag{4.14}$$

In the previous correlations the impacts are assumed to be elastic perpendicular collisions. A large fraction of the particle–wall contacts are however not of this type. Particles may have non-elastic impacts and also roll or slide along the heat exchanger walls. Impact duration is then longer and the force exerted on the walls lower. Sliding or rolling particles still disturb the laminar boundary layer and enhance heat transfer coefficients. Also ice may be removed (Rong et al., 1999). According to Meijer et al. (1986) however, more than 95% of the momentum transferred to the wall is the result of collisions in the perpendicular direction.

Bordet et al. (1972) developed an empirical correlation to predict the mean kinetic energy of the particles transferred during an impact. The transferred energy, E_t, is twice the kinetic energy of the particle before impact, E_x, this because the particles are assumed to move away from the wall after the impact with the same velocity as before the impact.

$$\bar{E}_t = 2 \cdot \bar{E}_x = m \cdot \bar{u}_x^{\ 2} = 9.13 \cdot 10^{-6} \cdot \left(\rho_p - \rho_l\right)^{0.38} \left(\frac{u_s \cdot d_p}{\varepsilon} \right)^{0.66} \cdot \mu_l^{\ 0.28} \tag{4.15}$$

Meijer et al., (1986) showed that in the experimental determination by Bordet et al. (1972) of Equation 4.15, the particle impacts with low kinetic energy were not detected because of a too high lower detection limit of the measurements. This implies that the mean kinetic energy of the particles is in fact lower than in Equation 4.15, while the impact frequency is higher. According to Meijer et al. (1986) the mean perpendicular velocity of solid particles in a stationary fluidized bed with bed voidage of 0.80 can be accurately estimated with:

$$\bar{u}_x = 0.10 \cdot u_s \tag{4.16}$$

The superficial fluid velocity, u_s, for a stationary fluidized bed is calculated using the method described in Chhabra (1995) and Chhabra et al. (1999).

4.3 Experimental Method

Experiments were carried out in a single tube stationary fluidized bed ice slurry generator. A schematic layout of the set-up is given in Figure 4.2. The 55 mm fluidised bed did not have a transparent section halfway, which was used in the 43 mm fluidised bed, displayed in Figure 3.2. Ice slurry production was considered stable if wall-to-bed heat transfer coefficients remained constant for 20 minutes, while also the fluidization process remained steady.

Unstable conditions could be observed not only by a decreasing heat transfer coefficient, but also by an increased height of the fluidized bed. If an ice layer builds up, the tube diameter narrows and the space available for the fluidized bed reduces, which causes the bed height to increase.

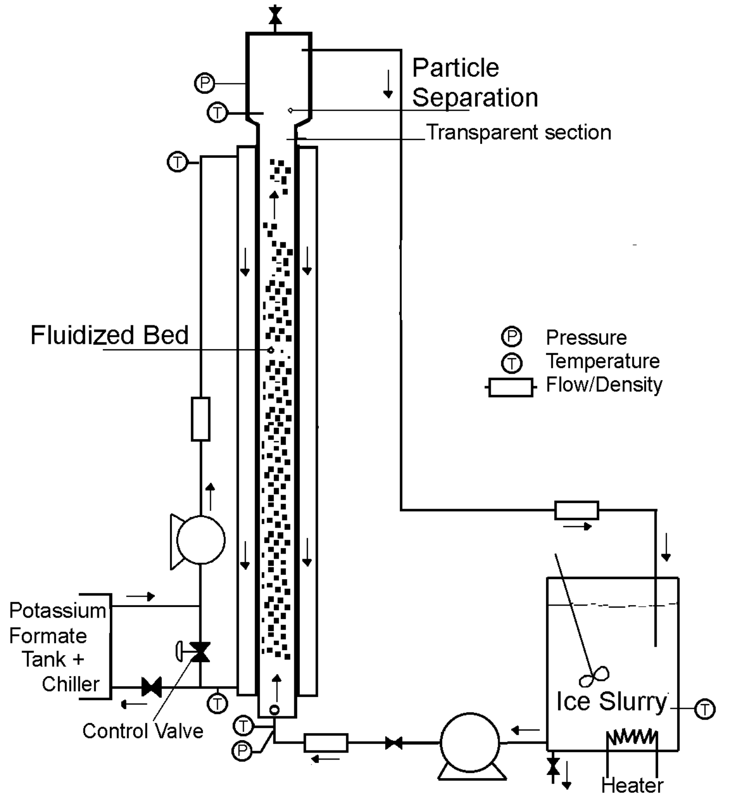

Figure 4.2: Experimental set-up of single tube fluidized bed heat exchanger

The fluidization particles were stainless steel cylinders, diameter and height both 4 mm. The bed was a stainless steel tube of 4.55 m high and 55 mm inner diameter with 2.8 mm wall thickness. Through an annular space of 5 mm around the fluidized bed a primary non-phase changing refrigerant, 34% potassium formate solution, was pumped counter-currently, with a flow of 4 m^3/h. The inlet temperature of the primary refrigerant could be controlled within 0.1 K. A water-cooled chiller was used with capacity of approximately 5 kW at 0 ^oC.

The ice slurry storage tank was equipped with an electrical heater of 3.4 kW capacity and a propeller type stirrer with which ice slurries could be kept homogeneous up to an ice fraction of 0.15. A pressure difference transmitter with accuracy of ±1 mbar was installed to monitor the pressure drop over the fluidized bed. An increased or unsteady pressure drop was another indication of unstable operation. At the top of the bed the fluidization height could be observed through a transparent section. The bed voidage was determined by weighing the solid particles present in the bed.

Temperature differences were determined with PT-100 sensors in the inlet and outlet flows of the ice slurry and the primary refrigerant. The sensors were calibrated with an accuracy of ±0.02 K. Coriolis-type mass flow meters, with accuracy of ±0.1% of the measured value, were used to determine flow rates of ice slurries.

The ice fraction of ice slurries was determined from the temperature measurements. The solid and liquid phases are assumed to be close to equilibrium, so that the ice slurries are practically at the freezing temperature. The ice formed is assumed to be pure, so that the concentration in the liquid phase is a function of the freezing temperature, $w_{fpd}(T_f)$ and the ice fraction can be determined if the initial freezing point depressant concentration is known. Freezing point data were obtained from Melinder (1997) and from Lide (1998).

At the start of an experiment the ice slurry flow was cooled with a constant inlet temperature of the primary refrigerant until the solution was approximately 0.5-1.5 K supercooled. In some experiments already ice was formed without seeding at this degree of supercooling. In most experiments however ice formation was initiated by seeding some ice crystals in the storage tank.
Test runs were either conducted at a constant temperature difference with the ice fraction increasing up to 0.15, or at a constant ice fraction kept under 0.15 with the heater in the storage tank. If stable conditions were obtained at certain operating conditions, the overall temperature difference was increased with a step of 0.5-1 K until unstable conditions were reached.

The enthalpy change of the primary refrigerant through the heat exchanger was calculated from the temperature measurements. With the mass flow of primary refrigerant the total heat transferred from the fluidized bed was determined, from which the overall heat transfer coefficient *U* followed. This overall heat transfer coefficient consists of the film heat transfer resistance on the primary refrigerant side, thermal conduction resistance through the wall and the ice slurry side heat transfer resistance. The model of Gnielinski (1976) for turbulent flow conditions, predicted film heat transfer coefficients of the primary refrigerant within an error of ±6% (Meewisse and Infante Ferreira, 2003). The wall-to-bed heat transfer coefficient, α_{in}, could then be calculated.
The wall-to-bed temperature difference followed from:

$$\Delta T_{wall-to-bed} = \Delta T_{wtb} = \frac{d_{out}}{d_{in}} \cdot \frac{U}{\alpha_{in}} \Delta T_{max} \tag{4.17}$$

The wall-to-bed heat transfer coefficients at the onset of instability were taken to predict the wall-to-bed temperature difference for the unstable conditions.
The following freezing point depressants were evaluated: NaCl, ethylene glycol and dextrose. A few additional experiments were done with potassium nitrate (Olea, 2003). The pH influence was investigated by addition of 0.1% wt. citric acid in some experiments with NaCl as freezing point depressant. This changed the pH from 7 to 3. The influence of the bed voidage was investigated at an increased bed voidage of 0.88, compared with 0.79 of most experiments.
After the experiments reported in section 5.5, the 55 mm column was inspected. Some damage (scratching) of the heat exchanger surface was observed, which was caused during the experiments with the rotor device. All experiments with NaCl and EG were done before, only the experiments with dextrose and KNO_3 were done after the rotor experiments.
The range of temperature differences investigated had an upper limit because of the cooling capacity of the chiller. The lower limit was formed by the accuracy of temperature control and heat transfer calculations at low temperature differences, where small measurement errors become relatively important. Temperature difference limits were obtained for initial freezing temperatures of the ice slurries from –0.5 °C to –4.0 °C. Experiments under stable conditions were done at initial freezing temperatures down to –7.0 °C.
The diameters and shapes of the ice crystals produced in the fluidized bed were evaluated using microscopic pictures for a few experiments. Samples for the pictures were taken from the stirred storage tank during ice slurry production, see also Section 2.4.

4.4 Results

In Figure 4.3 the wall-to-bed heat transfer coefficients of stable and of unstable ice slurry production runs with NaCl as freezing point depressant are displayed. The start of ice crystallization is set at t=0 s for both experiments. From microscopic pictures of the ice slurry of the stable experiment the average diameter of the ice crystals was estimated at 0.25 mm. The microscopic pictures of the ice slurry samples are discussed in detail in section 2.4.

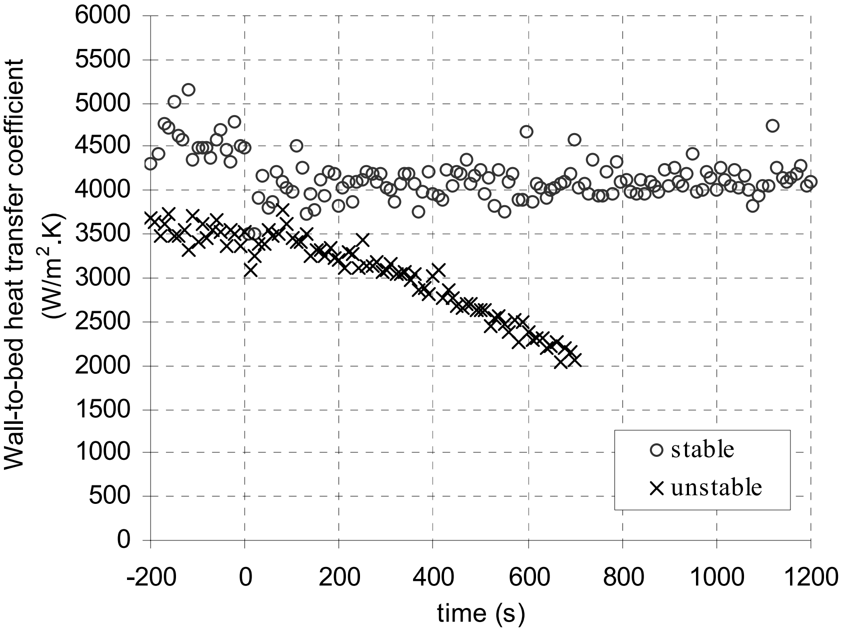

Figure 4.3: Heat transfer coefficients during ice slurry production. Stable conditions: 6.6 wt% NaCl, T_{f_init} =-4.1 °C. Unstable conditions: 3.9 wt% NaCl, T_{f_init}=-2.4 °C

In Figure 4.4, the maximum wall-to-bed temperature difference is displayed versus the NaCl concentration for the experiments at bed voidage 0.79. At increasing NaCl-concentration larger temperature differences could be applied before freeze-up occurred.

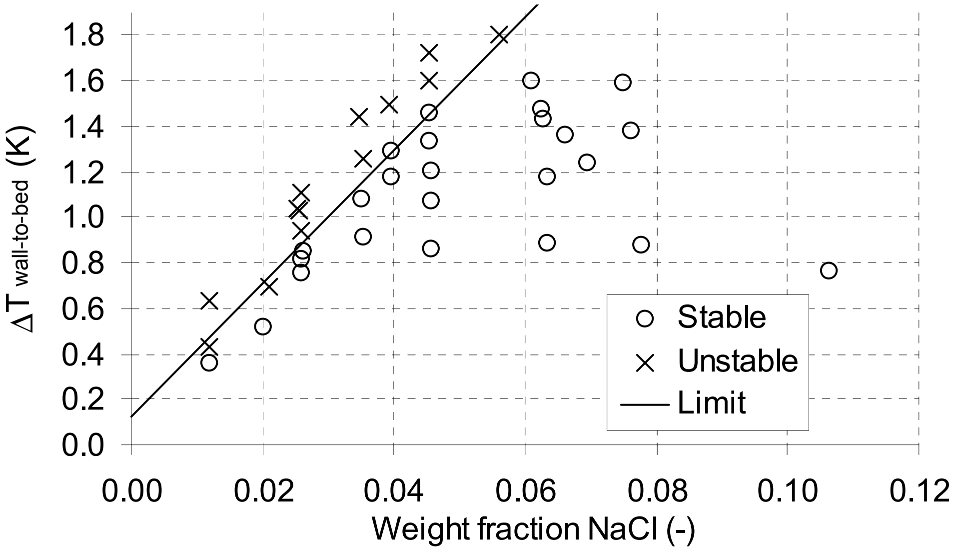

Figure 4.4: Wall-to-bed temperature difference versus NaCl-concentration for stable and unstable ice slurry conditions and the limit for the temperature difference allowable, ε= 0.79.

The average values between the highest stable and the lowest unstable temperature differences at each concentration of freezing point depressant, were used to fit a linear trend for the limit of the temperature difference allowable before freeze up. The least sum of squares method was used to fit coefficients c_1 and c_2 of Equation 4.18.

$$\Delta T_{max,wtb} = c_1 \cdot w_{fpd} + c_2 \tag{4.18}$$

The fit coefficients describe the limits fairly well, results are given in Table 4.2. For ethylene glycol and dextrose as freezing point depressant also a linear trend was observed, fit values are given in Table 4.2. For the experiments at varying pH, bed voidage or using KNO_3 only a few data were obtained, the fit data given in Table 4.2 are therefore only indicative values.

Table 4.2: Fit results for temperature difference allowable in Equation 4.18

Freezing point depressant	*Number of data points*	c_1	c_2	R^2
NaCl	39	29	0.13	0.96
NaCl, ε=0.88	5	37	-0.23	-
NaCl, pH=3	5	45	-0.04	-
Ethylene Glycol	13	25	-0.08	0.95
Dextrose	16	9.8	-0.19	0.96
KNO_3	4	11	0.09	-

The maximum allowable temperature differences determined for dextrose and KNO3 may have been influenced by the scratched heat exchanger surface. Build-up of an ice layer because of scratches is slower than if it is caused by a too high temperature difference, which would result in a more rapid decline of the heat transfer coefficient, similar to Figure 4.3. It may appear that conditions are stable in the first 15 minutes, after which however still freeze-up of the fluidized bed may occur and heat transfer coefficients decrease slowly. During the unstable experiments with dextrose, decrease of the heat transfer coefficients occurred rapidly and therefore is assumed not to be caused by the damaged surface. The presence of the scratches may however still have influenced freeze-up conditions, whereby the temperature difference allowable determined here for dextrose may be too low. Validation of the current result in a heat exchanger with smooth surface is necessary.

Also the KNO_3 experiments may have been affected by the damaged surface, so that also temperature differences allowable for KNO_3 may be higher than determined here. Too few experiments have however been conducted to clearly determine a trend. Further experiments should be carried out with a smooth heat exchanger surface.

Results of the experiments at bed voidage of 0.88 are displayed in Figure 4.5, together with the trend of Figure 4.4. It is observed that the allowable temperature difference at the bed voidage of 0.88 is comparable or slightly lower than at bed voidage of 0.79. In Figure 4.5 also the results are given of the pH=3 experiments. The limit for stable ice slurry production is at significantly larger temperature differences than at pH=7.

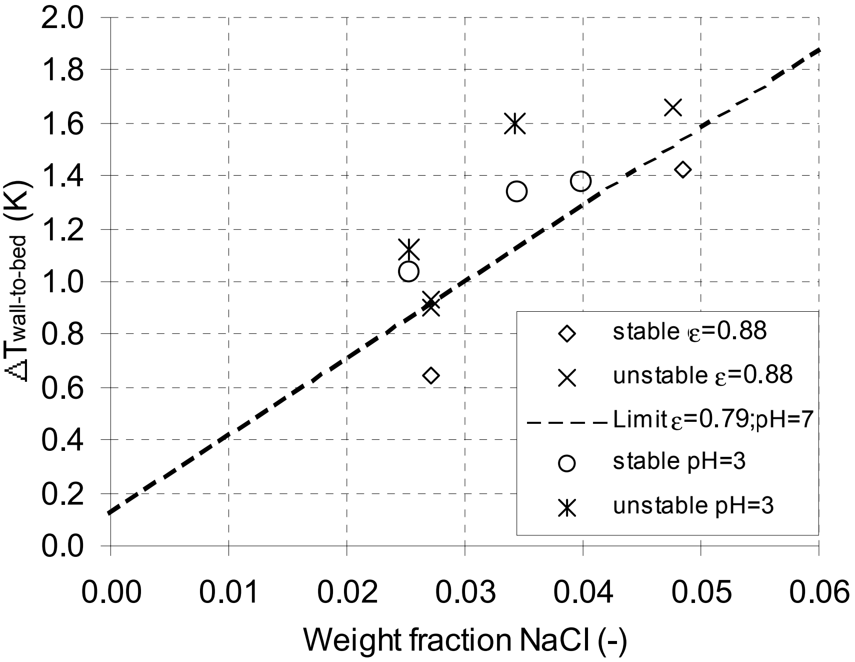

Figure 4.5: Wall-to-bed temperature difference versus NaCl-concentration for stable and unstable ice slurry conditions at bed voidage ε=0.88 and pH=7 and for experiments at bed voidage ε=0.79 and pH=3. Limit for bed voidage ε=0.79 and pH=7 is also given.

For the comparison of the freezing point depressants, the wall-to-bed temperature differences were plotted versus the initial freezing points of the ice slurries in Figure 4.6. For KNO_3 not enough experiments were done to obtain a meaningful curve, therefore only the experimental data are displayed. Ethylene glycol as freezing point depressant has the highest allowable temperature difference. It should be noted that both the dextrose and the KNO_3 experiments have been performed after the heat exchanger surface has been roughened by the rotor experiments.

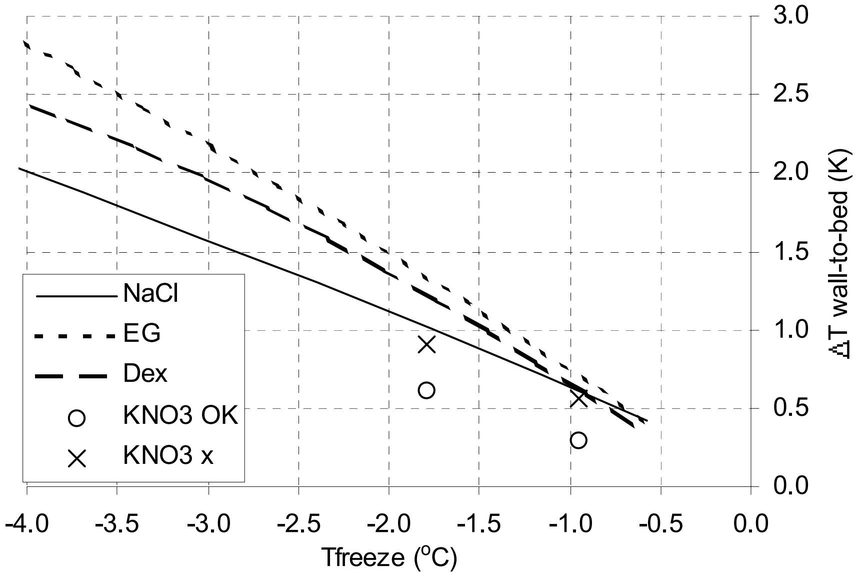

Figure 4.6: Maximum wall-to-bed temperature differences allowable for various freezing point depressants versus the initial freezing points of the aqueous solutions.

4.5 Discussion

4.5.1 Ice layer

In a number of experiments a small step down of the wall-to-bed heat transfer coefficients could be observed after initial ice nucleation. For example in Figure 4.3, the difference in heat transfer coefficients is approximately 10% for the stable conditions. For the unstable conditions however heat transfer coefficients just before and just after initial ice nucleation are almost equal, only after a few minutes heat transfer coefficients decrease upon freeze up of the fluidized bed.

If an ice layer of thickness δ is present at the wall, its heat transfer resistance would be measured as part of the wall-to-bed heat transfer coefficient, according to:

$$\frac{1}{\alpha_{wtb}} = \frac{d_{in}}{2\lambda_i} \ln\left(\frac{d_{in}}{d_{in} - 2\delta}\right) + \left(\frac{d_{in}}{d_{in} - 2\delta}\right)\frac{1}{\alpha_{in}} \tag{4.19}$$

Equation 4.19 is evaluated for the stable experiment of Figure 4.3 using the mean heat transfer coefficients two minutes before and two minutes after initial nucleation. The resulting thickness of the ice layer calculated is 53 µm. The average diameter of ice crystals observed in the storage tank is much larger, approximately 0.25 mm. Ice is therefore not formed only at an ice layer at the walls. A considerable part of the ice crystal growth takes place in the bulk of the fluidized bed. The ice layer thickness calculated here is an average, therefore larger ice crystals may still be attached to walls with the wall area in between free of ice.

No clear trend of the ice layer thickness could be determined for varying temperatures or freezing point depressants used. The ice layer was not observed in all experiments. The largest ice layer thickness found was 62 µm, the average for the experiments at a bed voidage of 0.79 was 20 µm, with standard deviation of 16 µm, indicating a large scatter in the occurrence of an ice layer. The average for all experiments, including pH and bed voidage effects, was 25 µm (±24 µm).

The heat exchanger surface roughness, defined as the difference between the highest and the lowest locations at the surface of the stainless steel, was not determined. However, for commercial grades of stainless steel without coatings or surface treatments the surface roughness has an order of magnitude around 1 µm, with maximum roughness up to 5 µm (Chesters et al. 1989; Whitley et al., 1987). This is an order of magnitude smaller than the thickness of the ice layer calculated. The ice layer is thicker than it would be if just the interstitial spaces of the surface roughness were filled with ice. The surface roughness is expected to be significant for the adhesion of ice, but is not likely to be the main cause.

4.5.2 Ice Crystallization

The mass transfer coefficient k_d is determined using the analogy between heat and mass transfer. Coefficients equal to the empirical correlation for heat transfer of Equation 4.1, are used to calculate the Sherwood number, according to:

$$Sh_h = \frac{k_d \cdot d_p}{D} \cdot \frac{\varepsilon}{(1-\varepsilon)} = c_1 \cdot Re_h^{c_2} Sc^{c_3} \tag{4.20}$$

with coefficients c_1=0.0612, c_2=0.724 and c_3=0.625.

The values of k_d were compared with a general correlation reported by Schmidt et al. (1999). The mean relative difference of the k_d-values calculated with Equation 4.20, with the values of Schmidt et al., was 17%. The relative difference was the largest for dextrose as freezing point depressant, where the model of Schmidt predicted k_d-values up to a maximum of 41% lower than Equation 4.20. Most likely cause of the differences is that experimental conditions are outside the range of experimental data on which the correlation of Schmidt et al. (1999) is based. Schmidt used Re_h from 0.9-1652 and Sc from 151-7021. In the current study Re_h was varied from 2147-8815 and Sc from 2816-15777, calculated with the liquid phase properties. The analogy between heat and mass transfer may not be valid exactly, but appears suitable to estimate k_d in this study.

The total ice crystal growth velocity at the wall calculated with Equation 4.8 is displayed in Figure 4.7 for the experiments with NaCl. The average ice layer thickness of 20 μm is used to calculate the heat transfer resistance. The marks indicate the experimental conditions of stable and unstable experiments. There is a relatively constant value of the growth rate above which freeze up of the fluidized bed occurs.

The solid line indicates the crystal growth velocity at the linear trend of the maximum temperature difference determined in the previous section. The dotted lines represent the relative contributions of the mass transfer and heat transfer to the total crystal growth velocity. The crystal growth velocity is clearly determined by the mass transfer resistance. The heat transfer resistance becomes an important factor only at temperatures above –2 ^oC. It should be noted that the mass transfer coefficients and the thickness of the ice layers are not known exactly and therefore also the relative influence of heat transfer may slightly differ from what Figure 4.7 indicates. If the ice layer is thicker than 20 μm, the influence of the heat transfer resistance extends. For example at an ice layer of 36 μm, the maximum ice crystal growth velocity at the wall is found at –2.7 ^oC.

For thicker ice layers heat transfer resistance becomes relatively important. If there is hardly an ice layer present, the mass transfer resistance is the limiting factor that controls the ice crystal growth velocity.

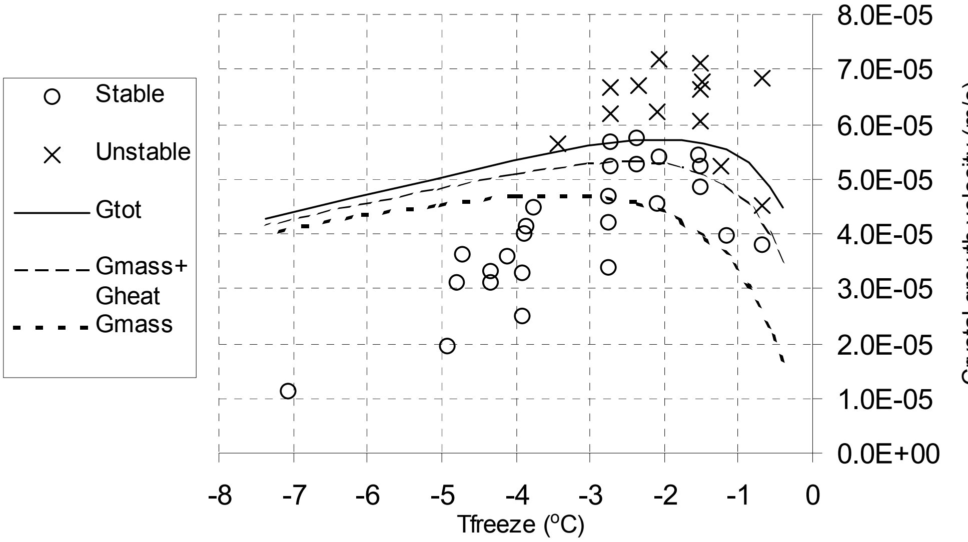

Figure 4.7: Total ice crystal growth velocity at the wall for the limit of Figure 4.4 and for the stable and unstable experiments with NaCl as freezing point depressant at bed voidage 0.79. The ice crystal growth velocity calculated with mass transfer resistance only and calculated with heat and mass transfer resistance only are also displayed.

The linear trend of the maximum allowable temperature difference versus concentration can be explained by the constant ice crystal growth velocity. Under certain conditions in the fluidized bed, the solid particles can remove a constant amount of ice from the walls by their impacts. If ice crystals grow faster than the removal capacity, freeze up of the fluidized bed starts.
At temperatures below approximately –2 °C, the ice crystal growth at the wall is controlled by the mass transfer resistance, calculated with Equation 4.5. In this equation the solute concentration w_{int} is present in both numerator and denominator: If the freezing temperature of the solution is lowered by addition of freezing point depressant, the driving force can be increased and the crystal growth velocity at the wall remains constant at the lower temperature. As the crystal growth velocity at the wall remains constant at lower temperatures, the additional heat transferred if a higher temperature difference is applied, must be transferred from the bulk of the fluidized bed, followed by ice crystal growth also in the bulk.
At increasing temperatures from –2 °C to –0.5 °C the mass transfer resistance decreases. The crystal growth velocity is however still relatively constant as the heat transfer resistance becomes significant in this temperature range.

In Figure 4.8 the total crystal growth velocities at the temperature difference limits of ethylene glycol and dextrose are displayed together with the total crystal growth velocity of NaCl. Both are also relatively constant in the temperature range of the experiments. The total crystal growth velocities for KNO_3 are also given in Figure 4.8, but at the experimental conditions only.

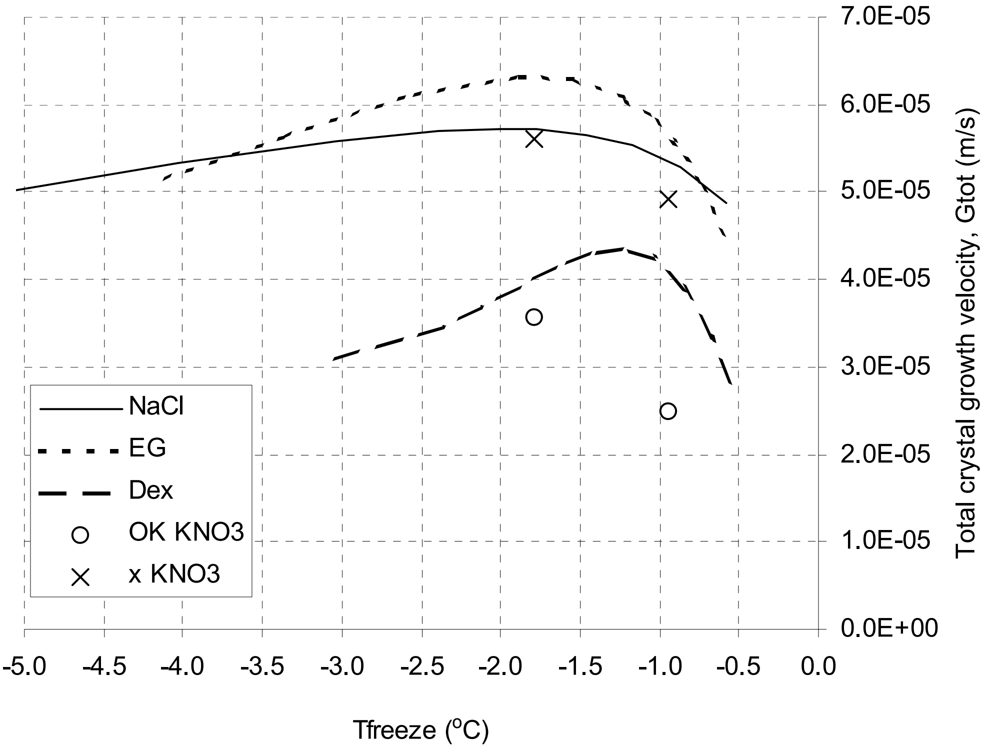

Figure 4.8: Total crystal growth velocity calculated at the limit of the temperature difference for NaCl, ethylene glycol and dextrose. Including additional experimental data for KNO_3.

The maximum crystal growth velocity calculated varies from approximately 44 μm/s for dextrose to 63 μm/s for ethylene glycol. Freeze up of the fluidized bed system occurs at lower crystal growth velocities if the freezing point depressant is dextrose or KNO_3, than if ethylene glycol or NaCl are used. However, the experiments with dextrose and KNO_3 may have been affected by the roughened surface of the heat exchanger. If results were influenced, the crystal growth velocity before freeze-up for smooth heat exchanger surfaces would be higher. Furthermore, only limited experiments have been done with KNO_3. The crystal growth velocities allowable before freeze-up are in the same order of magnitude for different freezing point depressants. Differences in the maximum allowable temperature difference can therefore not be explained using only the crystal growth velocity.

The range of experiments is relatively small. Measurements at both lower freezing temperatures and in the range from -1 °C to 0 °C may confirm the linear trend between temperature difference and concentration. Alternatively the crystal growth velocity may be constant throughout the temperature range.

4.5.3 Particle Impacts

The average perpendicular velocity of the solid particles calculated with Equation 4.15 for the stable experiment of Figure 4.3 is 30% higher than calculated with the method of Meijer et al. (1986), stated in Equation 4.16. At higher bed voidage the difference decreases. Because of the fluid viscosity influence, Equation 4.15 predicts an increasing kinetic energy of the solid particles at lower temperatures. The superficial velocity of a stationary fluidized bed, predicted with the method of Chhabra (1995), however decreases at decreasing temperature for NaCl, dextrose and KNO_3 solutions. Only for ethylene glycol the superficial velocity increases. It is considered unlikely that solid particles obtain higher kinetic energy at a lower superficial velocity. The assumption of Meijer is therefore preferred over Equation 4.15.

An overview of relevant particle impact parameters is given in Table 4.3 for the conditions of the stable experiment of Figure 4.3, calculated with two different mean particle velocities, and for the same conditions but at a bed voidage of 0.88. The ice crystals produced are assumed to be spherical with a mean diameter of 0.25 mm. The equivalent diameter of spherical particles is used in the calculations of the cylindrical particles. The total number of ice crystals produced in this experiment is calculated from the heat transfer coefficient of Equation 4.1, whereby all heat transferred is assumed to be used in ice formation at a constant latent heat effect.

If ice crystals would form only on the heat exchanger walls, every particle impact should transfer approximately 68 ice crystals from the wall. Apart from particle-wall impacts however also particle-particle impacts occur. In the horizontal plane, the ratio particle-wall to particle-particle collisions is assumed to be equal to the ratio particle surface to wall surface. The number of particle-particle collisions in the vertical direction is assumed to be equal to the number of collisions in the horizontal plane. There are approximately 5 times more particle-particle collisions than there are particle-wall collisions at a bed voidage of 0.80. The amount of ice crystals present in the fluidized bed, calculated at 5% vol. of ice, is large enough to expect each particle-particle collision to affect a few ice crystals. Only a small part of the ice crystals are formed directly at the heat exchanger wall.

Table 4.3: Fluidization Parameters for 6.6 wt% NaCl ice slurry, Initial T_{freeze}=-4.1 °C (stable conditions of Figure 4.3)

Bed voidage Method		0.79 Eq. 4.16	0.79 Eq. 4.15	0.88 Eq. 4.15
Superficial velocity	m/s	0.33	0.33	0.42
Mean particle velocity	m/s	0.033	0.044	0.046
Particle-wall impact frequency	$1/m^2s$	$0.35\cdot10^5$	$0.46\cdot10^5$	$0.29\cdot10^5$
Particle-particle impact freq.	$1/m^2s$	$1.75\cdot10^5$	$2.33\cdot10^5$	$0.86\cdot10^5$
Ice crystal production	$1/m^2s$	$2.2\cdot10^6$	$2.3\cdot10^6$	$2.1\cdot10^6$
Particle impact area	m^2	$1.65\cdot10^{-5}$	$1.65\cdot10^{-5}$	$1.65\cdot10^{-5}$
Ice crystal area	m^2	$4.91\cdot10^{-8}$	$4.91\cdot10^{-8}$	$4.91\cdot10^{-8}$
Ice crystals in fluid. bed, 5% ice		$5.2\cdot10^7$	$5.2\cdot10^7$	$5.7\cdot10^7$
Mean kinetic energy particle, E_0	J	$2.13\cdot10^{-7}$	$3.77\cdot10^{-7}$	$4.15\cdot10^{-7}$
Max force of impact at mean u_x	N	0.57	0.80	0.85

The total number of collisions is an order of magnitude lower than the number of ice crystals produced. The solid particles themselves are however significantly larger than the ice crystals: A solid particle of 4 mm impacts on a surface 336 times larger than the area covered by an ice crystal with diameter of 0.25 mm. If a smaller ice crystal diameter is assumed, because part of the crystal growth occurs in the bulk of the fluidized bed, even more nuclei may be formed per effective particle impact.

Contacts without solid particles involved, i.e. between ice crystals and between ice crystals and the wall, also can result in formation of fresh nuclei. These contacts occur at lower kinetic energies, but are more frequent than the contacts involving solid particles and may therefore contribute significantly to secondary nucleation.

Ice crystal removal from walls occurs only at high kinetic energy impacts. Bordet et al. (1972) found that the kinetic energy of the particles has a Maxwell-Boltzmann distribution. This distribution is used to predict the fraction of relevant particle-wall collisions. The number of particles N that impact with a kinetic energy above E_x is estimated with:

$$N = N_0 \exp\left(-\frac{E_x}{E_0}\right) \tag{4.21}$$

in which E_0 is the mean kinetic energy of the particles. N_0 is equal to the particle impact frequency. The mean kinetic energies of 4 mm cylindrical particles in a stationary fluidized bed of bed voidage 0.79 are given in Figure 4.9 for the four freezing point depressants of this study. For all temperatures ethylene glycol has the highest mean kinetic energy.

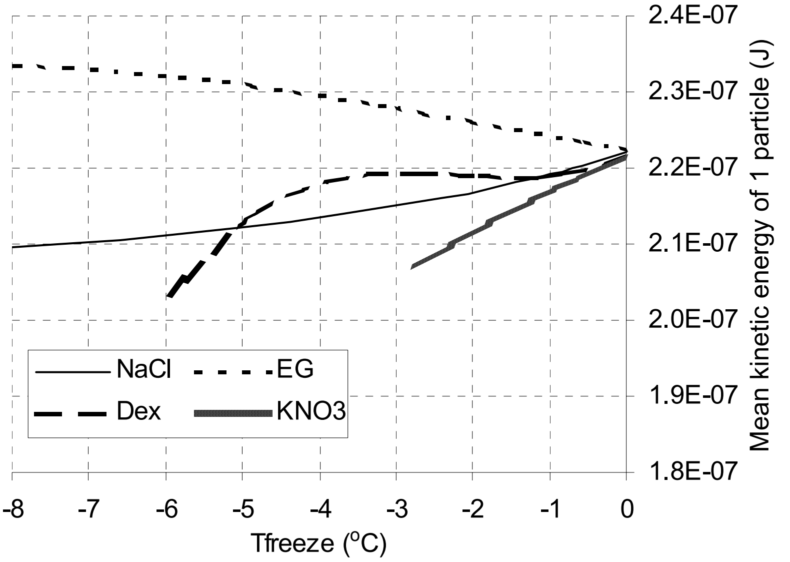

Figure 4.9: Mean kinetic energy of solid particles versus the initial freezing temperature at $\varepsilon = 0.79$. The mean velocity is taken at 10% of the superficial velocity (Equation 4.16).

The lower driving force allowable at a higher bed voidage in this study is probably caused by a reduction of the number of effective particle impacts. Calculation results are given in Table 4.3 using Equation 4.15, as the assumption of Meijer is only valid at a bed voidage of 0.80. At a higher bed voidage of 0.87 there are 37% less impacts. This negative effect is compensated only partially by a 10% increased average kinetic energy of the particles at a higher bed voidage.

4.5.4 Ice Adhesion

The work of adhesion calculated for the various freezing point depressants is given in Figure 4.10. The general trend for the work of adhesion is consistent with the results reported by Yamada et al. (2002): At decreasing freezing temperature the work of adhesion decreases.

The qualitative trend of the three different solutes is also consistent with the trend of Figure 4.6. For ethylene glycol the work of adhesion determined is the lowest while it has the highest allowable temperature difference. NaCl has the highest work of adhesion of the three solutes and it also has the lowest temperature difference allowable.

Surface tension data for stainless steel and ice have been assumed constant with temperature. Possible errors in estimates of ice and stainless steel properties are therefore equal for all solutes. An increase of the surface energy of stainless steel, for example if it is at a lower temperature than the solution and ice, results in a larger work of adhesion than the results of Figure 4.10.

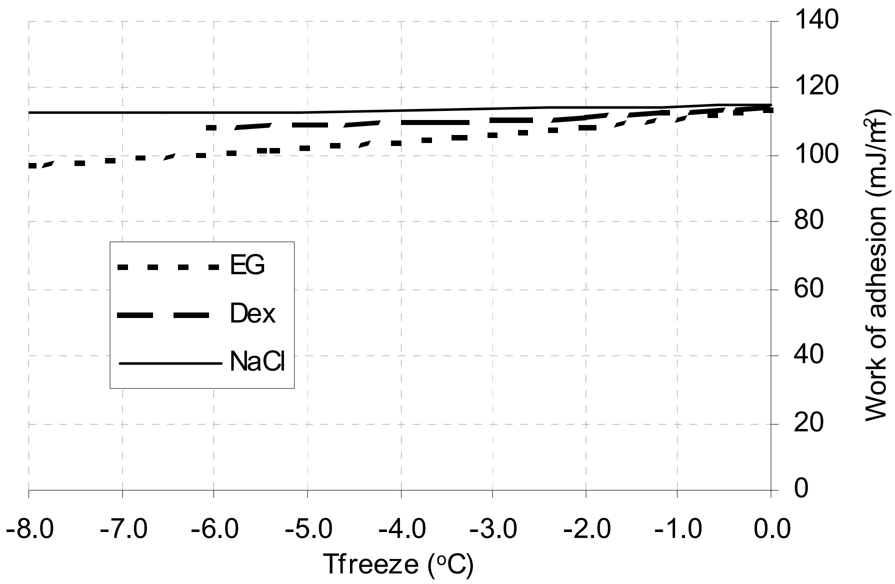

Figure 4.10: Estimated work of adhesion ice/stainless steel versus the initial freezing temperature for ethylene glycol, dextrose and NaCl aqueous solutions.

The work of adhesion as it is estimated by the method of Yamada, ignores several effects that may be relevant for ice adhesion. Petrenko and Qi (1999), have shown that there are electrostatic forces involved in ice adhesion, because of freezing into the crystal structure of traces of solute. The electrostatic forces are the result of a freezing potential that may occur if different ions are included in the ice crystal structure with different selectivity. Cl^- ions for example are included in ice more readily than Na^+ ions (Hobbs, 1974). The resulting freezing potential is compensated by H^+ entering the ice from solution or generated in the ice structure itself. The pH is therefore a decisive factor in the reduction of the freezing potential and may be the explanation for the increased driving force allowable at lower pH for NaCl solutions.

4.5.5 Ice Removal

The work of adhesion is an indicator for the adhesive strength, as shown by Sonwalkar et al. (1993). The force required to remove ice crystals from the heat exchanger surface can however not be determined exactly from the work of adhesion. The main reason is that the surfaces at atomic scale are not completely flat, and therefore the exact contact area between ice and walls is not known. Furthermore, the ice crystals removed from the surface do not obtain the equilibrium shape for lowest surface energy, because molecules are not free to move in the crystal as they are in the liquid phase. Other surface effects that have been disregarded are the occurrence of a 'liquid like layer' between ice and stainless steel (Hobbs, 1974) and the cleanliness of the surfaces.

The area at which the solid particles contact determines the outcome of the impact. Particles that hit a single ice crystal of 0.25 mm attached to the wall, fully exert the force of the impact on the relatively small contact area between crystal and wall. Contacts with single crystals are physically possible, because the cylindrical particles have edges, see for example the situation of Figure 4.1. The maximum force per unit area of the crystals of such impacts is 11.6 MPa at the mean impact velocity, evaluated for the conditions of the stable experiment of Figure 4.3. This impact force is large enough to overcome the adhesive strength, which varies from 0

MPa at 0 °C, to 1.6 MPa at –13 °C as determined by Jellinek for adhesion of ice to stainless steel (Petrenko and Whitworth, 1999). Sonwalkar et al., (1993) reported an adhesive strength of 0.416 MPa at –20 °C.
The particle impact force is also large enough to overcome the cohesive strength of the ice itself, which is around 1.6 MPa (Petrenko and Whitworth, 1999). An effective impact may therefore also remove ice while leaving a small part of the ice adhered to the walls.

If a particle impacts at a layer of ice rather than at single crystals, its impact force will be distributed over a much larger area, approximately equal to the size of the particle. The surface area under the impact is probably not completely covered with ice (Ishikawa et al., 2002). The force of the impact per unit area of crystal in contact with the wall is therefore proportionally larger than if the surface would be fully covered with ice. If 67% of the surface is assumed to be covered with ice, the force of a particle impacting at average velocity is 0.052 MPa. This force is relatively low so that only ice adhered at a low strength, i.e. at low temperature differences, can be removed (Petrenko and Whitworth, 1999). A number of the particles however impact at higher velocity: Using the exponential distribution of Equation 4.21, 10% of the particles for example impact with a maximum force of 0.087 MPa or more.

The kinetic energy transferred by a particle impacting on a single ice crystal yields a work of 8.7 J/m^2 at the crystal contact area at the wall. This work is in the order of magnitude of the works of adhesion of 1.1 to 19 J/m^2 observed by Wei et al. (1996). These experiments were however performed at macroscopic scale and the work of adhesion determined includes deformation and also cohesive fracturing of the ice. Particles impacting on a single ice crystal therefore have sufficient kinetic energy to remove the ice from the wall. Also breaking of the ice crystal may occur.
If the kinetic energy of a particle is related to the impact at an ice layer, a surface area equal to the size of the particle is affected. If again 67% of the surface is assumed to be covered in ice, the average work of the impact is 39 mJ/m^2. With the exponential distribution of Equation 4.21 it is then calculated that approximately 6.3% of the particle impacts transfer more energy than the work of adhesion of 107 mJ/m^2 that is calculated for this case (Figure 4.10). A similar amount of the particle impacts will be effective as estimated with the adhesion force.

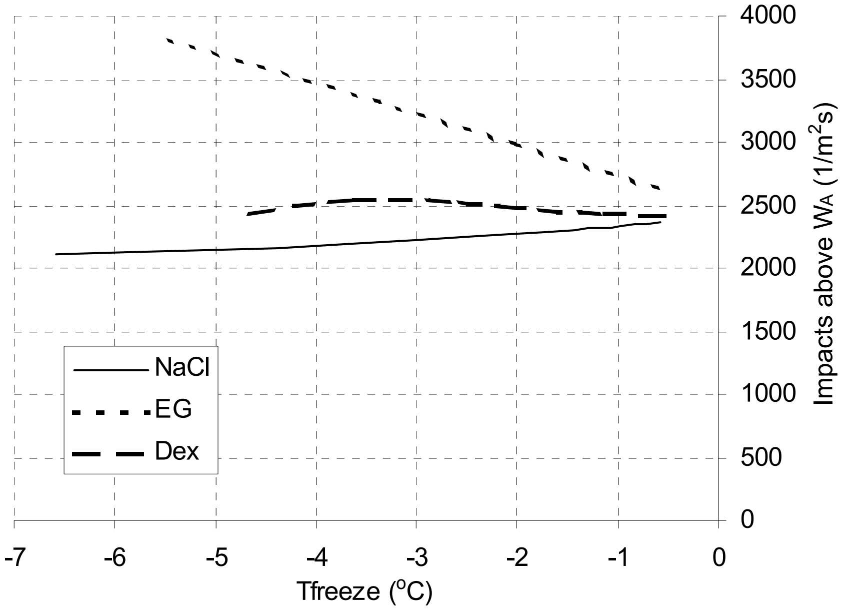

Figure 4.11: Number of particle impacts above the work of adhesion estimated in Figure 4.10

The number of particle impacts at kinetic energies above the work of adhesion calculated in the previous section is displayed in Figure 4.11, with the assumption that 67% of the surface under each particle impact is covered with ice. Ethylene glycol as freezing point depressant yields the largest amount of effective impacts. The trends are similar to the trends of the maximum allowable temperature difference observed in Figure 4.6. The approach to calculate the number of particle-wall impacts at kinetic energies above the work of adhesion of ice to the wall is therefore valid. For an accurate quantitative correlation between the maximum temperature difference allowable and the number of effective particle impacts, the work of adhesion and the mean particle impact velocities must be determined more accurately.

The variation of the maximum allowable temperature difference between the freezing point depressants qualitatively corresponds to the fluidization conditions. The positive effect of the lower pH however can not be explained using the fluidization conditions, because the fluidization conditions remain practically constant at changing acidity. The work of adhesion, to which the pH is an important parameter because of acid/base interactions and electrostatic forces, must therefore be included to determine the amount of effective particle-wall impacts.

4.6 Conclusion

The maximum wall-to-bed temperature difference allowable during ice slurry generation before freeze-up of the fluidized bed depends linearly on the concentration of freezing point depressant within the range of experiments considered. This is caused by a remarkably constant ice crystal growth velocity at the walls, which is primarily determined by the solute mass transfer. The heat transfer resistance is limiting for ice crystal growth at the walls only at relatively high temperatures, from approximately –2 °C to 0 °C. At increasing freezing point depressant concentration a larger temperature difference can be applied while the ice crystal growth velocity at the wall remains constant. Additional heat transferred above this crystal growth velocity at the wall, but under the maximum wall-to-bed temperature difference allowable, results in ice crystal formation in the bulk of the fluidized bed.

Fluidization conditions must be sufficient to remove the constant ice crystal growth velocity at the walls to prevent freeze-up. Variations of the maximum temperature difference allowable between freezing point depressants are caused by a varying ice removal capacity. In the current evaluation the crystal growth velocity allowable before freeze-up for dextrose ice slurries may have been negatively affected by local modification of the heat exchanger surface. The difference with ethylene glycol and NaCl may not be as large. Further experiments using a smooth heat exchanger surface are required to validate the results for dextrose. Also for KNO_3 more experiments are required to determine the limit more accurately.

The ice removal capacity can be determined from the number of effective particle-wall impacts. Whether a particle impact is effective depends on the adhesive strength of the ice to the wall and on the impact velocities of the solid particles at the wall of the fluidized bed.
An approach is introduced in which the work of adhesion of ice to the walls and an exponential distribution of the kinetic energies of the solid particles are used to determine the number of effective particle impacts. The results correspond qualitatively well with the trends of the maximum temperature differences allowable. The approach is expected to be applicable for quantitative prediction of freeze-up conditions during ice crystal formation.

Nomenclature

$c1..c3$	constant coefficients
Cp	Heat capacity (J/kgK)
D_H	hydraulic diameter (m)
D	diffusion coefficient (m^2/s)
d_p	particle diameter (m)
E	Elasticity (modulus)
E_t	kinetic energy transfer (J)
E_x	kinetic energy (J)
f	impact frequency ($1/m^2s$)
F	force (N)
G	crystal growth velocity (m/s)
ΔH_f	heat of ice formation (J/kg)
k	mass transfer coefficient (m/s)
m	mass of particle (kg)
$\dot{m}_d$	ice deposition rate (kg/m^2s)
$\dot{m}_r$	ice removal rate (kg/m^2s)
n	coefficient
N	number of particles
Nu_p	particle Nusselt no. ($\alpha d_p/\lambda$)
Nu_h	hydraulic Nusselt no.($Nu_p.\varepsilon/(1-\varepsilon)$)
Pr	Prandtl no. ($\mu Cp/\lambda$)
Re	Reynolds no. ($\rho.u_s.D_H/\mu$)
Re_p	particle Reynolds no.($\rho.u_s.d_p/\mu$)
Re_h	hydraulic Reynolds no. ($Re_p/(1-\varepsilon)$)
Sc	Schmidt number($\mu/\rho D$)
Sh	Sherwood number (kd_p/D)
t	time (s)
T	temperature (°C)
T_f	Freezing temperature (°C)
T_{f_init}	Initial freezing temperature (°C)
ΔT_{max}	Max. temperature difference (K)
ΔT_{wtb}	Temperature difference between wall and fluidized bed (K)
u	velocity (m/s)
U	Overall heat transfer coefficient (W/m^2K)
w	weight fraction
W_A	work of adhesion (J/m^2)

Greek

α	heat transfer coefficient (W/m^2K)
γ_{ij}	interfacial tension (J/m^2)
δ	ice layer thickness (m)
ε	bed voidage
θ	contact angle (rad)
λ	thermal conductivity (W/mK)
μ	dynamic viscosity (Pa.s)
ν	Poisson ratio
ρ	density (kg/m^3)

Superscripts

AB	*Acid/base*
d	dispersive
eq	equivalent
LW	Lifshitz/vanderWaals
nd	nondispersive
$*$	equilibrium

Subscripts

0	average conditions
1	ice
2	wall
3	solution
b	bulk
d	diffusive
fpd	freezing point depressant
$heat$	heat
i	ice
i,j	components
in	inside of tube
int	interface
l	liquid
max	maximum
out	outside of tube
p	particle
s	superficial
sol	solution
$surf$	surface integration
T_f	freezing temperature
tot	total
w	wall
wat	water
wtb	wall-to-bed
x	perpendicular

Other

Dex	Dextrose
EG	Ethylene glycol

References

Bordet, J., Le Goff, P., Vergnes, F., 1972, *Mesures statistiques de la vitesse horizontale de particules solides fluidisées par un liquide a l'aide d'un capteur piézoélectrique, analogie avec la théorie cinétique de gaz*, Powder Technology, 5, p365-375

Chhabra, R.P., 1995, *Wall effects on free-settling velocity of non-spherical particles in viscous media in cylindrical tubes*, Powder Technology, 85, p83-90

Chhabra, R.P., Agarwal, L., Sinha, N.K., 1999, *Drag on non-spherical particles: an evaluation of available methods*, Powder Technology, 101, p288-295

Chesters, S., Wen, H.Y., Lundin, M., Kasper, G., 1989, *Fractal based characterization of surface texture*, Applied Surface Science 40, p185-192

Docoslis, A., Giese, R.F., van Oss, C.J., 2000, *Influence of the water-air interface on the apparent surface tension of aqueous solutions of hydrophilic solutes*, Colloids and Surfaces B: Biointerfaces, 19, p147-162

Förster, M., Augustin, W., Bohnet, M., 1999, *Influence of the adhesion force crystal/heat exchanger surface on fouling mitigation*, Chemical engineering and processing, 28, p449-461

Fowkes, F.M., 1963, *Additivity of intermolecular forces at interfaces. I. Determination of the contribution to surface and interfacial tensions of dispersion forces in various liquids*. J. Phys. Chem. 67, p2538-2541

Freitas, A.M., Sharma, M.M., 2001, *Detachment of particles from surfaces: An AFM study,* Journal of Colloid and Interface Science 233, p73-82

Gnielinski, V., 1976, *New equation for turbulent heat transfer in pipe and channel flow*, Int. Chem. Eng. 16(2), p359-368

de Goede, R., van Rosmalen, G.M. 1990, *Modelling of crystal growth kinetics: A simple but illustrative approach*, Journal of Crystal Growth, 104, p392-398

Haid, M., Martin, H., Müller-Steinhagen, H., 1994, *Heat transfer to liquid-solid fluidized beds*, Chemical Engineering and Processing, 33, p211-225

Hobbs, P.V., 1974, *Ice Physics*, Oxford: Clarendon Press, ISBN 0198519362

Huige, N.J.J., Thijssen, H.A.C., 1972, *Production of large crystals by continuous ripening in a stirrer tank*, Journal of Crystal Growth. 13/14, p483-487

Ishikawa, M., Hirata, T., Fujii, T., 2002, *Force estimation of mechanical removing processes of mushy structure in aqueous solution*, International Journal of Refrigeration 25, p208-217

Jamialahmadi, M., Malayeri, M.R., Müller-Steinhagen, H., 1996, *A unified correlation for the prediction of heat transfer coefficients in liquid/solid fluidized bed systems*, Transactions of the ASME, Journal of Heat Transfer 118, 952-959

Jullien, C., Bénézech, T., Carpentier, B., Lebret, V., Faille, C., 2002, *Identification of surface characteristics relevant to the hygienic status of stainless steel for the food industry*, Journal of Food Engineering, 56, p77-87

Klaren, D.G., 2000, *Self cleaning Heat exchangers* In: Handbook heat exchanger fouling: Mitigation and cleaning technologies ed. by H. Müller-Steinhagen, Rugby Institution of Chemical Engineers, p186-199

Klaren, D.G., van der Meer, J.S., 1991, *A fluidized bed chiller: A new approach in making slush-ice*, Industrial Energy Technology Conference Houston Proceedings, Texas University

Lide, D.R. (ed.), 1997, *CRC Handbook of Chemistry and Physics*, 78th edition 1997-1998, CRC Press Boca Raton NY

Matubayashi N., Matsuo, H., Yamamoto, K., Yamaguchi, S., Matuzawa, A., 1999, *Thermodynamic quantities of surface formation of aqueous electrolyte solutions I. Aqueous solutions of NaCl, $MgCl_2$ and $LaCl_3$*, Journal of Colloid and Interface Science, 209, p398-402

Meewisse, J.W., Infante Ferreira, C.A., 2003, *Validation of the use of Heat Transfer Models in Liquid/Solid Fluidized Beds for Ice Slurry Generation*, International Journal of Heat and Mass Transfer, 46 (19), p3683-3695

Meijer, J.A.M., Wesselingh, J.A., Clobus, A., Goossens, M.L.A., 1986*, Impacts against the wall of a scaled up fluidized bed*, Desalination, 58, p1-18

Melinder, A., 1997, *Thermophysical properties of liquid secondary refrigerants*, Stockholm: Handbook no. 12 of the Swedish Society of Refrigeration

Olea, I., 2003, *Ice Scaling in fluidized bed heat exchanger*, M.Sc. thesis KK, TU Delft

van Oss, C.J., 1993, *Acid-base interfacial interactions in aqueous media*, Colloids and Surfaces A: Physicochemical and Engineering Aspects, 78, p1-49

Ottjes, J.A., 1981, *A measuring system for particle impact velocities and application in a pneumatic transport line*, Chemical Engineering Science 36, p1337-1347

Petrenko, V.F., Whitworth, R.W., 1999, *Physics of Ice*, Oxford University Press, ISBN 0198518951, p314-321

Petrenko, V.F., Qi, S., 1999, *Reduction of ice adhesion to stainless steel by ice electrolysis*, Journal of Applied Physics, 86 (10), p5450-5454

Rautenbach, R., Katz, T., 1996, *Survey of long time behavior and costs of industrial fluidized bed heat exchangers*, Desalination, 108, 335-344

Rong, D., Mikami, T., Horio, M., 1999, *Particle and bubble movements around tubes immersed in fluidized beds- a numerical study*, Chemical Engineering Science, 54, p5737-5754

Schmidt, S., Büchs, J., Born, C., Biselli, M., 1999, *A new correlation for the wall-to-fluid mass transfer in liquid–solid fluidized beds*, Chemical Engineering Science 54 (6), p829-839

Schneider, R. P., Chadwick, B. R., Jankowski , J., and Acworth, I., 1997, *Determination of physicochemical parameters of solids covered with conditioning films from groundwaters using contact angles. Comparative analysis of different thermodynamic approaches utilizing a range of diagnostic liquids*. Colloids and Surfaces A: Physicochemical and Engineering Aspects 126 (1), p1-23

Sonwalkar, N., Shyam Sunder, S., Sharma, S.K., 1993, *Ice/Solid adhesion analysis using low temperature Raman microprobe shear apparatus*, Applied Spectroscopy 47 (10), p1585-1593

Veeramasuneni, S., Yuehua Hu, Yalamanchili M.R., Miller J.D., 1997, *Interaction forces at high ionic strengths: the role of polar interfacial interactions*, Journal of Colloid and Interface Science, 188 (2), p473-480

Wei, Y., Adamson, R.M., Dempsey, J.P., 1996, *Ice/metal interfaces: fracture energy and fractography*, Journal of Materials Science*,* 31, p943-947

Whitley, J.Q., Kusy, R.P., Mayhew M.J., and Buckthal J.E., 1987, *Surface roughness of stainless steel and electroformed nickel standards using a HeNe laser*, Optics & Laser Technology*,* 19(4) p189-196

Yamada, M., Fukusako, S., Kawabe, H., 2002, *A quantitative evaluation of the production performance of ice slurry by the oscillatory moving cooled wall method*, International Journal of Refrigeration 25 (2), p199-207

5 Operating Modes of the Fluidized Bed Ice Slurry Generator

5.1 Introduction

Several operating modes are possible for liquid/solid fluidization. In this Chapter these are studied for ice slurry generation. Focus is on the methods available to calculate the fluidization conditions and their impacts on the ice slurry generation. A number of experiments are carried out in addition to the range of measurements and conditions discussed in the previous Chapters, which allows for a further model validation.

In the first section the methods to calculate fluidization conditions of liquid/solid fluidization are discussed. Size and shape of the solid particles of the fluidized bed is evaluated, as well as the type of fluidization.

Another potentially beneficial feature is the option to circulate the solid particles. In current commercially applied fluidized bed heat exchangers circulation is a common feature, that improves heat transfer coefficients and continuous operation capability. For ice slurry generation circulation may however be less advantageous because of increased heat losses, increased pumping power and increase of the chance of system blockages.

Another advantage of fluidized bed systems is the possibility to install multiple fluidized beds parallel. This greatly reduces the investment costs per square meter of heat transfer surface upon increased system scale.

Finally a possible improvement of the fluidized bed system is evaluated. It consists of a rotating device, that may increase operating range and heat transfer coefficients by actively moving the solid particles of the fluidized bed towards the wall.

5.2 Stationary Liquid/solid Fluidization

5.2.1 Fluidization Types

The hydrodynamic behavior of fluidization is determined principally by the geometry of the system, bed voidage and the physical properties of the solid and fluid phases. The mechanisms responsible for fluidization with a liquid are intrinsically the same as for fluidization with a gas. Differences are mainly caused by physical properties. A major factor is the density difference between solid and fluidization medium, which is much smaller in liquid/solid fluidization than in gas/solid fluidization. As a result of this liquid/solid fluidization is generally more homogenous. Phenomena as bubbling and slugging in fluidized beds can however also be encountered in liquid/solid fluidized beds.

The different types of fluidization distinguished are particulate or homogeneous fluidization and aggregative or heterogeneous fluidization (Foscolo and Gibilaro, 1984). In particulate fluidization the solid particles move homogeneously through the fluidized bed, in aggregative fluidization, small groups of solid particles are considered to move together through the fluidized bed as aggregates, whereby the bed voidage locally differs from

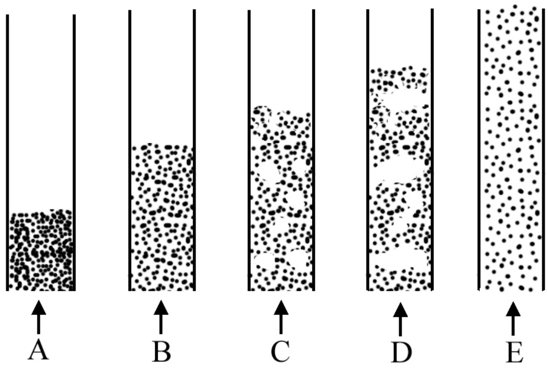

Figure 5.1: Various types of fluidization A: Packed bed; B: Homogeneous fluidized bed; C: Bubbling fluidized bed; D: Slugging fluidized bed, E: Fast or conveying fluidized bed

the average of the bed. Particulate and aggregative fluidization are in fact the extremes of a continuous range and various intermediate fluidization patterns are possible (Jamialahmadi, 1996). An overview of some possible fluidization modes is given in Figure 5.1 (Kwauk et al., 2000).

In the review of di Felice (1995) homogeneous fluidization and three types of heterogeneous fluidization are discussed. The three heterogeneous fluidization types are distinguished by their bed expansion characteristics, which are displayed in Figure 5.2, with the characteristic of homogeneous fluidization.

In the figure the superficial fluidization velocity required for a fluidized bed of a certain voidage is displayed on a logarithmic scale. For homogeneous fluidization this results in a straight line. In heterogeneous fluidization, sharp bends may occur representing transitions in fluidization behavior, e.g. from homogenous to bubbling fluidization. Also the curve may not be a straight line. For all types of fluidization the curves approach the unhindered settling velocity at a bed voidage of 1.

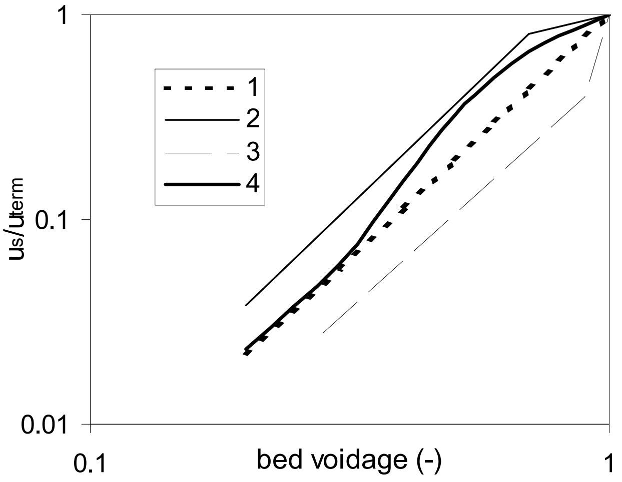

Figure 5.2: Various types of bed expansion behavior. 1:Homogeneous (Richardson-Zaki); 2,3: Heterogeneous with transitions to/from homogeneous; 4: Bubbling fluidization

To determine if fluidization occurs in aggregative or particulate mode, several criteria may be applied. One criterion was presented by Wilhelm and Kwauk and is based empirically on the Froude number at minimum fluidization velocity (Kwauk et al., 2000):

$$Fr_{mf} = \frac{u_{mf}^{2}}{g d_p} \tag{5.1}$$

For $Fr_{mf}<0.13$ the fluidization is particulate, for $Fr_{mf}>1.3$ fluidization is under aggregative conditions. In the intermediate range of Fr_{mf} also some sort of intermediate fluidization behavior is found. A weakness of this criterion is that it does not predict the dependence of the fluidization behavior on the bed voidage.

A criterion with a theoretical basis applies the Wallis stability criterion. In this approach the fluidized bed is seen as a set of elastic springs that continuously distribute and equalize disturbances. The velocity of these elastic waves through the fluidized bed is compared with the velocity of a disturbance in the bed voidage. If the elastic wave velocity is lower than the voidage propagation velocity, the disturbance can not be leveled throughout the fluidized bed and the disturbance remains or increases, so that bubble formation occurs.

The elastic wave velocity is given by (Foscolo and Gibilaro, 1984):

$$u_e = \left(\frac{3.2 g d_p (1-\varepsilon)(\rho_p - \rho_{is})}{\rho_p} \right)^{0.5} \tag{5.2}$$

The bed voidage propagation velocity is determined with (Jamialahmadi, 1996):

$$u_\varepsilon = (1-\varepsilon)\frac{du}{d\varepsilon} \tag{5.3}$$

in which the derivative is evaluated from Figure 5.2. The linear correlation of Figure 5.2 is the Richardson-Zaki correlation (Richardson and Zaki, 1954), which is discussed in the next sections. With the two velocities a dimensionless criterion is determined, the scale of aggregation, F_u (Jamialahmadi, 1996):

$$F_u = \frac{u_e - u_\varepsilon}{u_e} \tag{5.4}$$

Aggregative fluidization occurs if F_u is negative and particulate if positive. It should be noted that this criterion does not have a transition zone. The transition is however not necessarily sharp.

The distinction between particulate and aggregative fluidization through visual observation in liquid/solid fluidized beds can be difficult. Aggregative flow behavior does not necessarily occur as large bubbles, inhomogeneities may be present in the form of small local differences in the bed voidage, which are referred to as ‘parvoids’. For the case of ice slurry formation in the fluidized bed, these inhomogeneities do not prevent a stable ice slurry generation process. Aggregative fluidization behavior may even result in higher heat transfer coefficients and an extended operating range of the fluidized beds (Jamialahmadi, 1996).
Liquid/solid fluidization is generally fairly homogeneous: The solid particles level of a fluidized bed is usually very steady (di Felice, 1995). Also aggregative fluidization in liquid/solid fluidization appears smooth and under most conditions no large slugging or bubbling phenomena occur. A method similar to that of Richardson Zaki can be applied to predict the bed voidage and superficial fluidization velocity with reasonable accuracy (Jamialahmadi, 1996).

5.2.2 Prediction of Bed Voidage

For homogeneously expanding fluidized beds the logarithm of the bed superficial velocity is a straight line versus the bed voidage, as for case 1 of Figure 5.2. This is the well known Richardson-Zaki correlation, in which the settling velocity of a swarm of particles are related to the bed voidage and the unhindered settling velocity, or terminal velocity (Richardson and Zaki, 1954).

$$u_s = u_{\infty wall} \cdot \varepsilon^n \tag{5.5}$$

In Equation 5.5, n is the Richardson-Zaki coefficient and $u_{\infty wall}$ the terminal velocity corrected for the hindrance effect of the walls according to:

$$u_{\infty wall} = u_{\infty} \cdot 10^{\left(-\frac{dp}{D}\right)} \tag{5.6}$$

Both terminal velocity and the Richardson-Zaki coefficient *n* are determined by the size and shape of the solid particles and by the properties of the fluid. The terminal velocity is obtained from the equilibrium between drag and buoyancy forces for a particle falling in an infinite fluid:

$$V_p \cdot g \cdot \left(\rho_p - \rho_{is}\right) = C_{D\infty} \cdot A_p \cdot \frac{1}{2} \rho_{is} u_{\infty}^2 \tag{5.7}$$

In which $C_{D\infty}$ is the terminal drag coefficient on a particle. With the definition of the terminal Reynolds number:

$$Re_{\infty} = \frac{\rho_{is} u_{\infty} d_p}{\mu_{is}} \tag{5.8}$$

The force equilibrium of Equation 5.7 is rewritten for the case of spherical particles into:

$$Re_{\infty}^2 C_{D\infty} = \frac{4}{3} \frac{\rho_{is} \cdot d_p^3 \cdot g \cdot \left(\rho_p - \rho_{is}\right)}{\mu_{is}^2} \tag{5.9}$$

The drag coefficient is a function of the Reynolds number. If the appropriate correlation is known, it can be used with Equation 5.9 to solve for the terminal settling velocity. In literature several correlations have been reported for spherical particles, summarized by Clift et al. (1978).

If non-spherical particles are involved, Equation 5.9. is still applicable. The diameter of a sphere, d_p, should then be replaced by the equivalent diameter, d_{p_eq}, which is defined as the diameter of a sphere with the same volume as the particle.

For cylindrical particles, d_{p_eq} is obtained as follows:

$$d_{p\_eq} = \sqrt[3]{\frac{3}{2} \cdot d_{cyl}^2 \cdot h_{cyl}} = \sqrt[3]{\frac{3}{2} \cdot d_{cyl}^3} \tag{5.10}$$

where the simplification is valid if the cylinder height equals the cylinder diameter (equilateral cylinder).

Using the equivalent particle diameter also the particle sphericity, ψ, can be determined, which is a dimensionless shape factor that determines a particle's likeness to a sphere. It is defined as the ratio between the surface of the equivalent sphere and the surface of the actual particle:

$$\psi = \frac{\pi d_{p\_eq}^2}{\frac{1}{2} \pi d_{cyl}^2 + \pi d_{cyl} h_{cyl}} = \frac{d_{p\_eq}^2}{\frac{3}{2} d_{cyl}^2} \tag{5.11}$$

For the equilateral cylinders, such as the particles used in the present research, the sphericity is approximately 0.87.

Correlations between the drag coefficient and the terminal Reynolds number were summarized by Chhabra (1995) and Chhabra et al. (1999). One correlation of this summary makes use of the sphericity and was determined originally by Haider and Levenspiel:

$$C_{D\infty} = \frac{24}{Re_\infty}\left(1 + 8.1716 e^{-4.0655\psi} \cdot Re_\infty^{(0.0964+0.5565\psi)}\right) + \frac{73.69 \cdot e^{-5.0748\psi} Re_\infty}{5.378 \cdot e^{6.2122\psi} + Re_\infty} \tag{5.12}$$

Disadvantageous of the empirical Equation 5.12 is the large amount of coefficients. If the sphericity of an equilateral cylinder is filled into Equation 5.12, it reduces to:

$$C_{D\infty} = \frac{24}{Re_\infty}\left(1 + 0.2344 \cdot Re_\infty^{0.5825}\right) + \frac{0.8751 \cdot Re_\infty}{1223.1 + Re_\infty} \tag{5.13}$$

Once the terminal settling velocity is known, the hindered settling velocities of a fluidized bed can be obtained using Equations 5.5 and 5.6. For cylindrical particles of *h/d* ratios lower than 2, these equations predict the fluidization velocity fairly accurate.

5.2.3 Richardson-Zaki Coefficient

The coefficient *n* of Equation 5.5, the Richardson-Zaki coefficient, is required to predict the bed voidage and superficial velocity. This coefficient depends on the Reynolds number, according to:

$$\begin{aligned} &n = 4.65 && Re_\infty \le 0.2 \\ &n = 4.4 \cdot Re_\infty^{-0.03} && 0.2 < Re_\infty \le 1 \\ &n = 4.4 \cdot Re_\infty^{-0.1} && 1 < Re_\infty \le 500 \\ &n = 2.39 && 500 < Re_\infty \end{aligned} \tag{5.14}$$

These correlations were first determined by Richardson and Zaki (1954), who also observed a weak influence of the ratio particle diameter to bed diameter on the coefficient. This dependence was doubted by some authors (di Felice, 1995), but confirmed by others (Hirata and Bulos, 1990).

Several alternative correlations have been reported to calculate *n* continuously over the complete range of Reynolds numbers, for example by Rowe (1987):

$$n = \frac{2.35\left(2 + 0.175 \cdot Re_\infty^{0.75}\right)}{1 + 0.175 \cdot Re_\infty^{0.75}} \tag{5.15}$$

This correlation has been developed to predict the behavior of fluidized beds with spherical particles. A similar approach is applicable to calculate the fluidization conditions of non-spherical particles in liquid/solid fluidization (di Felice, 1995), where the superficial velocity plotted versus the bed voidage results in a straight line on a logarithmic scale. Several researchers have reported experiments with non-spherical particles, where the coefficients *n* observed were always higher than those found using Equations 5.14. No correlations are available in which the influence of shape factor or an equivalent diameter are reported over a wide range of conditions.

5.2.4 Experimental Determination of the Fluidization Behavior

In the experiments on ice slurry production in stationary fluidized beds a range of physical properties was encountered. An overview of typical properties is displayed in Table 5.1. Only the fluidization conditions of stable ice slurry generation experiments have been considered.

Table 5.1: Range of physical properties of experiments relevant for fluidization behavior

Property			*min*	*max*
Viscosity ice slurry	μ_{is}	mPa.s	1.70	4.51
Density ice slurry	ρ_{is}	kg/m^3	995	1082
Bed voidage	ε	-	0.76	0.88
Particle size	d_p	mm	2	4
Particle density	ρ_p	kg/m^3	7800	7800
Tube diameter	D	mm	43	55
Diameter ratio	$d_{p\ eq}/D$	-	0.054	0.107
Terminal settling velocity	u_∞	m/s	0.52	0.76
Terminal Reynolds number	Re_∞	-	534	1947
Min. fluidization velocity	u_{mf}	m/s	0.051	0.080
Fluidization velocity	u_s	m/s	0.23	0.46

The minimum fluidization velocity given in Table 5.1 was calculated with the Richardson-Zaki model for cylindrical particles, described in section 5.2.3, with a coefficient of n=2.39. The bed voidage at the onset of fluidization was assumed to be equal to the packed bed voidage, 0.43 for 4 mm particles. This value was experimentally determined using the transparent downcomer tube of the test set-up. For smaller particles the onset of fluidization occurs at lower bed voidages. For 2 mm particles a minimum fluidized bed voidage of 0.40 was determined and for 3 mm a value of 0.415 was interpolated. No bed expansion experiments have been carried out to determine the minimum bed voidage.

The minimum fluidization velocity can be calculated by setting the pressure drop of flow through the packed bed equal to the static pressure drop of the fluidized bed. At this point the drag force of the fluid on the particles is just high enough to keep the fluid bed buoyant. The pressure drop through a packed bed can be estimated with an Equation of the following form, proposed by Ergun (Foumeny et al., 1996):

$$\frac{\Delta p {d_p}^2 \varepsilon^3}{L \mu u_s (1-\varepsilon)^2} = c_1 \cdot \frac{\rho_l u_s d_p}{\mu (1-\varepsilon)} + c_2 \qquad (5.16)$$

Where c_1=1.75 and c_2=150 have been originally suggested for spherical particles. A range of values has been proposed for the parameters c_1 and c_2 by several authors, often valid for a limited range of operating conditions or particle shapes only. The following estimates have been determined by Foumeny et al. (1996) for cylinders of 3 mm and larger and may therefore be useful for the particles evaluated in the current study:

$$\begin{aligned} c_1 &= 3.81 - \frac{5.265}{D/d_p} - \frac{7.047}{(D/d_p)^2} \\ c_2 &= 211.0 \end{aligned} \qquad (5.17)$$

A comparison of the minimum fluidization velocities predicted by the two models with the Richardson-Zaki model indicates that the Ergun model is valid if n=2.39, i.e. for spherical particles. The Foumeny model is more accurate for cylindrical particles where the coefficient n tends to be higher, e.g. 2.80. It should be noted that both Richardson-Zaki evaluations of Table 5.2 include the sphericity factor and are therefore only valid for cylindrical particles.

A method similar to Equation 5.16 is valid, but the coefficients need to be determined accurately for the particle size and shapes and also for the viscosity range involved in ice slurry generation.

Table 5.2: Prediction of minimum fluidization velocity with Equation 5.16 (Ergun) or Equation 5.17 (Foumeny). Conditions: D=55 mm; ρ_{is}= 1039 kg/m^3; μ_{is}=3.1 mPa.s

Particle size	mm	2	3	4
Min. bed voidage	-	0.40	0.415	0.43
Min. fluidization velocity Ergun	m/s	0.040	0.067	0.091
Min. fluidization velocity Foumeny	m/s	0.028[a]	0.047	0.065
Fluidization velocity Richardson-Zaki (n=2.39)	m/s	0.052	0.068	0.080
Fluidization velocity Richardson-Zaki (n=2.80)	m/s	0.036	0.047	0.056

[a] Extrapolated to smaller particle diameter.

The type of fluidization encountered during ice slurry generation can be evaluated using the data of Table 5.1 and Equations 5.1. The Froude number at minimum fluidization velocity is in the intermediate range or in the particulate range: From 0.11 up to 0.17, while the limit for particulate fluidization is at 0.13. The lowest values are found for the 2 mm particles.

Equation 5.4 was also used to evaluate the fluidization behavior of the experiments. The state of aggregation F_u was negative for all experiments. F_u varied from –0.4 to –0.7. This indicates aggregative fluidization conditions in all experiments. Values of F_u are however relatively close to 0 and the fluidization can also be considered as in the transition zone.

Through the transparent section inserted in the fluidized bed of 43 mm internal diameter, irregularities in the fluidization behavior could be observed occasionally. This occurred as small variations in the bed voidage. Also minor fluctuations of the fluidized bed height, in the order of magnitude of a few cm, could be seen in some experiments. No bubbles of fluid or slugging behavior was however seen in any of the stable ice generation experiments. In the fluidized bed set-up of 55 mm internal diameter there was a transparent section on top of the system, where on some occasions irregularities could be observed, but also no bubbling behavior was detected.

The transition from particulate to aggregative fluidization is predicted with Equation 5.4 at a bed voidage of ε=0.36 for 4 mm particles in the 55 mm fluidized bed. At a bed voidage of ε=0.96, the fluidization becomes particulate again. This is calculated at an ice slurry density of ρ=1039 kg/m^3 and a viscosity of μ=3.1 mPa.s.

Fluidization during ice slurry generation is mainly in the aggregative or intermediate fluidization mode. Because no severe bubbling or slugging phenomena occur, the fluidization behavior is however not obstructing the ice slurry generation. Aggregative flow behavior may increase heat transfer rates and the operating range, because clusters of particles result in higher degrees of liquid mixing and have more impact on the heat exchanger walls. A cluster of particles moving together in the same direction has a higher kinetic energy and may therefore have more impact at the walls.

The terminal Reynolds number remained above 500 in all experiments, as given in Table 5.1. Fluidization conditions were turbulent and the Richardson-Zaki coefficient of 2.39 should be valid if spherical particles were involved.

Most of the experiments of the previous Chapters were done at a constant bed voidage of 0.79. Additional experiments were carried out at different bed voidages, mainly with NaCl as freezing point depressant and some with ethylene glycol. Dextrose was evaluated at a single bed voidage only.

The logarithms of the fluidization velocities determined in the experiments are displayed versus the logarithmic values of the bed voidage in Figure 5.3. In Figure 5.3 only the experiments at stable ice slurry generation conditions are included at a constant *dp/D*-ratio of 0.08. Two experiments are included where ice slurry generation was not stable, at bed voidages below 0.75.

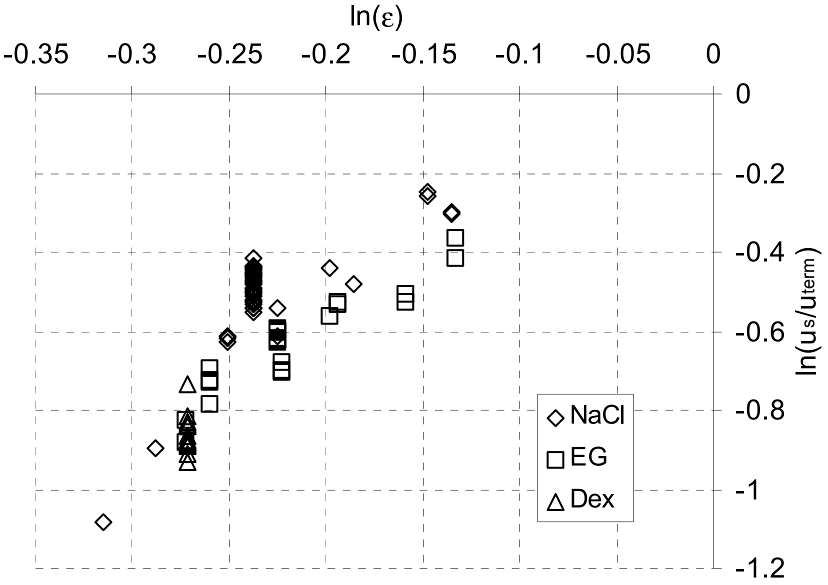

Figure 5.3: Superficial fluidization velocity versus bed voidage (logarithmic values)

Linear correlations through the origin were fit to the data of Figure 5.3 for all data and for NaCl and ethylene glycol separately. An overview of the coefficients found is given in Table 5.3.

As the data collected in Figure 5.3 appear to be similar to the bubbling behavior depicted by trend line no. 4 of Figure 5.2, i.e. a slightly concave trend, it was also attempted to fit a second order polynomial.

Table 5.3: Results of fits for Richardson-Zaki coefficient n

Data	n		R^2
Linear: $\ln(u_s/u_\infty)=n\cdot\ln(\varepsilon)$			
all	2.57		0.58
NaCl	2.25		0.59
EG	2.85		0.89
2^{nd} Order: $\ln(u_s/u_\infty)=n_1\cdot\ln^2(\varepsilon)+n_2\cdot\ln(\varepsilon)$			
all	n_1=-7.59	n_2=0.78	0.69

The values for the coefficients *n* obtained are slightly above the Richardson-Zaki coefficient for turbulent conditions of *n*=2.39 valid for spherical particles. This is in agreement with the trend for the coefficient to be generally higher if the solid particles are other than spherical. Only for the NaCl data a slightly lower coefficient is found. The accuracy of the NaCl experiments is however lower than for EG, because during the NaCl-experiments the ice slurry properties varied more widely.

The second order correlation fit to all data yields a higher accuracy than the linear correlation fit to all data. The accuracy is however less than the fit with only the ethylene glycol data. The value of a non-linear correlation to account for possible aggregative behavior of the fluidized bed is therefore doubtful. Accuracy of the coefficient *n* can be improved with experiments over a wider range of bed voidages at constant ice slurry properties. The coefficient of Richardson-Zaki of 2.39 is very similar to the experimental results and is therefore also useful for estimations, as well as the coefficient determined by Rowe.

The Richardson-Zaki coefficient of 2.57 applied to the experimental data results in a relatively accurate prediction of the superficial velocity for NaCl or ethylene glycol as the freezing point depressant, while the results are less accurate for dextrose. An overview is given in Table 5.4. Also if a value of 2.39 is applied, the dextrose data are predicted poorly while the NaCl data are predicted more accurately than with the value of 2.57. A possible explanation is that the cylindrical shape of the particles is more influenced by an increased viscosity than predicted with the Richardson-Zaki model.

Table 5.4: Absolute average relative error in prediction of the superficial fluidization velocity with the Richardson-Zaki model

n	*2.39*	*2.57*
NaCl	6.6%	8.9%
EG	10.5%	6.2%
Dex	24.0%	18.1%
All data	10.0%	9.6%

5.2.5 Heat Transfer Model Validation

In Chapter 3 a model was developed to predict wall-to-bed heat transfer coefficients for ice slurry generation in a stationary fluidized bed heat exchanger, similar to a model proposed by Haid (1997).

$$Nu_h = c_1 Re_h^{c_2} Pr^{c_3} \tag{5.18}$$

The parameters c_1=0.0612, c_2=0.724 and c_3=0.625 correlated the available data accurately.

During the determination of the maximum temperature differences allowable before freeze-up, described in Chapter 4, also heat transfer coefficients were calculated. Additional experiments were conducted with sodium chloride and ethylene glycol as the freezing point depressant and also heat transfer coefficients were determined for dextrose as the freezing point depressant. A few experiments were also performed with different particle diameters and different particle to bed diameter (*d_p/D*).

The heat transfer coefficients predicted with Equation 5.18 including the extra experiments are displayed versus the measured heat transfer coefficients in Figure 5.4. The +20% and -20% error margins are also given. It should be noted that the additional data were not used to obtain a new fit of the coefficients of Equation 5.18, the same constants as determined in Chapter 3 were again used to obtain Figure 5.4.

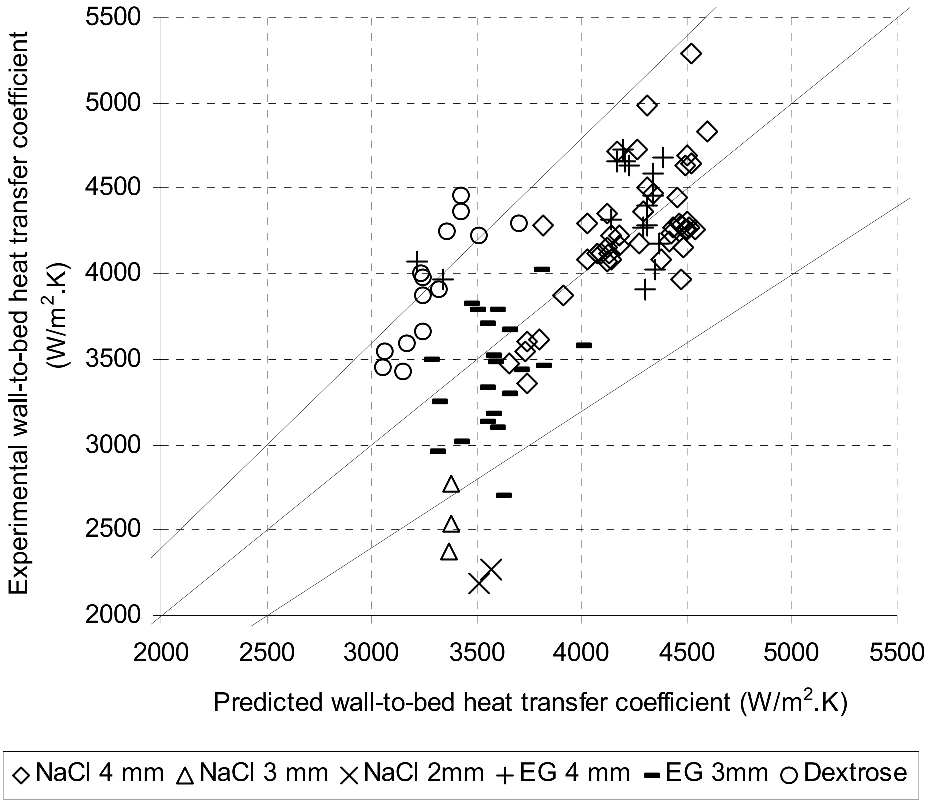

Figure 5.4: Heat transfer coefficients as predicted with Equation 5.19 and experimental results, with 20% margins

The measured heat transfer coefficients for dextrose, marked with ‘o’, appear to be slightly above the model predictions. Most measurements are however within the 20% error range. The model can therefore be used for heat transfer estimations with dextrose as freezing point depressant.

Heat transfer coefficients appear to be similar for dextrose, for NaCl (marked with diamonds ‘◊’) and for ethylene glycol (‘+’). The relatively high viscosity of dextrose based ice slurries, causes a lower Reynolds number both directly and indirectly, through a reduced superficial fluidization velocity, but also the Prandtl number increases. In the experiments with EG and NaCl a higher maximum heat transfer coefficient was observed, but for dextrose a smaller range of experiments was performed.

5.2.6 Particle Diameter

It is observed from Figure 5.4 that the heat transfer coefficients for smaller particles of 2 mm and 3 mm are lower than for 4 mm particles. The experiments with 3 mm particles were carried out in the smaller tube of 43 mm, so that the d_p/D-ratio was similar to the 4 mm particle experiments. A few experiments were carried out at both higher and lower d_p/D-ratios (2 mm particles in 43 mm tube and 4 mm particles in the 43 mm tube). For the lower ratio heat transfer coefficients are lower than predicted with the model, but this may be caused by the smaller particles of these experiments (2 mm). Results of an increased d_p/D-ratio, determined with 4 mm particles, are in accordance with the model predictions. It is concluded that for smaller particles the wall-to-bed heat transfer coefficients are lower. The d_p/D-ratio may also be of influence, but such effects were not confirmed in the experiments.
In the model presented by Jamialahmadi *et al.* (1996), which is an extended model of the form of Equation 5.18, heat transfer coefficients vary with the d_p/D-ratio to the power of 0.17:

$$Nu_p = c_1 Re_p^{\;c_2} Pr^{c_3} (1-\varepsilon)^{c_4} \varepsilon^{c_5} \left(\frac{d_p}{D}\right)^{c_6} \left(\frac{\rho_p - \rho_l}{\rho_l}\right)^{c_7} \tag{5.19}$$

The parameters of Equation 5.19 as determined by Jamialahmadi et al. (1996) are: c_1=0.1493, c_2=0.72, c_3=0.52, c_4=0.19, c_5=-1.41, c_6=0.17, c_7=0.03. In the current study not enough variation was applied in the experiments to be able to fit the coefficients c_6 and c_7 for the specific case of ice slurry generation. The coefficients c_4 and c_5 are embedded in the hydraulic Reynolds and Nusselt numbers. The particle diameter is also present in the Reynolds and Nusselt numbers and therefore a separate fit of the coefficient c_6 is not possible. Additional experiments with other particles sizes are required to confirm the influence of the particle size and the d_p/D-ratio.

Apart from the influence of the particle size on heat transfer coefficients, there is also a practical upper limit for the particle size, which is related to the tube size and is therefore a limit on the d_p/D-ratio. If the solid particles are too large, blocking of the bed by the particles will become likely. In the experiments of Richardson and Zaki (1954) an upper limit of approximately 0.11 was observed for fluidized beds of spherical solid particles. At higher d_p/D-ratios the fluidization results did not correspond well with the correlations proposed because the solid particles were observed to form horizontal layers or bridges from wall to wall. It should be noted that at higher bed voidages (ε>0.83) such effects reduced, so that higher d_p/D-ratios may be possible without blockages occurring. As a practical guideline the following limit is assumed, that prevents blockages at all bed voidages:

$$\frac{d_p}{D} \leq 0.11 \tag{5.20}$$

The d_p/D-ratios in this research satisfied this condition, the maximum d_p/D-ratio was 0.107, calculated with the equivalent particle diameter, d_{p_eq}. Lower d_p/D-ratios could still be obtained in the current research set-up but are of limited practical interest as heat transfer coefficients reduce for smaller particles and also freeze-up becomes more likely. In the experimental set-up still larger solid particles may be applied, up to 6 mm diameter. A downside is that these larger stainless steel particles are more difficult to produce. The particles are produced by chopping stainless steel wire: At a wire thickness of 4 mm and higher, the chopping knives wear out rapidly and many particles will not be fully cut, but already break halfway, leading to irregularities in the shape of the particles. Also unsuccessful cuts occur, so that a fraction of the particles are 8 mm long instead of 4 mm.

The particle size and d_p/D-ratio may also influence the fluidization behavior. In the current study it was assumed that the fluidization is uneven or aggregative, based on the criterion of Equation 5.4. Using Equation 5.1 the fluidization behavior could also be in the transition range to particulate fluidization. It is unknown if particulate fluidization is equally successful in the prevention of fluidized bed freeze-up. Limits on the particle size and d_p/D-ratio should be evaluated if tube diameters are reduced further or if particles larger than 4 mm are applied in ice slurry generation.

5.2.7 Further Evaluation of Freeze-up Conditions

In Chapter 4 the maximum driving force allowable before freeze-up was found to depend on three processes: Ice crystallization, ice adhesion and particle impacts. The first two processes are not influenced directly by the fluidization, the third however is. The fluidization conditions, such as particle and tube dimensions and fluid properties, determine the impact frequency and the impact velocities at the wall. The influence of the column diameter and the particle size is discussed theoretically here, extended with some experiments using smaller particles and a smaller fluidized bed.

The maximum force exerted by the particle impacts on the walls or on ice crystals adhered to the walls is estimated with the correlation developed by Ottjes (1981) for perpendicular impacts of spherical particles on solid walls.

$$F_{max} = 0.76 \cdot \left(\frac{\mathrm{E}}{1-\nu^2} \right)^{0.4} \cdot d_p^{\;2} \cdot \rho_p^{\;0.6} \cdot u_x^{\;1.2} \tag{5.21}$$

Larger and more dense particles yield a higher impact force at equal perpendicular velocity of the particles.

The mean impact frequency of spherical particles on the wall of a tube is given by (Meijer et al., 1986):

$$\bar{f} = \frac{6 \cdot \bar{u}_x \cdot (1-\varepsilon)}{4 \cdot \pi \cdot d_p^{\;3}} \tag{5.22}$$

Larger particles yield a lower impact frequency, at equal perpendicular velocity of the particles.

Comparing Equations 5.21 with 5.22, it may appear that larger particles will have a negative effect on the operating range as the force increases with a power of 2 to the particle diameter, while the frequency decreases by the power of 3. In the perpendicular particle velocity however also the particle size is of influence. The perpendicular velocity can for example be related to the superficial fluidization velocity using one of two methods, discussed in Chapter 4. Bordet et al. (1972) introduced:

$$\bar{E}_t = 2 \cdot \bar{E}_x = m \cdot \bar{u}_x^{\;2} = 9.13 \cdot 10^{-6} \cdot \left(\rho_p - \rho_l \right)^{0.38} \left(\frac{u_s \cdot d_p}{\varepsilon} \right)^{0.66} \cdot \mu_l^{\;0.28} \tag{5.23}$$

Meijer et al. (1986) proposed a method valid for a bed voidage of 0.80:

$$\overline{u}_x = 0.10 \cdot u_s \tag{5.24}$$

If Equation 5.24 is substituted into Equation 5.22 and the superficial velocity is estimated with the method of Richardson-Zaki, the impact frequency becomes:

$$\overline{f} = \frac{0.6 \cdot u_\infty \cdot \varepsilon^n \cdot 10^{\left(-\frac{d_p}{D}\right)}(1-\varepsilon)}{4 \cdot \pi \cdot d_p^{\,3}} \tag{5.25}$$

If conditions are turbulent, the drag coefficient on a particle can be assumed constant. Equation 5.9 can then be used to calculate the terminal velocity as a function of the particle size:

$$u_\infty = K \cdot d_p^{\frac{1}{2}} \tag{5.26}$$

Where K is a function including all parameters that do not depend on the particle size.
The particle impact frequency is then given by:

$$\overline{f} = \frac{0.6 \cdot K \cdot d_p^{\frac{1}{2}} \cdot \varepsilon^n \cdot 10^{\left(-\frac{d_p}{D}\right)}(1-\varepsilon)}{4 \cdot \pi \cdot d_p^{\,3}} \tag{5.27}$$

Assuming a constant d_p/D-ratio, it is seen that the wall impact frequency is influenced by the particle diameter to the power of –2.5. The d_p/D-ratio is also a strong parameter for the wall impact frequency: High ratios, i.e. large particles in small beds, yield low impact frequencies.
Following a similar approach, the dependence of the maximum impact force on the particle diameter and bed diameter is found:

$$F_{max} = 0.76 \cdot \left(\frac{\mathrm{E}}{1-\nu^2}\right)^{0.4} \cdot d_p^{\,2} \cdot \rho_p^{\,0.6} \cdot \left(0.1 \cdot K \cdot d_p^{\frac{1}{2}} \cdot \varepsilon^n \cdot 10^{\left(-\frac{d_p}{D}\right)}\right)^{1.2} \tag{5.28}$$

At a constant d_p/D-ratio, the particle size influences the maximum impact force to the power of 2.6. Larger particles should therefore yield a small positive effect on the ice removal capacity, as the force exerted upon impact increases more than the amount of impacts is reduced.
The d_p/D-ratio reduces the impact force: Higher ratios reduce the impact force as well as the impact frequency.

It is unknown at what area on the wall the particle exerts its force upon impact. In Chapter 4 also the kinetic energy of a single particle has been evaluated. The Richardson-Zaki model is inserted in the kinetic energy correlation of Equation 5.23:

$$\bar{E}_x = \frac{1}{2} m \cdot \bar{u}_x^{\,2} = 4.57 \cdot 10^{-6} \cdot \left(\rho_p - \rho_l\right)^{0.38} \left(\frac{u_\infty \varepsilon^n 10^{\left(-\frac{dp}{D}\right)} \cdot d_p}{\varepsilon} \right)^{0.66} \cdot \mu_l^{\,0.28} \tag{5.29}$$

Substitution of the terminal velocity, calculated with Equation 5.9 for turbulent conditions, into Equation 5.29 yields:

$$\bar{E}_x = 5.02 \cdot 10^{-6} \left(\rho_p - \rho_l\right)^{0.71} \left(\frac{g}{C_{D\infty} \rho_l} \right)^{0.33} \varepsilon^{0.66(n-1)} 10^{\left(-0.66\frac{dp}{D}\right)} d_p^{\,0.99} \mu_l^{\,0.28} \tag{5.30}$$

An increase of particle size benefits the kinetic energy almost linearly, to the power of 0.99. If the impact area of the particle at the heat exchanger wall depends on the square of the particle diameter, this would imply a decrease of the ice removal capacity at increased particle diameter. It is however uncertain what area is affected by a single particle impact, as a particle may also contact at an angle.

Under turbulent conditions an increased viscosity yields an increased kinetic energy of the particles according to Equation 5.30. At increased viscosity the particles may be dragged along more readily and thereby gain a higher kinetic energy. Doubts about the applicability of the empirical model were already discussed by Meijer (1986). The validity of the coefficients of the various parameters should be further confirmed.

It should be noted that Equation 5.22 does not yield the amount of impacts above the minimum impact force required for ice removal. To accurately determine the effects of particle size therefore the exponential distribution of the particle impact velocities should be included in the evaluation, together with a limit above which an impact is considered successful. An analytical evaluation then becomes complex and a numerical evaluation is more practical.

Fluidization parameters for a number of fluidized beds were determined assuming ethylene glycol ice slurry at initial freezing temperature of –2.9 °C. An overview of the predictions of the particle impacts for varying particle and column diameters is given in Table 5.5, assuming a bed voidage of 0.80 and a Richardson-Zaki coefficient of 2.57. The limiting value of 100 mJ/m^2 for the work of a particle impact at the wall, was chosen based on the data reported in Chapter 4. It corresponds in order of magnitude with the work of adhesion of ice, W_A.

Table 5.5: Predicted influence of fluidization parameters particle size and bed diameter on particle impacts. Ethylene glycol at Tfreeze_init of –2.9 °C, bed voidage ε=0.80

Case		*1*	*2*	*3*	*4*	*5*
dp	mm	4	2	3	4	5
D	mm	55	43	43	43	43
d_p/D	-	0.073	0.047	0.070	0.094	0.117
u_S (RZ)	m/s	0.34	0.26	0.30	0.32	0.33
u_x (Eq. 5.24)	m/s	0.034	0.026	0.030	0.032	0.033
E_x (Eq 5.30)	J/part	$2.1\cdot10^{-7}$	$0.17\cdot10^{-7}$	$0.75\cdot10^{-7}$	$2.0\cdot10^{-7}$	$4.2\cdot10^{-7}$
F_{max}	N	0.83	0.49	0.67	0.81	0.94
Impact frequency	1/m^{2}s	$33.7\cdot10^3$	$208.6\cdot10^3$	$71.1\cdot10^3$	$31.9\cdot10^3$	$16.9\cdot10^3$
no. impacts above W_A=100 mJ/m^2	1/m^{2}s	5430	462	3263	4167	3651

From Table 5.5 it is seen that there is an optimum for the particle diameter in a fluidized bed. If the *dp/D*-ratio becomes too large the number of successful impacts reduces again. It is also observed from Table 5.5 that the larger particles at equal d_p/D-ratio yield more successful impacts: Compare cases 1 and 3. Also if the tube diameters are slightly adjusted so that the *dp/D*-ratios are exactly equal, the larger particles yield a much larger amount of successful impacts.

The experiments of Chapter 4 were performed with 4 mm particles in a 55 mm fluidized bed. Additional experiments to determine the maximum driving force allowable were carried out with ethylene glycol, at a similar d_p/D-ratio with 3 mm particles in a 43 mm fluidized bed. Also an experiment was done with 2 mm particles in the 43 mm fluidized bed. For these conditions however the limit before freeze-up was not determined.

Additional experiments were also carried out with 6.5% NaCl. At this concentration the limit before freeze-up was determined with 2 mm and 3 mm particles in the 43 mm fluidized bed.

Results of the additional ethylene glycol experiments are displayed in Figure 5.5, together with the limit determined for ethylene glycol in the experiments of Chapter 4.

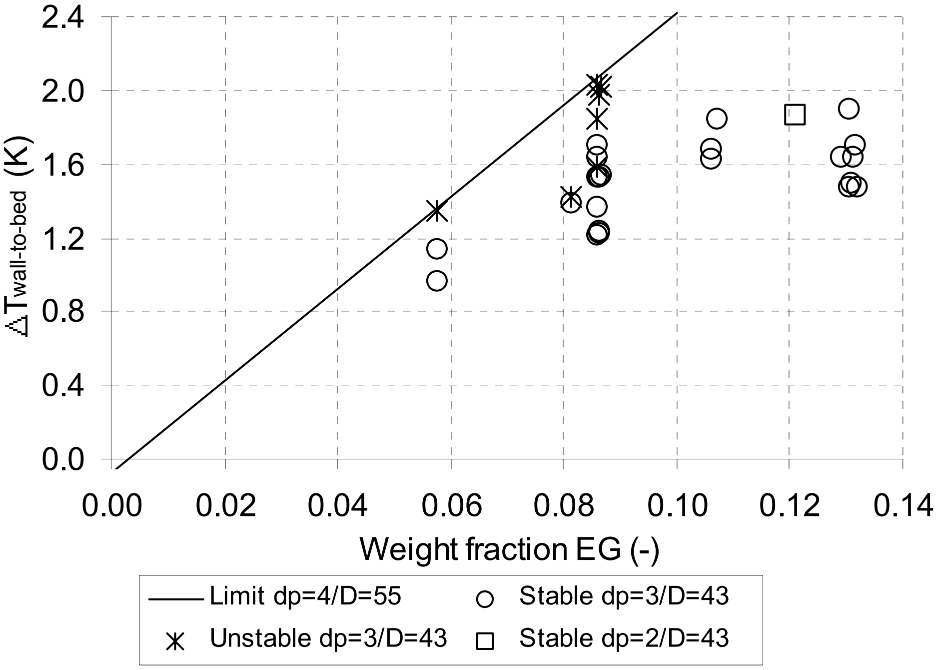

Figure 5.5: Wall-to-bed temperature difference for experiments with ethylene glycol in 43 mm fluidized bed; comparison with limit of 55 mm fluidized bed.

The limit before freeze-up using 3 mm particles is at a lower wall-to-bed temperature difference than for 4 mm particles at a similar d_p/D-ratio. This result is in agreement with the number of particle/wall impacts predicted in Table 5.5, where more impacts at high kinetic energy are predicted for case 1 than for case 3. The one experiment at the conditions of case 2 did not result in freeze-up of the fluidized bed. According to the result of Table 5.5 however, there are only limited successful particle impacts. Stable ice slurry production was possible and it is therefore likely that the limit of W_A=100 mJ/m^2 is overestimated.

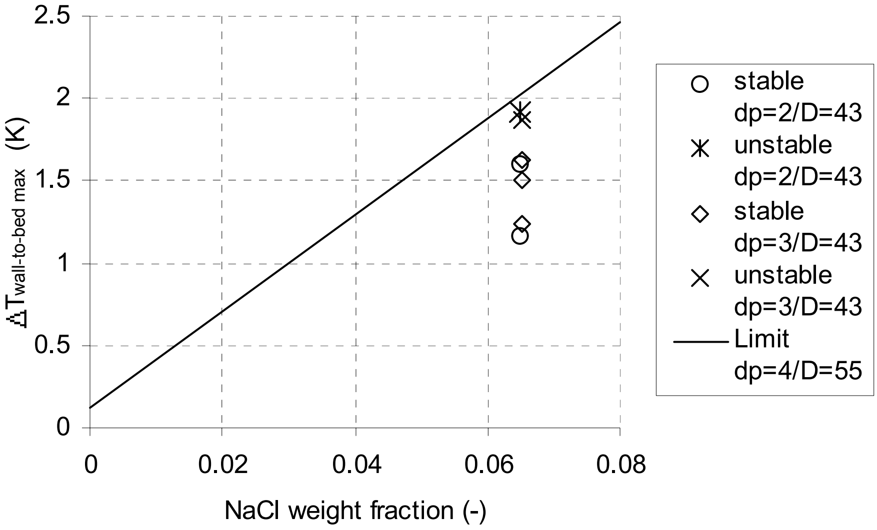

Figure 5.6: Wall-to-bed temperature difference for experiments with NaCl in 43 mm fluidized bed; comparison with limit of 55 mm fluidized bed

The additional experiments with NaCl were done under similar conditions as cases 2 and 3 of Table 5.5. Results are given in Figure 5.6, together with the limit determined in Chapter 4 for conditions similar to case 1. It is seen that for both cases the limit observed is lower than that for the 4 mm particles in the 55 mm fluidized bed, which is in agreement with the theoretical predictions of Table 5.5.
The limit of the work of ice adhesion is not exactly known, the quantitative results of Table 5.5 can therefore not be confirmed yet. In future experiments *dp/D*-ratios similar to cases 4 and 5 should be evaluated to determine if the optimum is indeed found. Furthermore the limiting W_A should be determined accurately.

5.2.8 Optimum Bed Voidage

Using the Richardson-Zaki coefficient determined in section 5.2.4, an optimum bed voidage can be determined for heat transfer. For this purpose the derivative of Equation 5.18 with respect to the bed voidage is evaluated.

$$Nu_p \frac{\varepsilon}{1-\varepsilon} = c_1 \left(\frac{Re_p}{1-\varepsilon} \right)^{c_2} Pr^{c_3} = c_1 \left(\frac{K_1 \varepsilon^n}{1-\varepsilon} \right)^{c_2} Pr^{c_3} \qquad (5.31)$$

In which K_1 includes the parameters of the Reynolds number that do not depend on the bed voidage. Rewriting Equation 5.31:

$$Nu_p = c_1 K_1^{c_2} Pr^{c_3} \varepsilon^{nc_2-1} (1-\varepsilon)^{1-c_2} = K_2 \varepsilon^{nc_2-1} (1-\varepsilon)^{1-c_2} \qquad (5.32)$$

The derivative:

$$\frac{dNu_p}{d\varepsilon} = K_2 \left((nc_2 - 1) \frac{1-\varepsilon}{\varepsilon} - (1-c_2) \right) \varepsilon^{nc_2-1} (1-\varepsilon)^{-c_2} \qquad (5.33)$$

Setting Equation 5.33 equal to 0 leads to the expression for the optimum bed voidage:

$$\varepsilon_{opt} = \frac{nc_2 - 1}{c_2(n-1)} \tag{5.34}$$

With the heat transfer model determined in Chapter 3, c_2=0.724, and the Richardson-Zaki coefficient of 2.57 determined in 5.2.4, the optimum bed voidage predicted with Equation 5.34 is ε=0.76. For spherical particles, n=2.39, and the model of Haid (1997), c_2=0.75, the optimum is very similar, also ε=0.76.

A similar evaluation is done for the impact frequency. The derivative with respect to bed voidage of Equation 5.27 is set equal to 0. This leads to the following result:

$$\varepsilon_{opt} = \frac{n}{n+1} \tag{5.35}$$

which yields the maximum particle impact frequency at a bed voidage of 0.72 for the cylindrical particles of this research. For spherical particles the optimum is found at ε=0.71. Both the maximum impact force and the kinetic energy of the particles do not have an optimum bed voidage: both are higher if the bed voidage is higher. This may explain that the optimum bed voidage for heat transfer is higher than the bed voidage of maximum impact frequency.

5.2.9 Conclusion

Stationary fluidization during ice slurry generation is aggregative or has an intermediate fluidization behavior. Because no large inhomogeneities as slugging or bubbling occur, this does not obstruct stable ice slurry generation and may even improve heat transfer.

The fluidization theory of Richardson and Zaki, modified by Chhabra (1995) for cylindrical particles, predicts the superficial velocity well. Discrepancies are found using dextrose, which is probably caused by the significantly higher viscosity.

A Richardson-Zaki coefficient n for turbulent conditions of 2.57 was determined, which is in agreement with reports of other researchers for cylindrical particles. Using this value an optimum bed voidage for heat transfer of 0.76 is predicted, which is close to the conditions of most experiments of the research.

Results of additional experiments for both heat transfer and maximum driving force are in accordance with the theory developed in the Chapters 3 and 4 respectively.

The particle diameter has a large influence on the heat transfer and the maximum driving force. Large particles are efficient, as well as high d_p/D-ratios. At too high d_p/D-ratios however the maximum driving force is expected to decrease. A method has been presented that allows for identification of the optimum d_p/D-ratio and bed diameter, based on an analysis of effective particle-wall impacts.

5.3 Circulating Fluidized Bed

5.3.1 Introduction

The stationary mode of the fluidized bed ice slurry generator has been investigated in section 5.2. In most fluidized bed heat exchangers applied in process industry, the circulating operating mode is used. The solid particles of the fluidized bed do not remain in the fluidized beds but are dragged out on top of the bed. After separation from the process flow, the solid particles are fed back into the fluidized bed at the bottom. In the downcomer duct the particles move as a packed bed, to prevent upward liquid flow through the downcomer. In Figure 5.7 a schematic lay-out of a circulating fluidized bed system with multiple parallel fluidized beds is given.

Circulation of the fluidized bed particles has a number of advantages which have resulted in wider industrial application of circulating fluidized beds than stationary systems. In a circulating fluidized bed system, the bed voidage is an independent variable that is not determined by the superficial fluid velocity. The superficial velocity can therefore be chosen and be set much higher during circulation mode. The liquid throughput is increased significantly and higher heat transfer coefficients may be achieved. The size of the heat exchanger can be smaller and investment costs are lower. Control of the amount of particles present in the fluidized bed and control of the fluidized bed height is also easier than during stationary operation. If there is an irregularity in the fluid flow, less solid particles will be transported through the bed, but the fluidized bed will still cover the entire heat exchanger area. Another advantage of circulation is that the solid particles can be removed from the system without shutdown of the heat exchanger operation.

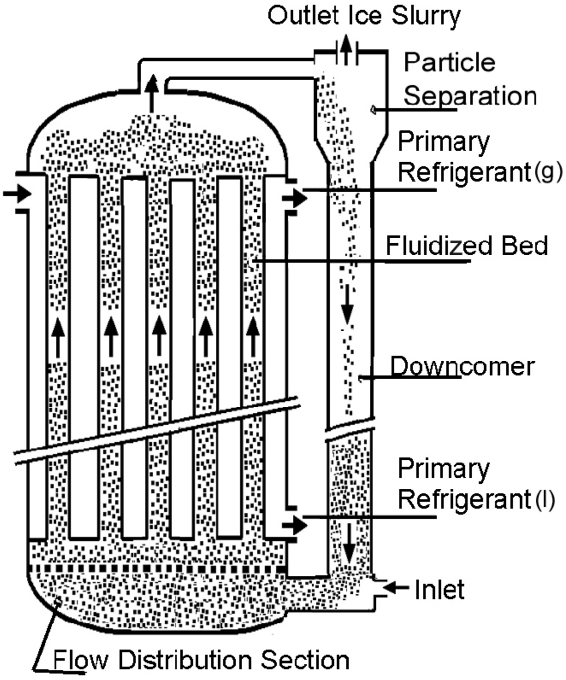

Figure 5.7: Schematic lay-out of a fluidized bed system with multiple parallel beds and external circulation

A disadvantage of the circulation mode is that more equipment is required than for a stationary bed. Also a higher pumping power input is required to provide the particle circulation. The higher pumping power input required may be a more significant disadvantage for ice slurry systems than for most industrial applications. Ice is melted as a result of the pumping power input, which reduces system efficiency in cooling applications.

5.3.2 Fluidization in Circulating Mode

In circulating fluidized beds the particles move through the fluidized bed and have a net upwards velocity. This velocity can be determined from the particle circulation rate.

$$v_p = \frac{\dot{m}_p}{\left(1-\varepsilon\right)\rho_p A} \tag{5.36}$$

The bed voidage of a circulating bed is determined by the particle velocity and the fluid velocity. The difference between these two is the slip velocity defined as:

$$u_{slip} = v_f - v_p = \frac{u_s}{\varepsilon} - v_p \tag{5.37}$$

For stationary beds the slip velocity is the actual fluid velocity relative to the tube wall. The method of Richardson-Zaki is assumed to be valid to predict the bed voidage. A circulating fluidized bed is then in fact considered as a moving stationary bed.

$$u_{slip} = u_{wall\infty} \cdot \varepsilon^{n-1} \tag{5.38}$$

in which $u_{w\infty}$ is the terminal settling velocity determined with the method of Chhabra et al., (1999), similar to the stationary bed calculations. The terminal settling velocity is also corrected for the wall friction effect:

$$u_{wall\infty} = u_{\infty} \cdot 10^{-\frac{dp}{D}} \tag{5.39}$$

A small error is made in the correction for the wall friction, because the liquid velocity relative to the wall is larger than the slip velocity. Particle velocities are however mostly relatively low compared with the slip velocity. The calculation using Equation 5.38 is shown to be valid by Kopko et al. (1975) for circulating fluidized beds with 7.8 mm aluminum particles, 1.9 mm iron and 3.3 mm iron particles, fluidized with water.

The exponent n of Equation 5.38, the Richardson-Zaki exponent depends on the flow conditions and the type of particles used. For turbulent conditions, Re_p>500 and spherical particles n=2.39. For differently shaped particles n tends to be higher, in section 5.2 a higher exponent was determined: n=2.57 for cylindrical particles.
For decreasing Reynolds numbers n increases, up to 4.65 under laminar flow conditions. In the fluidized bed heat exchanger these conditions are not encountered, in the downcomer tube however laminar flow conditions do occur.

The solid particles are gathered in the downcomer tube in the form of a packed bed. Part of the fluid flowing into the fluidized bed is used to transport the particles from the bottom of this packed bed to the fluidized bed. With this side flow the amount of solid particles in the fluidized bed is controlled.
The particles in the downcomer are preferably in packed bed form to provide a resistance for fluid flow upwards through the downcomer. Such a fluid flow bypasses the fluidized bed and reduces heat transfer efficiency. Mechanical devices, for example valves, may also provide

flow resistance. These are however likely to fail because of solid particles that can get stuck or damage the devices. Furthermore, in many valves upward flow of the fluid is still possible.

The bed voidage of a circulating fluidized bed is calculated from the pressure drop per meter bed height:

$$\frac{\Delta p}{h} = \rho_l g + (1-\varepsilon)\left(\rho_p - \rho_l\right) g + F_l + F_p \tag{5.40}$$

In Equation 5.40 it is assumed that wall friction is the sum of the frictions of the fluid and of the solid particles. The liquid friction force is determined with the Blasius equation for the fluid friction factor:

$$f_l = \frac{0.0791}{Re^{0.25}} \tag{5.41}$$

and the friction force is given by:

$$F_l = \frac{2 f_l \varepsilon \rho_l v_l^{2}}{D} \tag{5.42}$$

The particle friction factor has been determined experimentally by Grbavčič et al. (1992):

$$f_p = \frac{7.33 \cdot 10^{-3}}{v_p^{2}} \tag{5.43}$$

and the friction force exerted by the particles is:

$$F_p = \frac{2 f_p (1-\varepsilon) \rho_p v_p^{2}}{D} \tag{5.44}$$

After substituting Equation 5.43 into Equation 5.44, it is seen that the friction force of the particles does not depend on the particle velocity according to this method.

The contributions of wall friction of particles and fluid are relatively small (Grbavčič et al. 1992) compared with the static pressure difference of particles and fluid, especially if the solid particles have a high density. The last two terms of Equation 5.40 can therefore often be ignored. For example in a bed fluidized with an ice slurry of 0.05 NaCl fraction and an ice fraction of 0.10, the wall friction is 1.9% of the total pressure drop for the stationary case. This is calculated assuming a bed voidage of 0.80, 4 mm cylindrical particles of stainless steel, ρ=7800 kg/m^3, in a bed of 0.055 m diameter. If the fluid velocity is doubled, so that the particles are circulated, the pressure drop increases and 2.4% of the pressure drop is caused by wall friction. The particle velocity for this case is 50% of the fluid velocity.

In the evaluation of the wall friction using Equation 5.44 the shape of the particles has not been considered. It is likely that cylindrical particles will have a larger particle friction coefficient, because they are more likely to slide along walls than spherical particles, where sliding is assumed to result in a larger friction than rolling or impacting of the particles.

The degree of radial distribution can be analyzed with the Peclet number (*Pe)*, defined as the ratio between convective transport of particles and transport in radial directions.

$$Pe = \frac{convective\ transport}{radial\ transport} \tag{5.45}$$

At Pe=0 the situation is completely mixed. This is the case for a stationary bed, where no particle transport occurs. At Pe=∞ there is plug flow of the particles through the bed. There are no other particle impacts than those sliding along the wall.
The radial transport is the result the varying drag forces exerted on the particles at different radial positions. In the experimental work of Liang et al. (1996), who worked with glass beads of 0.4 mm, an empirical radial distribution of the bed voidage was determined:

$$\varepsilon_r = \bar{\varepsilon}^{\left(0.75+0.40\left(\frac{r}{R}\right)^{0.90}\right)} \tag{5.46}$$

In which $\bar{\varepsilon}$ is the mean bed voidage over the radius of the fluidized bed. The radial profile is similar at varying particle circulation rates and liquid velocities. Drag coefficients under turbulent conditions can be assumed constant versus the liquid velocity, therefore also the particle slip velocities are constant for a given particle size and density. For other types of particle, slip velocities however differ. From Equation 5.9 it is seen that the terminal particle slip velocity increases for larger and denser particles under turbulent conditions with similar shaped particles:

$$u_\infty = \left(\frac{4}{3}\frac{d_p g\left(\rho_s - \rho_l\right)}{\rho_l C_D}\right)^{0.5} \tag{5.47}$$

As the terminal settling velocity is larger for larger particles, the fluid velocity required for a similar slip velocity is also larger. The fluid friction force at the wall is determined by the fluid velocity to the power of 1.75:

$$F_l = 2\left(\frac{0.0791}{Re^{0.25}}\right)\frac{\varepsilon \rho_l v_l^{\ 2}}{D} \tag{5.48}$$

Furthermore, the particle friction at the wall increases because of the increased particle density:

$$F_p = 2\left(\frac{7.33\cdot 10^{-3}}{v_p^{\ 2}}\right)\frac{(1-\varepsilon)\rho_p v_p^{\ 2}}{D} \tag{5.49}$$

The total wall friction increases for larger and denser solid particles. The difference in liquid velocities between bulk and near walls will therefore be larger, and a more uneven radial distribution than predicted with Equation 5.46 is expected. It was found by Zheng et al. (2002) that for heavier particles a more uneven particle distribution develops.

For example small glass beads, ρ=2460 kg/m^3 and 0.4 mm diameter, are compared with large stainless steel particles, ρ=7800 kg/m^3 and 4 mm diameter. A particle velocity of 0.1 m/s is assumed for both types of particle. The drag force working on the glass beads is then estimated to be 24 times larger than the wall friction forces for the glass beads. For the stainless steel particles the drag forces are estimated to be only 5.4 times larger than the wall friction forces. Wall friction is relatively more important for larger, denser particles. The radial distribution of the stainless steel particles is expected to be more uneven than predicted with Equation 5.46.

Studies in gas/solid fluidized beds showed no clear influence of the particle size and density. The relative influence of the wall friction for gas/solid fluidized beds is much smaller than in liquid/solid fluidized beds, therefore the particle properties will have negligible influence on the radial particle distribution.

The bed diameter is also of influence for the radial distribution: In the experiments of Liang et al. (1996), a bed diameter was used of 140 mm. The wall area to bed volume ratio is smaller than for a bed diameter of 55 mm, wall friction effects are expected to be relatively less important for the 140 mm than for the 55 mm circulating fluidized bed.

5.3.3 Heat transfer in Circulating Fluidized Beds

Heat transfer coefficients are not necessarily increased if circulation of the solid particles is applied. General trends are given in Figure 5.8, in which heat transfer coefficients are displayed versus the superficial liquid velocity of stationary and of circulating fluidized beds. Figure 5.8 is based on heat transfer experiments in circulating fluidized beds with particles larger than 1 mm, done by Richardson and Smith (1962), Kollbach (1987) and Rautenbach et al. (1991).

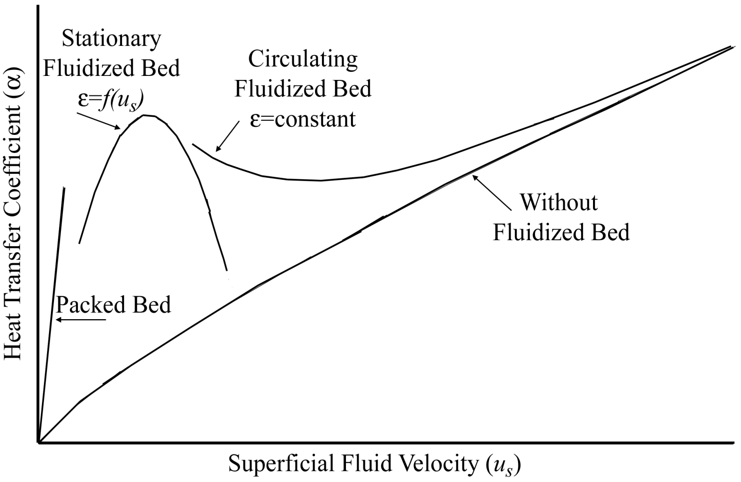

Figure 5.8: Trends of heat transfer coefficients at increasing fluid velocities for various fluidization modes (Erdmann, 1993; Haid et al. 1994)

Richardson and Smith observed a decrease in heat transfer for circulation compared with the stationary fluidized beds at the same bed voidage. Kollbach and Rautenbach also observed a decrease of heat transfer for circulation, but if the fluid velocity was further increased, higher heat transfer coefficients than for stationary fluidized beds were observed. The relative difference with heat transfer without particles decreases at increasing fluid velocity, until the heat transfer coefficients are almost equal to the single phase flow heat transfer coefficients.

The trend of the packed bed displayed in Figure 5.8 is based on results of Haid et al. (1994) who reported data for glass beads of 1.2 mm in packed beds and stationary fluidized beds.

The cause of the decreasing heat transfer coefficients at moderate fluid velocities may be an inhomogeneous radial distribution of the fluidized solid particles. It is likely that the solid particles are situated more near the walls of the fluidized bed than in the center if there is a net upwards particle transport. At increasing fluid velocity, necessary for particle transport, a velocity difference between wall and center develops, because of the friction of the fluid at

the walls. Fluid and also solid particles move faster in the center of the fluidized bed and solid particles are dragged out of the center of the fluidized bed.
Heat transfer coefficients increase at increasing fluid flow velocities and therefore still higher heat transfer coefficients are obtained than in stationary fluidized beds. The positive effects of the solid particles on heat transfer however reduce, until at a certain flow velocity particles may not impact on walls at all and heat transfer equals the non-fluidized bed case.

A model to predict wall-to-bed heat transfer coefficients for circulating fluidized bed systems was proposed by Erdmann (1993). The model is based on experiments with particles of 1.6-3.0 mm of the materials steel, glass, lead and ceramics. Fluid viscosities were in the range of 0.47-100 mPa·s. The heat transfer coefficient of a circulating fluidized bed consists of two parts: Heat transfer of a fluid flow without fluidized bed plus the heat transfer contribution of the fluidized bed particles. In the model of Erdmann the contribution of the particles of the circulating fluidized bed is correlated to the contribution of the particles in the stationary fluidized bed. The contribution exponentially decreases at increasing fluid velocities.

$$\alpha_{circ} = \alpha_{sp}(u_{circ}) + \left(\alpha_{stat}(u_{stat}) - \alpha_{sp}(u_{stat})\right)\exp\left(-0.0358 \cdot \left(\frac{u_{stat}}{u_{wall\infty}} - 1\right) Re_{p,\infty}^{0.185}\right) \tag{5.50}$$

Equation 5.50 predicted heat transfer coefficients for different particles with a maximum relative error below 20% for liquid viscosities of 0.47 and 10 mPa·s. Relative errors for liquid viscosities of 100 mPa·s were 28%.
Heat transfer coefficients of single phase flow is estimated with for example the Dittus-Boelter correlation, valid for turbulent flow conditions:

$$Nu_{sp} = \frac{\alpha_{sp} D}{\lambda} = 0.027 Re^{0.8} Pr^{0.33} \tag{5.51}$$

An increase of the fluid velocity in order to obtain higher heat transfer coefficients comes with a small increase of the pressure drop over the fluidized bed. The pump throughput also increases and therefore the pumping power input, which is estimated with:

$$P_{pump} = \frac{\Delta p \cdot \varphi_v}{\eta_{pump}} \tag{5.52}$$

in which η_{pump} is the efficiency of the pump expressed as a fraction; φ_v is the volumetric throughput. Part of the power consumption of the pump results in a heat input in the ice slurry, which melts part of the ice and thereby reduces the efficiency of the fluidized bed heat exchanger. This is contrary to fluidized bed systems where heating of process fluids is the objective, where the heat input of pumps does not reduce the heat exchanger's efficiency. An increase of the superficial velocity compared to the stationary fluidized bed case should therefore have a higher heat transfer coefficient to obtain an equal system efficiency. The heat transfer coefficient that compensates for the increased pumping power input is estimated with:

$$\alpha_{circ} = \alpha_{stat} + \frac{\left(P_{pump\_circ} - P_{pump\_stat}\right)\eta_{melt}}{A\Delta T_{wtb}} \tag{5.53}$$

It is assumed in this study that 50% of the pump power input results in melting of ice.

Typically heat transfer coefficients of a few per cent higher than the stationary case, compensate for the increased pumping power input required for the circulation. For example for a circulating system where the superficial velocity is twice that of a stationary fluidized bed, a 1.2% higher heat transfer coefficient is required than in the stationary fluidized bed. For this comparison a wall-to-bed temperature difference of 1.5 K is assumed, the ice slurry is a 5 wt% NaCl solution with ice fraction of 0.10, the fluidized bed has a bed voidage of 0.79 and consists of 4 mm stainless steel particles in a 55 mm diameter tube.

Heat transfer coefficients for the conditions mentioned, estimated using Equation 5.50 are 6.8% higher than for the stationary bed. The increase in heat transfer is therefore more than sufficient to compensate the extra power input of the pump required for circulation. Even if all of the pumping power input would melt ice, the extra heat transfer is sufficient. The relative influence of the pumping power input depends on the temperature difference. At small temperature differences, which are for example required at relatively high temperatures to prevent freeze-up of the fluidized bed, the extra pumping power required for circulation may become significant. It should be noted that for circulation the pressure drop in additional equipment, e.g. piping and valves, is also higher than for stationary fluidized beds. This may melt some additional ice, which may be prevented by adjusted equipment design, for example with larger pipe diameters.

Heat transfer coefficients for the same conditions as in the example discussed above are displayed in Figure 5.9. The estimated heat transfer coefficients for circulating fluidized beds of four bed voidages, including the optimum for spherical particles, ε=0.76, are compared with stationary bed heat transfer and single phase heat transfer.

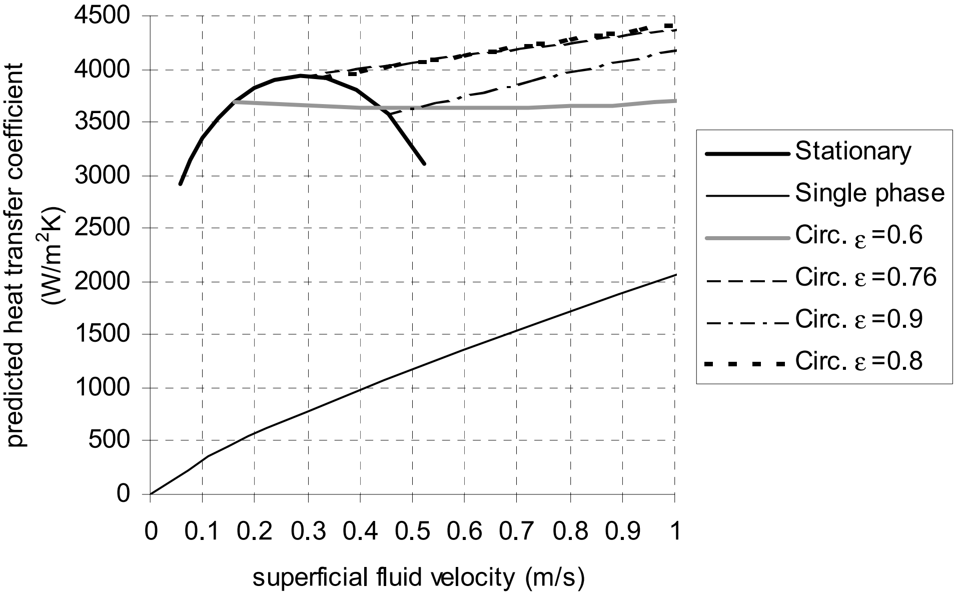

Figure 5.9: Heat transfer coefficients at increasing superficial velocity for ice slurries of NaCl fraction 0.05 and ice fraction 0.10. Stationary as in Chapter 3, circulating with method of Erdmann; Single phase with Dittus Boelter;4 mm spherical stainless steel particles, 55 mm fluidized bed

It is observed from Figure 5.9 that the initial decrease of the heat transfer coefficients at the start of circulation does not occur at the bed voidages of 0.76 and 0.90, where heat transfer coefficients are calculated with Equation 5.50. Also the advantage of circulation calculated is relatively moderate. At a superficial velocity of 1 m/s, or 4 times the optimal stationary fluidized bed case, heat transfer coefficients are approximately 8% higher during circulation.

The optimal bed voidage in the stationary case is not necessarily the optimum for the circulating fluidized bed. For example in Figure 5.9, at superficial velocities above approximately 0.7 m/s a bed voidage of 0.8 yields higher heat transfer coefficients than the optimal stationary bed voidage of 0.76.

5.3.4 Operating Range

In Chapter 4 the processes involved with the freeze-up of fluidized bed heat exchanger walls have been discussed: The crystallization rate at the walls, the ice adhesion force and the number of effective particle impacts at the walls. It is likely that circulation of the solid particles only affects the number of effective particle impacts.

In a circulating fluidized bed a radial distribution may arise. The solid particles are located more near the heat exchanger walls, where the bed voidage is lower than the average of the fluidized bed. This increases the particle impact frequency that can be calculated with Equation 5.22 that applies for stationary fluidized beds (Meijer et al., 1986).

On the other hand the mean particle velocity, u_x, as calculated with Equation 5.23, is likely reduced because of the inhomogeneous velocity profile over the fluidized bed, with the highest fluid velocities in the center of the fluidized bed and the lowest near the walls.

The maximum impact force of a particle impacting in perpendicular direction is given by Equation 5.21. Circulation is a factor in the particle impact force through the mean particle velocity u_x. The impact forces of the particles are likely to be slightly lower than for a stationary bed at the same superficial fluid velocity.

An effect of circulation is that hydrodynamic forces other than particle impacts will increase, as the fluid velocities are higher during circulation. Hydrodynamic forces are however still expected to be relatively small compared with the forces of the particle impacts.

Another effect of the circulation of particles is a different inlet temperature of the ice slurry into the fluidized bed. The particles separated at the outlet of the fluidized bed are at a lower temperature than the ice slurry feed flow to the fluidized bed. Assuming a well insulated downcomer tube, the mixing with the cold solid particles will pre-cool the ice slurry feed flow into the fluidized bed. Temperatures in the fluidized bed, and thereby the driving force, may be slightly different. During countercurrent operation however, the maximum temperature difference is still located at the top of the fluidized bed. During ice slurry production the temperature over the fluidized bed is fairly constant because of the ice slurry phase change. The maximum driving force during ice formation will therefore hardly be affected and the crystal growth velocity and the ice adhesion force will be comparable to the stationary operating conditions.

The increased superficial velocity may influence the supercooling effect of the ice slurry, because the formation of nuclei is also influenced by the degree of turbulence. If the nucleation rates increase upon circulation, the total ice production may also increase.

Solid particles in the downcomer tube may be slightly colder than the ice slurry feed flow. The particles that are fed into the fluidized bed are however continuously enclosed by an ice slurry flow. If the thermal conductivity of the solid particles is not too low, as for stainless steel, the temperature of the particles will rapidly equalize with the ice slurry. Adhesion of ice to particles, covering the particles or blocking the downcomer or conducts, is then unlikely.

If the flow resistance of the downcomer tube is not high enough, there may be an upwards flow of ice slurry through the downcomer. This reduces efficiency, as part of the flow bypasses the heat exchanger, but it also may stop the circulation. The solid particles form a packed bed in the downcomer tube which may act similar to a filter. Ice crystals flowing upwards slowly through the downcomer tube remain behind between the solid particles. This increases the flow resistance for the bypass flow upwards through the downcomer, but ice crystals can also adhere to the particles if they are immobile for too long. This may cause the formation of larger structures of particles or ‘bridges’ that may block the downcomer tube. Such blockages may be temporarily and can disappear if more and more particles are stacked above the bridges, so that eventually the structure breaks and circulation resumes. Before circulation resumes however, the feed of solid particles to the fluidized bed is reduced and therefore the bed voidage increases. At an increased bed voidage the number of particle impacts at the walls of the fluidized bed heat exchanger reduces and freeze-up may occur. Design of the downcomer and the fluidized bed particle feed system are significant for the operating range of bed voidages and temperature differences that can be applied.

Previous work on scaling in circulating fluidized bed systems has been reported by Kollbach (1987), who experimented with saturated calcium sulfate solutions of 100 °C, heated in a fluidized bed heat exchanger. The prevention of calcium sulfate scaling at the heat exchanger walls was compared for stationary and circulation modes. In Figure 5.10 the maximum heat flux before scaling occurs for fluidized beds of different kind of particles is displayed.
From Figure 5.10 it can be concluded that the maximum heat flux in the stationary mode was higher than in the circulating bed at the same superficial velocity. It is not known if the stationary fluidized beds were operated at the optimal bed voidage. The maximum heat flux before scaling starts, increases with increasing superficial velocity. The influence of varying solid particle materials used at similar liquid velocities was not clear, however only a few experiments were done. If it is assumed that the heat transfer coefficients increase rather mildly at increasing fluid velocities, according to the trends of Figure 5.9, the heat flux and the wall-to-bed temperature differences can be assumed to follow similar trends. The heat flux can then be evaluated as a temperature driving force.

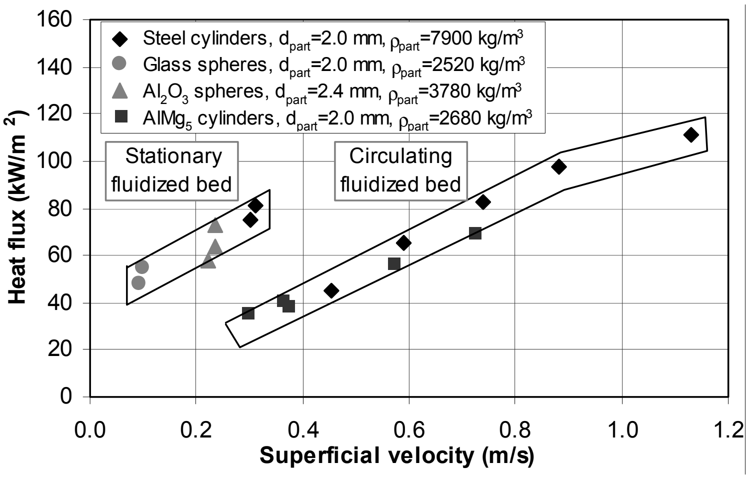

Figure 5.10: Maximum heat flux for heating a saturated calcium sulfate solution at 100°C (after Kollbach, 1987)

5.3.5 Experiments

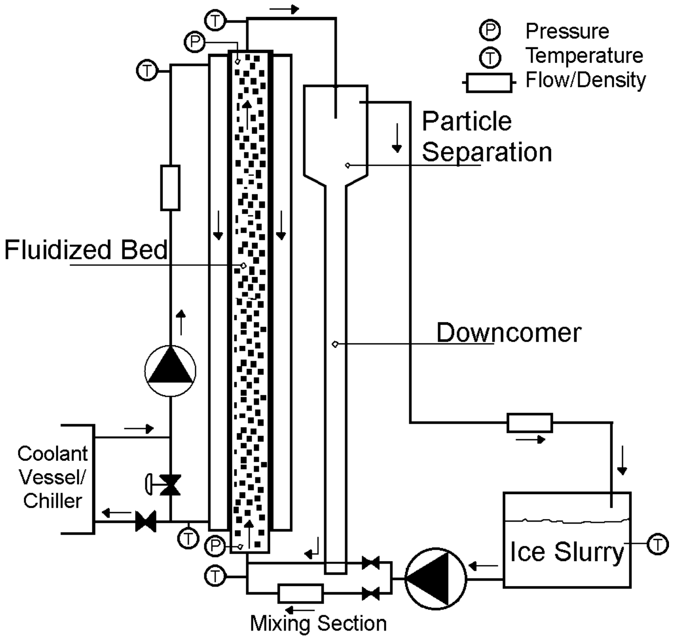

Figure 5.11: Set-up for circulating fluidized bed experiments

A single tube fluidized bed ice slurry generator was used to investigate ice slurry generation in circulating fluidized operation. A schematic layout is given in Figure 5.11. The same fluidized bed as for the stationary experiments was used: A stainless steel tube of 55 mm inner diameter and a height of 4.55 meter. Stainless steel cylindrical particles of 4 mm were used. The solid particles were circulated to the bottom of the fluidized bed through a downcomer tube with an internal diameter of 59.4 mm, made of transparent PVC. The transparent tube was only partially insulated, so that the downward motion of the particles in the downcomer could be observed, as well as a possible upwards liquid velocity. Under conditions in which the solid particles form a packed bed moving downwards at a constant velocity, this velocity was measured. This was done by timing the movement of individual particles in the downcomer. The averaged particle velocities were then used to determine the particle circulation rate.

In the set-up PT-100 sensors were used for temperature measurements and flow and density were measured with Coriolis type mass flow meters. Pressure transmitters were installed to measure the pressure drop over the fluidized bed. From pressure drop measurements also the liquid bypass flow upwards through the downcomer was estimated.

At the bottom of the fluidized bed there was a mixing section in which the particle feed to the fluidized bed was controlled. For this purpose part of the feed flow was directed through the bottom of the downcomer tube, dragging the particles into the fluidized bed. The horizontal tube of the mixing section was 36 mm in diameter, particles moved as a plug through this tube during stable circulation.

Using the Coriolis mass flow meters in the main flow to the fluidized bed and in the return flow from the circulating fluidized bed, the fluid flow was determined. From visual observation it was found that part of the liquid flow was directed upwards through the downcomer, thereby bypassing the fluidized bed heat exchanger.

The solid particles were separated from the ice slurry after the fluidized bed by means of gravity in a separation vessel that was situated on top of the downcomer. Particles plus ice slurry were fed from the top into the middle of this cylindrical tank. The outlet for the particles was directly below the inlet, in the middle of the bottom of the separation tank. The outlet for the ice slurry was above the inlet, at the side wall of the vessel near the top. During regular operation separation efficiency for solid particles was 100%.

During the circulation experiments ethylene glycol aqueous solutions were used as ice slurry feed with concentrations of 6.8, 10.2, and 11.8 wt%.

5.3.6 Fluidization Results

A fraction of the particle feed flow bypasses the fluidized bed heat exchanger upwards through the downcomer. The superficial velocity in the fluidized bed can therefore not be calculated from the total feed flow. At least part of the particle feed flow passes through the fluidized bed, which can be deduced from the fact that there is particle transport towards the fluidized bed, which occurs in the form of a plug.

The control of the particle dosage into the fluidized bed system in the experimental set-up allowed for only a small range of particle feed rates into the fluidized bed. At too low particle feed rates, the particle movement through the downcomer would stop at regular intervals and then resume at a relatively high rate. This led to a fluctuating bed voidage in the fluidized bed, which resulted in unstable ice slurry generation. Furthermore, if the bed in the downcomer is halted, there is a chance of the build-up of bridges or blockages in the downcomer tube, which have been observed on several occasions.
At too high particle dosage, the flow resistance in the downcomer tube would become too low compared with the flow resistance in the fluidized bed. The bypass flow then becomes too large, leading to a too loosely packed bed in the downcomer and to fluidization of the bed inside the downcomer, which causes solid particles to flow out of the system to the ice slurry storage tank.

In Table 5.6 the fluidization conditions of the circulating fluidized bed experiments are given for ice slurry production at three ethylene glycol concentrations. In these experiments there was a steady particle flow into the fluidized bed. The particle feed percentage indicates the percentage of the total ice slurry feed flow that was required to feed the solid particles into the fluidized bed. The bypass percentage indicates the amount of the total ice slurry feed flow that was estimated to flow upwards through the downcomer.

The bed voidage reported in Table 5.6 was calculated from the pressure drop measurements, whereby the wall friction of particles and ice slurry were assumed to be negligible compared with the static pressure drop. The superficial velocities reached during circulation in the fluidized bed system were up to 19% higher than for the stationary fluidized bed systems of the same bed voidage.

The bypass flow upwards through the downcomer was estimated using the total pressure drop over the fluidized bed. The same pressure drop was assumed over the downcomer tube. As the particles in the downcomer tube are present as a packed bed, the static pressure of the particles does not influence the flow resistance, only the flow resistance of the packed bed itself needs to be considered. A correlation similar to Ergun's, Equation 5.16, valid for packed beds of cylinders was presented by Foumeny et al. (1996) and was used to determine the upwards superficial velocity relative to the bed of solid particles:

$$\frac{\Delta p {d_p}^2 \varepsilon^3}{L \mu u_s (1-\varepsilon)^2} = \left(3.81 - \frac{5.265}{D/d_p} - \frac{7.047}{(D/d_p)^2} \right) \frac{\rho_l u_s d_p}{\mu(1-\varepsilon)} + 211 \qquad (5.54)$$

As the pressure drop measured over the fluidized bed does not include the outlet section of the fluidized bed, the total pressure drop is higher than the fluidized bed pressure drop measured. It was estimated that the outlet section increased the pressure drop with 0.1 bar. Also the pressure drop in the horizontal section at the bottom of the system between downcomer and fluidized bed is unknown. As this section is relatively wide compared with the outlet of the fluidized bed its influence is expected to be relatively small and was disregarded here.

The bed voidage of the downcomer is an important parameter in Equation 5.54. It was determined that the bed voidage of a packed bed formed by manually filling the downcomer from the top was 0.43. During the circulation experiments however this bed voidage was assumed to be slightly higher. This could be confirmed by visual observations of the downcomer bed height, that was slightly higher during circulation than after stopping the experiments. The downcomer bed voidage was however not determined accurately. A value of 0.50 was used in the calculations for Table 5.6.

Table 5.6: Hydrodynamic conditions of circulating fluidized bed experiments

EG	bed void.	part. feed rate	bypass through downc.	Δp fluid bed	u_s fluid bed	u_s downc.	u_s stat.	v_{part} downc. calc	v_{part} downc. meas.
wt%	-	%	%	bar	m/s	m/s	m/s	m/s	m/s
6.8	0.78	27%	20%	1.12	0.40	0.085	0.38	0.07	0.035
10.2	0.77	27%	19%	1.15	0.41	0.084	0.36	0.09	0.035
11.8	0.75	25%	20%	1.23	0.41	0.085	0.35	0.11	0.036

It is observed from Table 5.6 that the major part of the flow rate required for the dosage of particles into the fluidized bed flows upwards through the downcomer. A relatively easy solution to decrease this bypass flow is to increase the height of particles in the downcomer, as can be observed from Equation 5.54. Also a decreased downcomer diameter and smaller particles reduce the bypass flow, but these parameters also affect the system performance through other ways, for example in the fluidized bed heat transfer coefficients in case of the particle diameter.

Alternatively the flow resistance in the downcomer can be increased by installing valve systems. These however may increase risks of blockages. A small bypass flow may be preferable to a complex valve systems that reduces the system reliability.

The uncertainty in the bed voidage of the downcomer tube also affects the calculation of the superficial velocity in the fluidized bed. A large uncertainty is also present in the determination of the bed voidage in the fluidized bed, because of relatively inaccurate pressure drop transmitters. The accuracy of ±0.05 bar results in a bed voidage of ±0.03. This accuracy does not influence the superficial velocity in the fluidized bed much (±0.01 m/s), but it is significant for the velocity of the particles calculated in the downcomer tube which has accuracy of ±0.03 only because of the pressure drop measurements. This added to the bed voidage explains the discrepancy between the particle velocities calculated and those measured. In future experiments more accurate pressure difference transmitters should be installed and preferably also over the downcomer tube. Because the fluidized bed superficial velocity is not affected as much by the inaccuracy, still a relevant comparison can be made of the heat transfer coefficients with those of stationary fluidized beds.

Another effect that may influence the results is the radial distribution of the solid particles in the fluidized bed during circulation. If there is such a distribution, the particle slip velocity differs from the velocity used in the calculations of Table 5.6, where a homogeneous distribution was assumed.

5.3.7 Results Operating Range

The wall-to-bed temperature differences are determined for the experiments with a steady particle flow rate. Results are displayed in Figure 5.12. Hydrodynamic conditions of all experiments of the Figure are those of Table 5.6. Only at a single concentration freeze-up has been observed because of a too high temperature difference, in most experiments ice production was stable. Other experiments were performed where also unstable conditions occurred, but these were attributed to unstable particle circulation. In future experiments an improved design of the bottom section of the system and a higher flow resistance in the downcomer tube will allow for evaluation of other particle circulation rates.

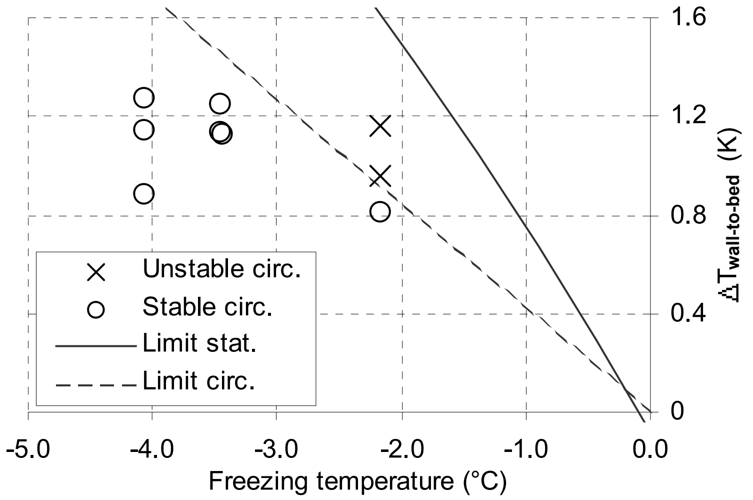

Figure 5.12: Wall-to-bed temperature differences for circulating fluidized bed experiments and the limit of stationary fluidization. Bed voidage 0.79; EG as freezing point depressant

In Figure 5.12 the maximum allowable temperature difference for stationary fluidized beds with ethylene glycol is also displayed, as it was determined in Chapter 4 for a bed voidage of 0.79. The bed voidage of the circulating fluidized beds is slightly lower and not as constant as for the stationary case. As the stationary bed voidage of 0.79 is within the accuracy range of the bed voidage determination of the circulating fluidized beds, a comparison is possible.

A dashed line is drawn in Figure 5.12 to indicate the operating limit for circulating fluidized beds. This limit is based on a single concentration only and is therefore only indicative. It is observed from the figure that the maximum allowable temperature difference under the current circulating conditions is clearly lower than for the stationary case.

The superficial velocity of the circulating fluidized bed in the experiments of Figure 5.12 was up to 20% higher than for the stationary fluidized beds at equal bed voidage. The results of the current experiments are therefore in accordance with the work of Kollbach (1987), displayed in Figure 5.10. At the onset of circulation, where the superficial velocities are only slightly above those of the stationary case, the maximum heat flux before scaling occurs decreases. Only at high superficial velocities a higher operating range is obtained compared with the stationary case.

In the current study the superficial liquid velocities were not increased further. Future experiments are required to confirm if the trend during ice slurry production is similar to Figure 5.10. The higher superficial velocity has the downside of an increased pumping power input, but it may increase heat transfer coefficients, see also section 5.3.3.

5.3.8 Results Heat transfer

The heat transfer coefficients were determined for the experiments with a circulating fluidized bed in the same manner as for the stationary bed experiments. The in- and outlet temperatures of the heat exchanger were measured. With the sensible heat and the mass flow of the secondary refrigerant, the heat transferred could be determined. Using the in- and outlet temperatures of the ice slurry, the overall temperature difference was determined, the wall-to-bed heat transfer coefficient was then calculated using the outside film heat transfer coefficient from the model of Gnielinski, see Equation 3.13 (VDI, 1994).

Results were compared with the theoretical heat transfer coefficients for a stationary fluidized bed of the same bed voidage. The stationary bed heat transfer coefficients were calculated using the model developed in Chapter 3. This model was also applied in the theoretical prediction of the heat transfer coefficients for the circulating fluidized beds, discussed in section 5.3.3. A Richardson-Zaki coefficient *n* of 2.57 was used in the calculations.

Results are given in Table 5.7, for the experiments of which the hydrodynamic results are given in Table 5.6. The relative advantage of circulation compared with stationary fluidized beds is given for the model predictions and for the measured heat transfer coefficients.

Table 5.7: Heat transfer results for circulating fluidized bed experiments

EG conc.	bed void.	u_s stat.	u_s circ.	α stat.	α circ. calc.	α circ meas.	gain calc.	gain meas.
wt%	-	m/s	m/s	kW/m^{2}K	kW/m^{2}K	kW/m^{2}K	%	%
6.8	0.78	0.38	0.40	4.28	4.38	4.03	2.3	-5.9
10.2	0.77	0.36	0.41	4.12	4.20	4.01	1.8	-2.7
11.8	0.75	0.35	0.41	4.03	4.09	3.63	1.4	-10.0

From the heat transfer measurements it followed that circulating fluidized bed ice slurry generation shows slightly lower heat transfer coefficients than during stationary operation. The measured heat transfer coefficients were up to 10% lower than those for stationary fluidized bed systems at equal bed voidage. This comparison is however based on a bed voidage that was determined with a rather large inaccuracy. The corresponding stationary fluidization velocity on which the stationary heat transfer coefficient is based also has this increased inaccuracy. The disadvantage of the circulation is not large enough to conclude that circulation is indeed disadvantageous for these experiments. The model of Erdmann predicted a 2% higher heat transfer coefficient for the circulating fluidized bed. More accurate measurements are required to further validate the model. It was observed in Figure 5.9 that it predicts a heat transfer coefficient that is always higher than the stationary case at bed voidages above the optimum stationary case. In the current measurements however a lower value was observed. Other researchers (Rautenbach et al., 1991) also observed similar lower heat transfer coefficients at only slightly increased superficial velocities upon circulation.

The Richardson-Zaki coefficient that was determined in the previous section on stationary fluidized beds, is slightly higher for cylindrical than for spherical particles, 2.57 versus 2.39. This higher coefficient implies a larger influence of the bed voidage. Uneven radial distribution of particles during circulation will result in a larger radial difference in superficial velocities if cylindrical particles are used instead of spherical particles.

Once the radial distribution of the particles in the fluidized bed is known, the average bed voidage can be adjusted so that the optimum bed voidage for maximum particle impacts is obtained near the heat exchanger walls. From Equation 5.46 it is expected that the average bed voidage for circulation is higher than the optimal bed voidage for stationary fluidization.

5.3.9 Conclusion

Stable ice slurry generation with a circulating fluidized bed was shown to be possible at similar heat transfer coefficients as for stationary operation. The maximum temperature difference allowable before freeze-up of the fluidized bed, is lower than for stationary fluidized bed systems at the same bed voidage. A likely cause is an uneven radial distribution of the solid particles through the fluidized bed during particle circulation.

Circulating fluidized bed heat transfer coefficients predicted with the method of Erdmann (1993) were slightly higher than for the stationary fluidized bed, the coefficients measured were however lower. Accuracy of the determination of the bed voidage and of the superficial velocity were rather poor during the current experiments. More accurate pressure measurements and a better determination of the downcomer bypass flow are required to validate the heat transfer and bypass flow models.

For the reasons discussed above attention should be directed towards circulating systems at much higher circulating fluidization rates and superficial fluid velocities. It is expected that under these conditions both operating range and heat transfer can be higher than for stationary operation.

5.4 Multiple Tube System

In order to take full advantage of the fluidized bed technology, ice slurry generation systems will likely consist of several parallel beds fluidized using a single pump. In this section the main issues of parallel fluidization are discussed, together with possible effects of ice slurries in it.

5.4.1 Introduction

The maximum height of an ice slurry generator will be determined mainly by the primary refrigerant side, if not by the ceiling height of the room in which the installation is located. Assuming a two section falling film system, the maximum height is in the order of 3-5 m. For a tube diameter of 50 mm the heat exchanging surface is 0.6 m^2 per tube. Assuming a 2.5 K wall-to-bed temperature difference and a tube side heat transfer coefficient of 4 kW/m^2K, the ice generation capacity of a single tube is approximately 6 kW.
Commercial applications are several times as large, for example in the order of 100 kW, so that a system with several fluidized beds is required, e.g. 17 parallel fluidized bed tubes. These are then mounted inside a shell where the primary refrigerant evaporates. In large scale installations the fluidized bed height may be doubled, but then applying two separate falling film systems on top of each other.
Technology of falling film evaporation has been established commercially, also in vertical shell-and-tube arrangement as is required for fluidized bed ice slurry generators.

Parallel fluidization of a number of tubes using a single pump has been realized commercially in a number of applications in process industry, however not for a crystallization process with an evaporating refrigerant yet. For crystallization processes it is essential that the fluidized bed particles cover the complete heat exchanging surface at all times at roughly equal bed voidage in all tubes. In other heat exchanging processes temporarily loss of heat transfer capacity by fouling may be regained once the beds are again fully fluidized, but in ice slurry generation freeze-up is almost irreversible without external actions. Heat exchanging capacity is lost permanently until the next defrost cycle.
No experiments have been reported with parallel fluidization combined with falling film evaporation. One reference however does describe such a system (Hewitt and McMullan, 1997).

5.4.2 Description of Multiple Bed Fluidization

Small differences in the manufacturing of tubes and in the number of particles present in the packed beds lead to slightly different pressure drop curves at start-up of the fluidization. In Figure 5.13, typical pressure drop curves of two fluidized beds are given. The two beds fluidized in parallel are displayed schematically in Figure 5.14. The two fluidized beds cannot exchange solid particles.
Initially, at low mass flows, the pressure drop of both beds is nearly equal so that the flow through both the beds is also similar. Bed 1 however starts to become fluidized at a lower pressure drop than bed 2. Bed 1 goes through the unstable region and becomes fully fluidized, while bed 2 is still fixed. In the fluidized bed state, the pressure drop increases because of wall friction and entrance pressure drop effects only. These are relatively small, so that the mass flow through bed 1 increases significantly before the pressure drop becomes equal to the minimum fluidization pressure drop of bed 2. This difference corresponds with a difference in

bed height up to several meters. It is especially large for relatively low density particles as glass beads. Only if the mass flow is further increased, both beds are fluidized fully and mass flows through both beds becomes similar again.

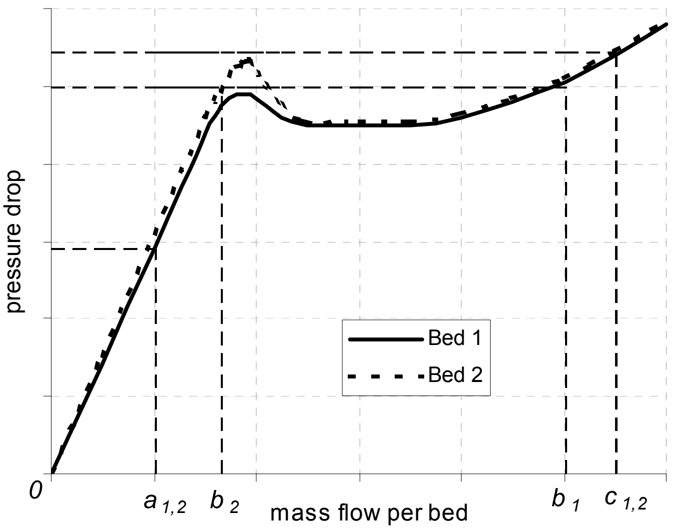

Figure 5.13: Pressure drop vs flow of two similar fluidized beds. a: Both beds fixed; b: Bed 1 fluidized while bed 2 is still fixed; c: Both beds fluidized

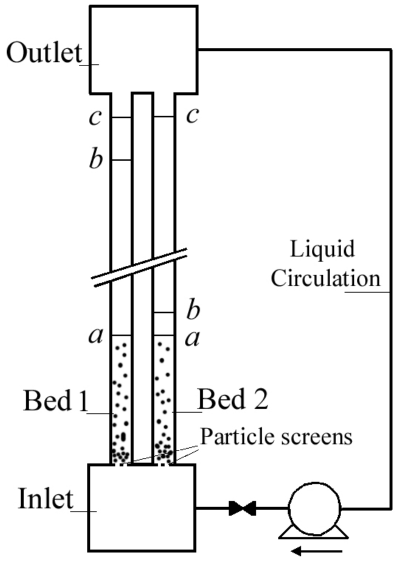

Figure 5.14: Two parallel fluidized beds of Figure 5.13 and bed heights of cases a,b and c

To avoid the difficulties caused by the large difference in mass flow at start-up of fluidization, throttling devices may be installed at the entrance of the fluidized beds. These devices increase entrance pressure drops. A typical pressure drop-flow characteristic for a fluidized bed with throttling device is given in Figure 5.15. After the initial start of fluidization, only a small increase of flow will lead to a sufficiently high pressure drop to also fluidize bed 2.

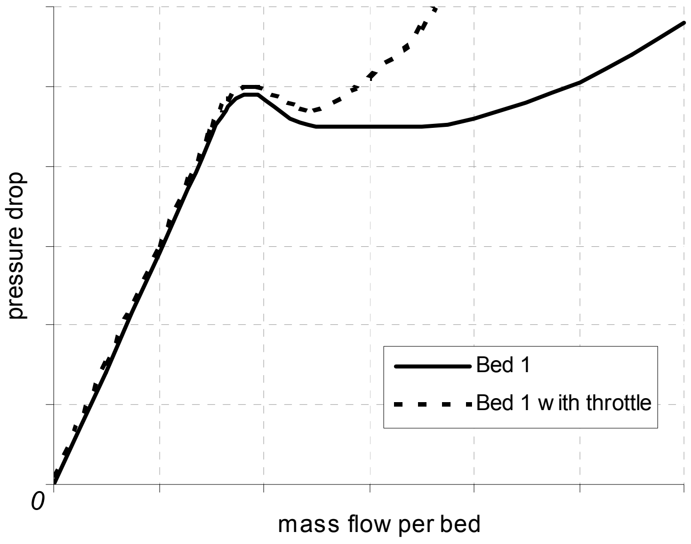

Figure 5.15: Pressure drop vs flow for a fluidized bed with and without throttling device at the inlet.

The throttling devices also do not yield exactly equal pressure drops, the fluidization height of the beds will therefore still differ between beds. As a result of this, on top of the fluidized beds a section should be installed where no heat transfer occurs. The height of this section is the difference between the beds with the lowest and the highest fluidization heights. The top section should be high enough to prevent the beds with the highest fluidization heights to spill out particles. After some particles are spilled, pressure drop reduces and the flow will increase, leading to a ‘blow-out’ of particles out of the tube. Some of the parallel fluidized bed tubes will then become nearly empty, while others return to fixed bed state.

A number of particles of larger diameter combined with a plate with holes of intermediate size can act as a backflow valve, to prevent particles flowing out of the bottom end of the fluidized beds into the throttling devices, during stops of the system.

By interconnecting the multiple fluidized beds, the disadvantage of different bed heights can be avoided. A particle outlet section is installed on top into which all of the parallel fluidized beds spill the excess particles. During regular operation there should be an excess of particles in the top section. The superficial velocity there is relatively low, so that the bed voidage is much lower as in the fluidized beds, particles may therefore be in fixed state or be only just fluidized. Small variations in the flow through individual fluidized beds can now occur without the system to malfunction. Also bed voidages may slightly differ between beds.

If particles in the top section are in fixed state, clogging problems may occur. A fixed bed of particles may act as a filter and get clogged locally. Also the formation of bridges (see Figure 5.16) may occur on top of the fluidized beds. A stirring or wiping device is then required to keep the fluidization going. This introduces disadvantages of additional power input and a mechanical device that requires maintenance.

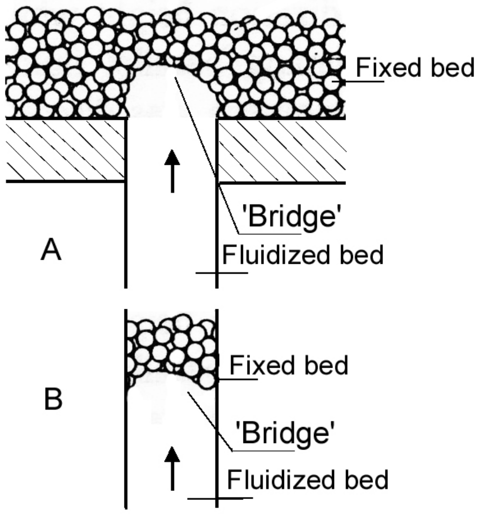

Figure 5.16: Bridging effect of particles above (A) or inside (B) relatively narrow tubes

In researching parallel fluidization, Klaren developed a fluidized bed inlet that has a stabilizing effect on parallel fluidization of multiple beds (Klaren, 1983). It consists of an extension of the tube that sticks into a bulk of solid particles at the bottom of the system. A short distance above the inlet, holes are made in the tube wall. These holes are connected to the top of the bottom section, above a plate that prevents the solid particles to reach the side holes. The side holes have a smaller diameter than the particles, so that only the fluid can pass through the holes.

During regular fluidization a significant part of the fluid flow enters the bed through the side holes. If at a given moment less particles are present in the fluidized bed, the fluid flow through the side holes will increase, thereby increasing the pressure drop over the side holes. As a result a relatively larger part of the fluid flow will now enter the fluidized bed through the bottom opening. This increased bottom flow will drag more solid particles into the fluidized bed, which reduces the bed voidage and stabilizes the operation of the fluidized bed.

In Figure 5.17 an example schematic lay-out of the bottom section of the fluidized bed is given. The stabilizing holes can be used both in stationary and circulating fluidization.

A careful design of the side holes is essential for a stable operation of multiple parallel fluidized beds. Designs were patented by Klaren (1983) and Rautenbach (1985). The design limits the operating range in terms of flow and bed voidage to some extent, however still a significant operating range can be achieved. A ratio of maximum/minimum flow of 1.6 can be handled, as reported by Klaren (1975). Most systems will be designed to operate at a constant flow and bed voidage, so that this will not impose limits on the applicability of multiple parallel fluidized beds.

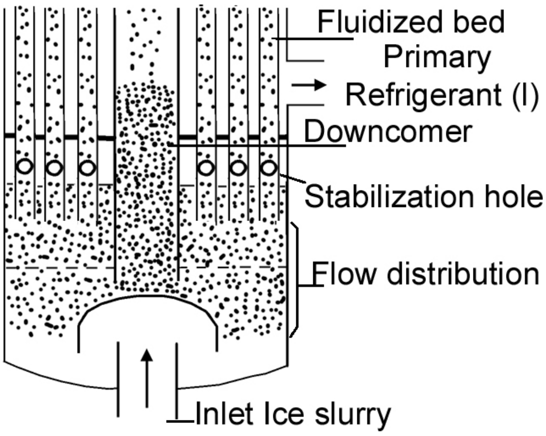

Figure 5.17: Bottom section of parallel fluidized bed system with stabilization side holes near the fluidized bed inlets

Alternatively a careful design of a flow distribution plate may be sufficient for an even flow and particle distribution over several parallel fluidized beds. For example a plate with small holes through which some radial flow is induced above the distribution plate was proposed by Rautenbach (1985).

Circulation of the solid particles can be accomplished with an internal downcomer and with an external downcomer tube. In Figures 5.7 (external) and 5.18 (internal) both systems are drawn schematically. The system with internal downcomer has the benefit of being compact and also particle transport during regular operation is relatively easy. Fluid velocities do not have to be as high as for external circulation, as the particles do not have to be transported out of the shell. The design of the shell is however relatively complicated and also replacement of particles may be difficult.

External circulation requires higher fluid velocities, but the amount of particles inside the fluidized beds can be controlled more accurately with the particle dosage flow. Particle replacement is easier and can be achieved during operation, if a particle holding vessel is installed parallel to the downcomer tube. Disadvantageous is the extra equipment outside the shell to separate the particles from the fluid flow.

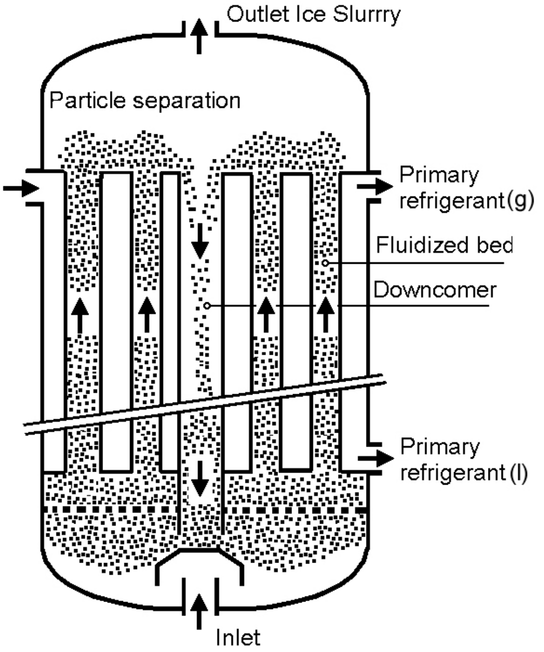

Figure 5.18: Schematic lay-out of multiple fluidized bed system with internal circulation of particles and falling film system (film distribution not shown)

5.4.3 Ice Slurries in Multiple Bed Fluidization

The main concern during ice slurry generation using multiple fluidized beds is that the particles are in fluidized state at all parts of the heat exchanger that are at a lower temperature than the ice slurry. Another concern is that the ice slurry flow should be high enough at all places where it passes through narrow gaps, so that ice crystals cannot cluster or attach to other solids. Narrow gaps of similar size as ice crystals can be expected in fixed beds and in flow distribution devices.

Systems with multiple parallel fluidized beds that can not exchange particles through either top or bottom, will have differences in fluidization height. All beds should be fluidized above the heat exchanging area. This heat exchanging area should end with an insulating section, so that the wall cannot become colder than the ice slurry because of thermal conduction through the wall above the fluidized bed height.

Throttling devices at the fluidized bed inlets should be based mainly on increased wall friction and not on a smaller tube diameter. A too small tube diameter may become clogged by the ice crystals of the slurry. It depends on the crystal sizes of the ice slurry what diameter is acceptable. Methods may be applied to prevent large ice crystals to be fed into the fluidized beds. Preferably however the feed flow should not be free of ice, because complete ice filtration was found to cause instabilities in the fluidized bed ice formation in experiments.

Design of stabilization side holes and holes in distributor plates should take into account the size of ice slurry crystals, to prevent clogging with ice of these holes. Especially if relatively small solid particles are used and ice crystal sizes are expected to be large, design and manufacturing of the holes should be done accurately.

Stationary fluidization where the fluidized beds can spill particles to a top section can lead to problems caused by the formation of bridges, as depicted in Figure 5.16. Without ice these bridges may already form, but with ice crystals the occurrence increases. The particle may function as a filter, catching ice crystals into their structure. This strengthens the bridges, which makes the use of a mechanical device inevitable to keep the system operational. Formation of bridges can be prevented by designing the top section in such a way that the superficial velocity remains high enough to keep the particles fully fluidized. For this purpose the fluid flow can be increased or the top section diameter decreased.

The top section diameter depends on the design of the falling film evaporation, which is discussed in Appendix 1. The falling film thickness is expected to be low, approximately 0.5 mm. Furthermore, flooding phenomena are not expected at tube clearances of approximately 10 mm, therefore the diameter of the top section can be small enough to keep the solid particles sufficiently fluidized.

A relatively high fluid flow to keep the particles in the top section fluidized, may lead to relatively high bed voidages in the fluidized beds themselves, so that circulation of the solid particles may be preferable above stationary fluidization.

It is unlikely that circulating fluidized beds with internal downcomer can be used for ice slurry generation. The evaporating primary refrigerant in the shell may eventually result in a small temperature driving force over the wall of the downcomer tube, e.g. by thermal conduction through walls. As a small ice slurry flow upwards through the downcomer tube cannot be avoided completely, freeze-up of the downcomer tube then becomes likely. The downcomer tube should therefore be surrounded by insulation or an annulus of upwards flowing ice slurry. Also insulation should be used to mount the downcomer tube. The shell-and-tube configuration then becomes complex, so that applying external circulation is the more likely choice for ice slurry generation.

In the downcomer tube the particles should move downwards as a packed bed to prevent ice slurry bypass flow through the downcomer. As long as the particles keep moving at a constant velocity, formation of bridges is not likely. Any blockages that may occur inside the packed bed are transported downward and broken up by the particle dosage flow. For this reason an external downcomer tube is expected to be advantageous over an internal.
Problems may occur if the particle velocity in the downcomer is not as steady. If fluctuations occur during which the particles in the downcomer slow or stop at certain moments, formation of bridges is likely. The tendency to form bridges is increased if there is a large ice slurry flow upwards through the downcomer. A large upwards flow through the downcomer should be prevented, not only for maximizing heat transfer performance inside the fluidized bed, but also for a stable particle circulation through the downcomer.
If multiple tubes are fluidized in parallel, still a single downcomer tube should be used to prevent a bypass flow upwards through the downcomer as much as possible, which allows a high packed bed height in the downcomer. Assuming that the pressure drop model for a packed bed of Ergun is valid (Equation 5.16), the diameter of the downcomer does not influence the pressure drop over the downcomer. The downcomer diameter should therefore be relatively small, so that the packed bed height is high and the bypass flow as low as possible. The resistance to bypass flow is then higher and the particle circulation more stable. If it is assumed that the packed bed pressure drop is described by Equation 5.54, the downcomer diameter should also be small to prevent bypass flow.
If a small tube is installed however, the formation of bridges becomes more likely. For a single tube with circulation this is a more significant problem than for multiple fluidized beds. In multiple fluidized bed systems there are significantly more particles to be transported through the downcomer. The downcomer diameter can be chosen more freely to optimize between flow resistance and likelihood of bridge formation.

Both stationary and circulating technology of the multiple parallel fluidized beds are expected to be applicable for ice slurry generation. The exact performance of circulating fluidized beds for ice slurry generation is however still under investigation, therefore a choice of cannot be made yet.

5.4.4 Conclusion

Fluidized bed ice slurry generators in which multiple tubes are fluidized in parallel that are mounted in a single shell are considered to be possible. However the tendency of ice to freeze-up systems by adhering semi-permanently to cold surfaces, makes several process designs less likely that are otherwise applied successfully in several industries.
Both stationary fluidization and circulating fluidized bed systems with external downcomer are expected to operate reliably for ice slurry generation. In both operating modes stabilization devices near the fluidized bed inlets are required. If stabilization holes are used, these should be significantly larger than the ice crystals, but smaller than the solid particles. Systems with internal downcomer are not expected to be reliable for fluidized bed ice slurry generation.

5.5 System Improvement by Rotating Action

5.5.1 Introduction

In Chapter 4 it was seen that the maximum allowable temperature difference depends on the particle impacts on the heat exchanger walls, among other effects. The kinetic energy of the particles of the fluidized beds is assumed to be exponentially distributed similar to the Boltzmann distribution. Only the fraction of particle impacts above a certain kinetic energy will be effective for the prevention of freeze-up of the fluidized bed. The number of effective particle impacts can be improved either by increasing the number of particle impacts or by increasing the kinetic energy of the particles.

In this section a novel concept based on rotating action is introduced in an attempt to improve operating range and heat transfer of the fluidized bed heat exchanger.

In some heat exchangers already the benefits of rotating action on heat transfer coefficients are applied (Yu et al., 2003). For example a static device is installed at the entrance of the heat exchanger or throughout the heat exchanger, in order to induce a swirling motion of the fluid. This swirling motion increases turbulence, thereby reducing the laminar boundary layer at the wall and improving heat transfer. If flow conditions are however already turbulent, benefits may be limited and could be obtained more easily by an increase of the flow rate. Static rotation is therefore applied mainly for highly viscous fluids (van der Meer and Hoogendoorn, 1978).

Rotation induced with a static device in fluidized beds would increase turbulence, but also the radial particle distribution may be altered by the rotation. The forces acting on the particles are all supplied directly or indirectly by the fluid flow. Improvement of the performance may therefore be limited.

A more active approach on improving the particle impacts may yield higher benefits. An active rotating device, a rotor, may push the solid particles towards the heat exchanger walls, where the particles are required for the ice removal. Also the particle velocity may be boosted because of the centrifugal forces exerted by the rotor. The particles may have larger impact and thereby increase the heat transfer coefficients and operating range of the heat exchanger. A schematic lay-out of a fluidized bed with active rotor is given in Figure 5.19.

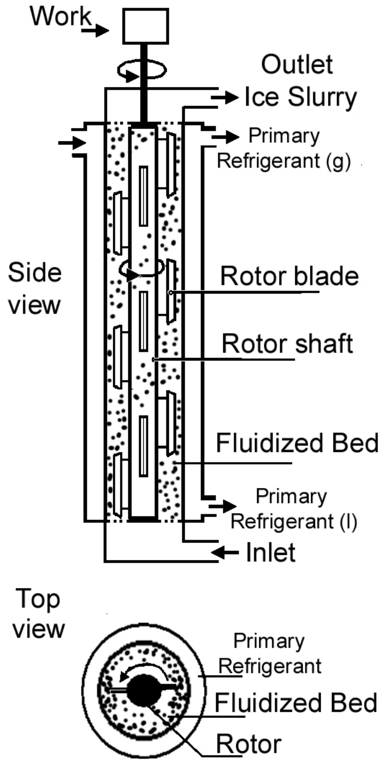

Figure 5.19: Fluidized bed system with rotor

A number of phenomena may occur that would reduce the effect of the rotor or would even turn it into a disadvantage. The improved particle velocity induced by the rotor may for example damp out in the swarm of particles. Also the particle distribution may be affected negatively by the rotor. The fluidization velocity may differ from the model of Richardson and Zaki, because an uneven radial distribution of the solid particles may also cause an uneven fluid flow, with high velocities in the center and low velocities near the walls.

For heat transfer in stationary fluidization the radial particle distribution may be a critical parameter, as there is an optimum value for the bed voidage where heat transfer is at a maximum. If the rotor transports too many particles to the wall area, the bed voidage may be reduced locally. In an extreme scenario almost a packed bed situation may occur near the wall: The rotor ‘pins’ the particles to the wall and they no longer have as many wall impacts. Particles stuck between rotor blades and the wall may also cause excessive wear, as the system then turns into a scraper.
The centrifugal forces exerted by the rotor may also affect the ice slurry directly. The ice crystals may be separated and the ice fraction may increase in the center of the fluidized bed.

Goal of the current evaluation is to determine if the fluidized bed ice slurry generator performance can be improved by actively inducing rotating motion in the fluidized bed. Possible effects of a rotor may furthermore increase the understanding of the mechanisms of heat transfer and ice build-up at the wall in fluidized bed ice slurry generators. The installation of a rotor obviously increases the complexity of the system. Possible advantages should therefore be significant, so that the extra investment and maintenance costs of the rotor can be compensated for.

5.5.2 Experiments

A rotor was constructed and installed in the fluidized bed experimental set-up of 55 mm internal diameter. The rotor consisted of a 14 mm steel shaft on which rectangular flat slabs were welded vertically, with 60 mm in between rectangles. The rectangles were approximately 80 mm high and 10 mm wide. Between the edge of the rectangles and the heat exchanger walls this leaves approximately 10 mm of open space. Each rectangle was welded at a position 60^{o} rotated compared with the rectangle just below it. In the intervals small bars were welded with a Teflon cap. These caps were cut to fit exactly into the 55 mm fluidized bed. The bars kept the shaft centered in the fluidized bed. A schematic lay-out of the rotor is given in Figure 5.20.
The shaft was driven by an electric motor of 2 kW maximum drive capacity. The motor was equipped with a gear system to control the rotational speed gradually. The motor was installed on top of the fluidized bed, directly above the separation section. The fluidized bed height was controlled using a pressure difference transmitter, installed over the top section of the fluidized bed, because there was no longer a transparent section on top of the fluidized bed. The pressure drop was calibrated to determine at which point solid particles are present in the top section. An increase of the pressure difference indicated that particles flow out of the fluidized bed and that freeze-up started.

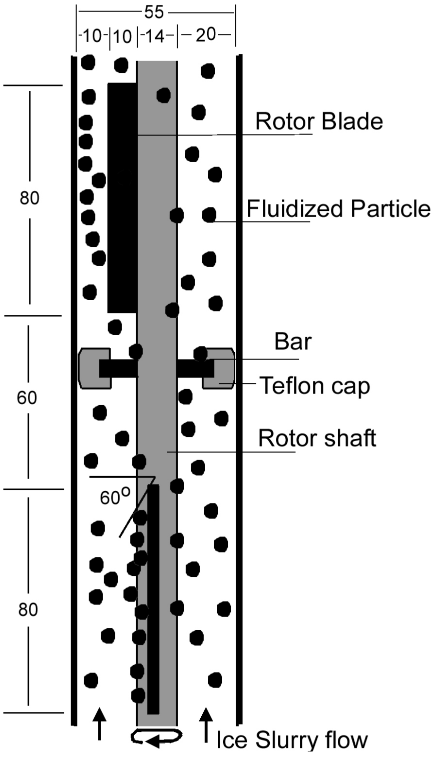

Figure 5.20: Detailed lay-out of the rotor installed in the experimental set-up

Experiments were carried out in stationary fluidized beds at varying rotor speeds for bed voidages of 0.79 and of 0.86. The rotor speeds were varied from 0 to the maximum capacity of the drive system. One experiment was done with circulation of the fluidized bed particles. In all experiments 4 mm cylindrical stainless steel particles were used. NaCl was used as the freezing point depressant at two initial freezing points, -2.2 °C and –3.3 °C. An overview of the rotor speeds and bed voidages of the experiments is given in Table 5.8.

In the experiments the heat transfer coefficients were determined. Then the temperature difference between ice slurry and secondary coolant was increased in steps until freeze-up of the fluidized bed occurred, indicated by decreasing heat transfer and an increased fluidized bed height. In some experiments the rotor speed was varied in an attempt to return to stable ice slurry generation conditions after freeze-up.

After the start of ice formation in a few experiments, the temperature sensor at the outlet of the fluidized bed displayed erroneous values, up to approximately 1 K too high. This was confirmed with the temperature sensor of the Coriolis density/mass flow meter. The location of the temperature sensor is no longer directly in the ice slurry flow, but in a side compartment, as the rotor is in the way. It is likely that this compartment fills with ice under certain conditions and therefore does not record the ice slurry temperature. If this effect occurred, heat transfer coefficients were estimated using the inlet ice slurry temperature.

5.5.3 Results and Discussion

The rotor could operate at a maximum rotation speed of 110 rpm in the fluidized bed. This rotation speed is considerably lower than without a fluidized bed present. At lower speeds the rotation speed could not be kept constant. This indicates that the rotor was subjected to high friction in the fluidized bed. When in operation the rotor was very noisy, often crunching or screeching noises could be heard. This would imply that the solid particles of the fluidized bed became stuck between the Teflon caps and the wall. However also other types of blockages could have occurred.

The rotor has a hindrance effect on the settling velocity of the particles. The fluidization velocity encountered in the experiments may differ from what is predicted with the method of Richardson-Zaki. In the current evaluation this is accounted for in the wall effect:

$$u_{\infty wall} = u_{\infty} \cdot 10^{\left(-\frac{d_p}{D_h}\right)} \tag{5.1}$$

The presence of the rotor reduces the cross sectional area of the fluidized bed. Instead of the fluidized bed diameter, now the hydraulic diameter of the fluidized bed is used in Equation 5.1, which is defined as:

$$D_h = D_{bed} - D_{rotor} \tag{5.55}$$

The hindrance effect of the rotor blades and the stabilizing bars is ignored here.

An overview of the fluidization velocities determined in experiments and predicted with the Richardson–Zaki model with n=2.39, valid for spherical particles, is given in Table 5.8. The superficial fluidization velocity of the experiments was higher than predicted with the model of Richardson-Zaki. It is likely that the rotor causes additional flow resistance in the fluidized bed. A higher flow rate is required to achieve fluidization at the same bed voidage as for a fluidized bed without internals. It should be noted that if the value determined in Section 5.2.4

of n=2.57 is used, the predicted fluidization velocity would be 3 to 5% lower than the values of Table 5.8. The results of the bottom row correspond to an experiment in which the solid particles were circulated.

Table 5.8: Results of rotor experiments: Fluidization velocity, heat transfer coefficients and maximum temperature difference allowable; Conditions at start of ice formation

NaCl	T_{f_init}	rotor speed	bed voidage	u_s exp.	u_s model Rich-Zaki	α model no rotor	α exp rotor	ΔT_{wtbmax} exp rotor	ΔT_{wtbmax} no rotor
wt%	°C	rpm	-	m/s	m/s	W/m^2K	W/m^2K	K	K
5.5	-3.3	15	0.86	0.45	0.39	3979	3503	1.6	1.7
5.5	-3.3	25	0.86	0.46	0.40	4069	3135	1.5	1.7
5.5	-3.3	55	0.86	0.45	0.39	3962	4029	1.5	1.7
3.6	-2.2	15	0.86	0.46	0.40	4108	3606	0.8	1.1
3.6	-2.2	55	0.86	0.45	0.39	4099	4057	1.1	1.1
3.6	-2.2	110	0.86	0.45	0.40	4073	3882	0.9	1.1
3.6	-2.2	55	0.79	0.36	0.33	4215	3830	1.2	1.2
3.6	-2.2	110	0.79	0.36	0.32	4165	3870[a]	-[a]	1.2
3.6	-2.2	55	±0.77[b]	0.50	$\pm 0.29+v_p$[b]	3926[b]	4101[a]	-[a]	0.9[c]

[a] No stable ice slurry generation

[b] Circulation, no exact bed voidage determined; model values for stationary case, v_p=particle transport velocity

[c] Value based on ethylene glycol

In Table 5.8 the heat transfer coefficients determined during ice slurry generation with the rotor are given, together with those predicted with the model of Chapter 3, valid for fluidized bed ice slurry generation without rotor. The model predictions are based on a fluidized bed with the same diameter, and thus a slightly larger cross section.

In most experiments, the heat transfer coefficients determined were lower than predicted for the same fluidized bed without a rotor present. The only experiments with a similar or higher heat transfer coefficient were at ε=0.86 and a rotor speed of 55 rpm. The experiments with a low rotor speed had a considerably lower heat transfer coefficient than the experiments at 55 and 110 rpm. It is not clear if there is an optimum rotor speed for the heat transfer coefficient, because only a limited number of rotor speeds has been investigated.

The rotor also affected the freeze-up conditions of the fluidized bed heat exchanger, an example of which is given in Figure 5.21. The heat transfer coefficients of an experiment at bed voidage of 0.86 and a 5.5 wt% of NaCl is given during initially steady ice slurry generation. The rotor is continuously in operation at approximately 55 rpm. At t=2500s, the rotor is slowed to 15 rpm. It is seen that the heat transfer coefficients immediately begins to decrease, which indicates the build-up of an ice layer at the heat exchanger walls. Also the pressure drop over the top section (not given in Figure 5.21) immediately starts to rise, indicating a rise of the fluidization height and also build-up of an ice layer.

After restoring the rotor speed to 55 rpm at t=4000 s, the decrease of the heat transfer coefficient slows down. Heat transfer is however still decreasing slowly. After the rotor is again slowed at t=4900 s, the heat transfer coefficient again decreases rapidly, towards freeze-up of the fluidized bed. The re-start of the rotor at t=4000 s, was at an estimated average ice layer thickness of 290 µm (Equation 4.19). This ice layer is thick enough to touch the Teflon caps, but there is still a large clearance with the blades. The rotor blades are not scraping through the ice layer itself.

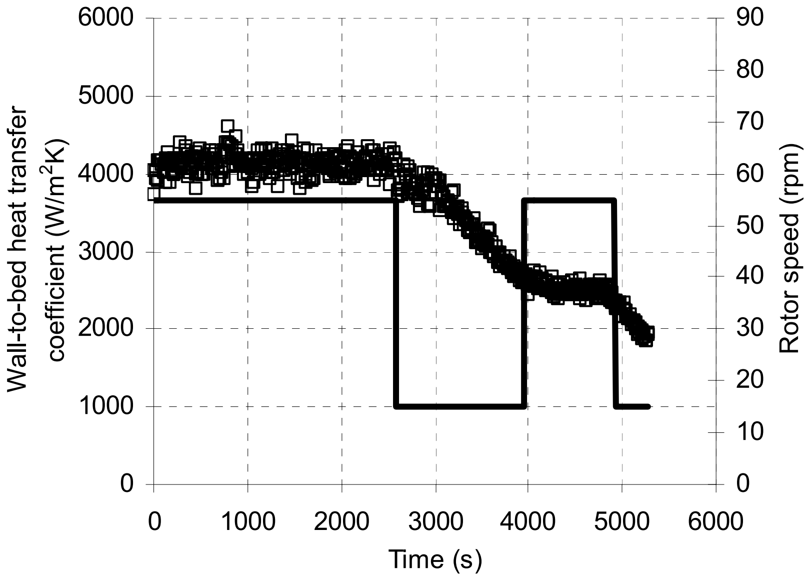

Figure 5.21: Wall-to-bed heat transfer coefficient and rotor speed during ice slurry generation with 5.5% NaCl, ε=0.86 and ΔT_{wtb}= 1.5 K

In most experiments the rotor speed was kept constant until the inlet temperature of the secondary coolant was low enough to start freeze-up of the fluidized bed. In none of the experiments an increase of the rotor speed could recover stable ice slurry generation conditions once build-up of an ice layer had started.

In Table 5.8 also an overview is included of the maximum wall-to-bed temperature difference of the experiments. The limits found in the experiments without rotor are also given, as determined in Chapter 4. Generally the maximum allowable temperature differences were lower than in the experiments without rotor. In two experiments the same allowable temperature difference was found, both using 3.6 wt% NaCl at a rotor speed of 55 rpm. At lower rotor speeds a lower allowable temperature difference was observed. Also at higher rotor speeds of 110 rpm the temperature differences allowable were lower or could not be determined due to freeze-up. At a concentration of 5.5% NaCl however, there was no clear advantage for the maximum allowable temperature difference of a rotor speed of 55 rpm over lower speeds.

In the current preliminary evaluation only limited experiments were performed at a certain rotor speed, bed voidage or concentration and therefore it is not clear if linear trends can be fit similar to the trends observed in Chapter 4. The error of the maximum wall-to-bed temperature differences is estimated in the range of ±0.1 K up to ±0.2 K, depending on the size of the temperature steps taken in the various experiments.

The presence of the rotor negatively influences heat transfer and maximum allowable temperature difference. The negative effects are likely caused by an increased pressure drop and by the obstructing effect the rotor has on homogeneous fluidization. Particles impacting on a stopped rotor, lose kinetic energy and do not impact as effectively at the walls.

In the current experimental set-up the negative effects were compensated at a rotor speed of 55 rpm only. Heat transfer and temperature differences were at a similar level as for the fluidized bed system without rotor.

The force acting on a particle at the tip of the rotor blade in the perpendicular direction can be estimated with:

$$F_C = \frac{m_{eff} v_{tip}^2}{R} = \frac{V_p \left(\rho_p - \rho_l\right) v_{tip}^2}{R} \tag{5.56}$$

in which R is the radius of the rotor and v_{tip} is the circumferential velocity of the tip of the rotor blades, which is 0.098 m/s at 55 rpm.
At the moment that the particle leaves the tip of the rotor, the velocity that the particle obtains in the perpendicular direction can be calculated with the drag force acting on a particle.

$$F_D = C_D \cdot A_\perp \cdot \rho_l \frac{v_p^2}{2} \tag{5.57}$$

In which C_D is the drag coefficient given by Equation 5.13, discussed in section 5.2.3.
After setting F_C=F_D, the particle velocity v_p can be solved iteratively. At a rotor speed of 55 rpm and ice slurry fluid properties, it follows that Re=418 and the flow regime is in transition between laminar and turbulent. The unhindered centrifugal particle velocity is 0.17 m/s. The drag coefficient is approximately 0.73. At lower rotor speeds the laminar region of Reynolds numbers is encountered and the drag coefficients will become relatively high, at 15 rpm: C_D=1.19 and v_p=0.037 m/s. The particle velocities will become low, which may explain that the particles do not have a positive effect at low rotor speeds.
Assuming a swarm effect similar to Richardson-Zaki, the actual particle velocity can be estimated more accurately:

$$v_p = v_{p\infty} \cdot \varepsilon^n \tag{5.58}$$

from which at 55 rpm, n=2.39 and ε=0.79: v_p=0.097 m/s.
The particle velocity is distributed over a wider surface area than the rotor tip travels. The particle velocity induced by the rotor will be distributed over several particles by mutual collisions. The wall area is approximately 61% larger in the current set-up than the area that the rotor tip covers. The average particle velocity at the wall as a result of the rotor is approximately 0.060 m/s. It will in fact be lower, as the particle collisions are not ideal and some kinetic energy is lost. Furthermore, in the current set-up the rotor blades do not cover the full area because of the vertical spacing, so that the increased particle velocity is also distributed in vertical direction.
The particle velocity is in the same order of magnitude as was calculated for the average perpendicular particle velocity in Chapter 4 (0.033-0.046 m/s). At 15 rpm, the extra particle velocity is small, approximately 0.01 m/s, so that the rotor effect does not add to the particle impacts.
The concentration of freezing point depressant is likely to influence the effectiveness of the rotor, because it also determines the particle velocities. If the particles already move faster at a certain concentration of freezing point depressant, the rotor effect will be relatively less important.
Too high rotation velocities might cause the particles to be clustered near the walls, which may explain why at a bed voidage of 0.79 no stable ice slurry generation was obtained, while this was possible at a bed voidage of 0.86.

5.5.4 Conclusion

No clear benefits were obtained using a rotor during stationary fluidization. The rotor did affect heat transfer and freeze-up conditions. At slow rotation velocities heat transfer decreased compared to fluidized bed ice slurry generation without rotor. At rotation speeds of 55 rpm, performance is similar to those of fluidized beds without rotor. At higher rotor speeds performance may reduce again because of an increasingly uneven radial particle distribution.
In the current set-up stable ice slurry generation in circulating fluidized bed mode was not obtained, because of the extra pressure drop induced by the rotor.

5.6 Conclusions

The stationary fluidization process has been quantified in detail. The general theory on liquid/solid fluidization of Richardson and Zaki is shown to be applicable also for ice slurry generation. Parameters determined experimentally are in accordance with literature. Additional experiments have confirmed the heat and mass transfer mechanisms determined in Chapters 3 and 4. Furthermore, the influence of particle size and fluidized bed diameter has been discussed. An evaluation of the number of effective particle-wall impacts has been used to further optimize the fluidized bed ice slurry generator in stationary operating mode. The optimal bed voidage is determined and also the influence of the d_p/D-ratio is evaluated.

Three operating modes that may extend the applicability of the fluidized bed ice slurry generator have been discussed. Preliminary experiments with circulation of the fluidized bed particles do not show an improvement of the fluidized bed heat transfer and allowable temperature difference, which is due to limitations of the experimental set-up. The installation of a rotor system also has not led to an improvement of the fluidized bed performance, mainly because of the hindrance effects of the rotor on the fluidization.

From the theoretical evaluations it is concluded that from circulation more benefits are to be expected. Circulation of the solid particles may yield particles impacting with higher kinetic energy, while still operation at the optimum bed voidage is possible. Key to a stable circulating fluidized bed ice slurry generator is prevention of ice slurry flowing upwards through the downcomer.
It is considered unlikely that a rotor system will lead to further improvements. Using the rotor system, the optimum bed voidage near the heat exchanger walls is disturbed and therefore benefits of increased particle kinetic energies are reduced by a low particle impact frequency.
From a theoretical study of parallel fluidization of multiple beds it is concluded that there are methods feasible for use with ice slurries, although some parallel fluidization systems are excluded.

Nomenclature

A	area (m^2)
$c_{1..7}$	constant coefficients (-)
C_D	drag coefficient (-)
D	diameter (m)
d_p	particle diameter (m)
d_{p_eq}	equivalent particle diameter (m)
$\bar{E}$	elasticity modus (-)
E	energy (J)
EG	ethylene glycol
f	friction factor (-)
F	force (N)
$\bar{f}$	average frequency (1/s)
Fr	Froude number (-)
F_u	scale of aggregation (-)
g	gravitational acceleration (m^2/s)
h	height (m)
K	helpfunction
L	length (m)
m	mass (kg)
$\dot{m}$	mass flow (kg/s)
n	Richardson Zaki coefficient (-)
Nu	Nusselt number (-)
P	power (W)
Δp	pressure drop (Pa)
Pe	Peclet number
Pr	Prandtl number (-)
r	radial position(m)
R	radius (m)
R^2	R-squared value
Re	Reynolds number (-)
T	temperature (^{o}C)
ΔT	temperature difference (K)
T_{f_init}	initial freezing temperature (^{o}C)
u	velocity (m/s)
u_s	superficial velocity (m/s)
v	velocity (m/s)
V	volume (m^3)
W_A	Work of adhesion (J/m^2)

Greek

α	heat transfer coefficient (W/m^{2}K)
ε	bed voidage (-)
η	efficiency (-)
λ	thermal conductivity (W/mK)
μ	dynamic viscosity (Pa.s)
ν^2	Poisson ratio (-)
ρ	density (kg/m^3)
φ_v	volumetric flow (m^3/s)
ψ	sphericity (-)

Subscripts

c	circular force
calc	calculated
circ	circulating fluidization
cyl	cylinder
D	drag
downc	downcomer
e	elastic wave
eff	effective
eq	equivalent
f	fluid
h	hydraulic
init	initial
l	liquid
max	maximum
meas	measured
melt	melting
mf	minimal fluidization
p	particle
is	ice slurry
s	superficial
sp	single phase
stat	stationary fluidization
t	transferred
term	terminal
τ	shock wave
wtb	wall-to-bed
x	perpendicular direction
∞	terminal

References

Bordet, J., Le Goff, P., Vergnes, F., 1972, *Mesures statistiques de la vitesse horizontale de particules solides fluidisées par un liquide a l'aide d'un capteur piézoélectrique, analogie avec la théorie cinétique de gaz*, Powder Technology 5, p365-375.

Chhabra R.P., 1995, *Wall effects on free-settling velocity of non-spherical particles in viscous media in cylindrical tubes*, Powder Technology 85, p83-90

Chhabra, R.P., Agarwal, L., Sinha, N.K., 1999, Drag on non-spherical particles: An overview of available methods, Powder Technology 101, p288-295.

Clift, R., Grace, J.R., Weber, M.E., 1978, *Bubbles, drops and particles,* Academic Press, New York

Erdmann, C., 1993, *Wärmeaustaucher mit zirkulierender Wirbelschicht zur Verhinderung von Belagbildung*, Ph.D-thesis RWTH Aachen, VDI-Verlag, Düsseldorf.

di Felice, R., 1995, *Hydrodynamics of liquid fluidisation*, Chemical Engineering Science 50 (8), p1213-1245

Foscolo, P.U., and Gibilaro, L.G., 1984, *A fully predictive criterion for the transition between particulate and aggregate fluidization*, Chemical Engineering Science 39 (12), p1667-1675

Foumeny, E.A., Kulkarni, A., Roshani, S., Vatani, A., 1996, *Elucidation of pressure drop in packed bed systems,* Applied Thermal Engineering 16(3), p195-202

Grbavčič, Ž.B., Garić, R.V., Vuković, D.V., Hadžismajlović, D.E., Littman, H., Morgan III, M.H., Jovanović, S.D., 1992, *Hydrodynamic modeling of vertical liquid-solids flow*, Powder Technology 72, p183-191.

Haid, M., Martin, H., Müller-Steinhagen, H., 1994, *Heat transfer to liquid-solid fluidized beds*, Chemical Engineering and Processing 33, p211-225

Haid, M., 1997, *Correlations for the prediction of heat transfer to liquid-solid fluidized beds*, Chemical Engineering and Processing 36, p143-147

Hewitt, N. J. and McMullan, J. T., 1997, *The replacement of CFCS in refrigeration equipment by environmentally benign alternatives*, Applied Thermal Engineering 17(8-10), p955-972

Hirata, A., and Bulos, F.B., 1990*, Predicting bed voidage in solid-liquid fluidization*, Journal of Chemical Engineering of Japan 23, p599-604

Jamialahmadi, M., Malayeri, M.R., Müller-Steinhagen, H., 1996, *A unified correlation for the prediction of heat transfer coefficients in liquid/solid fluidized bed systems*, Transactions of the ASME, Journal of Heat Transfer 118, 952-959

Klaren, D.G., 1975, *Development of a vertical flash evaporator,* PhD-thesis, Delft University of technology, WTHD n.69.

Klaren, D.G., 1983, US-patent no. 4401152.

Klaren, D.G., 2000, Self-cleaning heat exchangers, In: Müller-Steinhagen, H., *Handbook heat exchanger fouling: mitigation and cleaning technologies*, Institution of Chemical Engineers, Rugby: p186-198

Kollbach, J.S., 1987, *Entwickelung eines Verdampfungsverfahrens mit Wirbelschicht-Wärmeaustauscher zum Eindampfen krustenbildender Abwässer*, Ph.D-thesis RWTH Aachen.

Kopko, R.J., Barton, P., McCormick, R.H., 1975, *Hydrodynamics of vertical liquid-solids transport,* Industrial & Engineering Chemistry Process Design and Development 14, p264-269

Kwauk, M., Li, J., Liu, D., 2000, *Review-Particulate and aggregative fluidization-50 years in retrospect*, Powder Technology 111, p3-18

Liang, W.G., Zhu, J.X., Jin,Y., Yu, Z.Q., Wang, Z.W., Zhou, J., ,1996, *Radial non-uniformity of flow structure in a liquid-solid circulating fluidized bed,* Chemical Engineering Science 51 (10), p2001-2010

van der Meer, Th. H. , Hoogendoorn C.J., 1978, *Heat transfer coefficients for viscous fluids in a static mixer*, Chemical Engineering Science 33(9), 1978, p1277-1282

Meijer, J.A.M., Wesselingh, J.A., Clobus, A., Goossens, M.L.A. 1986, *Impacts against the wall of a scaled up fluidized bed*, Desalination 58, p1-18

Ottjes, J.A. 1981, *A measuring system for particle impact velocities and application in a pneumatic transport line*, Chemical Engineering Science 36, p1337-1347

Rautenbach, R., 1985, patent no. DE 3432864

Rautenbach, R., Erdmann, C., Kolbach, J.S., 1991, The fluidized bed technique in the evaporation of wastewaters with severe fouling/scaling potential-latest developments. applications, limitations. Desalination 81, p285-298

Richardson, J.F., Zaki, W.N., 1954, *Sedimentation and fluidization*, Transactions of the Institute of Chemical Engineers 32, p35-53

Richardson, J.F., Smith, J.W., 1962, *Heat transfer to liquid-fluidized systems and to suspensions of coarse particles in vertical transport,* Transactions of the Institute of Chemical Engineers 40, p13-22

Rowe, P. N., 1987, *A convenient empirical equation for estimation of the Richardson-Zaki exponent,* Chemical Engineering Science 42(11), p2795-2796

VDI, 1994, *VDI Wärmeatlas: Berechnungsblatter für den Wärmeübergang*, 7e Ed. VDI Düsseldorf.

Yu, T., Xiu Yu, Liu, Y., Gui Liu, Shao Jiang, Wu, J., 2003, *Fouling Preventing Technology for Water-Cooled Condensers With Self-Rotating Twisted Strips Driven by Spiral Inlet Bearings,* Proceedings of the 21st Congress of Refrigeration of the IIR, Washington DC, paper ICR0376

Zheng, Y., Zhu, J-X., Marwaha, N.S., Bassi, A.S., 2002 *Radial flow structure in a liquid-solids circulating fluidized bed,* Chemical Engineering Journal 88, p141-150

6 Optimization of the Stages of an Ice Slurry Secondary Cooling Cycle

6.1 Stages of a Secondary Cooling Cycle

The performance of an ice slurry system depends strongly on the application. In a system where cold needs to be distributed over long distances, transport properties and heat losses are important, while in applications that hardly require storage or transport of the cooling medium, the heat exchanger performance is more decisive. In this section the secondary cooling cycle is split into four stages, for each of which performance is optimized separately.

An ice slurry secondary cooling cycle can be characterized by four stages. These are ice generation, storage, transport and utilization stages, as displayed in Figure 6.1. Stage 1 is the ice slurry generation stage, where an ice slurry generator links the secondary cooling cycle with the primary cycle. The ice slurry generator is the evaporator of the primary cycle. Heat is extracted from the secondary cycle by the evaporation process, which produces ice in a slurry.

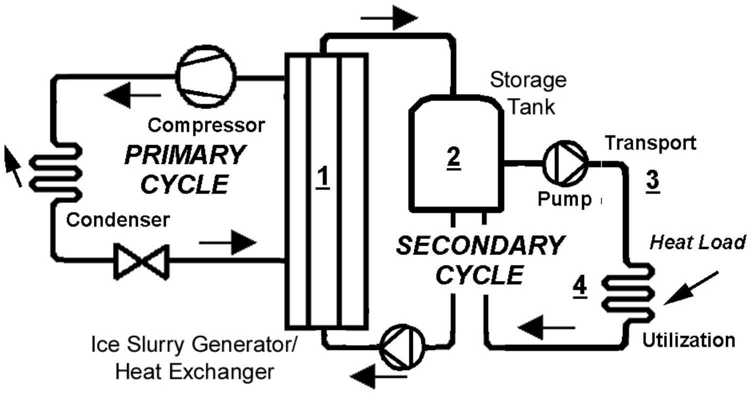

Figure 6.1: Stages of a secondary cooling cycle

A falling film evaporation system is assumed to be most suitable for the fluidized bed ice slurry generator. Falling film systems are expected to have a high heat transfer performance at low refrigerant charge. Also falling film systems can be higher than other evaporators as for example pool boiling systems. Disadvantageous may be a complicated film distribution system and a recirculation pump required for unevaporated primary refrigerant. A discussion of the evaporation side of the fluidized bed ice slurry generator is given in Appendix 1.

Stage 2, a storage tank, is not always required in a secondary cooling system, but the ability to store cold can be an important reason to install a secondary cooling cycle. Economic and energetic benefits can be obtained by shifting the cooling load to off-peak hours and by leveling of the cooling load to decrease the investments in the primary cycle. The cooling system can produce ice slurry during the night, with low electricity tariffs and low condensation temperatures, which is then used for the peak cooling load during the day.

In the third stage the ice slurry is transported to the areas where cooling capacity is required. The transport stage can be of considerable importance, for example in large supermarkets and in district cooling applications, where distances of several hundred meters may be required.

The final stage consists of the utilization heat exchangers, located in various types of consumer equipment. After melting the resulting fluid is returned to the storage tank in closed systems. The utilization stage and ice slurry generator may also be connected directly.

Ice slurry systems have also been reported that cool utilization heat exchangers without ice transport. In such systems ice is accumulated in high concentrations in a storage tank, from which only cold water without ice is extracted and pumped to utilization heat exchangers. The warm return water is inserted in the ice slurry tank. These systems may apply higher ice concentrations in the storage stage, but do not use the benefits of ice slurries during transport. In such systems the ice slurry technology is applied in a similar way as in ice banks.

6.2 Ice Slurry Generation

6.2.1 Introduction

Performance of the ice slurry generation stage is mainly determined by the heat transfer and the investment costs of the ice slurry generator. Further parameters are the operating range, additional power input required and maintenance costs. In this section these parameters are discussed for ice slurry generators in general and specifically for fluidized bed, scraped surface, direct contact and vacuum type ice slurry generators. Several other ice slurry generation methods have been reported that are not discussed here (Kauffeld et al., 1999; Fukusako et al., 1999).

6.2.2 Ice Slurry Generators

Fluidized Bed Ice Surry Generator

In the early nineties, Klaren and Van der Meer (1991) proposed the use of fluidized bed heat exchangers for the production of ice slurry. Up till then the fluidized bed as a refrigeration technique had only been used in desalination applications. In Chapters 3 to 5 heat and mass transfer and fluidization processes have been experimentally investigated.

The main advantage of the fluidized bed ice slurry generator is that there are little heat exchanging area limitations. The bed height can be up to 4-5 m, while the ice slurry generator can still be driven by a single pump. Heat transfer coefficients determined are high, 4 times that of single phase heat transfer. Disadvantageous may be the limited temperature driving force applicable at relatively high temperatures. Also small scale applications may have relatively high investment costs compared with large capacity applications.

Scraped Surface Ice Slurry Generator

Scraped surface ice slurry generators have been applied commercially for several years (Paul, 1997). A schematic lay-out is given in Figure 6.2. A primary refrigerant is evaporated in the annular space between the walls of two concentric tubes. The ice slurry feed flows through the inner tube, where ice is formed on or near the surface of the inner tube and removed by shaft-driven scrapers. The heat exchanging area is limited to the area in contact with the primary refrigerant. For an acceptable surface-to-volume ratio of the heat exchanger, a central non-flow region is used to reduce the flow area. A high superficial velocity is not always required in the scraped surface systems, as the systems are often used in single-pass mode. A large increase of the ice fraction from inlet to outlet may then be more important than a high heat transfer coefficient.

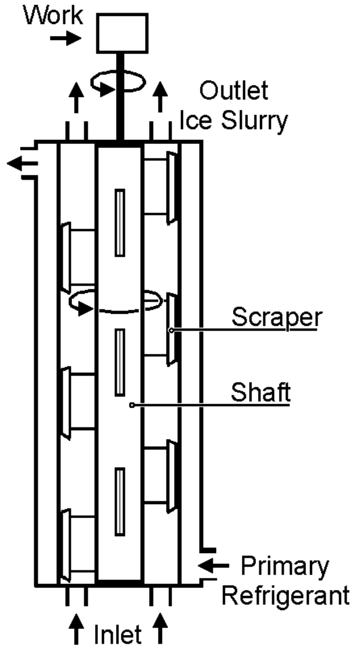

Figure 6.2: Scraped Surface Ice Slurry Generator

In a variation of the scraped surface heat exchanger there are no scrapers, but a rod is used that orbits along the inner surface of the tubes. The rods are reported to require less maintenance and also to have higher heat transfer performance than the scraper systems (Gladis et al., 1995).

Vacuum freeze systems

Vacuum freeze evaporators are based on the vacuum freeze triple point principle. An aqueous feed solution is introduced into a vacuum chamber where the pressure is maintained slightly below the triple point of the solution. A fraction of the feed flow flashes into vapor. The process is adiabatic and therefore the heat required for evaporation will be extracted from the rest of the solution, which results in the formation of ice crystals. The ice crystals become suspended in the fluid and form an ice slurry. The water vapor and the non-condensable gases have to be removed from the flash tank to keep the pressure at its original level. This can be achieved directly or indirectly.

Direct Vacuum System

Water vapor and non-condensable gases are removed from the flash tank and compressed with a water vapor compressor and subsequently condensed using water or air coolers. Although the amount of flash vapor produced in the flash tank may be small, the low operating pressure and the large specific vapor volume of water requires the use of compressors with large swept volumes (Paul, 1996). A schematic diagram of a direct vacuum system is given in Figure 6.3.

Indirect Vacuum System

The expensive compressor of the direct system can be avoided by replacing it with a refrigerated heat exchanger. The flash vapor is removed by condensing it or by freezing it onto the surface of an evaporator (desublimation). The evaporator is coupled to a primary compression refrigeration cycle. The non-condensable gases have to be removed by a vacuum pump. With the vacuum-sublimation process ice slurry may be produced at temperatures between 0°C and -20°C, depending on the additives used (Zakeri, 1997). If the flash vapor is desublimated, the heat exchanging surface needs to be defrosted regularly. A schematic layout of an indirect system is displayed in Figure 6.4.

Indirect systems can use volatile freezing point depressants, for example ethanol, to prevent freeze up of the indirect heat exchangers. The concentration of ethanol in the vapor phase is then higher than in the ice slurry solution, so that the freezing point of the condensed solution is much lower than in the ice slurry. Disadvantageous is that a lower pressure is required than the 6 mbar for the triple point of pure water. Furthermore, some ethanol may be removed by the vacuum pump with the non-condensables.

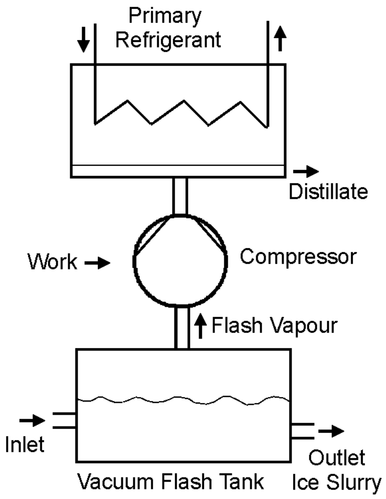

Figure 6.3 Direct Vacuum System

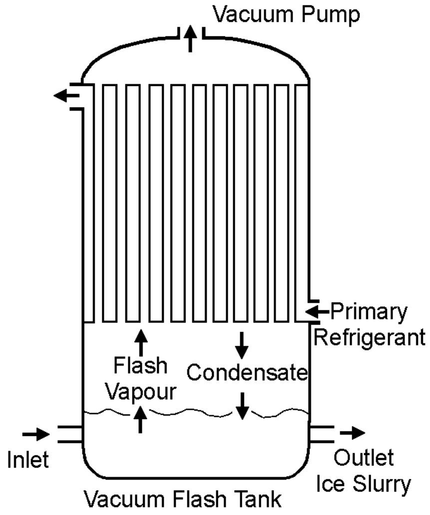

Figure 6.4: Indirect Vacuum System

<u>Direct Contact Ice Slurry Generator</u>

In a direct contact ice slurry generator a primary refrigerant immiscible with water is expanded and then injected into a water tank where it evaporates. The evaporation cools and supersaturates the water and small dispersed ice particles form. Injection devices are required in the evaporating tank that distribute the primary refrigerant so that ice slurry will be formed evenly throughout the tank. The injectors should be designed so that there is no risk of ice formation on the injectors themselves. Injection and evaporation have to induce enough turbulence to make sure that a finely dispersed ice slurry will form. Additional agitation by a stirrer may however be required to keep the ice slurry homogeneous.

Withdrawal of the ice slurry formed inside the tank may be difficult, because the primary refrigerant must fully remain in the system. A schematic diagram is shown in Figure 6.5 (Wobst and Wollmer, 1999).

The main advantage of the direct contact is that no physical boundary exists between the primary refrigerant and the ice slurry, reducing investments and increasing heat transfer rates. This however can also be disadvantageous: If the main reason to install an ice slurry system is to create a physical boundary between primary refrigerant and customer heat exchanger.

An alternative arrangement for a direct contact heat exchanger, is described in Fukusako et al. (1999). Here the primary refrigerant is used to cool a non-soluble liquid, which is then sprayed in the ice slurry feed water, using similar injection nozzles as for direct evaporation. Advantage of this method is that also primary evaporating refrigerants can be used that do mix with water, for example ammonia. Demands on the non-soluble liquid are however high, because it should have higher density than water and also a much lower freezing point (Fukusako et al., 1999; Inaba, 2001).

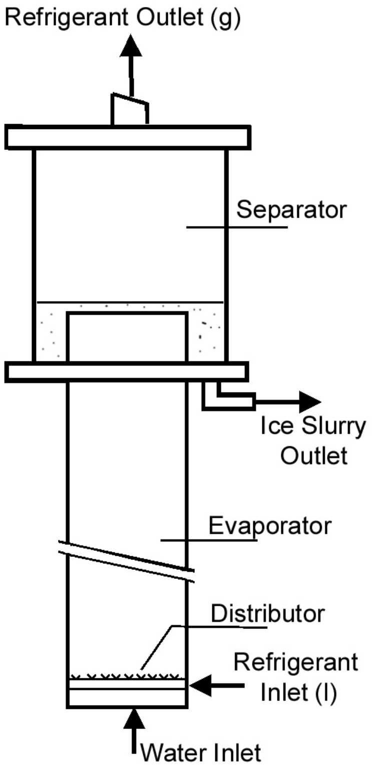

Figure 6.5: Direct Contact Ice Slurry Generator (Wobst and Wollmer.1999)

6.2.3 Heat Transfer Performance

Ice slurry generators can be improved by optimization of their heat transfer performance, so that a smaller generator is sufficient and investment costs are lowered. Heat transfer is governed by similar relations in various ice slurry generators and therefore requirements are similar for different ice slurry generators.

In the ice slurry generator a device or method is required to prevent build-up of ice layers on heat exchanging walls. If some kind of scraping action, as for example in the fluidized bed ice slurry generator or the scraped surface heat exchanger is involved (Paul, 1997), turbulent flow conditions are likely. Heat transfer on the slurry side of the ice generator can be estimated with a general expression of the Nusselt number:

$$Nu = c_1 Re^{c_2} Pr^{c_3} \tag{6.1}$$

Depending on the type of heat exchanger additional factors can be included, as for example discussed in Chapter 3 for fluidized bed ice slurry generators. For single phase heat transfer under turbulent flow conditions in tubes without scraping action, c_1=0.023, c_2=0.8 and c_3=0.33 (Holman, 1997).

For the scraped surface evaporator values were determined empirically by Bel and Lallemand (1999) for a screw-type scraper:

$$Nu = (Re_{rad} + Re_{ax})^{0.245} Pr^{0.142} \tag{6.2}$$

in which Re_{rad} is the radial Reynolds number relative to the rotational velocity and Re_{ax} the axial Reynolds number relative to axial velocity. The Reynolds numbers should be in the ranges $250<Re_{rad}<7000$ and $5<Re_{ax}<1500$. Values predicted with Equation 6.2 are relatively low compared with values of α reported by other authors for scraper or orbital rod systems (Gladis et al., 1995). Apparently the screw type lay-out of the experimental set-up limits the flow that can be achieved in the heat exchanger.

Another correlation of the form of Equation 6.1 was therefore also used, developed in a scraped system called the cooled disc column crystallizer (Vaessen, 2003):

$$Nu = 0.086 \cdot Re^{0.8} Pr^{0.3} \tag{6.3}$$

Wall-to-bed heat transfer coefficients of the fluidized bed ice slurry generator are predicted with the correlation developed in Chapter 3:

$$Nu_h = 0.061 \cdot Re_h^{0.72} Pr^{0.62} \tag{6.4}$$

The optimum bed voidage for heat transfer, determined in section 5.2.8, is ε=0.76, assuming cylindrical particles and a Richardson-Zaki coefficient of n=2.57. This value may increase by circulation of the fluidized bed particles, but since this has not been confirmed experimentally yet, stationary fluidization is assumed. In 55 mm tubes the optimum bed voidage of 0.76 is achieved at a superficial velocity of approximately 0.3 m/s, for typical ice slurry properties.

For the ice slurry generators discussed, the coefficients of Equation 6.1, are in the range 0-1 and also $c_2>c_3$, so that heat conductivity, density and heat capacity of the ice slurries need to be high for a high heat transfer coefficient, and the viscosity low.

Heat transfer in indirect vacuum systems can be estimated using the following laminar condensation heat transfer correlation (Green and Maloney, 2000):

$$Nu = \frac{\alpha L}{\lambda} = 0.925\left(\frac{L^3 \rho^2 g}{\mu \Gamma}\right)^{1/3} \tag{6.5}$$

in which Γ is the mass flow per unit periphery and L the cooled tube length. The ice generated is 7.4 times the amount of vapor to be condensed, the amount of condensate is therefore relatively low. If a non-volatile freezing point depressant is used, the condensate consists of pure water that may be supercooled. An ice layer will build-up and regular defrosting is required. If a volatile additive is used, for example ethanol, the concentration in the vapor phase will be determined by the concentration in the liquid phase and not directly by the ice fraction. Viscosity and thermal conductivity of the condensate will be relatively constant and also the heat transfer coefficients calculated with Equation 6.5 are fairly constant with ice fraction. Film heat transfer coefficients predicted are in the range of 1500 to 2000 W/m^{2}K for 0.025 m diameter tubes and a Γ of 0.05 kg/ms.

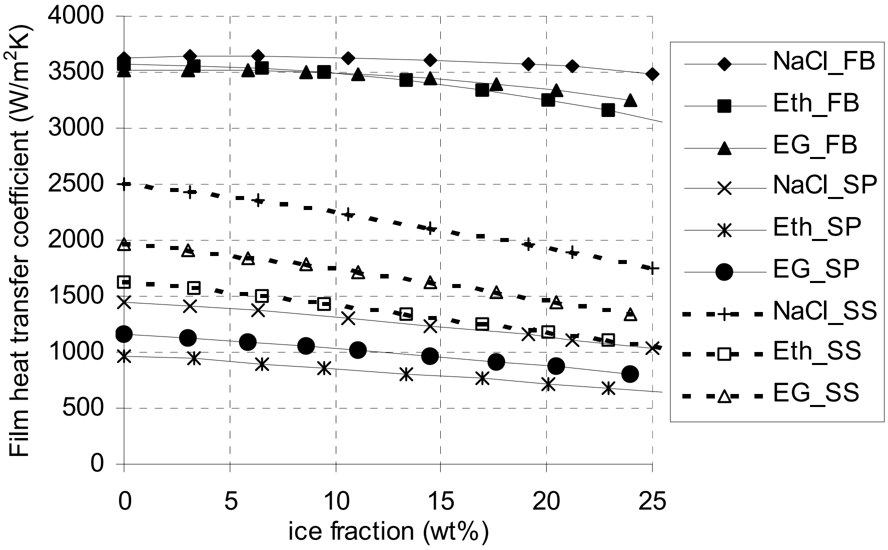

Figure 6.6: Heat transfer coefficients at –5 °C of three freezing point depressants at increasing ice fraction for Fluidized bed (FB), Scraped surface (SS) and Single phase (SP)

In Figure 6.6 internal heat transfer coefficients are displayed versus the ice fraction for a few freezing point depressing substances at –5 °C, a typical ice slurry temperature for cooling applications. Conditions assumed for the calculations are summarized in Table 6.1. Heat transfer coefficients are the highest in the fluidized bed ice slurry generator. Heat transfer for the scraped surface systems is likely underpredicted by Equation 6.2 and therefore Equation 6.3 is used. It should be noted that the markers of Figure 6.6 do not correspond with measurements but function to distinguish between the curves.

Table 6.1: Conditions for Figures 6.6 and 6.7

System		*Fluidized Bed*	*Scraped Surface*	*Single Phase*
tube diameter	m	0.055	0.055	0.028
fluid velocity -5°C	m/s	0.3	0.3	0.6
fluid velocity -20°C		0.25	0.25	0.5
bed voidage	-	0.76	x	x
particle size	mm	4	x	x

Heat transfer coefficients decrease at higher ice fractions for the ice slurry generators of Figure 6.6. Only if the scraped surface ice slurry generator coefficients are calculated with Equation 6.2, the heat transfer coefficients are predicted to increase at increasing ice fraction (not displayed in Figure 6.6). This corresponds with the trends observed by Bel and Lallemand (1999).

The condensation heat transfer coefficients of the indirect vacuum systems are nearly constant with ice fraction. The order of magnitude is similar to the scraped surface systems. The indirect vacuum systems are not included in Figure 6.6, because these systems can only be used for freezing point depressants that are more volatile than water. For less volatile freezing point depressants, ice layers build-up and defrosting cycles are necessary.

At –5 °C NaCl has the highest heat transfer performance of the freezing point depressants. Differences for the fluidized bed ice slurry generator are however small. Only above 0.20 ice fraction a significant difference is observed. In the scraped surface and single phase heat transfer systems, the freezing point depressant applied is more significant. NaCl again has the

highest heat transfer coefficients, up to 50% higher than ethanol for the scraped surface system and up to 60% higher than for ethanol in single phase heat transfer.
Heat transfer coefficients calculated at –20 °C are given in Figure 6.7. NaCl is now replaced by potassium formate (KFor), as the eutectic point of NaCl prohibits its application at –20 °C. At this lower temperature the share of latent heat in the apparent heat capacity decreases and the viscosity increases, as was seen in section 2.1.6. At –20 °C, ice slurries based on KFor in the fluidized bed ice slurry generator result in the highest heat transfer coefficients. The influence of the increased viscosity at increasing ice fraction becomes significant, especially for ethanol and ethylene glycol. Also for KFor ice slurries heat transfer coefficients become significantly lower at ice fractions above 0.15.

For direct contact systems and the direct vacuum ice slurry generators no heat transfer surfaces are involved and these systems have therefore not been included.

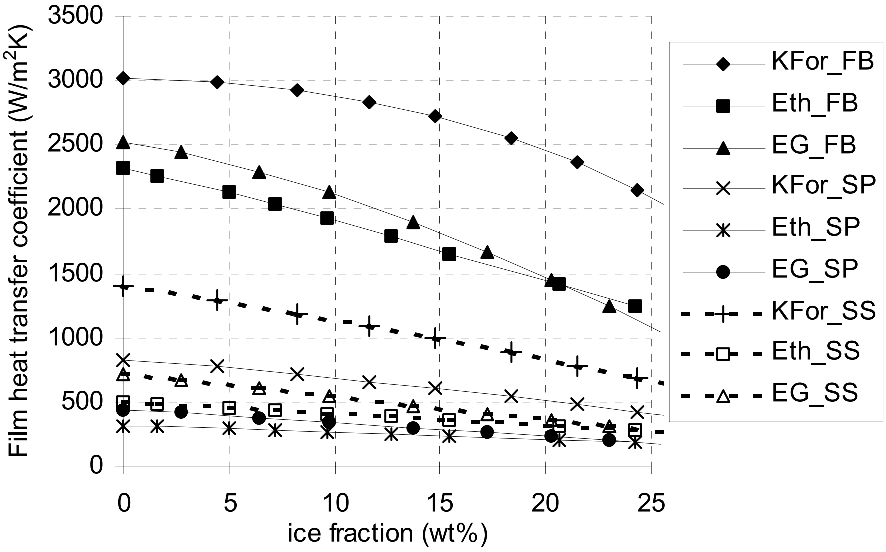

Figure 6.7: Heat transfer coefficients at –20 °C of three freezing point depressants at increasing ice fraction for Fluidized bed (FB), Scraped surface (SS) and Single phase (SP)

6.2.4 Operating Limits and Other Effects

The efficiency of ice slurry generators can also be improved by extending the operating range, so that a higher temperature difference can be applied. A smaller generator is then sufficient and investment costs are lowered. There is however an optimal temperature difference that minimizes total costs. The optimum overall temperature difference for most systems is estimated to be in the range of 6-8 K. This can be obtained for ice slurry temperatures below approximately –4 °C, for example with a NaCl ice slurry produced in a fluidized bed ice slurry generator. Only at higher temperature applications an extension of the operating range may be required.
In most types of ice slurry generator there is a maximum temperature difference above which freeze-up occurs. The method developed in Chapter 4 may be applied to compare different ice slurry generators. In some types of ice slurry generator however freeze-up cannot be avoided and temporary defrosting is required.

The operating range of the fluidized bed ice slurry generator can be optimized with the

particle size and the d_p/D-ratio. This ratio has an optimum at which the number of effective particle-wall impacts is at a maximum. In section 5.2.6 the optimum *dp/D*-ratio was determined at approximately 0.1. Using 4 mm solid particles therefore a 40 mm internal diameter fluidized bed can be applied. Larger particles yield a larger temperature difference allowable, but particles larger than 5 mm are difficult to produce.
Apart from fluidized bed conditions, also ice slurry properties can be optimized. An ice slurry in which the solid particles obtain high kinetic energy and in which there also is a low work of ice adhesion to the heat exchanger wall can be selected, for example an ice slurry based on ethylene glycol. Also the pH can be adjusted to improve the operating range. This is likely to be effective only for selected inorganic freezing point depressants (Hobbs, 1974).

For scraped surface ice slurry generators, the maximum ice crystal growth velocity at the walls is expected to be determined by the rotation frequency of the scrapers. At increasing rotation speeds, the maximum temperature difference that can be applied increases. At higher freezing point depressant concentrations but constant rotation speed, it is expected that the crystal growth velocity at the walls will remain constant similar to the situation in the fluidized bed ice slurry generator. The temperature difference can be increased and a larger fraction of the ice crystals is formed in the bulk of the slurry, away from the walls.
The occurrence of a maximum temperature difference allowable in scraped surface systems has been reported, but not in detail for ice slurry systems yet. In one study dealing with simultaneous crystallization of ice and KNO_3, a maximum temperature difference is reported above which the crystallizer freezes because of ice adhering to the walls (Vaessen, 2003).
The effect of a scraper on a heat exchanger wall may be evaluated using the force that a scraper exerts on an ice layer adhered to the walls. A first study was carried out by Ishikawa et al. (2002). In such an evaluation also the contact surface area of the ice adhered to the wall must be determined before a prediction can be made of the scraper force required. A qualitative evaluation can however be made. From such an evaluation it can be expected that by using materials and freezing point depressants that minimize the work of adhesion of ice to the walls, will result in a larger temperature difference that may be applied before freeze-up. It is also expected that an adjustment of the ice slurry pH can increase the operating range of the scraped surface ice slurry generator for inorganic freezing point depressants.
The orbital rod system does not use direct scraping action, but induces high hydrodynamic forces in the narrow space between the rod and the heat exchanger wall. Alternatively, the rod itself may contact ice adhered to walls, whereby ice is removed from the walls by adhesive fractures or because of cohesive fractures in the ice. An evaluation of the forces involved with the work of adhesion may also indicate possible extensions to the operating range.

Indirect vacuum systems are limited in applicability because of the amount of freezing point depressant used. High concentrations are required to obtain low ice slurry temperatures, freeze-up of the heat exchangers is then unlikely, but the system pressure required becomes low. Low pressures may be maintained by removing not only non-condensables, but also freezing point depressants, which makes the system more similar to a direct vacuum system. At low concentrations of freezing point depressant, freeze-up of the heat exchangers may occur. An evaluation based on the work of adhesion of ice to the walls may predict the rate at which this occurs and indicate possible ways to reduce such effects. In some systems already coatings have been applied to reduce adhesion of ice to the heat exchanger surface (Fukusako et al., 1999).
Direct vacuum systems can only operate with pure water or very low concentrations of salt added. Part of the water is evaporated and removed from the system through the compressor. If additives would be used, the concentration in the liquid phase would rise significantly and

the freezing point would lower, so that only a smaller amount of ice would be formed than using pure water. The evaporation heat effect would be required to reduce the temperature of the solution to the lowered freezing point. Freeze-up of direct vacuum systems is not likely, as there are no cooled surfaces.

In most ice slurry generation systems some additional equipment is needed to operate the ice slurry generator. In the fluidized bed ice slurry generator this is a pump, in scraped surface methods this is the drive of the rotating scrapers, in vacuum systems a vacuum compressor is required. Power input to this additional equipment largely depends on the operating conditions and on the properties of the ice slurry. Requirements on ice slurry properties for additional equipment are often contradictory to the requirements for a high heat transfer. For example, in a fluidized bed system high ice fractions lead to lower heat transfer coefficients, but the pump efficiency increases if a positive displacement type of pump is used. Power requirements of additional equipment in ice slurry generators is relatively small compared to the heat transfer coefficients. In section 5.3.3 it was shown that only a small increase of the heat transfer coefficients would be sufficient to compensate for the additional pumping effort required to achieve circulating fluidization instead of stationary. Typically additional power requirements are approximately 3% of the capacity of the ice slurry generator.

Often ice slurries are generated using multiple passes through the ice slurry generator, while increasing the ice content of the ice storage tank. In the storage tank the ice fraction can then be raised to the desired levels, while in the production stage the ice fraction can be much lower, keeping efficiency of the ice generation high. The ice slurry feed flow to the generator can be kept low in ice content by using an ice concentrator after the ice generator, or by using a storage tank that is not homogenous, so that a high ice content layer will form in the upper section of the storage tank and a low ice content feed to the ice slurry generator can be taken out at the bottom of the storage tank.

6.2.5 Investment Costs and Scale-up

High heat transfer coefficients do not solely determine the performance of a system, a system with increased heat transfer coefficient often also has higher investment costs and additional costs. The investment costs also depend on the equipment size in different ways, which makes the economically most efficient ice slurry generator depend on the capacity of the application required.

Advantageous of the fluidized bed ice slurry generator is the option of a vertical increase of the system size at relatively low cost. The limiting factor is the maximum height of the falling film that can be achieved, which is estimated to be 2-3 m. The maximum height of the fluidized bed is up to 8-10 meters, system heights which have been achieved in several industrial fluidized bed heat exchangers. If two or three falling film sections are applied in series, also high fluidized bed ice slurry generators are expected to be possible, at relatively low investment costs per m^2 heat exchanger area. The design of the flow distribution section and particle separation sections will increase investment costs of the fluidized bed systems, compared with regular shell-and-tube heat exchangers. Also the falling film distribution system and additional solid particle handling equipment increases investment costs.
The solid particles are inexpensive and also the wear of the system parts through which the particles flow is acceptably low, as was discussed by Rautenbach and Katz (1996).

Because of the benefits of scale-up, the fluidized bed ice slurry generator is expected to be especially efficient for large applications, where other systems would require several smaller ice slurry generators in parallel, a single fluidized bed system could deliver a similar ice generation capacity. The fluidized bed ice slurry generator will be relatively inefficient economically in smaller systems and in applications where there is little vertical space available.

Investments for the scraped surface evaporator are relatively high because the scrapers must exactly fit the heat transfer surface, which therefore needs to be smooth. Furthermore the scrapers have high maintenance costs because of the mechanical moving parts and the scrapers that need to be replaced on a regular basis. There are also little benefits from an increase of scale. The size of a single scraping tube is limited, up to 2-3 m maximum. For large installations several scraped tubes therefore need to be installed, each with its own scraping mechanism.

Vacuum systems require high investments for equipment and control of the system because of the low pressure required. For direct vacuum systems a large compressor is required because of the large specific volume of water vapor. Indirect vacuum systems may require regular defrosting, so that extra heat transfer area is required for continuous operation. Small scale applications of vacuum ice slurry generation have not been reported, mainly because of the high investment costs. Systems have been tested for applications of around 100 kW capacity, for example in supermarket cooling. Direct vacuum systems have been applied for large cooling demands in the mining industry.

No heat exchanging surface is required for direct contact systems and therefore investment costs are relatively low compared to systems with heat exchanging surfaces. Expensive in direct contact systems are the injection nozzles, installed in the ice slurry tank. Design of the generator tank should make sure that there are no areas in the tank without agitation, which might cause non uniform ice formation and therefore blockages. Operating costs will be low, because there are not many parts requiring maintenance and also energy consumption is low, due to high heat transfer rates.
A heat transfer rate per volume of the direct contact tank has been reported of approximately 1000 W/m^3K (Wobst and Wollmer, 1999). This implies that the size of installations will be rather large. The tank(s) may however also be used as storage tank, which excludes the need of additional storage tanks. For higher capacities several direct contact ice slurry generators are required, therefore economical benefits of increasing the scale are only moderate.

6.2.6 Conclusion

There is not one type of ice slurry generator most efficient for all applications. There are different requirements on operating conditions as for example number of passes and ice fraction. Also systems with high ice slurry generation capacity may have high investment costs or limits in applicability. A suitable ice slurry generator can therefore only be selected if size, temperature and other constraints of the application are known. The fluidized bed ice slurry generator is expected to perform well in relatively large applications. Possible effects of the limit on the allowable temperature difference should be investigated further.

6.3 Ice Slurry Storage

6.3.1 Storage Tanks

In the storage stage the amount of cold stored per m^3 needs to be as high as possible. In this way size and investments for storage vessels can be minimized, as well as the wall surface area and consequent heat losses. In order to achieve this, ice slurries with a high ice fraction are needed with corresponding high apparent heat capacity.
In Figures 6.8 and 6.9 the volumes of tanks that would be required for storage of 2000 MJ of cold is shown versus the ice fraction for different additives at a temperature of –5 °C and -20 °C. It is assumed that the amount of cold stored equals the heat effect of fully melting the ice in the storage tank, including both latent heat and the sensible heat of the freezing range.

It is observed from Figure 6.8 that the required storage volume is only mildly influenced by the type of freezing point depressant used in the ice slurry. The important factor is the ice fraction itself.
At –20 °C the storage volume tank required is similar to that of –5 °C, as can be observed in Figure 6.9. The storage tank volume required appears to be slightly smaller at –20 °C, but this is an effect of the freezing range: At both temperatures only the ice fractions were calculated. The temperature variation caused by the freezing range at –20 °C is much larger than at –5 °C.

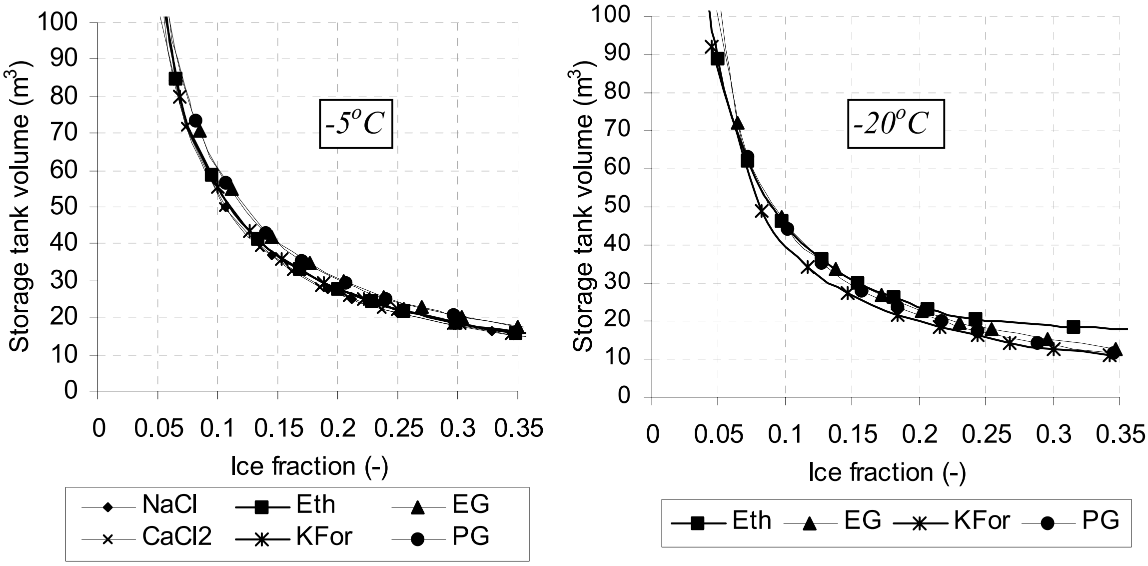

Figure 6.8 and 6.9: Storage tank volume required to store 2000 MJ (=556 kWh) of cold at –5 °C and –20 °C, assuming fully melting of the ice

6.3.2 Agitation

The density of ice in a slurry, approximately 915 kg/m^3, is significantly lower than the density of the liquid solution, which is typically in the range of 980-1200 kg/m^3. In a storage tank ice crystals will therefore separate and form a floating layer on top of the storage tank. It depends on the density difference, ice fraction and the size and shape of ice crystals how fast the crystals move upwards in the slurry. Typically a large transition zone will occur between an ice-rich layer in the top section of the tank and an ice-free layer at the bottom. This phenomenon can be used in applications, because ice slurries of the desired ice fraction can be extracted at various heights from the storage tank. Temperatures of ice free zones will not deviate from the equilibrium temperature in the ice slurry, because of natural convection. Liquid solution that has warmed up because of heat losses will rise in the storage tank and melt ice crystals.

If a homogeneous ice slurry is required in the storage tank, a low density difference between liquid and ice is efficient, as well as small ice crystals so that the liquid-ice settling is not as fast. The separation can be reduced by actively moving the ice crystals to the bottom of the tank. This is achieved by circulating pumps or by agitators or stirrers. Circulation pumps are not suitable for higher ice concentrations (>10%), because of a relatively high power requirements of the pump. More common is the installation of a stirrer or agitator. In some systems however other pumps already provide a substantial amount of kinetic energy, which may be applied for homogenization of the storage tank. For example in fluidized bed ice slurry generators, the ice slurry flow after the fluidized bed still has considerable velocity.

Power supplied for agitation will be dissipated and melt ice in the storage tank and therefore stirring power input must therefore be kept as low as possible. Power input required for a stirrer (*P*) can be estimated with the Power number N_P:

$$N_P = \frac{P}{D_s^5 N^3 \rho} = c_1 \cdot Re^{c_2} Fr^{c_3} \tag{6.6}$$

where *Fr* is the Froude number ($D_s N^2/g$) and c_1 to c_3 are constants depending on tank and stirrer geometry. *N* is the rotational speed of the stirrer, D_s the stirrer diameter. Under laminar flow conditions the index c_2 equals –1, which implies that stirring power in the laminar flow region is proportional to the viscosity and does not depend on other ice slurry properties. Low viscosity ice slurries will have the lowest power consumption for stirring. In the turbulent flow regime both indexes c_2 and c_3 tend to zero. Stirring power input then depends on the density of the ice slurry (Nagata, 1975). Ice slurries with low density will have lower power consumption.

The viscosity of the ice slurry determines the stirring power input in the laminar regime, but it is also significant for the stirrer design. At high viscosities, a relatively large stirrer is required that rotates slowly, while for low viscosities smaller stirrers are used at higher rotation speeds. Several stirrers for ice slurries have been discussed by various researchers, mainly similar in design to a propeller, but also stirrers specific for high viscosity have been discussed.

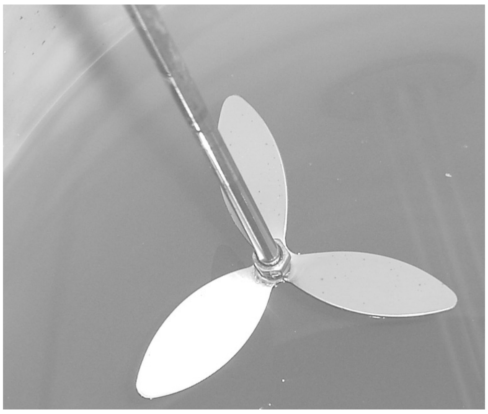

Figure 6.10: Stirrer used in experiments

In the current research also a propeller-type stirrer was used, displayed in Figure 6.10. It was not designed for viscous fluids or ice slurries. The propeller consisted of three blades that were slightly pitched. The radius of the propeller was 0.07 m. A storage tank of 0.55 m diameter containing 120 liters of ice slurry could be kept homogeneous up to ice fractions of approximately 0.15. The rotation speed of the stirrer was variable. At higher ice fractions, an increase of the rotational velocity did not result in a more homogeneous ice slurry in the storage tank. At too high rotation speeds, separation occurred, with a well mixed zone in the center of the tank near the stirrer and a nearly still standing zone near the walls of the tank. The rotor speed was varied in the range of 300-700 rpm. Stirring conditions were therefore in the turbulent regime, especially if the effect of the inflow of ice slurry returning from the fluidized bed ice slurry generator is also taken into account. Reynolds numbers near the stirrer are typically above 10^4.

The propeller was mounted at a variable angle, but operated at an angle of approximately 15^o from vertical in most experiments. The vertical position of the propeller was also variable. In most experiments it was in the center of the storage tank. The stirrer was powered with a motor of 50 W maximum capacity at a rotation speed of 2000 rpm.

At higher ice fractions than 0.15, a nearly still standing layer could be observed visually at the top of the storage tank. At lower ice fractions, the ice crystals visible from the top of the tank were continuously replaced.

The density of the outlet flow of the storage tank, which is near the bottom of the tank, decreased with increasing ice fraction up to an ice fraction of 0.15. This was determined using Coriolis mass flow/density meters. Above an ice fraction of 0.15, the outlet flow density did not decrease further, while the overall ice content of the ice slurry storage tank still increased.

Other researchers report that ice slurries were kept homogeneous up to higher ice fractions than 0.15, for example Christensen and Kauffeld (1998).

Agitation has considerable impact on several processes occurring in storage tanks (Pronk et al, 2002), which must be considered for each application and storage tank design. Due to recrystallization effects, the crystal size distribution of an ice slurry in a storage tank can change, which has impact on rheological and thermophysical properties of the ice slurry. Some researchers have suggested that these effects are responsible for the variation in experimental results of pressure drop and heat transfer studies in various laboratories.

Without agitation the floating top layer may stick together so that a Bingham type fluid is formed with a high yield stress. Drive power installed for stirrers should be designed so that it can deal with these yield stresses: It may be difficult to break up the top layer using basic stirrer equipment. Such effects were encountered during experiments. After a stop of the stirrer, an increased rotation speed was required to again homogenize the ice slurry in the storage tank.

In some systems effects of the storage stage can be compensated for in other equipment. If for example too large ice crystals are formed in the storage tank, these may be reduced by leading them again through the fluidized bed, where impacts of the solid particles may reduce their size.

6.3.3 Storage Heat Losses

Heat losses through the walls of the storage tanks can be limited by using high ice fractions, so that smaller tanks will suffice. The total wall surface area is relatively small, compared with the bulk of the ice slurry, especially for larger storage tanks. The heat losses of the storage tank are therefore relatively small compared with for example transport tubes, where the surface-to-volume ratio is much higher.

Heat transfer resistance of the walls of storage tanks can be efficiently improved with insulation. The resistance for heat transfer is then almost entirely in the walls and on the outside of the storage tanks. The ice slurry properties inside the storage tanks only slightly influence the heat losses.

An overall heat transfer coefficient for heat losses of 1-3 W/m^2K is typical for insulated stirred tanks. A layer of 1-3 cm of an insulation material with a thermal conductivity of 0.03

W/mK is assumed. The heat losses mainly depend on the tank design and insulation and are only marginally different for different ice slurries. For turbulent conditions, overall heat transfer coefficients may differ up to 5%, at approximately 3 W/m^{2}K. Under laminar conditions, up to 10% difference is found, with *U* at 1.5 W/m^{2}K at 0 ice fraction up to *U*=2 W/m^{2}K at 0.25 ice fraction.

The total stirring power input and heat losses under turbulent conditions hardly depend on the ice slurry properties. The trend of the power requirements in the storage tank are similar to Figures 6.8 and 6.9, i.e. decreasing at increasing ice fraction. The stirring power consumption is estimated at 70 W/m^3, based on the experiments of Kauffeld et al., 1999 in a tank of 9.5 m^3, with a propeller type stirrer of 700 mm diameter. The stirring power required in the current research for a tank filled with 0.1 to 0.2 m^3 was of the same order of magnitude. The total stirring power input and heat losses required to store 2000 MJ of cold at –5 ^{o}C is approximately 4.5 kW at an ice fraction of 0.20. This equals 0.8% loss of the cold stored per hour. Especially if long storage periods are required, it may be worthwhile not to stir the storage tank.

The trend of the additional power requirements for heat losses and stirring power under laminar stirring conditions, is displayed in Figure 6.11. At increasing ice fraction, the tank required is smaller and therefore heat losses decrease, but the stirring power required increases rapidly because of an increased viscosity. Therefore at ice fractions above approximately 0.15, the sum of stirring power and heat losses becomes constant or may increase with increasing ice fraction. Because of the widely varying viscosity of the ice slurries the additional power requirements under laminar conditions also differ widely between freezing point depressants, as can be observed in Figure 6.11.

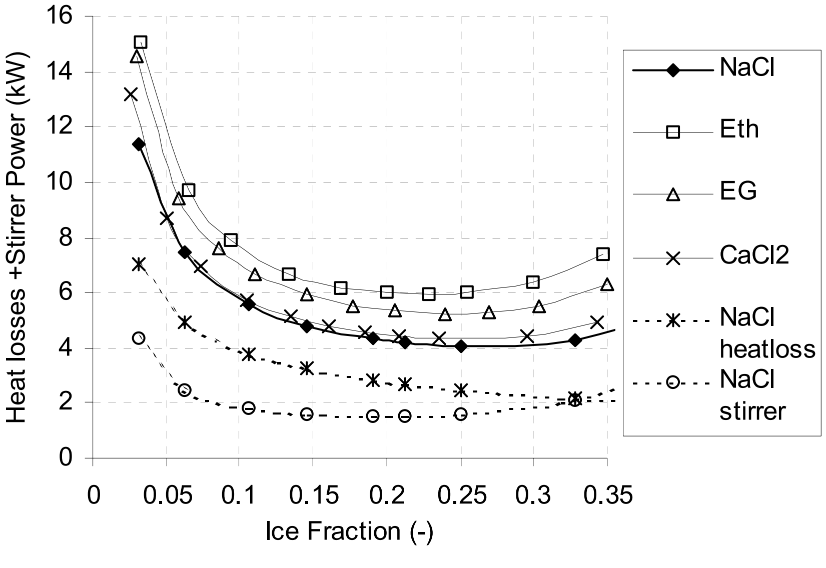

Figure 6.11: Additional power consumption of a stirred tank of 2000 MJ (=556 kWh) ice slurry at –5 ^{o}C. For NaCl the contributions of stirring and heat losses are given separately.

Heat losses to walls of Figure 6.11 were calculated with Equation 6.1 and coefficients c_1=0.332, c_2=0.5 and c_3=0.33 (Holman, 1997). The outside temperature was assumed to be 20 ^{o}C. The heat transfer coefficient of tank wall, insulation and outside heat transfer were estimated at 3 W/m^{2}K. The laminar stirring power input was estimated by assuming a proportional correlation with the viscosity of the ice slurry: 3 W/m^3 stirring power was assumed per 1 mPa.s ice slurry viscosity. Laminar stirring power requirements are much lower than turbulent stirring power requirements.

For NaCl as the freezing point depressant, the power requirements of stirring and heat losses are also displayed separately in Figure 6.11. It is observed that the relative contribution of the stirring power increases at increasing ice fraction. It should be noted that possible transitions to non-Newtonian flow behavior have not been considered here. A discussion of non-Newtonian rheology is given in Appendix 2.

6.4 Ice Slurry Transport

6.4.1 Introduction

In the transport stage performance of ice slurries is determined mainly by the apparent heat capacity, the heat losses and the pumping power consumption. At high apparent heat capacity, tube diameters of the cold transport system can be small, resulting in low investment costs and also low heat losses because of a small heat transfer wall area of the tubes. Small tube diameters however have a relatively high pressure drop, which increases the pumping power input. An optimization of ice fraction and tube diameter is therefore required in the design of transport tubes of secondary cooling cycles.

Plots of the tube diameters required versus the ice fraction result in similar curves as for the size of ice slurry storage tanks, compare Figure 6.12 with Figure 6.8. Pipe diameters required are mainly determined by the ice fraction and the freezing point depressant is relatively unimportant.

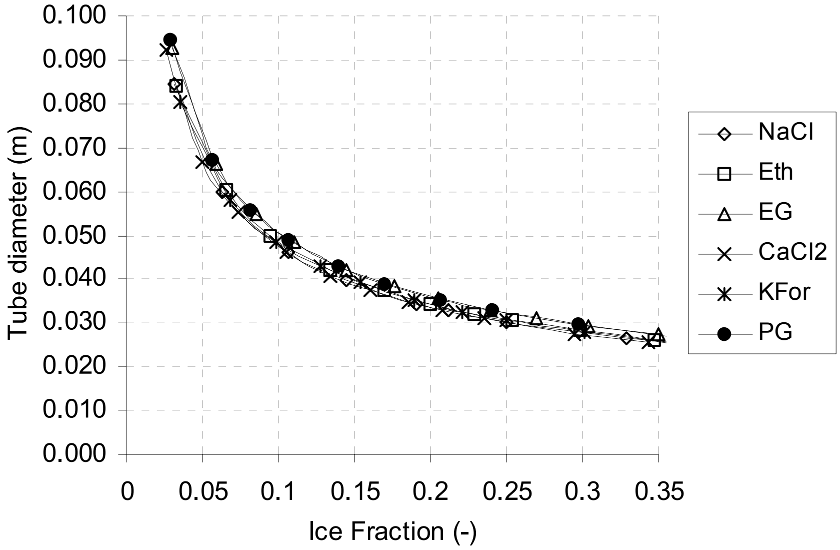

Figure 6.12: Tube diameters required to pump 100 kW cooling capacity at v=1.5 m/s

The ice fraction may be a requirement of the utilization heat exchangers, but if ice concentrators are applied, the ice fraction during transport may be varied. Such designs are however likely to be advantageous at relatively large transport distances only.

6.4.2 Pressure Drop

Pressure drop of ice slurries flowing in tubes is given by:

$$\Delta p = 2f \cdot \rho v^2 \cdot L / D \tag{6.7}$$

where f is the friction factor, for laminar flow conditions given by:

$$f = \frac{16}{Re} \tag{6.8}$$

For turbulent flow conditions the friction factor is estimated with the Blasius equation:

$$f = \frac{c}{Re^{0.25}} \tag{6.9}$$

where c is approximately 0.08.
The pressure drop is mainly determined by the viscosity for laminar flow conditions and by viscosity and density for turbulent flow conditions. The heat capacity and ice fraction are relevant indirectly, because these determine the tube diameter required.
In some applications, for example in fishery, ice slurry is used in open systems without return circuit. If a return is required, a small ice fraction may be left in the slurry after the utilization heat exchanger to keep the ice slurry return also at a constant low temperature. Since there is little ice left in the return flow, viscosity of the ice slurry is significantly lower and pumping effort is also lower than in the transport of the ice slurry to the application.

The pressure drop per meter tube is displayed in Figure 6.13 for –5 °C initial freezing point, for turbulent flow conditions in tubes of 25 mm diameter and 1 m/s transport velocity. Data markers do not correspond to experimental values. Only data for Reynolds numbers above 2000 are included in Figure 6.13. The pressure drop increases significantly at increasing ice fraction. Freezing point depressants NaCl and KFor result in the lowest pressure drops.

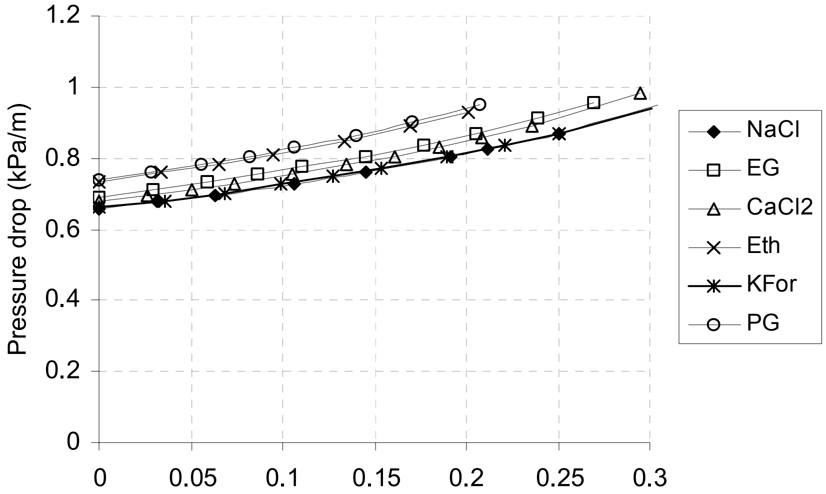

Figure 6.13: Pressure drop versus ice fraction for turbulent flow conditions (Re>2000) of various ice slurries. D=25 mm, v=1 m/s, initial freezing point –5 °C

An equal ice slurry transport rate and laminar flow conditions are obtained at a tube diameter of 100 mm and a velocity of 0.0625 m/s. Pressure drop for laminar conditions are displayed in Figure 6.14, where only data for Reynolds numbers under 3000 are included. For laminar flow conditions, pressure drops are considerably lower than for turbulent flows. The pressure drops increase exponentially with ice fraction, and therefore pressure drops become relatively high above ice fractions of 0.20. Also under laminar conditions NaCl and KFor have the lowest pressure drop.

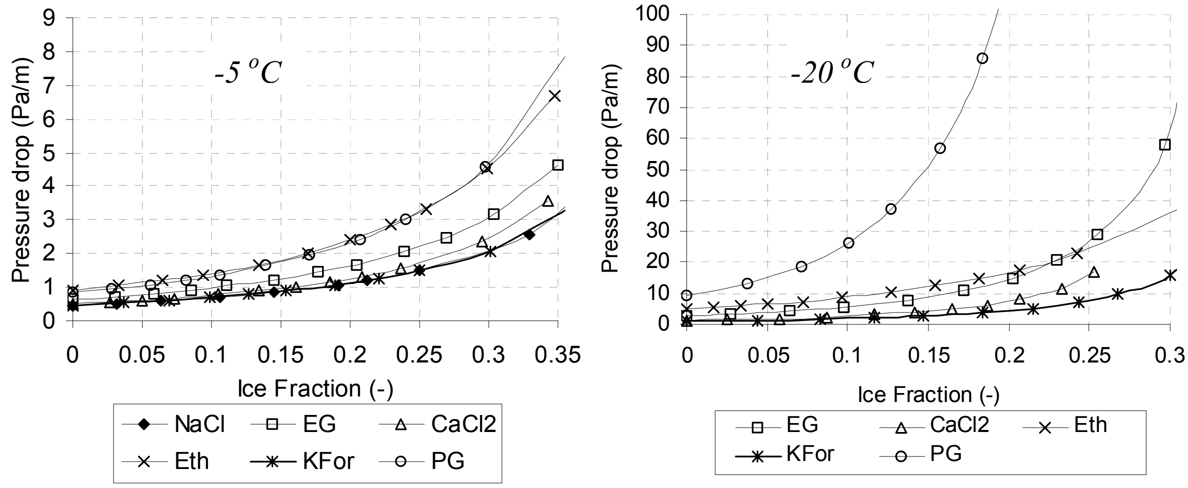

Figure 6.14 and 6.15: Pressure drop versus ice fraction for laminar flow conditions (Re<3000) of various ice slurries; D=100 mm, v=0.0625 m/s, T_{f_init}*= –5 °C and –20 °C*

In Figure 6.15 the pressure drop for laminar flow conditions are given at –20 °C. At this low temperature, viscosities are relatively high and therefore turbulent flow conditions are unlikely in transport tubes. Pressure drops are considerably higher than at –5 °C. Ice slurries based on KFor and $CaCl_2$ have the lowest pressure drop.

6.4.3 Ice Slurry Pumping

Power requirements of pumping ice slurries is estimated with:

$$P_{pump} = \frac{\Delta p \cdot \varphi_v}{\eta_{pump}} \cdot 100 \qquad (6.10)$$

in which η_{pump} is the efficiency of the pump, expressed as a percentage. The efficiency of the pump depends strongly on the design of the pump. Density and viscosity of the ice slurries are relevant ice slurry parameters, as well as the ice fraction. For centrifugal pumps, a low density of the ice slurry reduces power requirements and increases the pump efficiency. The presence of high ice fractions may reduce the performance of centrifugal pumps. The ice crystals may cause wear of the rotors, but also the ice crystals themselves may be affected. Attrition of crystals may occur because of high shear rates in the pump. Pump energy is then lost and pump efficiency reduced. Such effects are however small. Experimental ice slurry pump characteristics have been reported that are very similar to the pump characteristics with water (Kauffeld et al., 1999).

Alternatively an ice slurry pump of positive displacement type may be selected. A schematic view of the internals of such a pump is given in Figure 6.16. A pump of this type was used in the experiments of the present research. In these pumps, an increased viscosity increases the pump efficiency, because the leakage flow of the ice slurry through the rotating lobes of the pump is reduced. The lobes do not close off the separate spaces of the pump fully leak tight. The dynamic seals function more efficient at higher viscosity and also the presence of solids is of influence.

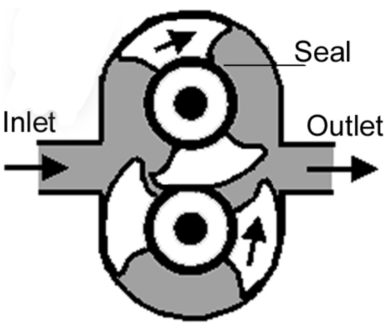

Figure 6.16: Schematic lay-out of rotary displacement pump used in experimental set-up (after Waukesha CB, 2003)

In Figure 6.17 the pump rotation speed required for a flow rate of 3300 kg/h is given versus the ice fraction of the slurry. In the experiment a NaCl based ice slurry at initial freezing temperature of -4.8 ^{o}C was used.

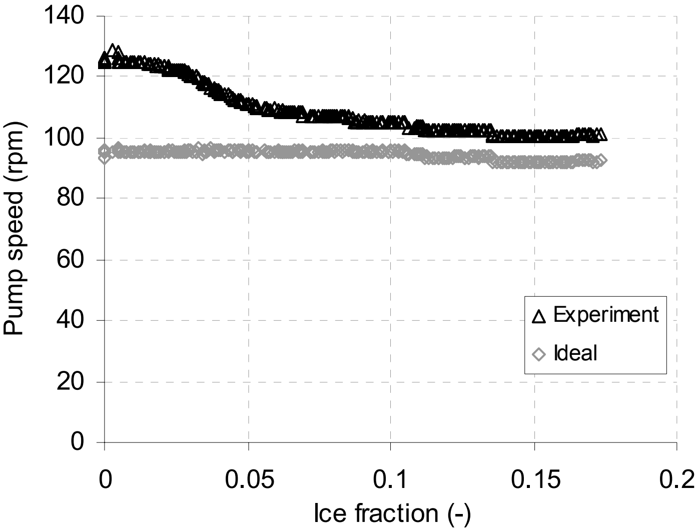

Figure 6.17: Ice fraction and corresponding pump rotation speed required for a constant flowrate of 3300 kg/h in the experimental set-up. Also the ideal situation for a perfect sealing pump is displayed. Ice slurry of 7.6 wt% NaCl, T_{f_init}= -4.8 ^{o}C

It should be noted that the work required by the pump in the experimental set-up also changes with ice fraction, so that the efficiency of the pump cannot be directly obtained from Figure 6.17. The pump used in the experimental set-up was a few years old. The effect of the efficiency improvement may have been larger because of wear of the pump from previous use. The total pressure drop over the experimental set-up was not measured and it is therefore not possible to compare the pump performance with the curve obtained from the manufacturer.

The ice crystals function as a sealant. At relatively low ice fractions, an increase of the ice fraction rapidly decreases the number of revolutions required. At higher ice fractions, an increase of the ice fraction only mildly reduces the pump speed, while the viscosity still increases rapidly.

6.4.4 Transport Heat Losses

For heat losses during pumping of ice slurries similar considerations are valid as for the storage tank. Heat losses can be prevented effectively by insulation. The internal heat transfer coefficient is then large compared to the heat transfer coefficient of the walls of the insulated tubes and the outside of the tubes. Heat losses are estimated with an overall heat transfer coefficient in the order of 1-3 W/m^{2}K.

The surface-to-volume area of ice slurry transport tubing is much higher than for the storage tanks. Heat losses may therefore be a significant factor, especially if the ice slurry must be transported over longer distances, for example over more than 10 m. These heat losses may be reduced by means of the ice slurry properties, if for example a higher ice fraction is chosen, pipe diameters required are smaller and also heat transfer coefficients of turbulent flow conditions are reduced. Alternatively, larger pipe diameters may be selected, which reduces the velocity of the ice slurry and may lead to a transition of the flow regime towards laminar flow conditions. Overall heat losses per m^2 are estimated to be in the range of 33% to 50% lower for laminar than for turbulent flow conditions. Total heat losses can therefore be reduced if the flow conditions are already relatively close to laminar.

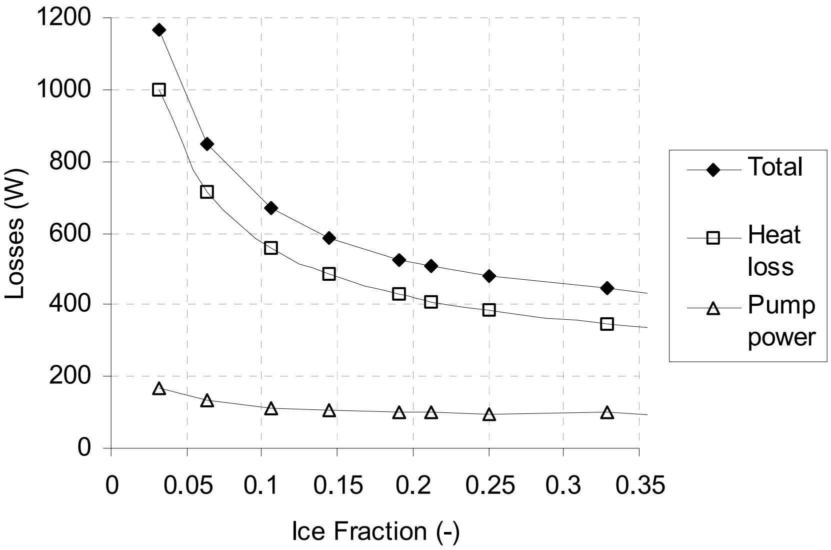

Figure 6.18: Heat losses and pumping power for transporting 100 kW of cooling capacity over a distance of 50 m. NaCl ice slurry of initial freezing point of –5 °C, v=*1.5 m/s*

In Figure 6.18 the total losses required to transport 100 kW of ice slurry to an application over a distance of 50 m is given versus the ice fraction. Tube diameters required vary from 85 mm at 0.03 ice fraction to 30 mm at 0.25 ice fraction. The ice slurry velocity was roughly optimized: At a velocity of 1.5 m/s the total losses because of pumping and heat input are approximately minimal.

The pumping power required and the heat losses are also included separately in Figure 6.18. The optimum tube diameter, ice slurry fraction and ice slurry velocity can be found once investment costs for tubes and insulation are known. For the case of Figure 6.18, the heat losses form the largest part of the additional power consumption required to transport ice slurries. If tube diameters are decreased, which decreases investment costs required, the share of the pressure drop in the additional power consumption increases.

The pumping power input required does not result for 100% in melting of ice. It can therefore be observed that the losses during transport of ice slurry will mainly be caused by heat input from surroundings.
At ice fractions below 0.05, the losses become more than 1% of the transported capacity. At ice fractions above 0.20 the losses are approximately 0.5%. Higher ice fractions in relatively narrow tubes are therefore preferable for low additional power consumption of ice slurry transport. A further increase of the ice fraction above 0.20 only slightly reduces heat inputs, while the ice slurry may become similar to a non-Newtonian fluid, which increases pumping power.

The ice fraction in the transport stage must be high for a high cold transport capacity and small tube diameters. At high ice fractions however, the viscosity of ice slurries increases and pumping power input and heat losses per m^2 will increase. Furthermore, a transition to non-Newtonian flow behavior becomes likely. A discussion of non-Newtonion rheology is given in Appendix 2. It may be advantageous to apply a lower ice content than in the storage stage to avoid such transitions. For example by not keeping the storage tank homogeneous and extracting ice slurry from lower parts of the tank. Although the cold storage capacity during transport is reduced in this way, the corresponding reduction in pumping effort may result in a net gain.

6.5 Utilization Heat Exchangers

6.5.1 Introduction

The utilization stage consists of the heat exchangers located at the site of the cooling application, where the ice slurry is melted. In the utilization stage therefore no device is needed to remove ice from heat exchanging walls. Various designs have been discussed, for example tubular heat exchangers and plate heat exchangers. An overview of pressure drop and heat transfer studies of ice slurry melting in utilization heat exchangers is given in Bellas et al. (2002). Various trends have been observed by different researchers, many of them seemingly contradictory. These contradictions are caused by the various conditions and the various designs of heat exchangers used. Also the size of the ice crystals may be relevant.
In some researches an increase of the ice fraction has a positive influence on the heat transfer coefficients (Celigueta Azurmendi, 2003). At relatively high flowrates however, this positive influence reduces or is no longer noticeable (Stamatiou et al., 2001). If an increase of the ice fraction leads to a flow regime transition, the heat transfer coefficients are decreased, which was observed by Knodel et al. (2000). Other researchers reported decreasing heat transfer in plate type heat exchangers with increasing ice fractions (Bellas et al., 2002).
Trends of the pressure drop in tubular heat exchangers are similar to the pressure drop during the transport of the ice slurries. To obtain high heat fluxes however the tubes of the heat exchangers are likely to be much smaller in diameter and therefore the pressure drops are likely higher than during transport. The utilization heat exchangers do not require separate pumps, the same pumps used for the ice slurry transport are used.
At increasing ice fraction, pressure drop over both tubular heat exchangers and plate heat exchangers increases. Because ice is melted, pressure drops decrease throughout the heat exchanger. Some authors observed an exponentially increased pressure drop at ice fractions above 0.20, which was attributed to local ice blockages in the plate heat exchangers (Bellas et al., 2002). Such effects may also cause a decrease of the average heat transfer coefficients.

Plate heat exchangers may result in a transition to turbulent flow conditions already at relatively low Reynolds numbers, in the range of 100-400, depending on the design. Plate heat exchangers may therefore be efficient for ice slurries of relatively high ice fraction or viscosity, if local ice blockages can be prevented.

Apart from pressure drop and heat transfer also the mass transfer of melting ice slurries is relevant: If melting of the ice crystals occurs more slowly than the heat transfer to the ice slurry, the temperature of the liquid phase of the ice slurry may increase locally. The temperature driving force over the utilization heat exchanger may then be lowered and the heat transfer performance decreased. No kinetic studies have been carried out for melting of ice crystals in a slurry so far and it is therefore unknown to what extent such phenomena may occur. Small ice crystals have a large surface-to-volume ratio and are therefore less likely to be limited by a mass transfer resistance during the melting of ice.

6.5.2 Heat Transfer

For heat transfer in circular tubes under laminar flow conditions the average Nusselt number is given by (Holman, 1997):

$$Nu = \frac{\alpha \cdot D}{\lambda} = 1.75 \cdot Gz^{1/3} \tag{6.11}$$

valid for an isothermal tube wall and for Gz>100, with *Gz* the Graetz number, for circular tubes:

$$Gz = Re \cdot Pr \cdot \frac{\pi D}{4L} \tag{6.12}$$

An empirical model to predict heat transfer coefficients specifically for ice slurries in circular tubes under laminar flow conditions was introduced by Guilpart et al, (1999).

$$Nu = 38.3 \cdot Gz^{0.15} \cdot w_i^{0.52} \tag{6.13}$$

which was developed for $3<Re<2000$ and $0.04<w_i<0.35$.

Heat transfer coefficients versus the ice fraction determined with Equations 6.11 and 6.13 for tubular heat exchangers are given in Figure 6.19 at –5 °C and in Figure 6.20 at –20 °C, for various freezing point depressants. The trends of the different models vary widely, it is therefore unclear which model can be used in heat transfer predictions. With Equation 6.11 a relatively constant heat transfer coefficient is predicted, while using Equation 6.13 the heat transfer coefficients are predicted to increase with increasing ice fraction. At –5 °C the freezing point depressant used is of minor influence. NaCl has the best heat transfer performance, but the difference with other additives is small. At –20 °C the freezing point depressant is more relevant, KFor has the highest heat transfer coefficients.

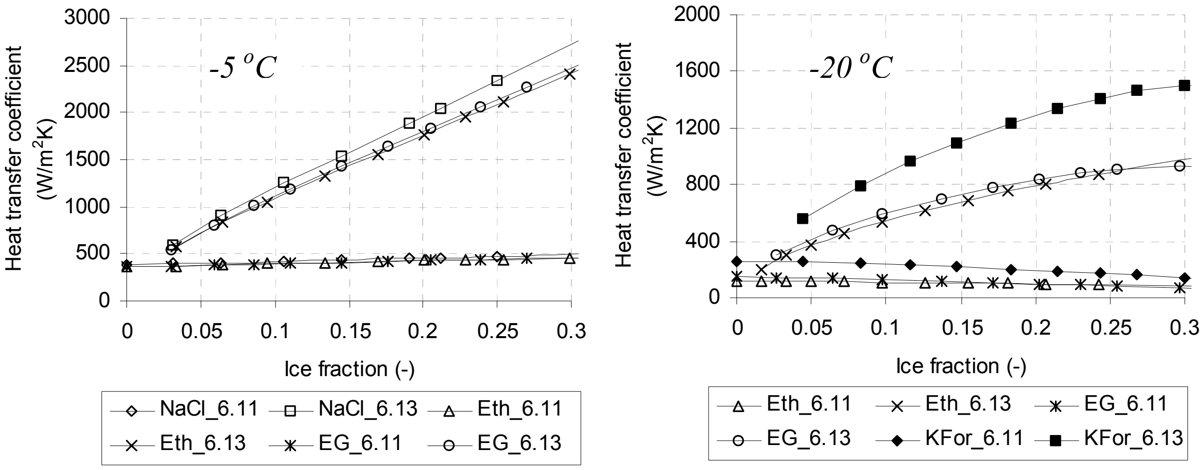

Figure 6.19 and 6.20: Heat transfer coefficients for laminar flow conditions in a tubular heat exchanger, d=10 mm, L=10 m, v=0.5 m/s. T_{f_init}*=-5 °C and –20 °C*

Higher heat transfer coefficients in tubular heat exchangers may be obtained under turbulent flow conditions. Similar considerations as for the production stage of the ice slurry cycle are then valid. Heat transfer coefficients can be estimated with a form of Equation 6.1, valid for single phase heat transfer, that may or may not be augmented because of the presence of ice crystals. Also reliable models still need to be established.

Bellas et al. (2002) observed a 30% increased heat transfer performance for ice slurry melting in plate heat exchangers compared with single phase heat transfer. The local heat transfer coefficients may however have been higher. Assuming that there are no mass transfer limitations during the melting of the ice, single phase heat transfer coefficients are estimated with a plate heat exchanger model, Equation 6.14 (Green and Maloney, 2000):

$$Nu = 0.26 \cdot Re^{0.65} Pr^{0.4} \tag{6.14}$$

in which the Nusselt and Reynolds number are based on the hydraulic diameter of the plate heat exchanger, which is taken at twice the gap space between two plates. Ice slurry heat transfer coefficients are estimated to be 30% higher than predicted with Equation 6.14.

Heat transfer coefficients determined with Equation 6.14 are displayed in Figure 6.21 versus the ice fraction for a number of freezing point depressants. The heat transfer coefficients are predicted to decrease at increasing ice fraction. Bellas et al., (2002) did not observe large difference in heat transfer with increasing ice fraction up to ice fractions of 0.20. The differences at increasing ice fraction calculated here however are also low up to an ice fraction of 0.20, typically around 10%. There may be a small positive effect of the ice crystals, so that the heat transfer coefficients become relatively more constant than predicted in Figure 6.21. This corresponds with experimental results of several authors (Bellas et al., 2002; Norgard et al., 2001).

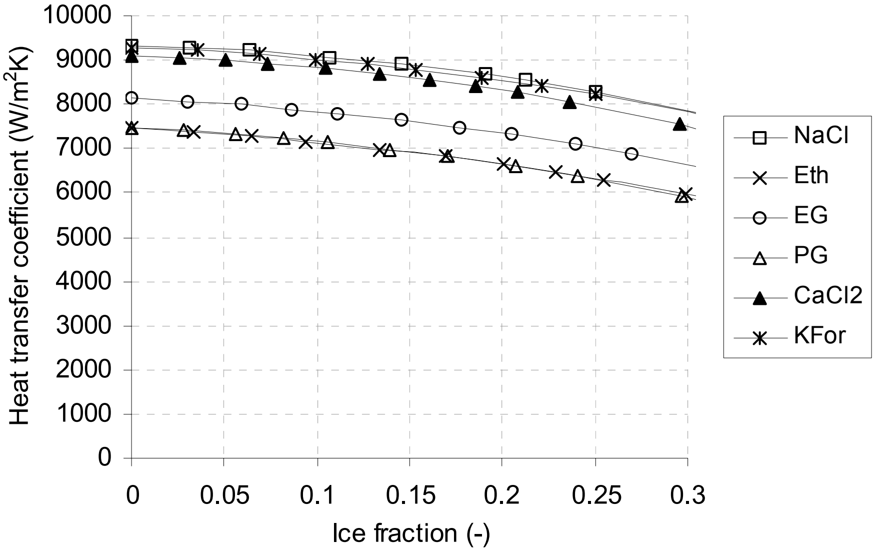

Figure 6.21: Heat transfer coefficients for turbulent flow conditions in a plate heat exchanger, d_h=4 mm, w=0.05 m, φ_v=3 m^3/h, 24 plates, T_{f_init}=–5 °C

For the utilization heat exchanger also a cost optimization may be done to find the optimum temperature difference. Often however, applications require a specific temperature and an optimization is not possible. In applications above 0 °C, the optimum temperature found may be outside the application range of ice slurries. Furthermore, heat exchangers in for example display cabinets may be relatively expensive and are therefore operated at an optimal temperature difference that is higher than applications where utilization heat exchangers are not as costly.

It depends on the application and the type of heat exchanger if it is efficient to melt all ice in the utilization stage. Especially if heat transfer coefficients decrease at decreasing ice fractions, it may be efficient to leave some ice content after the utilization heat exchanger.
In closed systems, where the ice slurry flow needs to be returned to the ice slurry generator or storage tank, it is probably most efficient to design the system so that all ice has just melted at the point where the ice slurry is returned to the storage tank or ice generator inlet. In open systems, for example in fishery, the ice fraction is more important than the heat transfer coefficients in the utilization stage.
Authors have reported different trends of the heat transfer versus the ice fraction. It is therefore likely that parameters as the ice crystal size and the heat exchanger design influence heat transfer. A limiting mass transfer step in the melting of ice crystals may have affected the results differently in various researches.

6.6 Overview of Ice Slurries in Secondary Cooling Cycles

The economic and energetic performance of systems with and without storage and transport stages are compared, whereby the entire secondary cooling cycle is evaluated. A system with a fluidized bed ice slurry generator with cooling capacity of 100 kW is assumed, in which ice slurries are generated at –5 °C (cooling) and at -20 °C (freezing). At –5 °C, NaCl and EG were compared as freezing point depressants, at –20 °C, KFor and EG.
The applications evaluated are characterized using typical sizes of the storage and transport stages. Size and lay-out of utilization heat exchangers are determined by the application

requirements and are not influenced by the size of transport and storage stages. An optimization of the utilization heat exchanger is therefore not included here.

Energy consumption and total costs are calculated per stage of the cooling cycle using the correlations discussed in the previous sections. Yearly investment costs are calculated using a 5 year depreciation period with an interest rate of 5%. A detailed description of the estimated investment costs is given in section 7.2.2. Investment costs estimations are used for the comparison only and do not represent actual prices of manufacturers. Calculations are made assuming an ice fraction of 0.25 in the storage and transport stages. The average ice fraction during ice slurry generation is assumed to be 0.10.

In the economical evaluation benefits of the storage stage are included by assuming that 50% of the cooling load can be shifted to the night-time at 50% of the daytime electricity tariff, 8 €ct/kWh vs. 4 €ct/kWh. The system is assumed to operate 24 hours per day, for 300 days a year. For the load that is shifted to the nighttime, also a 10% increase of overall energy efficiency is assumed. Due to the load shift the size of the primary cycle is assumed to be 45% smaller. Additional power consumption due to storage mixing, pumping and heat losses, is estimated with the methods described in the previous sections.

Results of the evaluation are given in Table 6.2.

Table 6.2: Yearly costs and energy consumption estimated for 100 kW applications with and without storage and for different transport stages data

Cold Stored	Transport distance	NaCl –5 °C		EG –5 °C		KFor –20 °C		EG –20 °C	
		costs	energy	costs	energy	costs	energy	costs	energy
-	m	k€/y	MWh/y	k€/y	MWh/y	k€/y	MWh/y	k€/y	MWh/y
0%	20	15.6	104.7	15.7	105.4	22.2	162.2	23.0	166.8
50%	20	14.0	105.2	14.1	107.1	19.3	169.7	20.5	192.5
0%	200	17.9	106.6	18.0	107.3	24.7	166.6	25.9	175.9
50%	200	16.3	107.1	16.4	109.1	21.8	173.5	23.4	201.5

It is observed from Table 6.2, that at –5 °C, the differences between freezing point depressants are relatively small, both for total costs and for yearly energy consumption. If a storage tank is used for 50% of the cooling load, there is also only a small difference between freezing point depressants: Costs of the systems with EG ice slurries are up to 1% higher than for NaCl ice slurry systems. Energy consumption is up to 2% higher using EG as the freezing point depressant. At –20 °C differences are larger. Systems with KFor as freezing point depressant are in the range of 4-7% less expensive than using EG as freezing point depressant, while the energy consumption is up to 16% lower for the KFor ice slurry systems. The increased differences are mainly caused by the relatively high viscosity of ethylene glycol at lower temperatures.

The lay-out of the secondary cooling cycle only has a small influence on the performance of freezing point depressants. The transport distance hardly influences the difference between freezing point depressants at –5 °C. At –20 °C the difference slightly increases at increasing transport distance. The presence of storage tanks in the secondary cooling system may also influence the performance of freezing point depressants. In the current comparison the differences between freezing point depressants are larger if storage tanks are included in the secondary cooling cycle. At –5 °C however the differences are not significant, at –20 °C the differences may be relevant.

In the current evaluation only two freezing point depressants are compared at two temperature levels, aiming only to indicate the general range in system performance between different freezing point depressants. Differences may be larger with other freezing point depressants, but are expected to be in the same range as those evaluated in Table 6.2. If the design of the utilization heat exchanger is also optimized for optimal ice slurry properties, the differences may be slightly larger.

The nightly storage of ice slurries leads to a decrease of total costs, but also to an increase of the energy consumption in the current comparison, mainly due to heat losses. This is a result of the assumptions of the current evaluation and is not necessarily the case for all applications. A 10% improvement of the nightly COP is assumed, but depending on the outside temperatures, higher reductions may be achieved. Also the ice fraction of 0.25 in the storage tank is relatively low. Ice fractions up to 0.40 have been reported, which will lead to smaller storage tanks, less heat losses and lower additional power input. Furthermore, a continuous operation of the stirrer is assumed, while in practice it is likely that stirring is not required for a large part of the daily cycle. Finally, the systems are assumed to operate 24 hours, thereby only shifting 50% of the cooling load. A full shift of cooling load to the nighttime may lead to a reduction in total power consumption. This may however lead to a reduced economic performance. A detailed simulation of the system over a 24 hour cycle, including cooling load variation and outdoor temperature variations, is therefore required to determine the optimal cooling system design. The results of Table 6.2 indicate that the shifting of cooling load to the nighttime primarily leads to economic benefits.

The type of freezing point depressant is relevant for the system performance, but effects are not necessarily large. At lower temperature levels, around –20 ^{o}C, differences are larger. At these temperatures ice slurries become more similar to non-phase changing cooling fluids and therefore also the properties of the liquid phase become more important. The ice fraction is however still the most relevant parameter.

6.7 Conclusion

The secondary cooling cycle has been divided into four separate stages and analyzed separately. The ice fraction is the most relevant design parameter in each stage. The use of ice concentrators or separation methods in between the stages is therefore likely to improve system performance. At lower temperatures, around –20 ^{o}C, the choice of freezing point depressant becomes more relevant, as freezing ranges widen and the ice slurries become more similar to non-phase changing secondary cooling fluids.

There is not one type of ice slurry generator most efficient for all applications. A suitable ice slurry generator can therefore only be selected if size, temperature and other constraints of the application are known. The fluidized bed ice slurry generator is expected to perform well in relatively large applications. Possible effects of the limit on the allowable temperature difference should be investigated further.

The storage and transport stages, investment costs and additional power consumption increase exponentially if systems are designed using low ice fractions. It is advisable to use ice fractions of 0.20 during storage and transport. Heat losses make up the largest part of the additional power requirements compared with stirring and pumping requirements for the current evaluation.

For the utilization stage it depends on the application what conditions are efficient. Several trends for heat transfer coefficients are possible, depending on the type of heat exchanger used.

Optimal system designs can only be obtained if the daily profile of the cooling load, outside conditions and energy costs are known, so that a dynamic simulation can be done.

Nomenclature

$c_{1..3}$	constant coefficients (-)
D	diameter (m)
d_p	particle diameter (m)
f	friction factor (-)
Fr	Froude number (-)
g	gravitational acceleration (m/s^2)
Gz	Graetz number (-)
L	length (m)
n	Richardson Zaki coefficient (-)
N	stirrer speed (1/s)
N_P	power number (-)
Nu	Nusselt number (-)
P	power input (W)
Δp	pressure drop (Pa)
Pr	Prandtl number (-)
Re	Reynolds number (-)
Tf_init	Initial freezing temperature (°C)
U	overall heat transfer coefficient (W/m^2K)
v	velocity (m/s)
w_i	ice fraction (-)
Greek	
α	heat transfer coefficient (W/m^2K)
Γ	mass flow per periphery (kg/ms)
ε	bed voidage (-)
η	efficiency (-)
λ	thermal conductivity (W/mK)
μ	dynamic viscosity (Pa.s)
ρ	density (kg/m^3)
φ_v	volumetric flow (m^3/s)
subscripts	
ax	axial
h	hydraulic
i	ice
p	particle
rad	radial
s	stirrer
other	
EG	ethylene glycol
Eth	ethanol
KFor	potassium formate
PG	propylene glycol

References

Bel, O., Lallemand, A., 1999, *Etude d'un fluide frigoporteur diphasique 1&2*, International Journal of Refrigeration 22, p164-187

Bellas, J., Chaer I., and Tassou, S.A., 2002, *Heat transfer and pressure drop of ice slurries in plate heat exchangers*, Applied Thermal Engineering 22 (7), p721-732

Celigueta Azurmendi, I., 2003, *Melting of ice slurry: Review of the preceding research and experimental study,* M. Sc. thesis Delft University of Technology, Report no. KK-1183

Christensen, K.G., Kauffeld, M., 1998, *Ice Slurry Accumulation*, Proceedings of the Oslo Conference of the IIF/IIR commissions B1, E1, E2, p701

Fukusako, S., Kozawa, Y., Yamada, M., Tanino, M., 1999, *Research and Development Activities on Ice Slurries in Japan.* Proceedings of the 1st Workshop on Ice Slurries by the IIR, Yverdon-les Bains, May 1999. Eds. Egolf, P.W., Sari, O., IIF/IIR, p83-105

Gladis, S.P., Marciniak, M.J., O'Hanlon, J.B., Yundt, B., 1995, *Ice crystal slurry TES system using the orbital rod evaporator.* ASHRAE Transactions vol. 101 (1), www.muel.com

Green, D.W., Maloney, J.O. (eds.), 2000, Perry's Chemical Engineering Handbook 7th edition, McGraw-Hill.

Guilpart, J., Fournaison, L., Ben Lakhdar, M.A., Flick, D., Lallemand, A., 1999, *Experimental study and calculation method of transport characteristics of ice slurries*, 1st workshop on ice slurries of the IIR, Yverdon-les-Bains, Switzerland, IIF/IIR, p74-82

Hobbs, P.V., 1974, *Ice Physics*, Oxford: Clarendon Press, ISBN 0198519362

Holman, J.P., 1997, *Heat Transfer* 8th ed. , McGraw-Hill.

Inaba, H., 2001, *Fundamental Research and Development of Ice Slurry for its Cooling System Design in Japan.* Proceedings of the 4th Workshop on Ice Slurries by the IIR, Osaka Japan, Nov 2001. Ed. Fukusako, published by IIF/IIR.

Ishikawa, M., Hirata, T., Fujii, T., 2002, *Force estimation of mechanical removing processes of mushy structure in an aqueous solution*, International Journal of Refrigeration 25(2) p208-217

Kauffeld, M., Christensen, K.G., Lund, S., Hansen, T.M., 1999, *Experience with Ice Slurry*, Proc. of the 1st workshop on Ice Slurries, Yverdon-les-Bains, Switzerland, IIR. p42-73

Klaren, D.G., van der Meer, J.S., 1991, *A fluidized bed chiller: A new approach in making slush-ice,* Industrial Energy Technology Conference Houston Proc.

Knodel, B.D., France, D.M., Choi, U.S., Wambsganss, M.W., 2000, *Heat transfer and pressure drop in ice-water slurries*, Applied Thermal Engineering 20, p671-685

Nagata, S., 1975, *Mixing Principles and Applications* Halstead Press, Wiley, 1975

Norgard, E., Sorensen, T.A., Hansen, T.M., Kauffeld, M., 2001, *Performance of components of ice slurry systems: Pumps, plate heat exchanger, fittings,* Proceedings of the 3rd Workshop on Ice Slurries by the IIR, Luzern, Switzerland, Eds. Boyman, T., Frei, B., Egolf, P.W., IIF/IIR, p129-136.

Paul, J., 1996, *Compressors for refrigeration plants and ice makers with 'water as refrigerant'*, Proc. Aarhus Conf., IIF/IIR: p.577-584

Paul, J.,1997, *Binäreis-Anwendungserfahrungen in der Supermarktkälte,* Ki Luft-und Kältetechnik, vol.5, p209-213

Pronk, P., Infante Ferreira, C.A., Witkamp, G.J., 2002, *Effects of long-term ice slurry storage on crystal size distribution,* Proceedings of the 5th Workshop on Ice Slurries by the IIR, Stockholm, Sweden, Ed. Melinder, A., IIF/IIR, p151-160

Rautenbach, R., Katz, T., 1996, *Survey of long time behavior and costs of industrial fluidized bed heat exchangers*, Desalination*,* Vol. 108, p335-344

Stamatiou, E., Kawaji, M., Lee, B., Goldstein, V., May 2001, *Experimental investigation of ice-slurry flow and heat transfer in a plate-type heat exchanger,* Proceedings of the 3rd Workshop on Ice Slurries by the IIR, Luzern, Switzerland, Eds. Boyman, T., Frei, B., Egolf, P.W., IIF/IIR, p61-68

Waukesha Cherry Burrel, (SPX Process Equipment), 2003, *Pump facts*, www.gowcb.com

Vaessen, R.J.C., 2003, *Development of scraped eutectic crystallizers,* PhD-thesis Delft University of Technology, ISBN 90-646-4208-7

Wobst, E., Wollmer, D., *Ice Slurry Generation by Direct Evaporating of Refrigerant,* Proceedings of the 1st Workshop on Ice Slurries by the IIR, Yverdon-les Bains Switzerland, May 1999. Eds. Egolf, P.W., Sari, O., published by IIR, p125-131

Zakeri, G. R., 1997, *Vacuum freeze refrigerated circuit, a new system design for energy effective heat pumping applications*, Proc. Linz (Austria) Conf, IIF/IIR, comm. E1,E2,B2: p. 182-190.

7 Ice Slurry Secondary Cooling Cycle Simulation

In this chapter the performance of ice slurry as cooling fluid in secondary cooling systems is evaluated. Aim is to determine accurately under what conditions and in which fields ice slurries can be applied successfully. A dynamic model is developed that incorporates all stages of a secondary cooling cycle. The model is used to evaluate different freezing point depressants and different system components as for example the ice slurry generator. The dynamic performance of applications with various cooling load profiles and temperature requirements is then evaluated.

7.1 Introduction

A number of conditions influence efficiency of secondary cooling systems: Application size and temperature level, variation of the cooling load during the day, electricity tariff structure, climatic factors as the variation of the outside temperature, ice slurry working temperature and ice slurry properties. Important is also the type of ice slurry equipment used, because the ice slurry generator requires extra investments compared to heat exchangers of secondary cooling cycles without phase change. Most of these parameters are different for each application, it is therefore necessary to evaluate for each case what benefits can be gained using ice slurries as the working fluid. Aim of this Chapter is to determine accurately under what conditions ice slurries can be applied successfully.

A model is developed to optimize the ice slurry system design and calculate its energetic and economic performance. The modeling is done in two parts with different level of detail: First the system dimensions are roughly optimized, secondly a dynamic model is developed to evaluate and further optimize the system performance during a 24-hour cycle. Effects of secondary conditions as electricity tariffs and outdoor temperature are included in the investigation. The model is used for system optimization and for comparison of single components such as the ice slurry generator. Effects of different freezing point depressants are also evaluated with the model. Apart from NaCl and ethylene glycol, also potassium formate and calcium chloride are evaluated.

The general lay-out of an ice slurry secondary cooling system is given in Figure 7.1. The primary cycle and the secondary cycle which consists of four stages, are displayed. Stage 1 is the heat exchanger or ice slurry generator that links the secondary cooling cycle with the primary cycle. Storage of the ice slurry in a tank, stage 2, allows for benefits of peak load leveling and load shifting. In stage 3 ice slurry is transported with a pump to where the cooling capacity is required in utilization heat exchangers, stage 4.

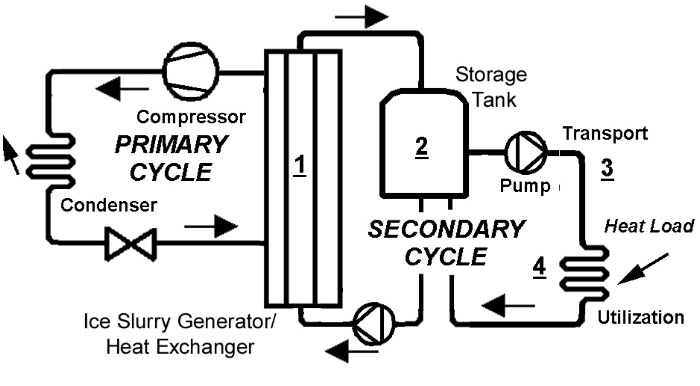

Figure 7.1: Secondary cooling system

The option to store ice slurry allows for significant economic benefits and is often the reason that secondary cooling systems can be cost-effective. Cold storage makes shifting of the electric load from daytime to the nighttime with lower electricity tariffs possible. Energy consumption is reduced by shifting of cooling load to the nighttime, because condensation in the primary cooling cycle may take place at lower outside temperatures. Furthermore peak loads can be leveled out over longer periods, reducing system capacity so that systems can be smaller than if they were designed to fully cool the maximum load directly. These advantages may outweigh the disadvantages of extra investment costs for ice slurry generator and storage tank and some heat losses during the storage period.

In Figure 7.2 two cooling load profiles are given. The profile of air-conditioning is based on Paul (1995), the supermarket cooling profile on Jensen et al. (1999). Shifting to nighttime operation of the air-conditioning load is given, as well as leveling of this cooling load over 24 hours. If the daytime cooling load of the air-conditioning case, with a peak demand of 275 kW, is leveled and/or shifted using an ice slurry storage tank, a cooling system with capacity of approximately 80 kW running 24 hours per day, can fully supply the cooling demand. If the load is completely shifted to the nighttime, a 160 kW capacity primary cycle is sufficient. In this example the required cooling capacity is assumed to be 6% higher than for the ideal case, because of heat losses and additional power inputs.

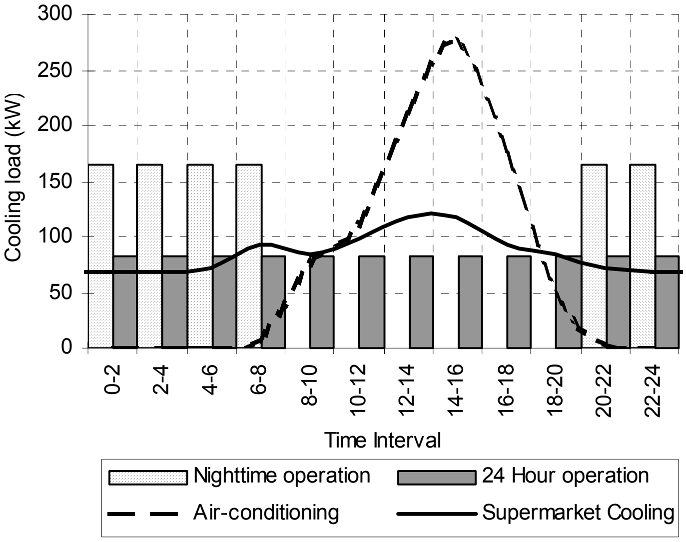

Figure 7.2: Cooling load profiles

Peak leveling and load shifting can not be accomplished fully at all times, as the two may interfere. An optimization is therefore required that takes electricity tariffs and investment costs for the primary cycle into account. Some secondary factors also need to be considered, as for example outside temperatures and surface/volume requirements of equipment and storage tanks. In this Chapter the optimization model is developed and evaluated in general, after which cases of air-conditioning, supermarket cooling and industrial cooling and freezing are evaluated in detail. Ice slurries have already been applied a number of times in similar applications.

The temperatures at which ice slurries are applied determine for a great part the feasibility of ice slurry systems. At high temperatures, the latent heat effect of the ice slurries is relatively important and the apparent heat capacity is high. At lower temperatures, more freezing point depressant needs to be added and the latent heat effect becomes less important. The apparent heat capacity decreases until at a certain temperature ice slurries will no longer be feasible. Ice slurry systems in low temperature applications are studied (typically -22 ^{o}C to -24 ^{o}C, deep freezing of food), to determine if ice slurry systems are feasible in these applications.

The model is also used to evaluate the fluidized bed ice slurry generator. The fluidized bed system has limits on its operating range, as discussed in Chapter 3. The most significant limit concerns a maximum temperature difference allowable between ice slurry and primary refrigerant. Above this limit ice will attach to heat exchanging walls and the ice slurry generator will eventually clog with ice and malfunction. The model is used to determine if these temperature limits affect the performance of the ice slurry generator in applications. Furthermore, a comparison is made with another ice slurry generator, the scraped surface heat exchanger.

7.2 Model Development

7.2.1 Static and Dynamic models

The dimensions of a cooling system and the optimal hours at which to operate the system need to be determined before the dynamic model of a system can be developed. The optimal operating period must be included in the model to take advantage of the load shifting benefits involved with ice slurry cooling. Systems of known dimensions can also be simulated, in which case still optimal operational hours need to be determined. With a static model the economic optimum of the following parameters is determined: Heat transfer surface area of the ice slurry generator, evaporating temperature of the primary refrigerant, storage tank volume and the optimal operating hours of the system. The optimal parameters are the input values of the dynamic simulation. In both static and dynamic models, efficiencies and heat losses of components as the compressor, heat exchangers, pumps and the stirrer are included.

The models evaluate the system performance during one day. The electricity tariffs are variable model inputs, in the cases of this study a two-tariff structure is assumed: A high tariff of 8 €ct/kWh from 8 am to 8 pm (day) and a low tariff of 4 €ct/kWh is taken for the remaining hours (night). Electricity tariffs were obtained from the DTe (2002), only the variable costs were taken into account and not the fixed costs. Ammonia is assumed as primary refrigerant, various freezing point depressants are evaluated. Initial freezing points of the ice slurries are constant during each simulation, but are varied between simulations in this study to find the optimal ice slurry temperature. In many cases the ice slurry temperature is a demand of the application, so that no optimization is possible. A fluidized bed ice slurry generator is used, with falling film evaporation on the ammonia side of the heat exchanger. Outside conditions of an average Dutch summer day are assumed initially, with a peak outside temperature of 21.5 ^{o}C and a night lowest temperature of 11.7 ^{o}C (KNMI, 2003).

7.2.2 Estimation of System Dimensions and Control Strategy

To determine the optimal operating schedule it is assumed that the primary refrigerant cycle only runs at full capacity, i.e. it is either on or off. The day is divided into 12 parts of 2 hours. For all combinations of hours that the system is on or off, 2^{12} combinations in total, the required cooling capacity of the primary system is determined. For example the total cooling load required of the air-conditioning case of Figure 7.2 is 1790 kWh. 24 hour operation would result in a minimum system capacity of 1790/24= 74.6 kW. A combination of operating hours that is running a total of 10 hours out of 24 would require a system capacity of at least 1790/10 =179 kW. The capacity actually required is slightly higher to compensate for heat losses during storage. In this way capacities for all possible operational hours are determined. The COP of the primary cooling cycle of each combination is then calculated, using an initial estimate for the ammonia evaporation temperature of 4 K below the estimated average ice slurry temperature. This ammonia evaporation temperature is assumed constant during the day in the static optimization. The ammonia condensation temperature is assumed to be 15 K above the outside temperature, which varies during the day.

The size of the ice slurry storage tank required to accommodate the shifting of the cooling load for each combination of hours on and off is then estimated. This is done by calculating the maximum and the minimum heat contents of the storage tank. At t=0 the heat contents of the tank are set equal to 0. Subsequently for each time interval the amount of heat removed from and the heat added to the ice storage tank are calculated. This is repeated until after 24 hours the heat contents of the tank are back at 0. The difference between the maximum and minimum heat contents encountered during the day (which may be a negative value) then gives the required storage capacity of the tank in terms of energy stored. With the apparent heat capacity estimated at the average ice slurry storage temperature and assuming a maximum ice fraction of 0.40 the volume of the storage tank required is calculated.

The size of the fluidized bed heat exchanger can then be determined. The temperature differences between ammonia and ice slurry, ΔT, and the amount of heat transferred, Q, are already estimated for all combination of hours on and off. Only the heat transfer coefficient, U, is still required to calculate the heat exchanger area, according to:

$$A = \frac{Q}{U \cdot \Delta T} \tag{7.1}$$

The overall heat transfer coefficient is assumed constant in the static evaluation. Only a dependence on the temperature is accounted for in the estimation. A linear proportionality as in Equation 7.2 is used:

$$U = c_1 + c_2 \cdot T_{f\_init} \tag{7.2}$$

where c_1=1750 and c_2=50 for the case of the fluidized bed ice slurry generator, with U in W/m^{2}K. Equation 7.2 is only used for a rough estimation.

Finally the total costs are calculated for each possible combination of operational hours. Total investment costs of the system are estimated using the heat exchanger area, size of storage tank and capacity of the primary cycle. Also investments for additional equipment as pumps are included. Total energy costs are determined, using different day- and nighttime electricity tariffs. Energy costs include power consumption of the compressor in the primary cooling cycle, pumping power consumption of ammonia and ice slurry pumps and power consumption of the stirrer of the storage tank.

After all on/off combinations have been evaluated, the least expensive combination is selected and stored. The ammonia evaporation temperature is then lowered with an initial step of 1 K and again all possible combinations are evaluated. If resulting costs are lower, the ammonia

evaporation temperature is again lowered. If costs are higher, this indicates the economic optimum has been passed. The ammonia evaporation temperature is then increased, but with a smaller step than 1 K. This procedure is repeated until the economic optimum evaporation temperature for the system is found within 0.1 K.
The maximum allowable temperature difference between fluidized bed wall and ice slurry in the ice slurry generator is taken into account. If in the static model the optimum temperature difference found becomes higher than the allowable maximum, the ammonia evaporation temperature is taken so that the temperature difference becomes equal to the limit.
It is possible to divide the day into 24 portions of 1 hour (2^{24} combinations), which makes the optimization more detailed. Computing time required would however become several hours (using a 800 MHz processor). For the applications considered in this study, this level of detail was not considered necessary.

In the static optimization the investment costs are estimated assuming a 5 year depreciation period (y) with a 5% interest rate (i). The investment costs are equally distributed over the depreciation period with:

$$Inv_{yearly} = \frac{i}{1-(1+i)^{-y}} \cdot Inv_{total} \tag{7.3}$$

Each component has a characteristic size parameter, x, that is assumed to determine its investment costs. For the fluidized bed ice slurry generator it is the heat exchanger surface area (A). Size of the ice slurry pump is assumed to be proportional to the size of the heat exchanger, investments are estimated using the pumping power (P_{pump}). The volume of the storage tank (V) and the compressor displaced volume (ϕ_v) are used as sizing parameter of the other components. For each component the investment costs are estimated with the following correlation (Sinnot, 1993):

$$Inv_{component} = c_1 \cdot x^{c_2} \tag{7.4}$$

In Table 7.1 the parameters c_1 and c_2 are given, with references from which the parameters have been determined. The size and lay-out of the ice slurry distribution lines and utilization heat exchangers are not considered in the evaluation. It should be noted that the values in Table 7.1 are estimates used for comparison purposes and not actual sales prices.

Table 7.1: Investment cost parameters for Equation 7.4.

Component	*x*		*c_1 (€)*	*c_2 (-)*	*References*
Fluidized bed generator	A	m^2	7500	0.52	Rautenbach (1996), Sinnot (1993)
Ice slurry storage tank	V	m^3	2000	0.60	Paul (1997), DACE (1995)
Ice slurry pumps	P	kW	1000	0.60	Paul (1997), DACE(1995)
Primary cycle (compressor)	ϕ_v	m^3/h	250	0.70	Sinnot (1993), DACE (1995)

7.2.3 Dynamic System Model

The optimum system dimensions and optimal operating hours determined with the static model are used as input parameters of the dynamic system model. Instead of estimated, heat transfer coefficients, COP and temperatures of ice slurry and ammonia are now calculated in detail in the dynamic model. Because values are no longer constants averaged over a day but variables actually calculated, limits may be encountered in the dynamic model that were not found in the static model. For example the maximum allowable temperature difference may be attained at some point during the day.
The cooling performance during the day will differ because of the continuously changing operating conditions. In the dynamic optimization it is verified that the required cooling load is actually generated with the system dimensions estimated in the static model. If this is not the case dimensions are slightly modified. This concerns mainly the compressor displacement volume, the heat exchanger surface area, the storage tank volume and the initial ice fraction in the storage tank. If the required modifications are significant (over 10%) the static model is evaluated again with other estimates for heat transfer coefficients and average temperatures. Especially a correctly estimated average ice slurry temperature is important for a good correspondence between static and dynamic model results.

The ice fractions at start and end of the 24 hour period are compared after the simulation. If the ice fraction has decreased over 24 hours, the cooling capacity of the system is too low and both heat exchanger surface area and compressor swept volume are increased by a small percentage (1 to 5%). By altering both at the same time, the temperature difference over the ice slurry generator remains similar. If the system is already at its limit temperature difference, only the heat exchanger surface area is increased.
The volume of the ice slurry storage tank and the initial ice fraction at midnight are modified so that the maximum ice fraction during the day is between 0.35 and 0.40. In the cooling temperature range this gives acceptable temperature variation in the ice slurry storage tank of up to a few degrees ^{o}C. At lower temperatures however, a 30% variation of ice fraction may lead to a higher variation of temperature. If this variation is larger than what would be acceptable in a non-phase change system, the volume of the storage tank is increased, which decreases the maximum ice fraction. A temperature difference of 10 K is assumed as the limit of the temperature variation in the storage tank. It is uncertain if such a temperature variation would be acceptable for actual applications, but temperature variations this large are typically encountered only at average ice slurry temperatures below –20 ^{o}C.
There is also a minimum ice fraction, defined by two criteria: There should be ice present in the storage tank at all times and there should be ice present in the return flow of the utilization heat exchanger. The utilization ice slurry flow rate is calculated using this second criterion: The utilization cooling load should be covered by melting of the ice in the slurry, so that the return flow into the storage tank contains exactly no ice. The volumetric flow rate is calculated using this criterion and the ice fraction of the storage tank:

$$\varphi_v = \frac{Q}{w_i \cdot \rho_{is} \cdot \Delta H} \tag{7.5}$$

At low ice fractions in the storage tank, Equation 7.5 would result in a high volumetric flow rate.

Therefore the flow rate of Equation 7.5 is compared with the flow rate that would be required using only the sensible heat capacity of the liquid phase and a 6 K temperature difference.

$$\varphi_v = \frac{Q}{\Delta T(=6K) \cdot \rho_{is} \cdot c_p} \tag{7.6}$$

A temperature difference of 6 K represents a typical practical value, rather than the 10 K mentioned before, which is the upper limit.
If the flowrate calculated without ice is lower than the flow-rate calculated with Equation 7.5, it is used instead. This implies that at some point in the utilization heat exchanger there will not be any ice left in the slurry and the temperature will rise above the initial freezing temperature. This reduces the efficiency of the system. Storage tank size and initial ice fraction are therefore modified so that the ice fraction is always high enough for the utilization cooling requirements and the return flow is at its initial freezing temperature.

A schematic lay-out of the dynamic model is given in Figure 7.3. The basic input parameters and the outputs that determine the energy consumption are shown. There are a number of algebraic loops, in which output signals determine inputs of the same calculation. These involve calculation of ice fractions, heat flux and superficial velocity in the fluidized bed heat exchanger. An integration algorithm is used to determine the ice fraction in the ice slurry storage tank. The 3rd order Bogacki-Shampine algorithm with variable time step as available in Matlab/Simulink, is used as solver in the dynamic model. With appropriate initial guesses of algebraic loop variables and a relative error tolerance of 10^{-3} the dynamic model performs accurately. Up to 4 min. is required for a single 24 h cycle simulation, using a 800 MHz processor.

The primary refrigeration cycle is evaluated with a constant compressor displacement volume. Power consumption therefore changes during the simulation, as also evaporation and condensation temperatures vary. If the maximum allowable temperature difference in the ice slurry generator/evaporator is reached, the compressor displacement volume and associated power consumption is reduced assuming ideal part-load control, so that the appropriate evaporation temperature is attained. If the compressor throughput is reduced during a simulation,

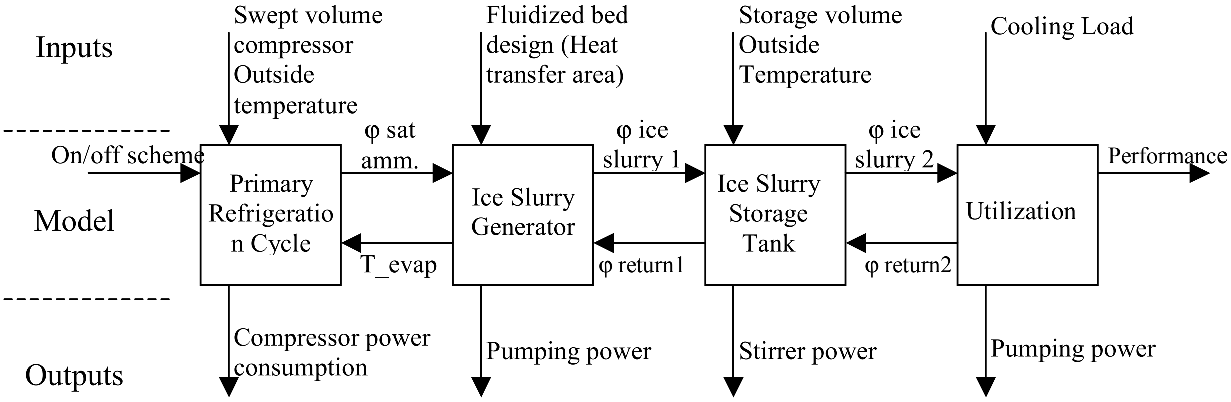

Figure 7.3: Schematic lay-out of the dynamic ice slurry simulation model

less ice is produced and performance of the system will be insufficient. The heat exchanger surface area needs to be increased so that the system fulfills the cooling requirements. A constant compressor efficiency of 0.80 has been assumed.

Heat transfer rates on the ice slurry side of the fluidized bed are calculated using the heat transfer model determined in Chapter 4:

$$Nu_h = 0.0612 \cdot Re_h^{0.724} Pr^{0.625} \tag{7.7}$$

which is valid for wall-to-bed heat transfer in stationary fluidized bed ice slurry generators. The Prandtl number (*Pr*) is calculated using the sensible heat capacity of the ice slurry, without the latent heat effect of the phase change. The model includes hydraulic Nusselt and Reynolds numbers, which are calculated using Equations 7.8 and 7.9:

$$Nu_h = \frac{\alpha \cdot d_p}{\lambda} \cdot \frac{\varepsilon}{(1-\varepsilon)} \tag{7.8}$$

$$Re_h = \frac{\rho \cdot v_s \cdot d_p}{\mu} \cdot \frac{1}{(1-\varepsilon)} \tag{7.9}$$

The superficial velocity of the ice slurry flowing upwards through the fluidized bed is determined with the iterative method of Richardson and Zaki (1954):

$$v_s = v_\infty \cdot \varepsilon^n \tag{7.10}$$

It is assumed in the model that the fluidized bed is fully turbulent and *n* is taken constant at 2.4. The terminal settling velocity for cylindrical particles is calculated with Equations 7.11 and 7.12 (Chhabra,1999):

$$v_\infty = \left(\frac{4 \cdot d_p \cdot g \cdot (\rho_s - \rho_{is})}{3 \cdot C_{D\infty} \cdot \rho_{is}} \right)^{0.5} \tag{7.11}$$

$$C_{D\infty} = \frac{24}{Re_\infty} \cdot \left(1 + 8.1716 \cdot e^{-4.0655 \cdot \psi} \cdot Re_\infty^{(0.0964+0.5565 \cdot \psi)}\right) + \frac{73.69 \cdot Re_\infty \cdot e^{-5.0748 \cdot \psi}}{Re_\infty + 5.378 \cdot e^{6.2122 \cdot \psi}} \tag{7.12}$$

with ψ the sphericity of the solid particles defined as the ratio between the surface-volume ratio of the particle and the surface-volume ratio of a sphere with the same volume as the particle. For cylindrical particles of equal height and diameter, ψ is approximately 0.87.

A drawback of the fluidized bed ice slurry generator is that it has a limited allowable wall-to-bed temperature difference. Above this limit the fluidized bed will freeze-up and malfunction because it gets clogged with ice. The maximum allowable temperature difference is discussed in Chapter 4. The maximum wall-to-bed temperature difference is estimated with:

$$\Delta T_{\max,wall-to-bed} = c_1 \cdot w_{fpd} + c_2 \tag{7.13}$$

values of c_1 and c_2 were determined in Chapter 4 and are given in Table 7.2.

Table 7.2: Limits on wall-to-bed temperature difference above which fluidized bed freezes

Freezing point depressant	Bed voidage	*c1*	*c2*
NaCl	0.79	29	0.13
NaCl	0.88	37	-0.23
NaCl, low pH	0.79	45	-0.04
Ethylene Glycol	0.79	25	-0.08
Dextrose	0.79	9.8	-0.19

Dextrose is not considered in the models of this Chapter. Limits for the other freezing point depressants discussed in this chapter, calcium chloride and potassium formate have not been determined experimentally. Limits of these freezing point depressants were assumed to be equal to sodium chloride under neutral pH conditions at a bed voidage of 0.79.
Temperatures are nearly constant on both sides of the heat exchanger because of the phase transitions. Equation 7.13 is therefore evaluated using the temperature difference between the average temperatures of the fluids on both sides.

Heat transfer coefficients on the ammonia side were calculated with the falling film theory, which is further discussed in Appendix 1. With the typical heat fluxes encountered in the ice slurry generator, it can be assumed that the evaporation is fully in the convective boiling regime (Fujita and Ueda, 1978; Krupiczka et al., 2002). If the falling film is under turbulent flow conditions, heat transfer coefficients are calculated using the following expressions:

$$Nu_{ff} = \frac{\alpha}{\lambda}\left(\frac{\nu^2}{g}\right)^{1/3} = 0.0038 \cdot Re_{ff}^{\ 0.4} \cdot Pr^{0.65} \qquad (7.14) \qquad Re_{ff} = \frac{4\Gamma}{\mu} \qquad (7.15)$$

with Γ the mass flow per unit periphery. A Re_{ff} of 10000 is assumed for the inlet flow of saturated liquid ammonia so that the falling film is fully in the turbulent flow regime. The falling film thickness is calculated with:

$$s = 0.909 \cdot \left(\frac{\nu^2}{g}\right)^{1/3} \cdot Re_{ff}^{\ 1/3} \qquad (7.16)$$

The film heat transfer coefficients are calculated taking the average of conditions at the in- and outlet. Part of the ammonia at the outlet is not evaporated and is recycled to the inlet of the ice slurry generator. Pumping power required for this is taken into account in the overall power consumption of the system.

The design parameters of the fluidized bed ice slurry generator are not optimized in this study, instead typical values are selected. The parameters of the fluidized bed design used in the simulations are given in Table 7.3.

Table 7.3: Parameters of the fluidized bed ice slurry generator (stainless steel walls)

Bed height	2.5	m	Thermal conductivity st. steel	15	W/mK
Outside tube diameter	51	mm	Bed voidage	0.76	-
Wall thickness	2	mm	Stainless steel particles	cylindrical, h=d=4 mm	
Reynolds inlet fall.film	10000	-			

The ice slurry storage tank is assumed to be ideally mixed, with a maximum ice fraction of 0.40. The initial ice fraction present in the tank (at midnight) is adjusted so that at the point during the day with the lowest ice fraction, there still is enough ice present to fulfill the cooling load requirements. Furthermore, the size of the ice slurry storage tank is increased if the maximum ice fraction attains values above 0.40 during the simulation, or, if the maximum ice fraction in the tank remains below 0.35, the size of the storage tank is decreased slightly. Pumping and stirring power inputs are accounted for in the storage tank. It is assumed that 50% of power requirements of additional equipment results in melting of ice in the storage tank. Also heat losses to the surroundings are included. Cylindrical storage tanks are assumed, with well insulated walls and an overall heat transfer coefficient to the (outside) surroundings of 1 W/m^{2}K.
The stirring power input per m^3 storage tank for laminar stirring conditions is assumed to depend on the ice fraction according to:

$$P_{stirrer} = 0.01 + 0.075 \cdot w_i \tag{7.17}$$

In Equation 7.17 the type of stirrer and the level of homogeneity required in the ice slurry storage tank are ignored.

In the utilization heat exchanger the required flow rate and consequently the pumping power effort is estimated with the assumption that there is enough heat exchanging surface available for the application. Investment costs of the utilization heat exchanger were not considered. Pumping power of standard centrifugal pumps is estimated based on the throughputs as calculated in the dynamic model:

$$P_{pump} = \frac{\Delta p \cdot \varphi_v}{\eta_{pump}} \cdot 100 \tag{7.18}$$

where the pressure differential over the pumps (Δp) is set to 200 kPa in the application pump, 100 kPa per m of fluidized bed height for the ice slurry generator pump and 20 kPa per m of fluidized bed height for the ammonia circulation pump. The pump efficiency is assumed at 80%. Effects of ice fraction and pump type are not considered in the simulation.

After each dynamic simulation the data required to evaluate the system's performance are recorded. These include ice slurry temperatures, ammonia evaporation temperatures, COP's, heat transfer coefficients, flowrates and energy requirements as well as energy costs. For some simulation runs the variation of these parameters during 24 hours was saved for comparison, for the rest the minimum, maximum and averaged values were saved. For costs and energy consumption at least the 24 hour totals are saved for comparison. Possible occurrences of the upper limit on the temperature difference in the ice slurry generator, the limits on the ice fraction in the storage tank or limits on ice slurry temperatures in the utilization stage are also saved.

In the dynamic model a single day is simulated. To evaluate costs of systems per year, the simulations should be extended with incorporation of seasonal influences. Depending on the application the cooling load required may vary from season to season. Also outside temperatures, important for the condensation temperature of the primary cooling cycle, vary. Some simulations are therefore done at different outside temperatures. Also some simulations are done to evaluate the performance of systems at different cooling loads, both higher and lower, while keeping the systems dimensions constant. For these simulations it is again assumed that the compressor of the primary cooling cycle can be ideally controlled for part-load operation with the same efficiency as for its design conditions.

The model comparisons have been limited to secondary cooling cycles using conventional fluids and ice slurries. Comparisons with direct systems or other secondary cooling options, for example with carbon dioxide in deep freezing applications, were excluded. The simulation model needs to be to extended to include other system types. The current comparison is sufficient to determine strong and weak points of ice slurry systems.

It should be noted that the ice slurry systems considered are closed systems. The overall concentration of freezing point depressant throughout the system is kept constant, no ice is removed and no fresh liquids are added.

7.3 Simulation Results

7.3.1 General

An example of the results of a typical simulation after static and dynamic optimization is given in Figures 7.4 and 7.5. The temperature and ice fraction in the ice slurry storage tank and the ammonia evaporation temperatures are displayed for ice slurry in an air-conditioning application, running 24 hours per day. Parameters of this simulation and the estimates of the static model are given in Table 7.4 with the total energy consumption and costs of one day. In the Table also results are given for a system running only during the nighttime. The cooling load profile of this application corresponds to the air-conditioning example given in Figure 7.2. A 6.4 wt% sodium chloride solution is used as ice slurry, with initial freezing temperature of –4 °C. The installation is running 24 hours per day.

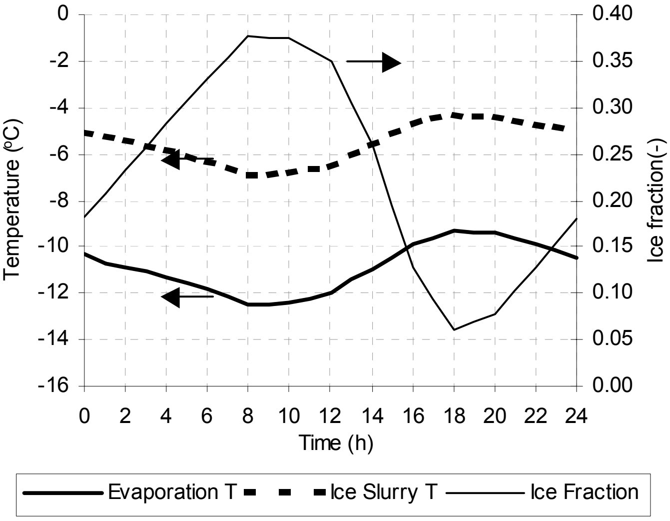

Figure 7.4: Variation of ice fraction and temperature for 1 day, NaCl T_{f_init}=-4 °C, fluidized bed, 24 hours on.

At midnight, when there is no cooling required, the ice fraction in the storage tank is approximately 0.18, as can be seen in Figure 7.4. The ice slurry temperature then is –5 °C and the corresponding ammonia evaporating temperature –10.3 °C. As the ice fraction in the storage tank is increased, the temperature decreases and the evaporation temperature also decreases. At 8 to 10 am the cooling load becomes high enough to reduce the ice fraction in the slurry storage tank. The ice fraction then drops during the day. At 6 pm the ice content is at its lowest value: 0.06. At the minimum point there is still a small ice fraction present to ensure that the cooling load is fully covered using the latent heat effect. Then until 12 pm the ice fraction is increased again until it is back at its starting point of 0.18.

At this temperature level the fluidized bed ice slurry generator is operated near its maximum allowable temperature difference during the entire 24 hours. The compressor is therefore relatively small, because larger compressors would result in lower evaporation temperatures which are not allowed. The temperature difference over the heat exchanger, ammonia-to-ice-slurry, is relatively constant between 5.0 K and 5.6 K, at an average of 5.4 K.

Variation of COP and power consumption of the compressor cycle are displayed in Figure 7.5. Operation during the day is less energy efficient than during the nightly hours. Also at higher ice fractions the power consumption is higher. Compare for example the hours 6-8 with the hours 18-20. In the period 6-8 there is a much higher ice fraction and also a higher power consumption than during the hours 18-20, while the outside temperature is equal for both periods, at 16.6 °C.

Of the total cooling capacity 6.7% is used for auxiliary components, determined with the dynamic model. In further simulations percentages in the range of 5% to 10% are found. The 5% estimate therefore is a good estimate for the minimum additional power consumption.

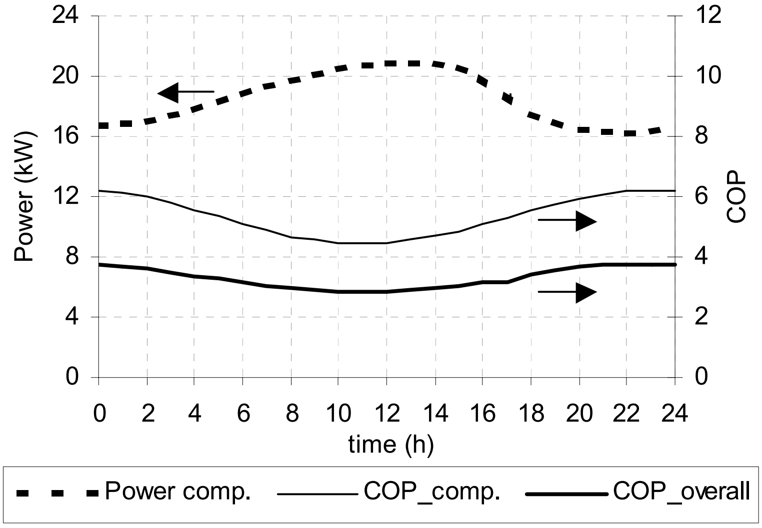

Figure 7.5 Variation of compressor power and COP for one day, NaCl, T_{f_init}=-4 °C, fluidized bed, 24 hour operation

The economically most favorable operating mode is 24 hours per day, determined in the static optimization. The ammonia evaporation temperature found in that simulation is however averaged over 24 hours. Although the average temperature found in the dynamic simulation corresponds rather well, with 0.1 K difference, the optimal operating hours could still be the 12 nightly hours. The simulation was therefore also evaluated dynamically with operation only at night. As initial estimate for the nighttime operation case, the static model could not be used as it results in the 24 hour operation mode. For initial estimates double the values of the heat transfer area, compressor swept volume and storage tank size of the 24 hour operation mode were used. These parameters were then optimized to match the cooling load of the system in the dynamic model.

The results of the nightly simulation are displayed in Table 7.4. The COP is slightly higher during the nightly operation, but the overall power consumption is still higher because of some extra heat losses compared to 24 hour operation. Energy costs are lower than for 24 hour operation, but under these conditions the extra investments for the larger equipment are higher for nightly operation. Overall costs for one day are 13% higher. This confirms that 24 hour operation is indeed the optimal operating strategy.

Table 7.4: Simulation results for 6.4 wt% NaCl ice slurry, initial freezing point -4 °C. Fluidized bed ice slurry generator for air-conditioning application

Operation mode		24 hours		Nightly operation (8 pm - 8 am)	
Model		Static	Dynamic	Static	Dynamic
Heat exchanger surface area	m^2	8.9	8.9	17.8	21.4
Compressor swept volume	m^3/h	111	111	221	239
Storage tank size	m^3	26.8	26.8	53.5	53.5
Avg. Evaporation T.	°C	-11.3	-10.9	-11.3	-10.6
Avg. Ice Slurry T.	°C	-5.6	-5.5	-5.6	-5.5
Avg. overall heat transfer c.	W/m^2K	1550	1644	1550	1649
Heat transferred	kWh	*x*	1868	*x*	2107
Ice produced	kWh	*x*	1766	*x*	1977
Avg. Compressor COP	-	*x*	6.10	*x*	6.18
Avg. Overall COP	-	*x*	3.26	*x*	3.34
Total power consumption	kWh	*x*	573	*x*	631
Total additional power cons.	kWh	*x*	125	*x*	169
Total energy costs (1 day)	€	32.3	35.0	*x*	26.5
Total invest. costs (1 day)	€	29.3	30.8	*x*	48.1
Total costs for 1 day	€	61.7	65.8	*x*	74.6

x = value not determined in static model

7.3.2 Application Temperature

At decreasing temperatures the freezing range of a solution increases. The relative importance of the latent heat effect becomes lower and the apparent heat capacity of the ice slurry is also lower. This will make a secondary cooling system less energy efficient. Added to a lower COP of the primary cooling cycle at lower temperatures, systems will become more expensive at lower temperatures. The static and dynamic models are used to evaluate the trends in costs and power consumption at lower temperatures. A hypothetical application with the same cooling load as the air-conditioning case of Figure 7.2 is assumed. Ice slurries just below 0 °C already have a relatively low temperature compared to other non-phase changing fluids in air-conditioning. For the current evaluation it is however assumed that each ice slurry temperature evaluated corresponds to the temperature required in a hypothetical application, not necessarily being air-conditioning. The heat transfer in the utilization stage is not further evaluated in the model, therefore the cooling load profile of Figure 7.2 is assumed to be valid at any temperature.

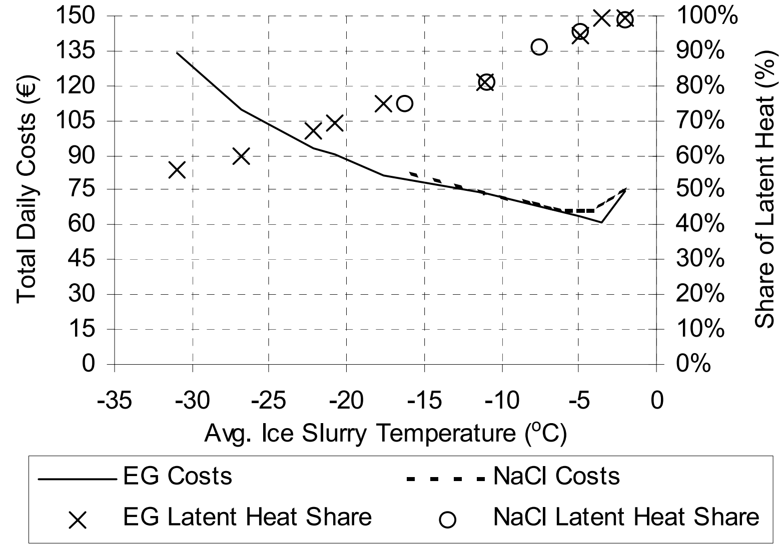

Figure 7.6: Total daily system costs and % of latent heat (ice production) for Ethylene Glycol and NaCl

In Figure 7.6 results of ice slurry simulations with NaCl and ethylene glycol are given. Initial freezing points for NaCl ice slurries were varied from -1.5 °C to –12 °C. NaCl has a eutectic point of –20.7 °C. At initial freezing point of –12 °C the average temperature found in the simulation is –16.5 °C and the lowest temperature encountered –20.4 °C. This is close to the eutectic point. Applications with NaCl at lower temperatures are not possible. Ethylene glycol can be applied until much lower temperatures. Simulations were performed down to initial freezing temperatures of –24 °C, which results in an average ice slurry temperature of –31 °C.

In Figure 7.6 the costs of a single day as predicted with the dynamic simulation are given. Also the share of latent heat effect in the total heat transferred is given. This is the percentage of the heat transferred that is actually used for ice formation and not for decreasing the temperature of the ice slurry.

At temperatures just below 0 °C the maximum allowable temperature difference results in a low energy consumption but also in relatively large equipment, which makes total costs high. The least expensive systems are in the temperature range of –3 °C to –5 °C, with daily costs of €61 for the least expensive ethylene glycol operating conditions at an average ice slurry temperature of –3.5 °C. The maximum allowable temperature difference in this range is not a strongly limiting factor, while temperatures are still relatively high. Temperatures of this range are typical for cooling applications. At lower temperatures, for example around –25 °C, typical for deep freezing applications, daily costs are around €105 using ethylene glycol as freezing point depressant. Systems for deep freezing are approximately 1.7 times more expensive than for cooling.

Most favorable operation mode determined in the static model for all simulations was 24 hour operation, only in the simulation with ethylene glycol at initial freezing point of –24 °C nightly operation was found to be most cost effective.

The fraction of heat transferred that is actually used for the formation of ice, decreases at lower temperatures, following a nearly linear trend. In the cooling range down to –5 °C more than 90% of the heat transferred is applied for ice formation. At freezing temperatures around –25 °C approximately 65% is used for this, the rest is required for sensible temperature change.

For ethylene glycol at low temperatures the maximum ice fraction in the storage tank was reduced to keep the temperature variation below 10 K. At points below –20 °C average ice slurry temperature the volume of the storage tank was enlarged. At –31 °C the maximum ice fraction in the storage tank during the day was only 0.21. Applications that require a lower variation of temperature may require an even larger storage tank and a lower maximum ice fraction. Benefits of the use of the latent heat effect then reduce.

As the freezing point of a solution decreases, the freezing range of the solution increases. The ice fraction becomes more important for the operating temperature and thus also for the total system costs. For example a system with ethylene glycol at initial freezing point of –15 °C operating at ice fractions between 0.03 and 0.33, has an average ice slurry temperature of 2.4 K higher than if it were operated at ice fractions between 0.08 and 0.38. Total system costs per day are approximately 5% higher at the higher ice fractions. Because of this wider freezing range exact determination of the freezing temperature has more impact on the accuracy of the calculations. Furthermore the average ice fraction should be kept as low as possible during the operation, but high enough to fully meet cooling requirements.

In Figure 7.7 the overall heat transfer coefficients calculated in the dynamic simulations for NaCl and ethylene glycol are displayed versus the average ice slurry temperature. Also the average temperature difference between ice slurry and evaporating ammonia in the fluidized bed ice slurry generator is given. The marks indicate conditions at which the dynamic simulation was performed.

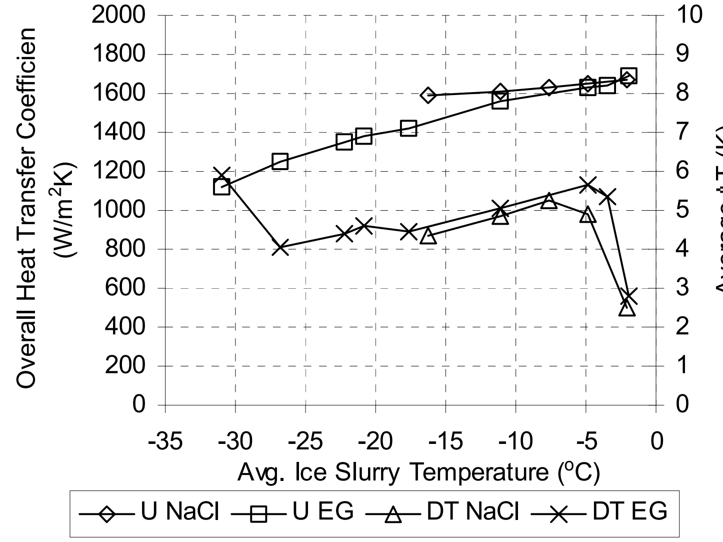

Figure 7.7: Overall heat transfer coefficients and overall temperature differences (primary refrigerant-ice slurry) for NaCl and Ethylene Glycol vs. ice slurry temperature

Heat transfer coefficients at cooling range temperature, down to –5 °C, are marginally higher for sodium chloride than for ethylene glycol. In the deep freezing range, around –25 °C, heat transfer coefficients have dropped from over 1600 W/m^{2}K to below 1300 W/m^{2}K. The optimum temperature difference found also decreases, from around 6 K to 4 K. Small deviations from the general trend are caused by slightly different ice fractions used in the calculations.

At approximately –30 °C, the optimum operating hours are no longer 24 hours a day, but the 12 hours in the night. With only nightly operation the installation required is much larger and investment costs are relatively high, which causes the jump in the optimum temperature difference to approximately 6 K. The overall heat transfer coefficient is hardly affected by the different operation hours.

For temperatures just under 0 °C the effect of the maximum allowable temperature difference is observed. The temperature difference is going towards zero, causing the increase in total costs just below 0 °C, as was displayed in Figure 7.6.

7.3.3 Freezing Point Depressants

In Figures 7.6 and 7.7 results for the freezing point depressants NaCl and ethylene glycol are displayed. The total costs and heat transfer performance in the ice slurry generator are similar in the range from –5 °C to –15 °C average ice slurry temperature. At lower temperatures sodium chloride cannot be applied because the eutectic point is encountered. At temperatures above –5 °C average ice slurry temperature, the higher allowable temperature difference of ethylene glycol makes this freezing point depressant more advantageous than sodium chloride. At the optimum point for ethylene glycol at –3.5 °C, total daily costs are €61.2, while at this temperature for sodium chloride costs are €69.6, 14% higher. If ice slurry temperatures are further increased, the difference between freezing point depressant reduces again.
Sodium chloride at a low pH has a higher limit for the maximum allowable temperature difference. Simulations were done using sodium chloride at a lower pH of 3. The lower pH resulted in a shift of the point of minimum costs to higher ice slurry temperatures. Total daily costs at an average ice slurry temperature of –3.5 °C (initial freezing temperature of -2.5 °C) were €64.3, compared to €69.6 for the same temperature at a pH of 7. The lowest point at pH=7 was €65.8 at an average temperature of –5.5 °C. For the simulation it was assumed that no other thermophysical properties are affected by the change of pH.

Two more freezing point depressants were evaluated at temperatures in the cooling and freezing range. These were calcium chloride and potassium formate. These freezing point depressants were selected because they are widely applied as secondary cooling fluids without phase change and may therefore also be profitable if used in ice slurries. For these freezing point depressants no experiments were done to obtain the maximum allowable temperature difference. The same limit as for sodium chloride was assumed, which was the lowest limit encountered in the experiments. Also the enthalpy of mixing of calcium chloride with water and of potassium formate with water were not as accurately known as for the other freezing point depressants. This because literature data were only available at high temperatures or at low concentrations.

Results of the dynamic simulations are given in Figure 7.8, where the total daily costs are displayed versus the average ice slurry temperature of the four freezing point depressants sodium chloride (NaCl), Ethylene Glycol (EG), Potassium Formate (KFor) and Calcium chloride ($CaCl_2$). The air-conditioning cooling load profile of Figure 7.2 was used for all freezing point depressants. The lines of NaCl and EG are the same as in Figure 7.6. The marks indicate the dynamic simulations performed for the other freezing point depressants.
For KFor around –5 °C, costs were very similar to ethylene glycol and NaCl. At temperatures around –20 °C, costs of KFor were higher than for EG.

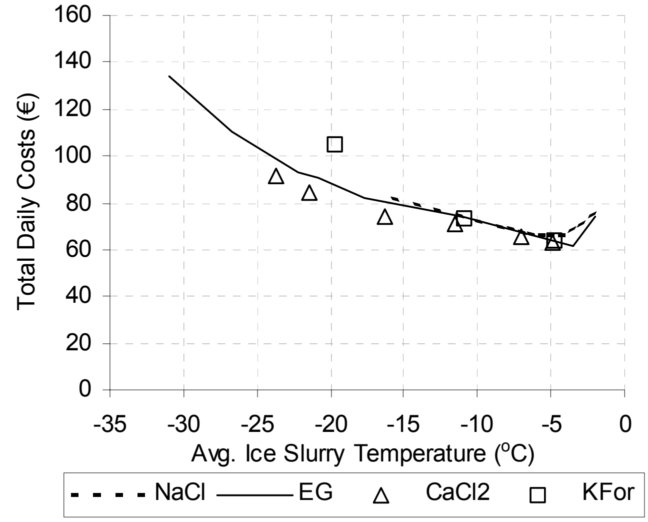

Figure 7.8: Costs of four freezing point depressants

Calcium chloride as freezing point depressant also results in similar costs as for ethylene glycol and NaCl down to –15 °C average ice slurry temperature. At lower temperatures total costs of calcium chloride were significantly lower than for ethylene glycol and for potassium formate.
The influence of the ice fraction in this temperature range is more important, therefore the overall accuracy of calculations reduces at lower temperatures. This is caused by the increasing influence of small errors in calculations of the freezing point and the heat of mixing at lower temperatures.

The type of freezing point depressant used in the ice slurry at temperatures between –5 °C and –15 °C does not influence the heat transfer performance greatly. Other factors as safety or the choice of materials will be decisive. At temperatures above –5 °C the maximum allowable temperature difference of a freezing point depressant is the decisive factor. At deep freezing temperatures, below –15 °C, the type of freezing point depressant appears to be important for the total system costs. More detailed knowledge of the freezing curve and of the heat of mixing is required to improve the accuracy of the predictions in this application range.

7.3.4 Fluidized Bed Compared with Scraped Surface Ice Slurry Generator

The ice slurry generator in the model was replaced with a scraped surface heat exchanger. As primary refrigerant still ammonia falling film evaporation was assumed. The air-conditioning cooling load profile of Figure 7.2 was again used for the model simulations. The system dimensions used are displayed in Table 7.5. These system dimensions were not optimized in the modeling, but based on data from literature (Gladis et al. 1995 ;Bel et al. 1996)

Table 7.5: Dimensions of scraped surface ice slurry generator

Scraped tube outside diameter	m	0.12
Rotor diameter	m	0.1
Rotor speed	rpm	500
Rotor angle	°	5
Scraper height	m	2.5
Wall thickness	mm	2
Throughput per scraped tube	m^3/h	4

Wall to ice slurry heat transfer coefficients were calculated using the model presented by Bel et al. (1996), who developed an empirical correlation for the Nusselt number for apparatus with a screw-type scraper:

$$Nu = \frac{\alpha \cdot D_h}{\lambda_{is}} = (Re_{rad} + Re_{ax})^{0.245} \cdot Pr^{0.142} \tag{7.21}$$

where D_h is the hydraulic diameter or the inside tube diameter, D_{in}, minus the diameter of the rotor shaft, D_r. The radial and axial Reynolds numbers are given by:

$$Re_{rad} = \frac{\rho_{is} v_{rad} D_{in}}{\mu_{is}} \tag{7.22}$$

$$Re_{ax} = \frac{\rho_{is} v_{ax} (D_{in} - D_r)}{\mu_{is}} \tag{7.23}$$

In Equations 7.22 and 7.23, the axial velocity, v_{ax}, and the radial velocities, v_{rad}, are related by:

$$v_{rad} = v_d + v_{ax} \cdot \cot \beta = \frac{-\pi \cdot D_{in} \cdot N}{60} + \frac{4 \cdot v_{is}}{\pi \cdot \left(D_{in}^{2} - D_{r}^{2}\right)} \cdot \cot \beta \tag{7.24}$$

in which β is the angle of the rotor blade to the radial direction and v_d the velocity of the rotor tip. Overall heat transfer coefficients calculated were around 850 W/m^2K for cooling range temperatures, decreasing to below 700 W/m^2K for temperatures down to –20 °C. The scraped surface system was not evaluated at lower temperatures because of the eutectic point of NaCl.

Overall heat transfer coefficients calculated using this method were higher than most of the data that Bel *et al.* used to determine the heat transfer correlation. The heat transfer coefficients calculated were however similar to what is actually obtained in commercial installations (Jans, 2001; Beismann, 2001; Gladis et al., 1995). For initial estimations in the static model the coefficients of c_1= 1000 and c_2=50 were used in equation 7.2:

$$U = c_1 + c_2 \cdot T_{f\_init} \tag{7.2}$$

For the scraped surface heat exchanger it was assumed that there is also a maximum allowable temperature difference between wall and ice slurry, above which ice will attach to walls and the ice slurry generator will malfunction. No experimental data were available on ice slurry generation with sodium chloride as freezing point depressant. An estimate of the limit was therefore made, based on Vaessen (2003), who did experiments on potassium nitrate crystallization. The temperature difference above which ice scaling occurred in these experiments was taken as the maximum allowable difference for ice slurry generation. The limit was considerably higher than for the fluidized bed ice slurry generator. Probably because the force with which the scrapers can press against the walls is higher than the force the fluidized beds can exert on the walls or on ice at these walls. A larger allowable temperature difference is therefore likely for the scraped surface ice slurry generator. Coefficients of Equation 7.13 were assumed c_1=143 and c_2 =0.

$$\Delta T_{\max, wall-to-slurry} = c_1 \cdot w_{fpd} + c_2 \tag{7.13}$$

Additional power inputs of ice slurry pumps was assumed equal to power input of slurry pumps in the utilization stage. For the power consumption of the scrapers, 3% of the cooling capacity was assumed. Half of the heat dissipated by the scrapers was assumed to result in the addition of heat and in melting of ice.

Investment costs of the scraped surface ice slurry generator were calculated using c_1=6000 and c_2=0.75 (Jans, 2001; Sinnot, 1993). For the parameter x the heat transfer surface area is used.

$$Inv_{component} = c_1 \cdot x^{c_2} \tag{7.4}$$

The results of the comparison are given in Figure 7.9. The point where total costs are lowest for the scraped surface heat exchanger is at a higher average ice slurry temperature than that of the fluidized bed system. The total costs using the fluidized bed ice slurry generator are however lower. It should be noted that the comparison does not include the costs of maintenance.

At –4 °C costs of both ice slurry generators differ approximately 8%. At lower temperatures the difference increases up to 20%.

It is likely that with ethylene glycol as the freezing point depressant there will also be a larger allowable temperature difference in the scraped surface evaporator, which would improve the system performance.

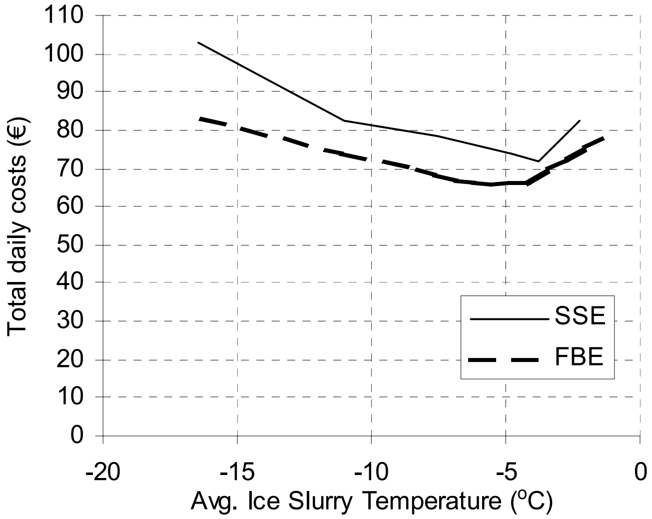

Figure 7.9: Comparison of fluidized bed (FBE) and scraped surface evaporator (SSE)

7.3.5 Large Scale Applications

The comparisons of the previous paragraphs were done for the cooling load profile of the air-conditioning case as given in Figure 7.2. This cooling load profile was considered for general applications, disregarding whether or not the temperature levels are actually required in air-conditioning. Another cooling load profile at a much larger scale is considered here. This profile is obtained from Bellstedt and Xiao (2002) and is displayed in Figure 7.10. It is based on the cooling load requirements of a pork slaughterhouse, with a peak load of 600 kW and a minimum load of 100 kW during the night. The cooling load profile given in the reference is four times larger than the profile given in Figure 7.10, but for the comparison a portion of that large profile is taken. This large capacity is also evaluated disregarding if the temperature level of the ice slurry is actually required by an application.

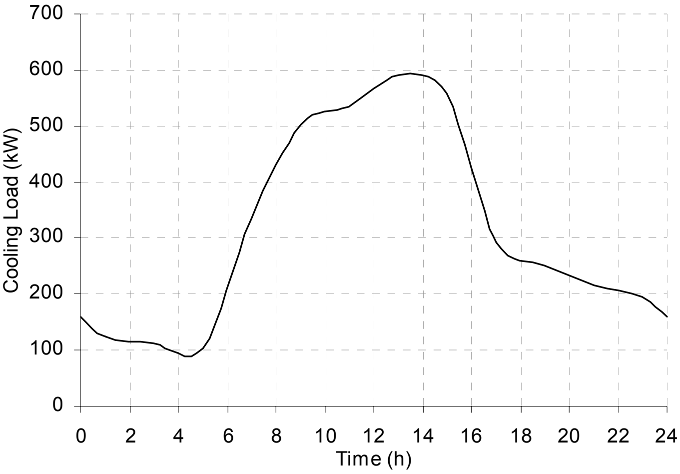

Figure 7.10: Cooling load profile based on pork slaughterhouse (example of large scale application)

For the larger capacity a lower electricity tariff is used of 2.5 €ct/kWh during the night and 5 €ct/kWh during the day. In all simulations the system in operation for 24 hours a day is found to be most efficient.

Resulting total costs after static and dynamic optimization are displayed in Figure 7.11. NaCl and ethylene glycol are evaluated as freezing point depressants in the fluidized bed ice slurry generator. Also the system is simulated using NaCl in the scraped surface heat exchanger.
The difference between ethylene glycol and sodium chloride as freezing point depressant is similar to the smaller application. The ice slurry temperature at which the costs are lowest is marginally shifted towards lower temperatures.
The difference in using a scraped surface ice slurry generator or a fluidized bed ice slurry generator is larger than for the small cooling load. At the point of lowest costs, at –5 °C, the scraped surface evaporator is 23% more expensive than the fluidized bed system. The difference with the ethylene glycol fluidized bed system at –4 °C is 34%. The increased difference at large scale applications is mainly caused by the higher investment costs of the scraped surface system, which has less benefits of an increase of scale than the fluidized bed ice slurry generator.

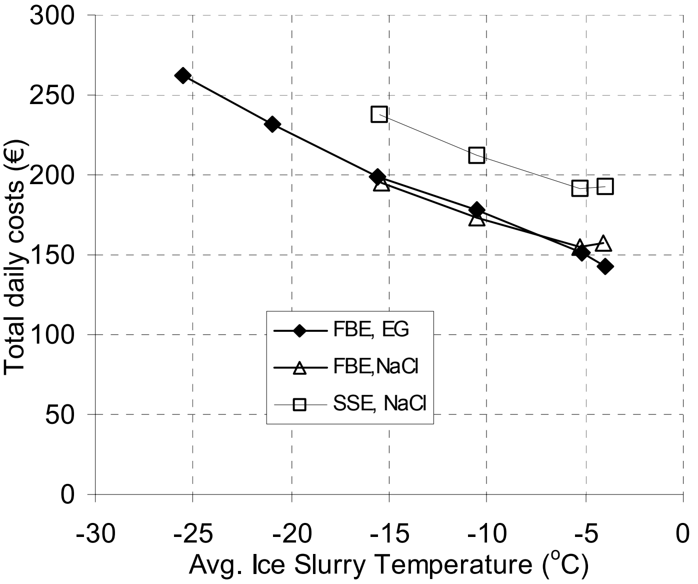

Figure 7.11:Comparison for larger scale application, freezing point depressant and ice slurry generator

7.3.6 Comparison with Non Phase Changing Secondary Fluids

The ice slurry system with ethylene glycol as freezing point depressant is compared to a secondary cooling system with aqueous solutions of ethylene glycol without phase change as the working fluid. The cooling load profile based on the air-conditioning case from Figure 7.2 was again used. A shell and tube evaporator is assumed to cool the ethylene glycol solutions. Falling film evaporation of ammonia is assumed on the shell side of the evaporator. The tubes through which the ethylene glycol flows are stainless steel and have an outside diameter of 0.02 m, with 2 mm wall thickness. The superficial velocity of the ethylene glycol is 1 m/s. Length of the tubes is assumed to be 2.5 m. For calculation of pumping power requirements for the evaporator 1 bar pressure drop over the evaporator is taken. Wall to ethylene glycol heat transfer coefficients are calculated using the Dittus-Boelter model (Holman, 1997):

$$Nu = 0.027 \cdot Re^{0.8} \cdot Pr^{0.33} \tag{7.25}$$

Overall heat transfer coefficients calculated are in the range from 1100 W/m^{2}K around 0 °C, down to 500 W/m^{2}K at –25 °C.

Investment costs required for the evaporator are assumed to be 40% of the fluidized bed ice slurry generator (DACE, 1995). Coefficients of equation 7.4 are then: $c_1 = 3000$ and $c_2 = 0.52$. The heat transfer area is used for the quantity x.

$$Inv_{component} = c_1 \cdot x^{c_2} \tag{7.4}$$

Because there is no ice formation there is also no maximum allowable temperature difference. The only requirement is that the ethylene glycol fraction should be high enough so that the solutions stay above the freezing temperature at all times. The ethylene glycol weight fraction is varied from 0.25 at –1 °C to 0.50 at an average temperature of –20 °C. The temperature variation in the storage tank is limited at 10 K.

For all non-phase changing systems evaluated, 24 hour operation was identified as the optimal operation strategy. Results of the comparison with ice slurries based on ethylene glycol in the fluidized bed system are displayed in Figure 7.12. The total costs required for the non-phase changing systems are 20% to 28% higher than of the ice slurry systems at average temperatures below –3.5 °C. Investment costs required for the evaporator of the non-phase changing systems are typically lower, but the size of the storage tank required is much larger. Therefore total investment costs of the non-phase changing systems are higher than for the ice slurry systems. Size of tanks without phase change calculated was typically around 105 m^3, compared to 25 to 30 m^3 for the ice slurry systems. At higher temperatures, the maximum allowable temperature difference makes the ice slurry systems more expensive. At a temperature of –2.5 °C system costs are equal. Non-phase change systems without storage tanks have not been considered.

The lowest cost of the ethylene glycol ice slurry system was €61.2 per day at –3.5 °C. The highest temperature encountered during the 24 hours for this system is –2.7 °C. The least expensive non-phase changing system evaluated in this system at an average temperature of –1 °C costs €70.6 per day, 15% higher than for the ice slurry system. The maximum temperature encountered during the day is 3 °C for this evaluation.
Assuming a linear trend in the costs of the non-phase changing system, an extrapolation to temperatures above 0 °C can be made, assuming that the total system costs reduce €1.7 per °C temperature increase. It will depend on the temperature requirements of the secondary cooling application if the non-phase changing system will be less expensive than the ice slurry system.
It should be noted that in this comparison positive effects of the use of ice slurries in the utilization stage have not been included. Size of heat exchangers and of tubing in the utilization stage may be smaller because of the higher heat contents of the ice slurries.

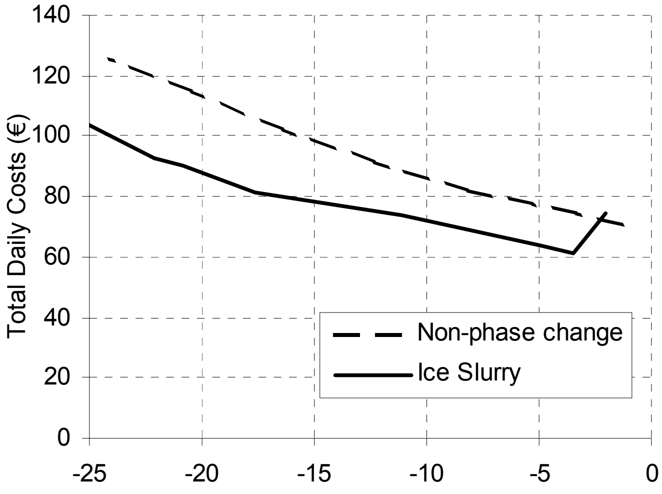

Figure 7.12: Comparison Ice Slurry and Non-phase change systems (Ethylene Glycol)

7.4 Other Conditions

7.4.1 Electricity Tariffs

The electricity tariffs and the difference between day and nighttime tariffs are of considerable influence on the design of ice slurry cooling systems. For the air-conditioning case, the static model was run at varying electricity tariffs at an ice slurry initial freezing temperature of –3.5 °C. In Figure 7.13 the horizontal axis displays the electricity tariff during the nightly period, on the vertical axis the ratio that the electricity tariff is higher during the day than during the night is given.

Two types of optimal operation schedule were found: 24 hour operation and operation only during the night. At high electricity tariffs and high differences between day-and nighttime tariff, shifting to the nighttime is more favorable, at low tariffs and low differences, 24 hour operation is more favorable. In Figure 7.4 the limit between the two schedules is also given for half the cooling load and for double the cooling load. For larger applications, nighttime operation is more feasible at lower electricity tariffs.

Tariffs considered in this Chapter are at point 'A' in Figure 7.13. These applications, using in the order of 100.000 kWh per year, are charged with 0.6 €ct/kWh 'ecotax' (DTe, 2002). Larger applications, above 10^6 kWh yearly usage, are exempt of ecotax, typical tariffs will be around point B in Figure 7.13. Smaller applications, below 50.000 kWh yearly usage, are charged with 2.1 €ct/kWh ecotax and typical tariffs are near point C. It appears likely that a 24 hour operation will be the most favorable for ice slurry applications in air-conditioning in the Netherlands. It should be noted that the fixed electricity costs are not included and therefore electricity tariffs are relatively low.

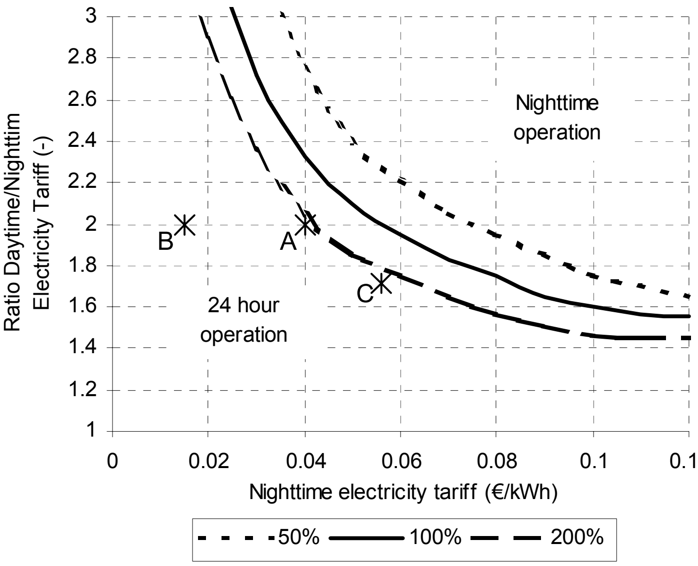

Figure 7.13: Operation strategy at various electricity tariffs and application sizes (100%=Air-conditioning case, 1790 kWh/day)

7.4.2 Seasonal Influences

In all simulations so far the outside temperatures of an average Dutch summer day are used. The temperature profile is given in Figure 7.14, with the average Dutch temperatures in fall, winter and spring over the period 1971-2000 (KNMI, 2003). The difference between maximum and minimum temperatures determines how large the benefits for the power consumption are if the cooling load is shifted to the nighttime using ice slurries. In the Netherlands this difference is not large: 9.8 K in the summer, reducing to 5.5 K in the winter. If systems are installed in countries with larger day/night gradients, ice slurry systems would become more feasible.

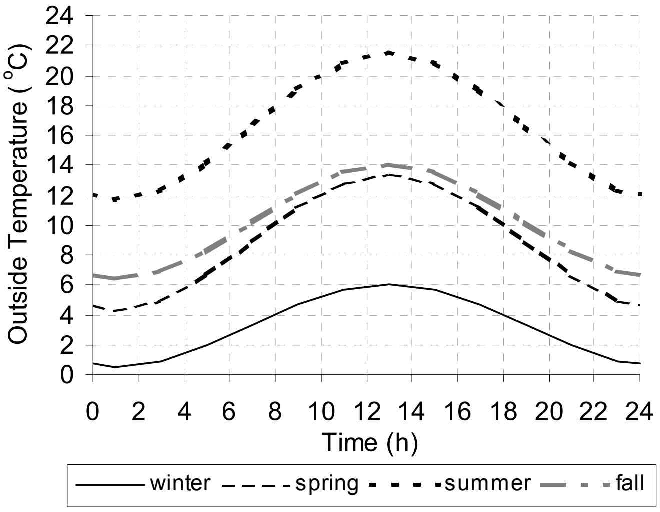

Figure 7.14: Temperature variation per day in the Netherlands

The case based on the cooling load profile of air-conditioning, optimized with the static and dynamic model for summer outside conditions is again simulated in the dynamic model, but now with different outside temperatures. All other parameters and dimensions were kept equal to the optimized case in the summer. The point of lowest costs with NaCl as freezing point depressant, initial freezing temperature of –3.5 °C, in the fluidized bed ice slurry generator was evaluated. The total cooling demand was kept equal. The efficiency of the compressors was assumed to remain constant at 0.8.
If outside temperatures are lower, condensation temperatures can be lower. COPs improve and the energetic performance of the system also increases. At the end of the 24 hours the ice fraction has increased. As system dimensions are not changed, the total operational hours are reduced, so that there is no net change in ice fraction over 24 h. The system was stopped during the day-period around noon first, where the compressor operation is most expensive. Results of the simulations of the four seasons are given in Table 7.6.

Total power consumption is significantly lower in winter. The ice slurry generator can be stopped for over an hour per day. The higher COP in the winter results in a 35% lower power consumption. Total costs are €9.8 lower per day in winter, a reduction of approximately 15%.
In this evaluation it was assumed that the cooling demand during the day did not change from season to season. Though this may be true in some applications, probably in industrial applications, it is more likely that the cooling demand will be lower in the winter, especially in air-conditioning applications. Power consumption is then further reduced than indicated in this evaluation. In the Netherlands especially air-conditioning will not be required at all in the winter. Power consumption will be negligible, but investment costs will remain at the same level.

Table 7.6: Seasonal influences on costs of NaCl ice slurry system

		Summer	Fall	Winter	Spring
Average Temperature	°C	16.6	10.2	3.3	8.9
Difference Max T-Min T	K	9.8	7.6	5.5	9.1
Operational hours	h	24	23.4	22.7	23.3
Primary power consumption	kWh	448	367	304	352
Auxiliary power consumption	kWh	125	123	121	122
Investment costs	€	30.8	30.8	30.8	30.8
Total costs	€	65.8	60.5	56.0	59.6

7.4.3 Part-load Operation

The NaCl ice slurry system was also simulated under part-load conditions. All parameters and system dimensions were kept the same, while the load was reduced with a proportional factor during the entire day. Summer outside conditions were used in the simulations, as there may also be other reasons than seasonal influences for a lower cooling demand. The demand was varied from 50% to 110%. A reduced cooling demand was simulated by a reduction in the operational hours. An increased cooling load was made possible by increasing the compressor swept volume, during which the efficiency of the compressor was assumed to remain equal. As this assumption only holds for a slightly increased cooling load, the maximum load evaluated was 110%.

The results for the total costs are given in Figure 7.15. Also the required operational hours are given. The total operational hours are higher than the percentage of cooling demand would suggest. For 50% of the cooling load, more than 12 hours operation is required, approximately 13 hours. This is because of heat losses during storage and because of power consumption of auxiliary equipment. The total power consumption therefore reduces with less than 50%. As the system is stopped mainly during the expensive daytime period, power costs reduce with more than 50%. In the evaluation of Figure 7.15, power costs are approximately 60% lower for a 50% cooling load reduction. At 25% load reduction, power costs are 30% lower.

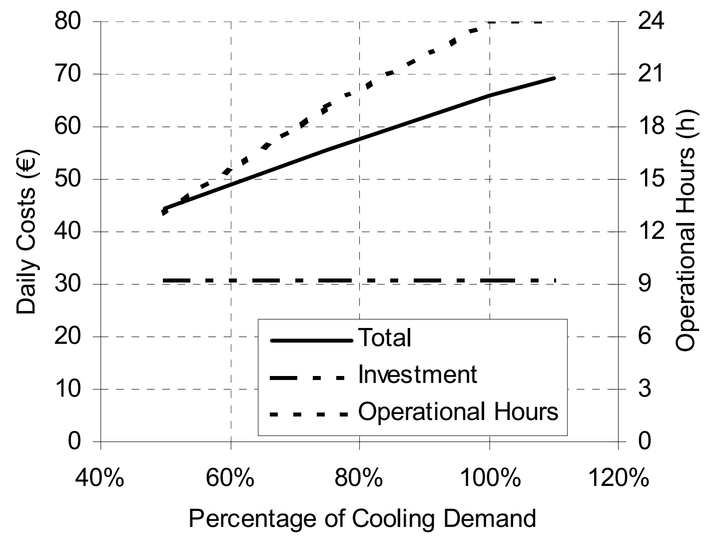

Figure 7.15: Costs and operational hours at part-load operation, summer conditions

Once the variation of the cooling demand throughout the year is known, seasonal influences and part-load conditions can be implemented in the dynamic simulation model and the cost estimation can be extended to the yearly costs.

7.5 Application Case Studies

The results of the dynamic simulations discussed in the previous sections are applied to evaluate ice slurry system designs in air-conditioning, supermarket cooling and food industry cooling and freezing. Temperature requirements and different cooling load profiles of the applications are evaluated. Results of the simulations are indicative values: A competitive offer by a manufacturer may alter results. As was shown in 7.4.1, also a different electricity tariff can be of considerable influence.

7.5.1 Case 1: Air-conditioning

In air-conditioning most of the cooling load is required during the hottest parts of the day, during the night no cooling is required. The cooling load profile of Figure 7.2 is used, with peak cooling load of 275 kW and a total cooling demand of 1790 kWh per day. The electricity tariff was assumed at 4 €ct per kWh during the night and 8 €ct per kWh during the day.

Secondary cooling fluids without phase change in air-conditioning are typically used at temperatures above 0 °C, up to 6 °C. Relatively high temperatures are preferable in the utilization heat exchangers. For higher ice slurry temperatures 24 hour operation is economically most efficient. Results of the simulations are given in Figures 7.16 and 7.17. In Figure 7.16 the costs of a single summer day at varying ice slurry initial freezing temperatures are given for a fluidized bed evaporator with sodium chloride as freezing point depressant. In Figure 7.17 the corresponding ammonia and ice slurry temperatures averaged over the day are given. System characteristics after optimization are given in Table 7.7 together with results of dynamic simulations of other systems.

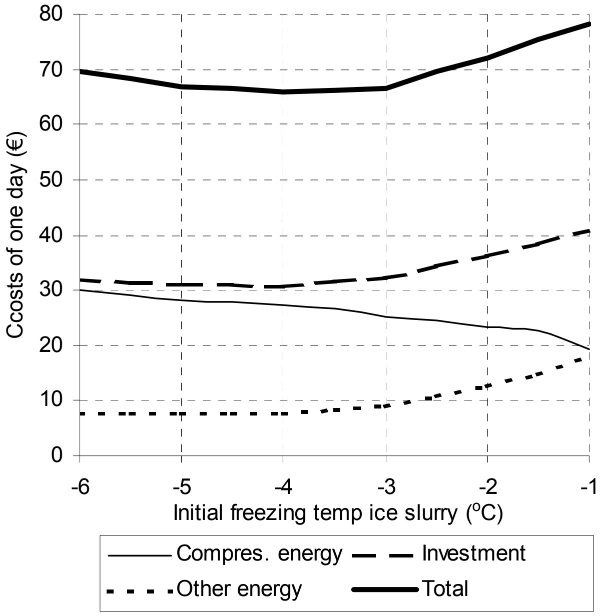

Figure 7.16: Air-conditioning costs, NaCl, FBE

In Figures 7.16 and 7.17 it is seen that at high ice slurry temperatures the maximum allowable temperature difference of the fluidized bed ice slurry generator will cause the system to operate at smaller temperature differences than the economic optimum. A larger than optimal heat exchanger is then required and investment costs are relatively high. The lowest costs are found around –4 °C initial freezing temperature. At this temperature the system operates at an average ice slurry temperature of –5.5 °C and an average ice fraction of 0.23 in the storage tank. The fluidized bed ice slurry generator required has a heat exchanging area of 8.9 m^2, which can be achieved with 22 parallel fluidized tubes of 2.5 m height and 51 mm diameter. The average overall heat transfer coefficient is 1644 W/m^{2}K. The latent heat effect of ice formation takes up about 95% of the heat transferred in the ice slurry generator, so that the temperature variation during the day is small: 2.6 K.

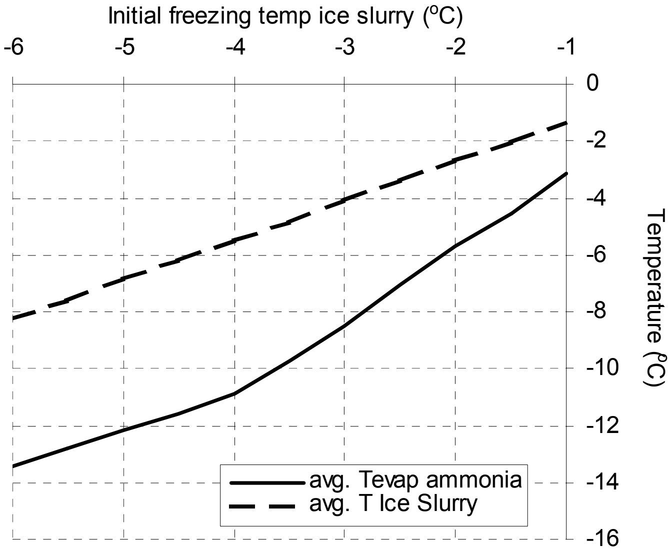

Figure 7.17: Ice slurry and ammonia temperatures for air-conditioning, NaCl, FBE

Table 7.7: Results of air-conditioning after dynamic optimization

		Ice Slurry NaCl	Ice Slurry +2.6 K	Ice Slurry Part load	Ice Slurry EG	Ice slurry low pH	Ice Slurry SSE	Non phase change
Peak load	kW	275	275	138	275	275	275	275
Total daily load	kWh	1790	1790	895	1790	1790	1790	1790
Freezing pt. depress.		NaCl	NaCl	NaCl	EG	NaCl	NaCl	EG
Initial T freeze	^oC	-4	-1.5	-4	-2.5	-2.5	-3.5	-
Avg. ice slurry T	^oC	-5.5	-2.1	-5.4	-3.5	-3.5	-4.8	-1.3
Ice slurry T change	K	2.6	0.9	2.6	1.8	1.7	2.3	7.9
Tot. heat transferred	kWh	1868	1909	1029	1831	1884	1836	1966
Tot. ice produced	kWh	1766	1884	957	1771	1854	1645	-
Avg. evaporation T	^oC	-10.9	-4.5	-10.8	-8.9	-8.8	-16.0	-4.6
Avg. COP overall	-	3.26	3.08	3.36	3.40	3.43	2.92	3.70
Heat transfer coeff.	W/m^2K	1644	1670	1666	1644	1648	775	1104
Storage tank	m^3	27	26	27	27	26	27	106
Compressor ϕ_v	m^3/h	111	90	111	100	106	131	90
Heat exchanger	m^2	8.9	19.1	8.9	8.3	9.0	8.8	25.1
Total daily costs	€	65.8	75.6	45.0	61.3	64.3	73.7	70.6

The optimum of –4 ^oC found here is not sharp, as can be seen in Figure 7.16. At –3 ^oC daily costs are only 1% higher. At higher temperatures the maximum allowable temperature difference becomes more and more important. In Table 7.7 results are given at 2.6 K average ice slurry temperature above the optimum point. Costs are 15% higher, mainly because the generator becomes more than twice as large. The additional power consumption increases significantly and the overall COP becomes lower than at –4 ^oC, while the COP of the primary cooling cycle is higher.

The ice slurry system with sodium chloride was also evaluated at 50% of the cooling load. The system then needs to be operated during approximately 13 hours, 12 during the night and one hour during the day. The size of the storage tank is large enough so that the maximum ice fraction remains below 0.40. As the system can operate mainly during the less expensive nightly hours, the costs of power consumption reduce with more than 50% per day. Investment costs remain €30.8 per day, the energy costs become €14.2 per day, compared to €35 per day for the full load.
Ethylene glycol has a higher allowable temperature difference and therefore the lowest operation costs are found at a higher temperature: -3.5 ^oC average ice slurry temperature. At this temperature the ethylene glycol system is 7% less expensive than the system using NaCl.

The maximum allowable temperature difference using sodium chloride can be increased by lowering the pH. The lowest costs are then also found at higher temperatures. At an average ice slurry temperature of –3.5 ^oC, total daily system costs become 2.3% lower compared to pH neutral conditions. Costs are however still higher than for the ethylene glycol ice slurry system.
The scraped surface evaporator system is more expensive mainly because of the lower heat transfer coefficient. In the simulation a lower evaporation temperature is found, at a heat exchanger area similar to the fluidized bed system. Additional costs of for example maintenance are not included in the comparison.

Finally a non-phase change system based on ethylene glycol is included in the comparison. The system simulated had an average temperature of –1.3 °C and a maximum temperature during the day of 3 °C. Total costs of one day are 15% higher than for the ethylene glycol ice slurry system. This is caused mainly by the large storage tank required to accommodate the cold storage. The simulation was done at a temperature approximately 3 K lower than the maximum design temperature of 6 °C common in air-conditioning systems. Extrapolating the simulation results of section 7.3.6, the total costs at the maximum are estimated at €65.5. This is similar to the optimal sodium chloride ice slurry case and approximately 7% higher than the ethylene glycol ice slurry system at –3.5 °C. It should be noted that effects of temperature glides in utilization heat exchangers and transport lines are not included in the current comparison. Also the performance of heat exchangers in the utilization stage has not been included.

The economically most feasible system that follows from the dynamic optimization is the ice slurry system with the fluidized bed evaporator and ethylene glycol as the freezing point depressant. Use of sodium chloride with reduced pH is the second best alternative.

7.5.2 Case 2: Supermarket Cooling

In supermarkets cooling is required 24 hours a day, mainly for storage rooms and cooling cabinets. During shop hours there is additional heat input because of customers and equipment as lighting and fans. There are peaks in demand as cabinets are refilled with products. Temperatures required in supermarket cooling are typically between 0 °C and 5 °C, so that a secondary coolant temperature of –1 °C and –6 °C is mostly used (Crielaard *et al.*, 2000). A typical cooling load profile is displayed in Figure 7.2. The peak cooling load of 117 kW is lower than the air-conditioning case, but the total cooling demand of 2076 kWh for one day is of similar size. Electricity tariffs are assumed at 4 €ct per kWh during the night and 8 €ct per kWh during the day. In supermarkets also air-conditioning may be required. A supermarket ice slurry storage system can also be applied for this, with similar effects as discussed in the previous section. In this section however only the cooling load involved with the food storage and displays cabinets is included in the cooling load profile.

The optimal initial freezing temperature found after dynamic simulations is –4 °C for a system with NaCl as freezing point depressant and a fluidized bed evaporator. Characteristics of this optimized system are given in Table 7.8. There is a relatively constant cooling demand, also during the night, therefore the storage tank is small compared to the air-conditioning case. In Table 7.8 also results of other system simulations are given for comparison.

Ice slurries with ethylene glycol as freezing point depressant result in slightly lower system costs than with sodium chloride. The difference in the air-conditioning case was 7%, because of a higher temperature difference allowable using ethylene glycol as the freezing point depressant. Temperatures required in a supermarket cooling application are lower than in air-conditioning. In supermarket applications both freezing point depressants are used at a temperature where the maximum allowable temperature difference is not encountered during the 24 hours.

Table 7.8: Results of supermarket cooling after dynamic optimization (peak load=117kW, total cooling load=2076 kWh)

		Ice Slurry NaCl	Ice Slurry EG	Ice Slurry 50% of Load	Ice Slurry SSE	Non phase change	Ice Slurry Freeze	Nonphase change Freeze
Freeze pt. depress.		NaCl	EG	EG	NaCl	EG	EG	EG
Concentration fpd	wt%	6.5	12	12	6.5	35	32	50
Initial T freeze	^oC	-4	-4	-4	-4	-	-16	-
Avg. ice slurry T	^oC	-5.4	-5.2	-5.7	-5.1	-5.4	-19.9	-22
Ice slurry T change	K	2.0	1.9	3.6	1.5	6.7	6.1	5.7
Tot heat transferred	kWh	2128	2097	1371	2139	2180	2177	2267
Total ice produced	kWh	1971	1879	1127	1914	-	1388	-
Avg. evaporation T	^oC	-10.9	-10.5	-11.0	-16.0	-8.9	-24.7	-24.7
Avg. COP overall	-	3.36	3.35	3.32	2.98	3.32	2.30	1.95
Heat transfer coeff.	W/m^{2}K	1669	1676	1625	1462	790	1449	527
Storage tank	m^3	4.3	4.3	4.3	6.3	19	5.4	19
Compressor ϕ_v	m^3/h	128	120	120	153	117	222	239
Heat exchanger	m^2	9.8	10.0	10.0	10.5	32.1	16.2	73.5
Total daily costs	€	64.3	64.1	52.9	76.9	66.5	91.8	107.9

The storage tank leads to less flexibility if only part of the cooling load is required. For 50% of the cooling load, the ice slurry generator is again stopped during several hours of the day. As the ice fraction rapidly increases above the maximum of 0.40 if at a partial cooling load, shorter stops are required several times during 24 hours, including stops during the nighttime. In total the system at part-load is operational for 16 out of 24 hours. As a result of this the energy costs are only reduced with 37%, while in the air-conditioning case energy costs could be reduced with 60%. For supermarket applications it might therefore be advisable to install a storage tank that is larger than optimal for full load conditions, to obtain larger energy costs reduction at part-load operation.

The storage tank is relatively small, therefore also the non-phase change system with ethylene glycol solutions is relatively inexpensive. It is 4% more expensive than the most economic ice slurry option. The non-phase change fluids do not have an advantage of a higher operation temperature as large as in air-conditioning applications.
The supermarket application evaluated is 16% larger than the air-conditioning case. Total costs are however only 5% higher, as a much smaller storage tank is sufficient to accommodate the load shifting.

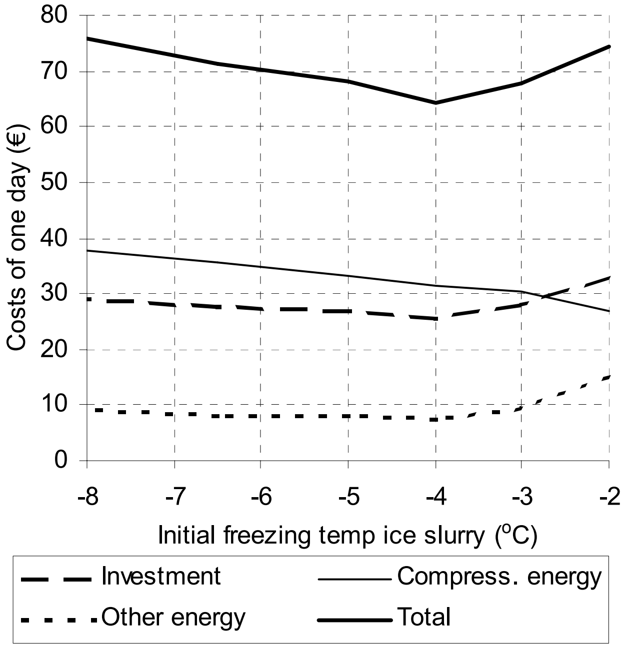

Figure 7.18: Supermarket cooling costs, NaCl, FBE

Ice slurry generators required are relatively large, which is disadvantageous for the scraped surface evaporator. Total daily costs are 19% higher than for the fluidized bed system, using NaCl as freezing point depressant. The scraped surface system with EG might be less expensive. The difference between the freezing point depressants for the fluidized bed evaporator is however not large and therefore also a small difference is expected for the scraped surface evaporator.

In Figure 7.18 the total costs of supermarket cooling is given at varying initial ice slurry freezing temperatures. Also investment costs, primary cycle energy costs and auxiliary energy costs are given. In Table 7.8 data at an initial freezing temperature of –4 ^{o}C are given. This corresponds with an average ice slurry temperature of –5.4 ^{o}C. Lowest costs are at -4 ^{o}C, at higher temperatures the maximum allowable temperature difference is encountered.

Costs of systems at lower temperatures also increase. If a similar cooling load profile is assumed for deep freezing applications in supermarkets, for example at –20 ^{o}C, costs are €91.8 per day. The temperature variation is 6.1K and only 64% of the heat transferred is used for ice formation. The difference at deep freezing temperatures with non-phase change systems is 15%.

Ice slurry systems with fluidized bed heat exchangers can be feasible for supermarket cooling applications. Ethylene glycol as the freezing point depressant resulted in the system with the lowest costs. As the cooling load profile allows for less cold storage possibilities, advantages of ice slurries are not as large as in air-conditioning. On the other hand there is no disadvantage of temperature level compared with non-phase changing fluids. Possible benefits of ice slurries in transport lines and application heat exchanger may increase the advantage of ice slurry systems in supermarket applications.

7.5.3 Case 3: Cheese Factory Cooling

A food industry application is evaluated in this section: Cooling in a cheese factory. The cooling load profile of Figure 7.19 has been obtained from Gladis (1997).

For cheese production mild cooling is required in various stages of the production process. There is a peak in demand of 230 kW at the start-up of a new production batch. There is also a permanent cooling demand because of storage rooms. The total cooling load during 24 hours is 2544 kWh. Electricity tariffs of 4 €ct/kWh and 8 €ct/kWh are assumed.

As cheese production and storage do not require low temperatures, the secondary cooling fluid temperature should be just below 0 ^{o}C. The maximum allowable temperature difference of the fluidized bed may therefore be a limiting factor for application of ice slurries in a secondary cooling cycle in a cheese factory.

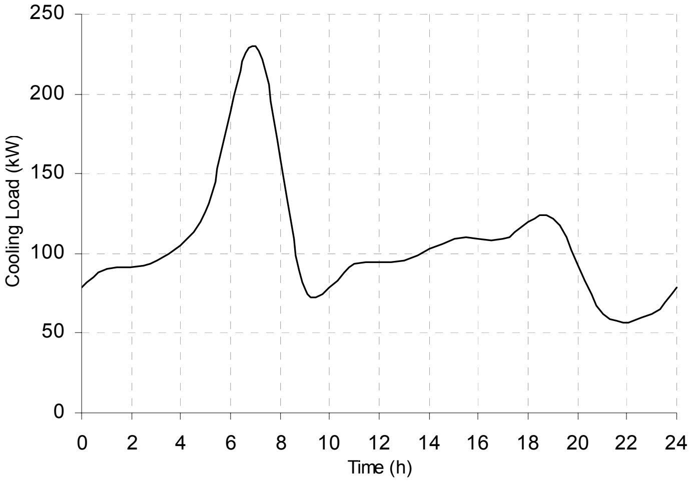

Figure 7.19: Cooling load profile of a cheese factory

Results of the dynamic optimizations are given in Table 7.9. The ice slurry systems using ethylene glycol and sodium chloride as freezing point depressant are compared, as well as systems with a scraped surface evaporator and a non-phase change system using ethylene glycol solutions. The ice slurry system with a fluidized bed evaporator and ethylene glycol as freezing point depressant is the least expensive. The advantage over the non-phase change system is however small, only 2% less total daily costs.

Table 7.9: Results of cheese production after dynamic optimization. Peak load=230 kW, total daily cooling load=2544 kWh

		Ice Slurry NaCl	Ice Slurry EG	Ice Slurry SSE	Non phase change
Freeze pt. depress.		NaCl	EG	NaCl	EG
Concentration fpd	wt%	6.5	9	6.5	35
Initial T freeze	^{o}C	-4	-3	-4	-
Avg. ice slurry T	^{o}C	-5.3	-4.0	-5	-1
Ice slurry T change	K	1.9	1.9	1.8	7.3
Tot heat transferred	kWh	2611	2631	2640	2642
Total ice produced	kWh	2323	2363	2368	0
Avg. evaporation T	^{o}C	-10.7	-10.2	-15.8	-5.2
Avg. COP overall	-	3.35	3.47	2.99	3.80
Heat transfer coeff.	W/m^{2}K	1680	1664	796	977
Storage tank	m^3	8.2	8.2	8.2	32
Compressor ϕ_v	m^3/h	152	145	188	124
Heat exchanger	m^2	12.1	10	12.9	31
Total daily costs	€	77.7	70.7	92.7	71.9

The relatively high temperatures required in cheese cooling are disadvantageous for the ice slurry systems. The maximum temperature encountered in the non-phase change system is 3 ^{o}C, which is considered to be acceptable in cheese cooling. Also a relatively small storage tank is sufficient to have enough storage capacity for the peak cooling demand during the morning hours. Benefits of the storage of ice slurries are therefore relatively small. If additional benefits of ice slurries during transport and utilization are taken into account, application of ice slurries may become more feasible.

7.5.4 Case 4: Pork Cooling and Freezing

Pork cooling and freezing are evaluated as examples of large applications in food industry. A cooling load profile of a pork slaughterhouse is displayed in Figure 7.10. In a pork slaughterhouse cooling is required mainly in work rooms, freezing tunnels and storage rooms. Pork may also be frozen, requiring deep freezing temperatures of the secondary cooling fluid. It is not known which part of the cooling load is required for freezing and which part for cooling. The cooling load profile of Figure 7.10, which is 25% of the cooling load given by Bellstedt and Xiao (2002), is therefore evaluated as a whole at two temperature levels. The profile is characterized by a constant basic demand during the night, required for cooling of storage rooms, and a large demand during working hours. For temperatures in the cooling range it is assumed

that the temperature for which costs are the lowest is acceptable, between –4 ^{o}C to –6 ^{o}C. For deep freezing, temperatures below –20 ^{o}C are assumed.
For all systems evaluated in the pork cooling and freezing application, the electricity tariff is assumed at 2.5 €ct/kWh during the night and 5 €ct/kWh during the day. For all simulations 24 hour operation is found as the optimal operating strategy.

Results of the simulations of the pork application are given in Table 7.10. Ice slurries with ethylene glycol as freezing point depressant, generated in a fluidized bed evaporator are the least expensive systems found. These systems are 8% less expensive than the sodium chloride ice slurries in the cooling range, mainly because of a higher operation temperature allowable in the fluidized bed evaporator.
The scraped surface evaporator system is 34% more expensive than the ethylene glycol fluidized bed system and it is 23% more expensive than the sodium chloride fluidized bed system. Also cooling with non-phase changing ethylene glycol solutions is 16% more expensive than the least expensive ice slurry system. In the pork cooling application there is no disadvantage of a high temperature required of the ice slurries, while there are significant benefits of load shifting to the nighttime, making ice slurries feasible in this pork cooling application. The large storage tank and volumetric flow of the non-phase change fluids increases auxiliary power consumption, which results in a slightly lower overall COP for the non-phase change systems.
The same cooling load profile has been evaluated at temperatures required for deep freezing of pork. The ethylene glycol ice slurry system with the fluidized bed evaporator is less expensive than the non-phase change system using ethylene glycol solutions. The difference is 9%, which is lower than in the cooling temperature range. This is because the temperature variation of the ice slurries increases at lower temperatures. The ice slurry storage tank required is then relatively large for the freezing application. Possible effects of using ice slurries in long transport lines and utilization heat exchangers have not been included in the comparisons.

Table 7.10: Results of pork slaughterhouse after dynamic optimization (peak load=592 kW, total cooling load =7628 kWh)

		Ice Slurry EG	Ice Slurry NaCl	Ice Slurry SSE	Non Phase Change	Ice Slurry Freeze	Non Phase Change Freeze
Freeze pt. depress.		EG	NaCl	NaCl	EG	EG	EG
Concentration fpd	wt%	9	6.5	6.5	35	32	50
Initial T freeze	^{o}C	-3	-4	-4	-	-16	-
Avg. ice slurry T	^{o}C	-3.9	-5.3	-5.3	-5.2	-20.9	-23
Ice slurry T change	K	1.9	2.3	2.5	8.2	8.3	10.1
Tot heat transferred	kWh	7620	7855	7840	8006	8628	8379
Total ice produced	kWh	6997	7317	6984	-	4936	-
Avg. evaporation T	^{o}C	-8.9	-10.1	-16.8	-8.3	-24.3	-26.1
Avg. COP overall	-	3.39	3.30	2.91	3.28	2.22	1.97
Heat transfer coeff.	W/m^{2}K	1678	1675	781	924	1408	514
Storage tank	m^3	53	53	53	209	61	160
Compressor ϕ_V	m^3/h	391	436	581	421	861	935
Heat exchanger	m^2	36.5	40.9	36.7	126	76.7	236
Total daily costs	€	142.9	154.8	191.1	166.2	231	251

7.6 Conclusions

The static and dynamic models developed are efficient tools to optimize secondary cooling systems using ice slurries or non phase change fluids. For a given temperature and cooling load profile the economically most feasible system dimensions and operating strategy can be found. The model is also suitable to evaluate the influence of single components on the system performance. Significant parameters as electricity tariffs and climate factors are included in the simulations.

Ice slurry systems are economically feasible in applications with temperatures in the cooling range down to deep freezing range. Costs of deep freezing systems are approximately 1.7 times higher than in the cooling range. At temperatures just below 0 ^{o}C, the maximum allowable temperature difference of the ice slurry generators makes ice slurry systems relatively less attractive.

Other freezing point depressants used in the ice slurries result in relatively small differences if the cooling systems can be operated at the same temperature level. Significant differences are only obtained if additives make ice slurries available at higher temperatures because of a higher maximum allowable temperature difference in the ice slurry generator. This is the case for ethylene glycol, which is less expensive in air-conditioning and mild cooling applications in food industry.

The limited temperature difference allowable in the fluidized bed ice slurry generator does not prevent its application at relatively high temperature applications. The advantages of the ice slurries because of cold storage options compensate for a relatively low operation temperature in most applications.

The scraped surface evaporator has a higher maximum allowable temperature difference, but because it also has lower heat transfer coefficients, the lowest costs are found at similar temperatures as in the fluidized bed evaporator. For all temperatures and applications evaluated, systems with fluidized bed evaporators are less expensive.

The application size is a major factor. The relative difference between the fluidized bed evaporator and the scraped surface evaporator increases for larger applications because the fluidized bed systems can be scaled up more efficiently. Also electricity tariffs are lower for large applications. It was shown that for larger applications and for lower electricity tariffs a 24 hour operating strategy becomes more likely. Only at high electricity tariffs a complete shift of the cooling load to the nighttime may be economically feasible.

Operation of a system optimized for summer conditions at lower outside temperatures, for example in the winter with a 13 K lower average outside temperature, resulted in 15% lower total daily costs, assuming the same cooling load. Also if the system is only required for part of the cooling load, significant energy savings can be obtained. By stopping the system for some hours during the expensive day period, 60% energy costs reduction is obtained at 50% of the cooling demand.

In systems with only a small storage tank, though suitable for shifting the load at full load operation, storage capacity may not be enough for shifting an additional load if the system is stopped for a few hours. In the cases evaluated, the air-conditioning and the pork cooling application could be operated efficiently at part-load. For the supermarket and the cheese cooling application a larger storage tank is required than the optimum, so that the maximum ice fraction in the storage tank will not be attained.

The case studies showed that the cooling load profile and the temperature requirements are decisive factors for the feasibility of ice slurries in cooling applications. For a cooling load profile in which there are only small load shifting options, the relative advantage of ice slurries is small. Ice slurries can only be applied at temperatures a few degrees below 0 ^{o}C and have a disadvantage compared to non-phase changing systems in applications where cooling at higher temperatures is required. The benefits obtained with load shifting can however be large enough to compensate for this disadvantage. The advantage of ice slurry systems over non-phase change systems in the air-conditioning case was larger than in the supermarket case.
The cheese factory case is not as advantageous for ice slurries because of a relatively high temperature required and because of little cold storage benefits. The pork cooling case did not have the temperature disadvantage for ice slurries and also had large load shifting benefits, therefore ice slurries are relatively efficient in the pork cooling case.
Possible effects of the use of ice slurries in long transport lines, so that for example pipe diameters can be smaller, and in utilization heat exchangers, have not been included in the model. Depending on the application some further advantages are expected using ice slurries.

At decreasing temperatures the relative advantage of ice slurries over non-phase changing cooling fluids reduces. The freezing range of ice slurries increases at lower temperatures. The maximum ice fraction obtainable decreases and the ice slurries become more similar to non-phase changing fluids.

Nomenclature

A	surface area (m^2)
c_1..c_2	constant coefficients
c_p	heat capacity (J/kgK)
$C_{d\infty}$	terminal drag coefficient
d_p	particle diameter (m)
D_h	hydraulic diameter (m)
D	diameter (m)
ΔH	enthalpy change (J/kg)
Δp	pressure drop (kPa)
ΔT	temperature difference (K)
g	gravitational constant (m/s^2)
h	particle height (m)
i	interest rate
Inv	Investment costs (€)
n	Richardson/Zaki coefficient
N	rotation speed (min^{-1})
Nu_h	hydraulic Nusselt number
Nu_{ff}	falling film Nusselt number
P	power (kW)
Pr	Prandtl number ($=\mu.cp/\lambda$)
Q	total heat transfer/cooling load (W)
Re_h	hydraulic Reynolds number
Re_{ff}	falling film Reynolds number
Re_∞	terminal Reynolds number
s	film layer thickness (m)
T	temperature (^oC)
T_{f_init}	Initial freezing point (^oC)
U	Overall heat transfer coefficient (W/m^2K)
V	storage volume (m^3)
v_s	superficial velocity (m/s)
v_d	rotor tip velocity (m/s)
v_∞	terminal settling velocity (m/s)
w	weight fraction (kg/kg)
x	sizing parameter
y	no. of years (years)

Greek

α	film heat transfer coefficient (W/m^2K)
β	rotor angle (^{o})
Γ	periphery mass flow (kg/m.s)
ε	bed voidage
η	efficiency
λ	thermal conductivity (W/mK)
μ	dynamic viscosity (Pa.s)
ν	kinematic viscosity (m^2/s)
ρ	density (kg/m^3)
ϕ_v	displaced volume (m^3/s)
φ_v	pump throughput (m^3/s)
ψ	sphericity

subscripts

ax	axial direction
evap	evaporation
fpd	freezing point depressant
ff	falling film
i	ice
in	inside
is	ice slurry
l	liquid
r	rotor
rad	radial direction
s	solid

Abbreviations

COP	Coefficient of Performance
EG	Ethylene Glycol
FBE	Fluidized Bed Evaporator
SSE	Scraped Surface Evaporator

References

Beismann, R.A.M., 2001, personal communications, York Inham Refrigeration B.V. Dordrecht the Netherlands.

Bel, O., Hunyadi-Kiss, I., Zweig, S., Lallemand, A., 1996, *Thermal study of an ice slurry used as refrigerant in a cooling loop*, Proc. Aarhus Conf.*,* IIF/IIR: p.507-516.

Bellstedt, M., Xiao, A., 2002, *An annual power cost comparison of conventional & slurry ice systems indicates impressive potential for abattoir refrigeration*, AIRAH Journal, nov. 2002. www.minus40.com.au

Chhabra, R.P., Agarwal, L., Sinha, N.K., 1999, *Drag on non-spherical particles: An evaluation of available methods*, Powder technology*,* vol.101, p288-295

Crielaard, G.A., Vreman, A., 2000, *Marktintroductie ijsslurriesysteem voor supermarkten in Nederland*, Report of project 375007/0040*,* NOVEM the Netherlands.

DACE, 1995, Dutch Association of Cost Engineers, *Prijzenboekje*, 18^{e} ed. Misset, Doetinchem, the Netherlands.

DTe, 2002, *Tarievenoverzichten 2002,* Dienst Uitvoering en Toezicht Energie, part of Nederlandse Mededingings Autoriteit NMA, the Netherlands, www.dte.nl,.

Fujita, T., Ueda, T., 1978, *Heat transfer to falling liquid films and film breakdown, part I & part II*, International Journal of Heat and Mass Transfer 21 pt I: p97-108, pt II: 109-118.

Gladis, S.P., Marciniak, M.J., O'Hanlon, J.B., Yundt, B., 1995, *Ice crystal slurry TES system using the orbital rod evaporator*. ASHRAE Transactions vol. 101, part 1, www.muel.com

Gladis S.P., 1997, *Ice slurry thermal energy storage for cheese process cooling*, ASHRAE Transactions vol. 103, part 2, www.muel.com

Holman, J.P., 1997, *Heat Transfer* 8th ed. , McGraw-Hill.

Jans, R., personal communication, 2001, Fri-jado B.V., Etten Leur, the Netherlands.

Janssen, L.P.B.M., Warmoeskerken, M.M.C.G., 1991, *Transport Phenomena Data Companion*, Delftse Uitgevers Maatschappij, Delft, the Netherlands, ISBN 90-6562-074-5.

Jensen, J.M., Rasmussen, B.D., Jakobsen, A., Larsen, L., 1999, *Energy Analysis of a Supermarket Refrigeration System*, Scanref International Edition, August 1999

KNMI, 2003, *Climatic data files,* Koninklijk Nederlands Meteorologisch Instituut, de Bilt, the Netherlands, www.knmi.nl

Kupriczka, R., Rotkegel, A., Ziobrowski, Z., 2002, *Heat transfer to evaporating liquid films* *within a vertical tube,* Chemical Engineering and Processing 41, p23-28

Paul, J., 1995, *Binary Ice as Secondary Refrigerant*, Proceedings of the 19th Int. Congress of Refrigeration, the Hague, vol. IVb, IIF/IIR, p947-954

Paul, J., 1997, *Binäreis- Anwendungserfahrungen in der Supermarktkälte*, Ki Luft- und Kältetechnik*,* 5, p209-213

Rautenbach, R., Katz, T., 1996, *Survey of long time behavior and costs of industrial fluidized bed heat exchangers*, Desalination*,* Vol. 108, p335-344

Richardson, J.F., Zaki., W.N., 1954, *Sedimentation and Fluidization*, Transactions of the Institution of Chemical Engineers, vol. 32, p35-53

Sinnot, R.K., 1993, *Coulson & Richardson's Chemical Engineering vol. 6,* 2nd ed., Pergamon, Oxford, chapter 6, p209-243

Vaessen, R.J.C., 2003, *Development of scraped eutectic crystallizers,* PhD-thesis Delft University of Technology, ISBN 90-646-4208-7

8 Conclusion

General

The fluidized bed ice slurry generator can enhance secondary cooling systems by reducing both investment costs and energy consumption. The investment costs required for the ice slurry generator are lower compared with other ice slurry generators because of higher heat transfer coefficients. For larger applications the investments are relatively even lower because the fluidized bed ice slurry generator can be scaled up more efficiently than for example scraped surface systems.

Because of the high heat transfer coefficients the energy consumption of secondary cooling systems is reduced with the fluidized bed ice slurry generator. A low temperature difference between primary refrigerant and ice slurry is sufficient in the fluidized bed ice slurry generator and the evaporation temperature of the primary cooling cycle can be relatively high. A maximum temperature difference between wall and fluidized bed has been observed in the experiments, above which a permanent ice layer forms on the heat exchanger walls and freeze-up of the fluidized bed occurs. Because of the high heat transfer coefficients however, only a small temperature difference is required. It was shown that the fluidized bed ice slurry system may be a competitive option even in air-conditioning applications. The load shift and peak leveling benefits make up for the relatively low temperatures of ice slurries compared with non-phase change secondary cooling systems in air-conditioning.

The ice slurry crystals produced in the experimental fluidized bed ice slurry generator set-up are similar to those generated with other methods already successfully applied in cooling systems. Performance of the fluidized bed ice slurry generator in this respect is therefore also concluded to be sufficient. The influence of several factors on crystal sizes, such as type of freezing point depressant, fluidization conditions and storage times is noted, however only limited pictures have been evaluated, so that predictive modeling is not possible yet.

Heat Transfer

The formation of ice crystals did not have a large effect on heat transfer coefficients in the fluidized bed ice slurry generator. If at a given set of operating conditions stable ice slurry production was possible, heat transfer coefficients were similar to those in fluidized beds before start of ice crystal formation. Heat transfer coefficients measured using the fluidized beds were significantly higher than those predicted for single phase flow.

The ice fraction is the most relevant parameter that determines the thermophysical properties of ice slurries. Property models predicting freezing point, density, thermal conductivity, enthalpy and heat capacity of ice slurries reported in literature could be applied in models to predict wall-to-bed heat transfer coefficients. An empirical model using hydraulic Nusselt and Reynolds numbers was proposed that predicted heat transfer coefficients in the fluidized bed ice slurry generator accurately:

$$Nu_h = 0.0612 \cdot Re_h^{0.724} Pr^{0.625}$$

Exponents of this model were similar to those of generalized models for liquid/solid fluidized beds found in literature. Significant differences were only found in the proportional factor. Relatively low temperature levels during ice slurry production were the most likely cause for the differences, because no clear influence of the ice crystals was observed.

Mass Transfer

The maximum wall-to-bed temperature difference allowable during ice slurry generation before freeze-up of the fluidized bed was observed to depend linearly on the concentration of freezing point depressant in the range of experimental conditions investigated. This is caused by a remarkably constant ice crystal growth velocity at the walls, which is primarily determined by the solute mass transfer. The heat transfer resistance is limiting for ice crystal growth at the walls only at relatively high temperatures, from approximately –2 ^{o}C to 0 ^{o}C. At increasing freezing point depressant concentration a larger temperature difference can be applied while the ice crystal growth velocity at the wall remains constant. Additional heat transferred above the crystal growth velocity at the wall, but under the maximum wall-to-bed temperature difference allowable, results in ice crystal formation in the bulk of the fluidized bed.

Fluidization conditions must be sufficient to remove the constant ice crystal growth velocity at the walls to prevent freeze-up. The maximum temperature difference allowable between freezing point depressants is determined by the ice removal capacity. The ice removal capacity can be determined from the number of effective particle-wall impacts. Whether a particle impact is effective depends on the adhesive strength of the ice to the wall and on the impact velocities of the solid particles at the wall of the fluidized bed.

An approach is introduced in which the work of adhesion of ice to the walls and an exponential distribution of the kinetic energies of the solid particles are used to determine the number of effective particle impacts. The results correspond qualitatively well with the trends of the maximum temperature differences allowable. The approach is therefore expected to be applicable for quantitative prediction of freeze-up conditions during ice crystal formation.

Fluidization

The stationary fluidization process of the experimental set-up has been quantified in detail. The general theory on fluidization of Richardson and Zaki has been validated and parameters obtained are in accordance with literature. The evaluation of the number of effective particle-wall impacts has been used to further optimize the stationary fluidized bed ice slurry generator.

Three operating modes that may further extend the fluidized bed ice slurry generator have been discussed. The preliminary experiments with circulation of the fluidized bed particles has not led to an improvement of the fluidized bed systems, which is due to limitations of the experimental set-up. The installation of a rotor system also did not show an improvement of the fluidized bed performance, mainly because of the hindrance effects of the rotor on the fluidization. From the theoretical evaluations it is concluded that from circulation more benefits are to be expected, while it is considered unlikely that a rotor system will lead to further improvements.

From a theoretical study of parallel fluidization of multiple beds it is concluded that there are methods feasible for use with ice slurries, although some parallel fluidization systems are excluded.

Ice Slurry Secondary Cooling Cycle

The choice of freezing point depressant is of considerable influence mainly at lower temperature applications, where the viscosity and the apparent heat capacity may vary widely depending on the freezing point depressant used.

The secondary cooling cycle has been divided into four separate stages, ice slurry generation, storage, transport and utilization. The ice fraction is the most relevant design parameter in each stage. The use of ice concentrators or separation methods in between the stages is therefore likely to improve system performance.

There is not one type of ice slurry generator most efficient for all applications. A suitable ice slurry generator can only be selected if size, temperature and other constraints of the application are known. The fluidized bed ice slurry generator is expected to perform well in relatively large applications. Possible effects of the limit on the allowable temperature difference have been investigated. The limited temperature difference allowable in the fluidized bed ice slurry generator does not prevent its application at relatively high temperature applications.

In the storage and transport stages, investment costs and additional power consumption increase exponentially if systems are designed using low ice fractions. It is advisable to use ice fractions of at least 0.20 during storage and transport. Heat losses make up the largest part of the additional power requirements compared with stirring and pumping requirements for the current optimization.

System Optimization

The static and dynamic models developed are efficient tools to optimize secondary cooling systems using ice slurries or non phase change fluids. For a given temperature and cooling load profile the economically most feasible system dimensions and operating strategy can be found. The model is also suitable to evaluate the influence of single components on the system performance. Significant parameters as electricity tariffs and climate factors are included in the simulations as well as the option of part-load operation.

Ice slurry systems are economically feasible in applications with temperatures in the cooling range down to deep freezing range. Costs of deep freezing systems are approximately 1.7 times higher than in the cooling range.

At decreasing temperatures the relative advantage of ice slurries over non-phase changing cooling fluids reduces. The freezing range of ice slurries increases at lower temperatures. The maximum ice fraction obtainable decreases and the ice slurries become more similar to non-phase changing fluids

Other freezing point depressants used in the ice slurries result in relatively small differences if applied at cooling level temperatures. Significant differences are only obtained if additives make ice slurries available at higher temperatures because of a higher maximum allowable temperature difference in the ice slurry generator. This is the case for ethylene glycol, which is less expensive in air-conditioning and mild cooling applications in food industries.

The case studies showed that the cooling load, the cooling load profile and the temperature requirements are decisive factors for the feasibility of ice slurries in cooling applications. For a cooling load profile in which there are only small load shifting options, the advantage of ice slurries is small. Ice slurries can only be applied at temperatures below 0 ^{o}C and have a disadvantage compared to non-phase changing systems in applications where cooling at higher temperatures is required. The benefits obtained with load shifting can however be large enough to compensate for this disadvantage.

Appendix 1 Primary Cooling Cycle: Falling Film Evaporation

A1.1 Type of Evaporation in Fluidized Bed Ice Slurry Generator

Equipment used in the primary refrigeration cycle is similar for ice slurry systems and non-phase changing systems. Only the design of the evaporator in the primary refrigeration cycle directly depends on the method of ice slurry generation. In case of a fluidized bed ice slurry generator, the evaporator is a vertical tube bundle, where the primary refrigerant evaporates either in- or outside the tubes.

For ice slurry generation the fluidized beds are most likely situated inside the tubes, as a result of the requirements on solid particle size and d_p/D-ratio, discussed in Chapter 5. Operating conditions of fluidized beds inside tubes can be controlled more accurately than for fluidized beds outside tubes, so that freeze-up or uneven fluidization can be prevented. Also the ratio heat exchanger surface area to system volume is maximized by placing the fluidized beds inside the tubes. The tubes can then be spaced closer to each other, because the evaporating refrigerant does not require as much space as a fluidized bed.

Two types of evaporation are widely used in vertical shell-and-tube systems. These are flooded evaporation and falling film evaporation. Flooded evaporation, or pool boiling, is advantageous because of a relatively simple design. The height of flooded evaporators is however limited by the static pressure difference that occurs between top and bottom of the system. Increased pressure at the bottom of the system increases the evaporation temperature, making evaporation at the bottom of the system unlikely. The fluidized bed evaporator has a vertical design and is especially cost efficient at relatively high bed heights. Several separate sections with pool boiling are then required, which complicates the design. Another disadvantage is that the charge of primary refrigerant is high, as the system is filled for the largest part with liquid refrigerant.

Falling film evaporators can be higher than pool boiling systems and the primary refrigerant charge is much lower, because the primary refrigerant is for the largest part in the vapor phase in the evaporator. Disadvantageous is that a robust flow distribution system is required to create an even film thickness in the evaporator, so that heat transfer rates are even throughout the evaporator. Also a recirculation pump is required for unevaporated primary refrigerant.

The maximum falling film height is expected to be around 3 m, which is smaller than the maximum fluidized bed height possible (8-10 m). It may therefore still be required to install two separate falling film evaporation sections in one fluidized bed system.

Falling film evaporation is expected to be most efficient for fluidized bed ice slurry generation, especially for relatively large systems. Furthermore, higher heat transfer and improved control of temperature driving force are expected in falling film systems. In falling film evaporation heat transfer and temperature difference can be controlled with recirculation of unevaporated liquid refrigerant.

In this section an overview is given of methods to predict heat transfer and operating range for a falling film evaporator with ammonia as example refrigerant.

A1.2 Theory of Falling film Evaporation

General designs and some patents of falling film evaporators with a film on the outside of vertical tubes in a shell-and-tube configuration have been reported. Hewitt and McMullan (1997) have reported falling film evaporation in such a set-up, also with fluidized beds in the tube side of the heat exchanger.

General methods to predict heat transfer coefficients between film and tube wall are assumed to apply. These correlations have been determined mostly with water as evaporating fluid (Chun and Seban, 1971; Fujita and Ueda, 1978). Other fluids that have been tested generally comply with these methods, as for example methanol and isopropanol, (Krupiczka et al. 2002). If other fluids are used, for example refrigerants as ammonia, differences may be observed in heat transfer predicted or in operating limits. For most refrigerants, literature on falling film phenomena is however sparse.

It is assumed that the liquid ammonia on top of the falling film is saturated. The vapor formed in the expansion device needs to be separated from the liquid. The liquid distributor system is assumed to be suitable to also function as separator. The tubes need to be covered by the falling film at all times, so at the bottom there is still a significant flow of liquid ammonia. This needs to be collected, separated from the vapor and recycled to the inlet of the shell. At the top of the shell the ammonia vapor is withdrawn from the shell. In Figure A1.1 a schematic lay-out of a falling film evaporator is given.

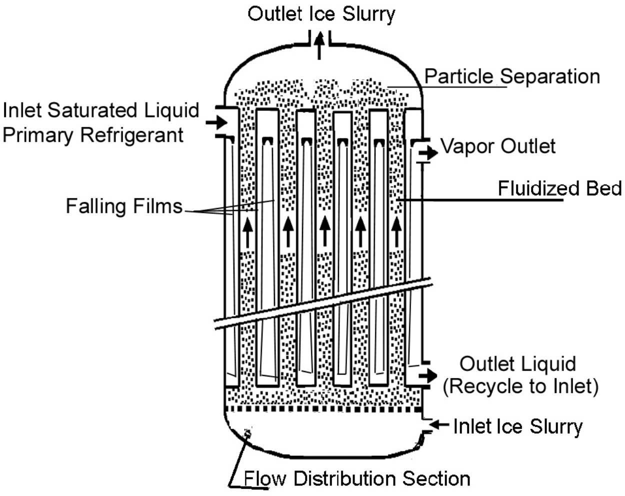

Figure A1.1:Schematic lay-out of fluidized bed ice slurry generator with shell-and-tube falling film evaporation

Boiling type

Depending on the heat flux a different boiling type is encountered in falling films. Fujita and Ueda report convective boiling until heat fluxes of 30 to 70 kW/m^2. Evaporation in convective boiling takes place only at the phase boundary between vapor and saturated liquid. At higher heat fluxes nucleate boiling becomes more significant. During nucleate boiling bubbles are formed in the film, which increases heat transfer coefficients, but also can break the film. Furthermore the bubbles can entrain droplets, which are then separated from the film, thinning the film and affecting heat transfer coefficients lower in the falling film.
Experimental results for water as investigated by Fujita and Ueda are displayed in Figure A1.2. If nucleate boiling is dominant, the heat flux determines heat transfer rates. During convective boiling, heat transfer is determined by the liquid flow velocity or the Reynolds number.

Correlations predicting the transition from convective to nucleate boiling are reported by Krupiczka et al. (2002). These are based on the boiling number (*Bo*) and, more accurately, on the combined Boiling and Kapitza numbers.

$$Bo = \frac{\dot{q}}{m\Delta H} \qquad \text{(A1.1)} \qquad Ka = \frac{\mu^4 g}{\rho\sigma^3} \qquad \text{(A1.2)}$$

Nucleate boiling occurs if conditions A1.3 or A1.4 are valid:

$$Bo > 10^{-5} \qquad \text{(A1.3)} \qquad BoKa^{1/11} > 10^{-6} \qquad \text{(A1.4)}$$

at lower values of Bo or $BoKa^{1/11}$ only convective boiling occurs.

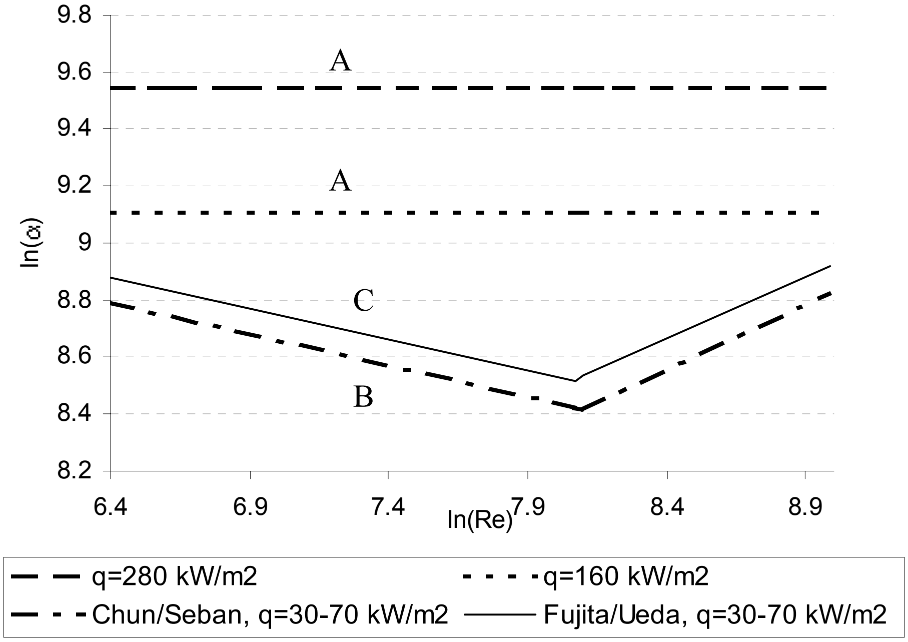

Figure A1.2:Heat transfer coefficient to boiling liquid films (water)(after Fujita and Ueda, 1978), A: heat fluxes not relevant for ice slurry generation (McAdams et al., 1949) B: Chun and Seban (Equations A1.12 and A1.13), C: Fujita and Ueda (similar results as Chun and Seban)

If nucleate boiling occurs, the heat transfer coefficient can be estimated from the Nusselt number for convective boiling (Nu_z):

$$\frac{Nu}{Nu_z} = 1 + 8.1\times 10^6 \cdot Bo^{1.727} \qquad \text{(A1.5)} \qquad \frac{Nu}{Nu_z} = 1 + 7.05\times 10^7 \cdot (Bo \cdot Ka^{1/11})^{1.6} \qquad \text{(A1.6)}$$

Experimental data for the liquids methanol, water and isopropanol determined by Krupiczka et al. (2002) showed that the transition to nucleate boiling as defined by Equation A1.3 is not very sharp. At *Bo* numbers just above 10^{-5}, effects of nucleate boiling are still relatively small, for example at a *Bo* number of $3\text{x}10^{-5}$, the Nusselt number is increased by only 12.5% because of nucleate boiling.

Convective boiling heat Transfer

The falling film thickness can be determined using:

$$s = 0.909 \cdot \left(\frac{\nu^2}{g}\right)^{1/3} Re^{1/3} \qquad \text{(A1.7)}$$

Three different flow regimes can be distinguished: Laminar flow, laminar flow with waves or ripples, and turbulent flow. The transition between the regimes is determined with the Reynolds number, which depends on the mass flow rate per unit periphery, Γ (kg/ms).

$$Re = \frac{4\Gamma}{\mu} \qquad \text{(A1.8)}$$

For laminar flow the Nusselt theory is used to calculate local heat transfer coefficients:

$$Nu_z = c \cdot Re_z^{-1/3} \qquad \text{(A1.9)} \qquad Nu_z = \frac{\alpha}{\lambda} \cdot \left(\frac{\nu^2}{g} \right)^{1/3} \qquad \text{(A1.10)}$$

with c=0.823 for constant wall temperature and c=0.905 for constant heat flux. The Nusselt theory only holds for small Reynolds values, as capillary waves are formed at higher Reynolds numbers. These waves reduce the film thickness locally and increase heat transfer coefficients.

Transition from laminar to laminar ripple flow (or wavy flow) takes place at:

$$Re_{rip} = 2.43 \cdot Ka^{-1/11} \qquad \text{(A1.11)}$$

Local heat transfer for laminar ripple flow is predicted with:

$$Nu_z = 0.822 \cdot Re_z^{-0.22} \qquad \text{(A1.12)}$$

The transition from laminar ripple flow to turbulent flow is assumed to occur at the Reynolds number where the heat transfer coefficients of both flow regimes are equal. This is also a local minimum in the heat transfer, experimentally confirmed in various researches (Chun and Seban, 1971; Krupiczka et al., 2002).

Local turbulent heat transfer coefficients are predicted with:

$$Nu_z = 0.0038 \cdot Re_z^{0.4} Pr^{0.65} \qquad \text{(A1.13)}$$

The transition from laminar ripple to turbulent flow regime occurs at:

$$Re_{tur} = 2460 \cdot Pr^{-0.65} \qquad \text{(A1.14)}$$

Under turbulent flow conditions only a small liquid fraction evaporates, so that Equation A1.13 may also be used to calculate heat transfer coefficients over the length of the tube. More extensive correlations are available for Equation A1.13, which describe the turbulent flow regime with theoretical background on eddy diffusivity (Alhusseini and Chen, 2000).

If the liquid at the entrance of the falling film is turbulent, heat transfer coefficients will decrease because of evaporation along the tube, until the flow makes a transition to laminar ripple flow. For laminar flow at the entrance, heat transfer coefficients will increase because of evaporation. The trends of the three different flow regimes can be observed in Figure A1.3, where heat transfer coefficients determined by Krupiczka et al. (2002) are given. The trends for the laminar ripple flow and turbulent flow regimes during convective boiling are also given in Figure A1.3.

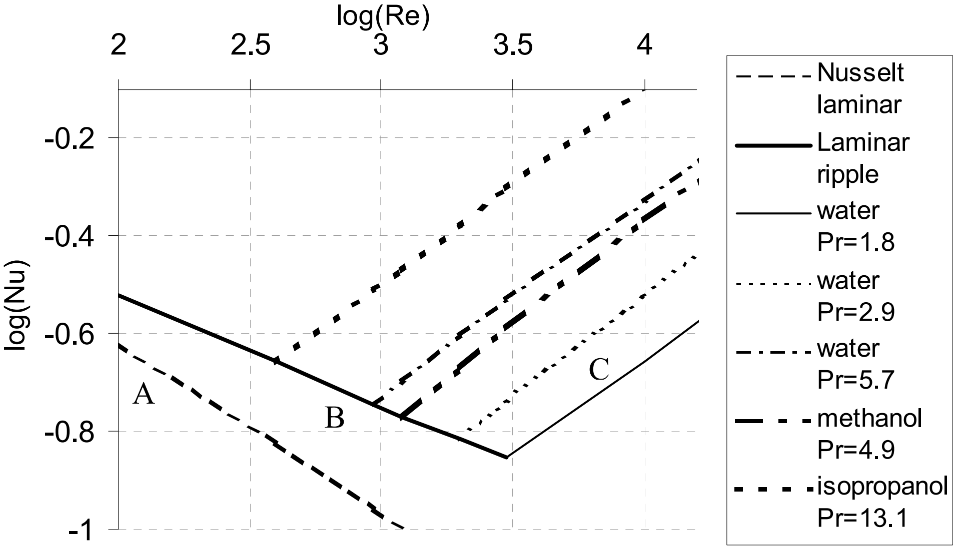

Figure A1.3:Local Heat transfer coefficient of convective flow to evaporating liquid films as a function of Reynolds number. A: Laminar flow, B: Laminar ripple flow, C: Chun and Seban for turbulent flows for different Prandtl numbers (based on Krupiczka et al., 2002).

Break-up or dry-out of the falling film

A number of processes can disturb the falling film, causing dry patches. At these dry patches the wall temperature will increase and heat transfer coeffcients decrease.

Four effects are distinguished:

1. Dry-out through evaporation
2. Dry patches because of high heat flux
3. Flooding
4. Droplet entrainment

In Figure A1.4, the limits caused by the first three phenomena are displayed.

1. *Dry-out through evaporation*

Fujita and Ueda reported a minimum Γ at the bottom of the falling film of 0.02 kg/ms to prevent dry sections, determined for water.

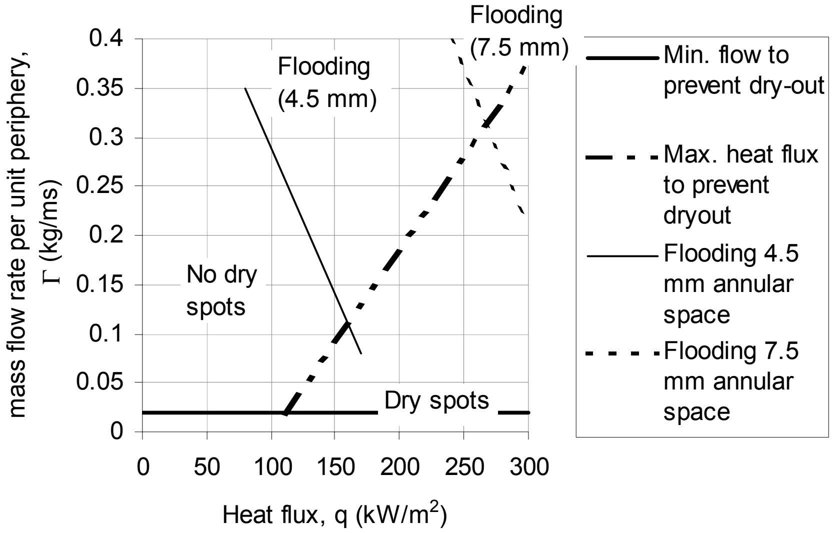

Figure A1.4: Limits on heat flux and mass flow rate to prevent occurrence of dry spots in the falling film by break-up or dry-out of the falling film. Adapted from Fujita and Ueda (1978)

2. Dry patches through high heat flux
At high heat fluxes nucleate boiling results in bubbles large enough to instantly form a dry patch on the surface of the tube. Based on Fujita and Ueda (1978), the minimum Γ without dry patches is estimated with Equation A1.15, with q in kW/m^2:

$$\Gamma_{\min} = 0.0018 \cdot q - 0.17 \tag{A1.15}$$

3. Flooding
During flooding large waves are formed on the falling film by the upwards flowing vapor. These large waves can move upwards or break up the film, reducing heat transfer. Flooding is strongly determined by the system design: Enough clearance should be build in to allow the vapor to be removed countercurrently, without high vapor velocities. In Figure A1.4 two lines are given above which conditions Fujita and Ueda encountered flooding. They used a tube of 16 mm diameter with an annular space of 4.5 mm or 7.5 mm around it. The vapor outlet was near the top of the falling film. It is assumed that the tube spacing can be large enough in the fluidized bed ice slurry generator to prevent flooding phenomena.

4. Droplet Entrainment
During evaporation liquid may be removed from the film through entrainment by the vapor. The droplet entrainment is predicted with:

$$\Gamma_{drop} = 5.3 \times 10^{-15} \cdot L \cdot \Gamma^{0.5} q^{2.5} \tag{A1.16}$$

The film becomes thinner because of droplet entrainment. If multiple tubes are used or if the film is on the inside of a tube, entrained droplets may land on other tube films. This reduces the negative effects of the droplet entrainment.

A1.3 Ammonia Falling Film Evaporation in Fluidized Bed Ice Slurry Generator

Maximum heat flux and type of boiling
Because of the limit on the operating range of ice slurry fluidized beds, it is assumed that an ammonia to ice slurry temperature difference of 10 K is the maximum that can be attained. Under optimal conditions the maximum wall-to-bed heat transfer coefficient in fluidized bed ice slurry generators is assumed to be 5000 W/m^{2}K.
In this section 3.00 m high fluidized beds with outside tube diameter of 51 mm and 2 mm wall thickness, stainless steel tubes are assumed (λ=15 W/mK). Without heat transfer resistance on the falling film side ($\alpha_0=\infty$), the overall heat transfer coefficient (based on outside tube diameter) would be U_o=3621 W/m^{2}K, calculated with:

$$\frac{1}{U_o} = \frac{1}{\alpha_o} + \frac{d_o}{2\lambda} \ln\left(\frac{d_o}{d_i}\right) + \frac{d_o}{d_i} \cdot \frac{1}{\alpha_i} \tag{A1.17}$$

The maximum flux encountered is then 36.2 kW/m^2. This is already near the lowest fluxes used by Fujita and Ueda (1978), therefore convective boiling is assumed in the fluidized bed evaporator.

The criteria of Equations A1.3 and A1.4 are then evaluated for ammonia evaporating at –10 °C. Saturated liquid properties are given in Table A1.1. In Table A1.2 results of evaluations with ammonia at –10 °C are given.

Table A1.1: Properties of saturated liquid ammonia at –10 °C

ΔH_{evap}	kJ/kg	1295
μ	mPa.s	0.212
ρ	kg/m^3	654
ν	m^2/s	3.24×10^{-7}
σ	mN/m	42.5
λ	W/mK	0.562
Pr	-	1.708

For the ammonia properties of Table A1.1 and heat flux of 36.2 kW/m^2 (case 1), a mass flux is required of 2796 kg/m^2s to attain a *Bo* of 10^{-5}, which is shown in Table A1.2. The corresponding values for *Re* and Γ are well in the turbulent regime. At these and higher Reynolds numbers nucleate boiling will not occur. If the temperature difference and thus the heat flux is only half as high (case 2), the layer thickness will be much smaller, as well as the Reynolds number below which nucleate boiling occurs. It can therefore be assumed that nucleate boiling may occur under normal operating conditions, but that a sufficient flow can be applied to have fully convective boiling in the fluidized bed ice slurry generator. Around the transition zone only a small error is made because the effect of nucleate boiling is small.

In Case 3 the same conditions as for Case 1 apply, only the criterion of Equation A1.4 is used instead of Equation A1.3. Below a mass flux of 2088 kg/m^2s nucleate boiling occurs. No heat transfer resistance on the falling film side was applied. If an α of 5000 W/m^2K is applied (case 4), *Re* and Γ attain values that make the assumption that there is no nucleate boiling, valid. Only if low Reynolds numbers, below 10000 are applied, or temperature differences between ice slurry and ammonia of 10 K or more occur, effects of nucleate boiling may appear.

Table A1.2: Examples of transition to nucleate boiling at different conditions

Case		1	2	3	4
Criterion above which nucleate boiling occurs		$Bo = 10^{-5}$	$Bo = 10^{-5}$	$BoKa^{1/11} = 10^{-6}$	$BoKa^{1/11} = 10^{-6}$
Assumed α_fallingfilm	W/m^2K	∞	∞	∞	5000
Overall heat transfer coefficient U	W/m^2K	3621	3621	3621	2100
heat flux	kW/m^2	36.2	18.1	36.2	21.0
mass flux, $\dot{m}$	kg/m^2s	2796	1398	2088	1211
Falling film thickness	mm	1.82	0.64	1.17	0.52
Reynolds no.	-	34340	12075	22151	9811
Γ	kg/ms	1.82	0.64	1.17	0.52

Dry-out of Falling Film

A minimum Γ of 0.02 is required according to Fujita and Ueda (1978) to prevent dry-out of the falling film. With Equation A1.8 this leads to a minimum Re at the bottom of the falling film of 377 for ammonia at –10 °C. The Reynolds number for the transition laminar to laminar ripple flow is 32.5 (Equation A1.11). The ammonia film is therefore either in the turbulent or the laminar ripple flow regime.

Dry patches because of a too high heat flux do not occur. The theoretical maximum heat flux of 36.2 kW/m^2 does not cause extra constraints for Γ because of Equation A1.15, which can also be observed from Figure A1.4.

Flooding

Based on Figure A1.4 it is assumed that no flooding occurs, because heat fluxes are relatively low in ice slurry applications. This is however determined with water, flooding phenomena for ammonia need to be verified.

Droplet Entrainment

With Equation A1.16 the droplet entrainment rate can be estimated for the theoretical maximum heat flux (36.2 kW/m2) and Γ of 1.17: $\Gamma_{drop}=4.3\text{x}10^{-3}$ kg/ms. This is 0.37% of Γ and is considered small enough to ignore.

Heat transfer

Either a flow rate in the turbulent or a flow rate in the laminar ripple flow regime needs to be selected. Assuming laminar ripple flow, a minimum Reynolds number of 377 can be achieved at the outlet at the bottom of the heat exchanger, because of the minimum Γ of 0.02. At this point heat transfer coefficients are the highest. Higher up the falling film has higher Reynolds numbers but also lower heat transfer coefficients. The maximum Boiling number found under these conditions is just in the nucleate boiling regime (maximum of $6.0\text{x}10^{-5}$ or $\text{BoKa}^{1/11}=4.5\text{x}10^{-6}$).

The laminar ripple flow heat transfer coefficient at the outlet is determined iteratively using Equations A1.12 and A1.5: α= 6249 W/m^{2}K. The iteration is required to determine the heat flux. Other assumptions are a 10 K temperature difference and a slurry side heat transfer coefficient of 5000 W/m^{2}K. The average film side heat transfer coefficient is 6206 W/m^{2}K. An inlet flow Γ of 0.074 is required to achieve this. Heat transfer coefficients under these conditions are 10% to 45% augmented because of nucleate boiling. Using equation A1.6 and A1.12, the average heat transfer coefficient is 5549 W/m^{2}K. Using this criterion, nucleate boiling increases heat transfer with 5% to 20% only).

Under turbulent conditions, equal heat transfer coefficients as for optimal laminar ripple flow are achieved at an average Reynolds number of 14000. The boiling type for this flow conditions is within the range of where nucleate boiling may occur. The Boiling number calculated for a average Reynolds number of 14000 has a maximum Bo of $1.6\text{x}10^{-5}$ ($\text{BoKa}^{1/11}=1.2\text{x}10^{-6}$). This maximum is situated at the falling film outlet.

To obtain high heat transfer coefficients, turbulent flow conditions are preferred in the design. This because in the turbulent regime the Reynolds number can still be increased above 14000, thereby increasing heat transfer coefficients, while in the laminar regime already the maximum heat transfer conditions are found.

Heat transfer resistance in case of ice slurry generation is determined more by the heat transfer coefficient on the ice slurry side (3000 to 5000 W/m^{2}K on the slurry side versus 5000 W/m^{2}K or higher at the ammonia falling film side). Heat transfer augmentation on the ammonia side, e.g. by using finned tubes, may however still be worthwhile.

A1.4 Conclusions

Falling film evaporation is technically possible and high heat transfer coefficients can be obtained. If ammonia is applied as the primary refrigerant, falling film heat transfer coefficients of over 5000 W/m^{2}K are expected, leading to overall heat transfer coefficients, *U,* of up to 2000 W/m^{2}K. Falling films in the turbulent flow regime result in higher heat transfer coefficients than falling films in the laminar flow or laminar ripple flow regime, because of the minimum mass flow rate per unit periphery to prevent dry-out, recommended by Fujita and Ueda.

The limited temperature difference allowable in the fluidized bed ice slurry generator will lead to moderate heat fluxes in the falling film, so that the falling film is expected not to be affected by dry-out, flooding or droplet entrainment phenomena.

Nomenclature

Bo	Boiling number (-)
c	constant coefficient (-)
d	diameter (m)
g	gravitational acceleration (m/s^2)
ΔH	enthalpy change (J/kg)
L	length (m)
$\dot{m}$	mass flux (kg/m^2s)
Pr	Prandtl number (-)
Re	Reynolds number (-)
Ka	Kapitza number (-)
Nu	Nusselt number (-)
$\dot{q}$	heat flux (W/m^2)
s	layer thickness (m)
U	Overall heat transfer coefficient (W/m^2K)
Greek	
α	film heat transfer coefficient (W/m^2K)

Γ	mass flow per unit periphery (kg/ms)
λ	thermal conductivity (W/mK)
μ	dynamic viscosity (Pa.s)
ν	kinematic viscosity (m^2/s)
ρ	density(kg/m^3)
σ	surface tension (N/m)

subscripts

drop	droplet entrainment
evap	evaporative
i	inside
min	minimal
o	outside
rip	ripple flow
tur	turbulent flow
z	convective boiling

References

Alhusseini, A.A., Chen, J.C., 2000, *Transport phenomena in turbulent falling films,* Industrial Engineering Chemistry Research 39, p2091-2100

Chun, K.R., Seban, R.A., 1971, *Heat transfer to evaporating liquid films,* Journal of Heat Transfer 93, p391-396

Fujita, T., Ueda, T., 1978, *Heat transfer to falling liquid films and film breakdown, pt I Subcooled liquid films, pt II Saturated liquid films with nucleate boiling,* International Journal of Heat and Mass Transfer 21, pt I: p97-108, pt II: 109-118

Hewitt, N. J. and McMullan, J.T., 1997, *The replacement of CFCS in refrigeration equipment by environmentally benign alternatives,* Applied Thermal Engineering 17, p955-972

Kupriczka R., Rotkegel, A., Ziobrowski, Z., 2002, *Heat transfer to evaporating liquid films within a vertical tube,* Chemical Engineering and Processing 41, 23-28

McAdams, W.H., Kennel, W.E., Minden, C.S., Carl, R., Picornell, P.M., Dew, J.E., 1949, *HEat transfer at high rates to water with surface boiling,* Industrial and Engineering Chemistry 41 (9) p1945-1953

Appendix 2 High ice fractions: Non-Newtonian Rheology

A2.1 Rheology

Experimental validation of the viscosity model of Thomas by Kauffeld et al. (1999) for ice slurries with ethanol as freezing point depressant, showed considerable errors at ice fractions above 0.20. It was assumed that at higher ice fractions ice slurries no longer have Newtonian flow behavior. The boundary of the transition into non-Newtonian behavior is however not sharp. In the transition area around 0.20 ice slurries may still be considered as Newtonian fluids if a small inaccuracy is allowed in calculations.

For ice fractions above 0.20, two types of rheology have been proposed: Pseudo-plastic (Guilpart et al., 1999; Ben Lakhdar, 1998) and Bingham type flow behavior (Egolf et al., 1999; Frei and Egolf, 2000). In all researches the rheology is purely viscous.

A diagram of shear stress versus the shear rate for the three types of rheology is given in Figure A2.1. Experimental results of various researches differ widely, therefore a conclusion about the type of rheology that is valid for ice slurries above 0.20 cannot be drawn.

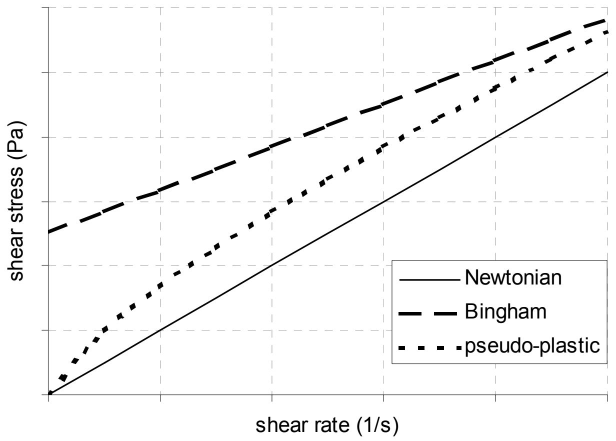

Figure A2.1: Rheograms of three types of flow behavior

Pseudo-plastic rheology is described by a power law correlation:

$$\tau = K \cdot \gamma^n \tag{A2.1}$$

in which *n* is the power law index and *K* the consistency. For a Newtonian fluid n=1, $K=\mu$ and Equation A2.1 reduces to the Newtonian case. If *n* is smaller than 1, the flow behavior is pseudo-plastic. Correlations for *K* and *n* versus the ice fraction were determined by Guilpart et al. (1999).

The viscosity of power law fluids depends on the shear rate and is therefore an *apparent* viscosity. It is determined with:

$$\mu_{app} = \frac{\tau}{\gamma} = K \cdot \gamma^{(n-1)} \tag{A2.2}$$

For Bingham type flow behavior, a critical shear stress (τ_0) is included:

$$\tau = \mu \cdot \gamma + \tau_0 \tag{A2.3}$$

If the shear stress is lower than the critical value ($\tau<\tau_0$) the shear rate is zero ($\gamma=0$). For Bingham rheology also an apparent viscosity depending on shear rate is defined:

$$\mu_{app} = \frac{\tau}{\gamma} = \mu + \frac{\tau_0}{\gamma} \tag{A2.4}$$

A2.2 Rheology Effects on Ice Slurry Cooling Cycle Performance

Laminar Heat Transfer

For the case of an isothermal tube wall theoretical correlations have been developed for heat transfer in circular tubes under laminar flow conditions. The average Nusselt number is given by (Chhabra and Richardson, 1999):

$$Nu = \frac{\alpha \cdot D}{\lambda} = 1.75 \cdot \Delta^{1/3} Gz^{1/3} \tag{A2.5}$$

valid for Gz>100, with *Gz* the Graetz number:

$$Gz = \pi \cdot Re \cdot Pr \cdot \frac{D}{4 \cdot z} \tag{A2.6}$$

in which the Reynolds number is calculated using the apparent viscosity, which leads to:

$$Re = \frac{\rho \cdot \mathrm{v}^{2-n} \cdot D^n}{8^{n-1} \cdot K \cdot \left(\frac{3 \cdot n + 1}{4 \cdot n} \right)^n} \tag{A2.7}$$

which reduces to the Newtonian Reynolds number for $n=1$ and $K=\mu$.
For Newtonian fluids $\Delta=1$, for Power law fluids:

$$\Delta = \frac{3 \cdot n + 1}{4 \cdot n} \tag{A2.8}$$

The values of *n* determined by Guilpart et al. (1999) for ice slurries are always smaller than 1, as can be seen in Equation A2.9, valid for $0 \le w_i \le 0.28$:

$$n = 0.263 + \frac{0.737}{1 + \left(w_i / 0.122 \right)^{8.34}} \tag{A2.9}$$

Values of *K* reported by Guilpart et al. for $0 \le w_i \le 0.13$ are:

$$K = \exp\left(-5.441 + 832.4 \cdot w_i^{2.5} \right) \tag{A2.10}$$

and for $0.13 \le w_i \le 0.28$:

$$K = \exp\left(-6.227 + 16.478 \cdot w_i^{0.5} \right) \tag{A2.11}$$

From Equations A2.8 and A2.5 it may appear that laminar heat transfer coefficients are augmented at decreasing values of *n*, which increases the value of Δ. It should however be noted that this is not necessarily the case, as also the Reynolds number is affected by *n*.

For Bingham fluids:

$$\Delta = \frac{3}{\left(3-\varphi-\varphi^2-\varphi^3\right)} \qquad \text{(A2.12)} \qquad \text{with:} \qquad \varphi = \frac{\tau_0}{\tau} \qquad \text{(A2.13)}$$

If flow occurs, the shear rate is higher than the critical shear stress and $\varphi<1$ and $\Delta>1$, similar to power law rheology. The apparent viscosity of Bingham fluids also decreases at increasing shear rates.

Turbulent Heat Transfer

Heat transfer coefficients for non-Newtonian flows under turbulent conditions may be estimated with (Chhabra and Richardson, 1999):

$$j_H = \left(\frac{\alpha}{\mu\cdot \mathrm{v}\cdot Cp}\right)\cdot Pr^{2/3}\left(\frac{\mu_{wall}}{\mu_b}\right)\cdot\left(\frac{L}{D}\right)^{1/3}\cdot\Delta^{1/3} = 1.86\cdot Re^{-1/3} \qquad \text{(A2.14)}$$

in which also the apparent viscosity must be used. This viscosity influences the heat transfer coefficient to the power of -1/3. This effect combined with $\Delta>1$ in Equation A2.14, indicates that turbulent heat transfer coefficients for ice slurries are lower than predicted with Newtonian rheology.

Pressure Drop

For non-Newtonian fluids, the pressure drop for flow in tubes is estimated with:

$$\Delta p = 2f\cdot\rho \mathrm{v}^2\cdot L/D \qquad \text{(A2.15)}$$

In which the friction factor is influenced by the rheology. For Bingham fluids the friction factor is given by (Frei and Egolf, 2000):

$$f = \frac{16}{Re}\cdot\left(1+\frac{He}{6\cdot Re}-\frac{He^4}{3\cdot f^3 Re^7}\right) \qquad \text{(A2.16)}$$

where He is the Hedstrom number, defined as:

$$He = \frac{\rho\cdot D^2\cdot\tau_0}{\mu^2} \qquad \text{(A2.17)}$$

In which the apparent viscosity is used in both the Hedstrom and Reynolds numbers. The friction factor is not explicit in Equation A2.16 which complicates modeling. For ice slurries it is determined that a high apparent viscosity results in a high pressure drop and high pumping power dissipation.

An empirical form of the Blasius equation for flows of turbulent Power law fluids is (Irvine, cited in Chhabra and Richardson, 1999):

$$f=\left[\frac{2^{n+4}}{7^{7n}}\left(\frac{4n}{3n+1}\right)^{3n^2}\cdot\frac{1}{Re}\right]^{\frac{1}{3n+1}} \tag{A2.18}$$

where the Reynolds number is given by Equation A2.7. The Reynolds number is calculated with the apparent viscosity. At decreasing values of *n,* the friction factor predicted with Equation A2.18 increases.

For turbulent Bingham flow conditions an empirical method was presented by Darby (cited in Chhabra and Richardson, 1999), where a turbulent friction factor, f_T, is combined with the laminar friction factor, f_L,, for example calculated with Equation A2.16.

$$f=\left(f_L{}^b+f_T{}^b\right)^{1/b} \tag{A2.19a}$$

$$f_T=10^a\,Re^{-0.193} \tag{A2.19b}$$

$$a=-1.47\cdot\left(1+0.146\cdot\exp(-2.9\cdot10^5\cdot He)\right) \tag{A2.19c}$$

$$b=1.7+40.000/Re \tag{A2.19d}$$

At increasing yield stresses the friction factor increases, thereby also increasing the pressure drop.

Throughput
The throughput of ice slurries evaluated as Power law fluids can be predicted with:

$$\varphi_v=\frac{n}{3\cdot n+1}\pi\cdot r^3\left(\frac{r}{2\cdot K}\cdot\frac{\Delta p}{\Delta z}\right)^{1/n} \tag{A2.20}$$

The predicted throughput of ice slurries at equal pressure drop evaluated as pseudo-plastic fluids will be lower than for Newtonian fluids, mainly because the value of *K* predicted with Equation A2.10 and A2.11 is generally higher than the viscosity of ice slurries evaluated as Newtonian fluids.
The correlation between pressure drop and throughput for Bingham fluids is known as the Buckingham-Reiner equation (Janssen and Warmoeskerken, (1991):

$$\varphi_v=-\frac{\pi\cdot r^3}{\mu}\cdot\left(\frac{\tau_0{}^4}{12}-\frac{r}{8}\cdot\frac{\Delta p}{\Delta z}-\frac{\tau_0}{3}\right) \tag{A2.21}$$

in which the apparent viscosity must be used. An increased yield stress leads to a reduced throughput at the same pressure drop. High shear rates reduce the apparent viscosity of Bingham fluids and increase throughput.

Liquid/Solid Fluidization

An extensive review of non-Newtonian fluid flow in fixed and fluidized beds is given by Chhabra et al. (2001). Fluidization conditions of power law fluids may be estimated with the Richardson and Zaki correlations if no visco-elastic effects occur. Since it is assumed that ice slurries have purely viscous flow behavior, the Richardson and Zaki model can be used for ice slurries. The Reynolds number of Equation A2.7 is calculated using the particle diameter.
For 4 mm spherical particles in a 56 mm fluidized bed, the fluidization velocities predicted using the pseudo-plastic rheological data of Guilpart et al., (1999) are considerably lower than the velocities of the Newtonian fluids. At an ice fraction of 0.25 for ethanol based ice slurry at –5 ^{o}C, the predicted fluidization velocity is 25% lower than for the Newtonian flow. During the experiments the maximum ice faction in the fluidized bed system was 0.15. At this ice fraction the difference between the predictions is 8%.

Only very limited research has been done with non-spherical particles fluidized with non-Newtonian fluids. For the fluidized bed ice slurry generator, effects of non-Newtonian flow conditions will be relatively unimportant, as it is seen that low ice fractions are relatively efficient.

A2.3 Conclusion

Some of the effects of non-Newtonian rheology on the ice slurry secondary cooling cycle have been discussed using general correlations. The transition to non-Newtonian rheology will lead to a reduced system performance, as the apparent viscosity is generally higher than the viscosity of Newtonian fluids. Heat transfer coefficients and pressure drops are predicted to increase. High shear rates may be applied to reduce negative effects, because both the Bingham and the power law evaluation of ice slurries lead to decreasing apparent viscosity at increased shear rates.

It was already seen that too high ice fractions in certain parts of the system decrease system performance also for Newtonian fluids. Negative effects of non-Newtonian rheology are therefore not expected to occur frequently in actual cooling systems. Furthermore, it has been reported that the errors induced by assuming non-Newtonian rheology are small for ice fractions up to 0.25.

Nomenclature

a	function (-)
b	function (-)
Cp	heat capacity (J/kgK)
D	diameter (m)
f	friction factor (-)
Gz	Graetz number (-)
He	Hedstrom number (-)
j_H	heat transfer factor (-)
K	consistency (Pa.s^n)
L	Length (m)
n	power law index (-)
Nu	Nusselt no. (-)
Δp	pressure drop (Pa)
Pr	Prandtl number (-)
r	radius (m)
Re	Reynolds number (-)
v	velocity (m/s)
w_i	ice fraction (-)
z	height (m)

Greek

α	heat transfer coefficient (W/m^{2}K)
$\dot{\gamma}$	shear rate (1/s)
Δ	non-Newtonian ratio (-)
λ	thermal conductivity (W/mK)
μ	dynamic viscosity (Pa.s)
φ	Bingham ratio (-)
φ_v	volumetric flowrate (m^3/s)
ρ	density (kg/m^3)
τ	shear stress (Pa)
τ_o	yield stress (Pa)

Subscript

app	apparent
b	bulk
i	ice
L	laminar
T	turbulent
wall	wall

References

Ben Lakhdar, M.A. 1998, *Comportement thermo-hydraulique d'un fluide frigoporteur diphasique: Le coulis de glace*, Thesis de l'INSA de Lyon, France, 1998

Chhabra and Richardson, 1999, *Non-Newtonian flow in the process industries*, Butterworth-Heinemann, ISBN 0-7506-3770 6

Chhabra, R.P., Comiti, J., Machac, I., 2001, *Flow of non-Newtonian fluids in fixed and fluidised beds (review)*, Chemical engineering science 56, p1-27

Egolf, P.W., Sari, O., Meili F., Moser, P., Vuarnoz, D., 1999, *Heat transfer of ice slurries in pipes*. Proceedings of the 1st workshop on ice slurries of the IIR, Yverdon-les-Bains, Switzerland, IIF/IIR, p106-123

Frei, B. and Egolf, P.W., 2000, *Viscometry applied to the Bingham substance ice slurry*, Proc. of the 2nd workshop on Ice Slurries, IIR Paris, p48-60

Guilpart, J., Fournaison, L., Ben Lakhdar, M.A., Flick, D., Lallemand, A., 1999, *Experimental study and calculation method of transport characteristics of ice slurries*, 1st workshop on ice slurries of the IIR, Yverdon-les-Bains, Switzerland, IIF/IIR, p74-82

Janssen, L.P.B.M., Warmoeskerken, M.M.C.G., 1991, *Transport phenomena data companion*, 2e druk, Delftse Uitgevers maatschappij (DUM)

Kauffeld, M., Christensen, K.G., Lund, S., Hansen, T.M., 1999, *Experience with Ice Slurry*, Proc. of the 1st workshop on Ice Slurries, Yverdon-les-Bains, Switzerland, IIR, p42-73

Acknowledgments

This research has been funded in part by Novem in the framework of the BSE-NECST program, contracts no. 249.402.0220 and 249.01.04.12.0010.

Dick Klaren and Koppe van de Meer of Klarex Technology B.V. (Now: Klaren BV) are acknowledged for supplying vital components and materials for the experimental set-up, accompanied with valuable technical advice.

Dankwoord

Tot slot wil ik mijn dank betuigen aan iedereen die een bijdrage geleverd heeft aan het tot stand brengen van dit proefschrift en/of aan mijn prettige bestaan als promovendus.

Allereerst gaat mijn dank uit naar Carlos Infante Ferreira, een betere begeleider had ik mij niet kunnen wensen. Al mijn ideeën en problemen kon ik altijd uitvoerig met hem bespreken, ook in tijden dat studenten zijn deur platliepen voor projecten en colleges.
Zonder de brede visie van Dick Klaren had dit onderzoek nooit bestaan. Zijn ideeën van begin jaren negentig lagen aan de basis van dit onderzoek. Henk van der Ree wil ik bedanken voor het promotorschap en het blijven volgen van het onderzoek, ook na zijn emeritaat en verhuizing naar de andere kant van het land.
De bijdrage van Pepijn Pronk aan dit onderzoek was zeer groot. Eerst als uitstekende afstudeerder, vervolgens als collega-promovendus aan de wervelbed-kristallen-generator. Door zijn inbreng werd het onderzoek enorm vooruit geholpen en kon ik mijn proefschrift tot op het laatst aanscherpen. Behalve de discussies over het onderzoek zijn ook de diverse uitstapjes zeer memorabel, zoals de internationale ijs slurry workshops en andere bijeenkomsten, maar ook de California Energy Tour. Pepijn, bedankt.
Koppe van der Meer wil ik bedanken voor de vele wervelbed-adviezen en het doen van een aantal experimenten. Na zijn bezoekjes aan het lab konden grote stappen vooruit gezet worden met de proefopstelling.
Marius van der Gun werkte een tijd mee aan het project als postdoc, waardoor de kristallisatie aspecten goed voor het voetlicht gebracht konden worden. Met hem bedank ik ook de mensen van Apparatenbouw, Raymond Vaessen, Chrismono Himawan en natuurlijk prof. Witkamp. Behalve kristallisatie expertise stelden zij ook hun (foto-) apparatuur ter beschikking.

De proefopstelling is mede door de inspanningen van de technische mensen van het lab tot stand gekomen. De bijdrage van Martin Verwaal was hierin erg groot, ook Jasper, Tjibbe, Sam, Johan, Wim en Henk bedank ik voor hun deskundigheid.

De heren die in Nederland actief bezig zijn met ijs slurries wil ik graag even noemen: Rob Jans (Fri-jado), Richard Beissman (York Inham), Jelle Nijdam en Pieter Jellema (Solutherm), Jan Gerritsen (Grenco) en Erik Hoogendoorn (GTI), met hen bedank ik ook Jos Reinders van Novem. De internationale contacten waren ook goed, maar zouden nooit zo goed geweest zijn zonder de oprichters van de IIR Ice Slurry Workgroup, Peter Egolf en Michael Kauffeld.

Dan bedank ik alle mensen die voor de goede sfeer op de vakgroep zorgden, waarbij ik met vakgroep iedereen van KK, EV, ET en ETh bedoel. Ik ga niet iedereen bij naam noemen, maar wel Dmytro Zaytsev en Dongseon Kim, mijn kamergenoten, Roland, Jan, Luciënne,

Bing, Wojtek, Francesco, Ana Abel, Johanna, Ömer, Marco, Duco en Rob. Zonder jullie had ik het een stuk minder naar mijn zin gehad.
Ook bedank ik alle studenten van het dispuut en anderen die bijdroegen aan de organisatie van studiereizen en bedrijfsbezoeken: Dankzij jullie kon ik het lab vaak op prettige wijze verlaten, er iets van leren en ook nog de goede zaak van de ijs slurries verkondigen.

Pepijn Pronk en Erik van der Werf bedank ik speciaal dat ze mij tijdens de promotiezitting bij willen staan als paranimf.

Mijn ouders bedank ik voor de uitstekende basis die ze mij meegaven en hun luisterende oren tijdens mijn promotie. Buiten mijn onderzoek waren er genoeg mogelijkheden om mijn verhaal kwijt te kunnen en om even aan iets anders te denken. Aan mijn broers, familie, huisgenoten, vrienden van Jansbrug, AV'40 en daarbuiten: Bedankt voor jullie ontspanning, hier is dan het resultaat van mijn inspanning van de afgelopen jaren.

Lieve Wilma, bedankt voor je steun en geduld. Ik heb regelmatig gezegd dat het proefschrift bijna af was, waarna zich uiteraard weer nieuwe ontwikkelingen voordeden, maar nu is het dan écht zover. Vakantie?

Curriculum Vitae

Op de 22e juni van 1975 werd Jeroen Meewisse geboren te Pijnacker. Zijn eerste werkervaring deed hij al snel op in de komkommerkas van zijn ouders. Hoewel hij nog altijd tuinder zou kunnen worden, wijst voorlopig weinig in die richting.

1987-1993	Gymnasium-β, St. Stanislascollege, Delft
1993-1998	Scheikundige Technologie, Technische Universiteit Delft
1999-2004	Promovendus Werktuigbouwkunde, sectie Engineering Thermodynamics (voorheen Koudetechniek en Klimaatregeling)
2004-	Technisch Adviseur bij het Bureau voor de Industriële Eigendom